OFET SEMICONDUCTOR BLENDS FOR ADVANCED ELECTRONIC DEVICES

ORGANIC FIELD EFFECT TRANSISTOR SEMICONDUCTOR BLENDS FOR ADVANCED ELECTRONIC DEVICES INCLUDING UV PHOTOTRANSISTORS AND SINGLE WALLED CARBON NANOTUBE ENHANCED DEVICES

By CHAD STEVEN SMITHSON, B.Sc., M.Sc.

A Thesis Submitted to the School of Graduate Studies in Partial Fulfilment of the Requirements for the Degree Doctor of Philosophy

University of Guelph HONOURS BACHELOR OF SCIENCE (2007), Guelph Ontario (Chemical Physics)

University of Guelph MASTER OF SCIENCE (2010), Guelph Ontario (Synthetic Inorganic Chemistry)

TITLE: Organic Field Effect Transistor Semiconductor Blends for Advanced Electronic Devices Including UV Phototransistors and Single Walled Carbon Nanotube Enhanced Devices: Chad Steven Smithson, B.Sc. (University of Guelph), M.Sc. (University of Guelph) SUPERVISOR: Professor S. Zhu NUMBER OF PAGES: xxxi, 215

Lay Abstract

An emerging field of electronics is the use of organic materials that can be solution processed, to reduce manufacturing costs and make new and interesting products. Here we used unsorted carbon nanotubes blended into the semiconductor layer of a transistor, providing a bridge for the energy mismatch between the electrodes and the semiconductor. This allowed us the freedom to choose different metals to act as our electrodes when making electronic devices. Additionally through the correct choice of semiconductor, we added device functionality, making it responsive to UV-A light. This produced a device that could act as a UV-A sensor, logic switch or memory device. These devices are air stable and solution processable, a necessity if they are to be used in real world applications.

Abstract

Two major projects involving the use of solution processed blended semiconductors for organic field effect transistors (OFET) were explored. The first incorporated unsorted single walled carbon nanotubes (SWCNTs) into a diketopyrrolopyrrole-quarterthiophene (DPP-QT) semiconductor to enhance the mobility of the OFET. 2 wt % SWCNT was found to be the optimal blend ratio, nearly doubling the device mobility (0.6 to 0.98 $cm^2/V \cdot s$). Beyond this ratio, the metallic content of the SWCNT's dropped the on/off ratio below acceptable levels. When source drain metals who's work function poorly matched that of the DPP-QT semiconductors highest occupied molecular orbital (HOMO) were used, the SWCNT could dramatically reduce the charge injection ratio with best results achieved for Al, dropping the contact resistance from 10^5 to 45 MΩ. The second project explored the addition of small molecule additives into a UV-sensitive semiconductor 2,7-dipentyl[1]benzothieno[3,2-*b*][1] benzothiophene (C5-BTBT) mixed with a polymethyl methacrylate (PMMA) polymer binder. We generated a C5-BTBT based phototransistor sensitive to UV-A light. The HOMO and lowest unoccupied molecular orbital (LUMO) of C5-BTBT and the various additives were measured and discovered to play a critical role in how the device operates. We discovered if an additive has a LUMO lower in energy than C5-BTBT, it can act as a charge trap for a photogenerated electron. Electron deficient additives were found to retain a trapped electron for an extended period of time, allowing the

device to remain in a high current state for an extended period of time (>1 hour). This provides an opportunity for the device to be used as an optical memory system or photoswitch. The best system could detect UV-A with a $P_{ill} > 10^5$ and a photoresponsivity of 40 A/W at a P_{inc} of 0.0427 mW/cm^2.

Acknowledgments

After obtaining my MsC degree, I was not sure I was up to the task of going through the process again to obtain a PhD, which would take twice as long. Luckily I was convinced by a man much smarter than I, that this would be a good life decision. Thank you Dr. Archie Hamielec for introducing me to Dr. Shiping Zhu, and taking the time to teach me the fundamentals of polymer engineering. This has sent me down a path I did not believe I would have pursued otherwise.

Thank you Dr. Shiping Zhu for being an excellent supervisor, who believed in me from the start, and allowed me an incredible amount of academic freedom during my PhD. It was through your insistence and kindness that I was able to travel China, visiting research facilities and the Zhejiang University. You taught me a great deal about being a leader and how to focus my research without getting sidetracked on small irrelevant details. I believe the most important thing you taught me was that everything in life needs balance. Whether it be polymer production using a continuous flow process or how to split my time between my fiancé, friends, family and work, balance is the key.

Dr Wu, you have been instrumental in guiding me into the world of organic electronics. Thank you for being both my supervisor at the Xerox Research Centre of Canada and my teacher. Coming from chemistry, there was so much for me to learn about printed electronics, be it device design, manufacturing, operating principles, or just how to make a simple transistor. You taught me all

this and were always there to help keep me inspired in my work. Thank you for all the effort you provided me, I could not have done it without you.

Additionally, I would like to thank the Xerox Research Center of Canada for allowing me to perform my research at your facilities as well as providing me a fluctuating office location.

Thank you to my committee members Dr. Petric and Dr. Thompson for providing another perspective for how and where my research was to go. Your input was greatly appreciated.

To everyone I met at both McMaster and Xerox, thanks for all your help academically, while showing me that being a scientist doesn't mean you can't have fun every day.

Thanks to all my friends who have continued to be an incredible group of people I can always count on. I know many of you believe I spend my days working in a lab making flubber, but that hasn't deterred you from always providing me with an excellent outlet from the stress of school. With all the bachelor parties/weddings and baseball games, I don't know where I found the time to actually get any research done.

To my parents John and June, I owe an extra special thank you. Your continued faith in me after all these years of schooling has been truly incredible. Thank you for letting Erin and I stay with you at the start of this endeavor despite not

knowing how long it would take for us to move on. Your continued belief that I will one day be a millionaire has remained un-waivered after all these years, despite the bank statements showing otherwise. I am always hearing how proud you are of me, which continues to motivate me to achieve more. I look forward to sharing many drinks with you on the porch to commemorate this achievement.

I must thank my future father and mother in law Dave and Cathy Dodds, who have taken me in, and provided an additional support network for me. From the start you have always shown faith in me despite my lack of a clear future once school ends.

Most importantly I must thank my soon to be wife Erin Dodds, who has been with me through my entire post graduate career. Despite not having a lot of money, I have always felt rich with you. I know when I finished my Masters degree I said I would not put you through four more years of school, but you supported me anyways when I told you there were about to be four more years in our future. I could not have enjoyed my time in China without you, where you made the culture shock both bearable and enjoyable. Years ago you won my heart, but now recently have won over my stomach with your career change to being a pastry chef. Our future is ahead of us, and this degree will only springboard us to greatness. Thanks for being with me through this adventure.

Table of Contents

Abstract

Acknowledgments vi

Table of Contents ix

List of Tables xv

List of Figures xvii

List of Abbreviations xxviii

Important Labelled Molecules xxxi

Declaration of Academic Achievement xxxii

Chapter 1 Introduction/Background Information

1.1 Motivation 2

1.2 Introduction to organic field effect transistors 2

1.3 Device design 5

1.4 OFET device materials/fabrication 5

1.5 OFET parameter extraction

1.5.1 Transfer and output curve extractable parameters 6

1.5.2 Contact resistance 11

1.5.3 Charge carrier density 12

1.6 Movement of an electron in an organic thin film 13

1.7 Historical progression of OFET design 15

1.8 Phototransistor review

1.8.1 General photodetectors 17

1.8.2 Photochromic devices 19

1.8.3 Phototransistors 22

1.8.4 UV sensitive organic phototransistors 23

1.9 Outline of thesis chapters 29

1.10 References 31

Chapter 2 Using Unsorted Single-Wall Carbon Nanotubes to Enhance Mobility of Diketopyrrolopyrrole-Quarterthiophene Copolymer in Thin-Film Transistors

2.1 Abstract 38

2.2 Preface 39

2.3 Start of Journal Article: Introduction 39

2.4 Results and Discussion

2.4.1 Materials 42

2.4.2 Dispersion and thin film characterization 43

2.4.3 Electronic characteristics 51

2.5 Conclusion 55

2.6 Experimental section

2.6.1 Materials and general methods 56

2.6.2 OTFT fabrication and evaluation 57

2.7 Supporting information

2.7.1 Additional information about SWCNT 58

2.7.2 SWCNT dispersion 60

2.7.3 Depiction of transistor device 61

2.7.4 Additional SEM images 62

2.7.5 Additional AFM images 64

2.7.6 Electrical characterization 65

2.8 Appendix A 66

2.9 References 71

Chapter 3 Unsorted Single Walled Carbon Nanotubes Enabled the Fabrication of High Performance Organic Thin Film Transistors With Low Cost Metal Electrodes

3.1 Abstract 77

3.2 Start of paper 78

3.3 Supplementary information

3.3.1 Experimental 87

3.3.2 OTFT fabrication and evaluation 89

3.3.3 Instrumentation 90

3.3.4 Atomic force microscopy 91

3.3.5 Additional electrical characterization 91

3.4 Appendix B 94

3.5 References 104

Chapter 4 A More Than Six Orders of Magnitude UV-Responsive Organic Field-Effect Transistor Utilizing a Benzothiophene Semiconductor and Disperse Red 1 for Enhanced Charge Separation

4.1 Abstract 107

4.2 Start of paper: Introduction 107

4.3 Experimental section 122

4.4 Acknowledgements 124

4.5 Supporting information

4.5.1 Synthesis of p-DR1 124

4.5.2 Solution preparation 126

4.5.3 Addition electronic characterization 127

4.5.4 Long term irradiation measurements at various V_{GS} 128

4.5.5 Biexponential fitting curves 130

4.6 134

Chapter 5 Effect of Azobenzene Derivatives on UV-Responsive Organic Thin-Film Phototransistors Using a 2,7-dipentylbenzo[b]benzo[4,5] thieno[2,3-d]thiophene Semiconductor

5.1 Abstract 139

5.2 Start of paper: Introduction 140

5.3 Experimental / results 145

5.4 HOMO LUMO energy level determination 152

5.5 Charge transfer and trapping based upon HOMO LUMO energy levels 155

5.6 Conclusions 161

5.7 Acknowledgements 162

5.8 Supporting information

5.8.1 Experimental 163

5.8.2 Experimental Data 165

5.9 References 173

Chapter 6 UV Response Time Manipulation Using Non Isomerizable Naphthalene and Anthracene Based Additives

6.1 DFT calculations 177

6.2 Results / discussion

6.2.1 Transfer curves 178

6.2.2 UV response times 180

6.2.3 V_{GS} reset 183

6.3 Conclusion 185

6.4 Experimental / additional characterization

6.4.1 Materials 185

6.4.2 UV-Vis sample preparation / measurements 186

6.4.3 Electrical measurements 187

6.4.4 Optical microscopy measurements 188

6.4.5 UV-Vis measurements 189

References 190

Chapter 7 Rapid UV-A Photo Detection, Using a BTBT Organic Field Effect Transistor Enhanced by a 1,5-dichlor-9,10-dintiro-anthracene Additive

7.1 Abstract 192

7.2 Start of paper 193

7.3 References 202

Chapter 8 Conclusion and Future Work

8.1 Conclusion

8.1.1 SWCNT research conclusions 207

8.1.2 Phototransistor research conclusions 209

8.2 Future Work

8.2.1 Building a more efficient system 211

8.2.2 Altering the electronic nature of C5-BBT 211

8.2.3 Electrode design 212

8.2.4 Generating an all organic device 213

8.3 Contributions of this thesis work 214

8.4 Final thoughts 215

8.5 References 215

List of Tables

1.1 Typical values for gain and response time of common photodetectors 22

1.2 List of major organic and inorganic phototransistors sensitive to UV light .. 26

2.1 Unsorted SWCNT's and their properties used in this study 43

2.2 Average CNT density determined from a visual count of the SEM images (average of 4 images for each CNT loading concentration)..... 49

S2.1 Electrical characterization data for the three systems studies at various SWCNT loadings. 65

A2.1 Mobility and on/off data gathered during device testing for DPP-QT..... 66

A2.2 Mobility and on/off data gathered during device testing for DPP-QT with various loadings of CNT-A..... 67

A2.3 Mobility and on/off data gathered during device testing for DPP-QT with various loadings of CNT-B, no wt% given as it could not be determined..... 69

A2.4 Mobility and on/off data gathered during device testing for DPP-QT with various loadings of CNT-C..... 70

3.1 Contact resistance for a gate voltage of -25 V..... 87

A3.1 Electrical Characterization of devices using Au electrodes at various channel lengths (bold values are the average for each channel length)..... 94

A3.2 Electrical Characterization of devices using Al electrodes at various channel lengths (bold values are the average for each channel length) 97

A3.3 Electrical Characterization of devices using Cu electrodes at various channel lengths (bold values are the average for each channel length)..... 100

A3.4 Extrapolated contact resistance for various V_{GS} values..... 103

4.1 Fitting parameters used to model the UV writing and relaxation curves 118

S4.1 Materials used to prepare solutions for spin coating 127

S4.2 Electronic properties of the OTFTs under ambient conditions and exposed to UV light (V_{DS} = -60 V) 128

S4.3 Electronic properties of the OTFTs under ambient conditions and exposed to UV light (V_{DS} = -0.1 V) 128

5.1 Electronic Characterization Data for the systems studied in dark and under UV light 149

5.2 Values used to model the rise and decay curves of the samples 152

5.3 Cyclic Voltammetry and UV-Vis Data used to experimentally determine the HOMO and LUMO levels as well as the calculated HOMO and LUMO values. 158

S5.1 Materials used to prepare solutions for spin coating 163

S5.2 Materials used to prepare solutions for cyclic voltammetry 164

S5.3 Cyclic Voltammetry Data, all values in (eV)..... 168

6.1 Electrical characterization parameters of the systems studied at a P_{inc} = 3.8 mW·cm^{-2} and V_{DS} = -60 V..... 182

6.2 Materials used to prepare solutions for spin coating..... 186

6.3 Additional electrical characterization..... 187

List of Figures

1.1 The most common OFET device designs. (*a*) top-contact bottom-gate, (*b*) bottom-contact bottom-gate, (*c*) bottom-contact top-gate, (*d*) top-contact top-gate 4

1.2 The basic operation of a p-type OFET. The I_{DS} current is held constant at a negative value. (*a*) With no V_{GS} voltage, charge cannot pass through the channel, (resistance is high), so the current must remain low. (*b*) As a negative V_{GS} is applied, it induces a separation of p^+ and e^- in the semiconductor, allowing for p^+ conductivity. (*c*) A larger V_{GS} causes more e^-/p^+ separation, further lowering channel resistance, increasing current 4

1.3 Cartoon depiction for the fabrication of OFETs made in this thesis 7

1.4 (*a*) Sample I_{DS}-V_{GS} curve with curve features labelled. (*b*) Sample transfer curve. (*c*) Hypothetical curve showing contact resistance (*d*) Cartoon depiction showing contact resistance is independent of channel length 11

1.5 Cartoon representation of a hypothetical device which has both band transport in crystalline areas and hopping transport in amorphous areas..... 14

1.6 The three major forms of nanocarbon SWCNT image courtesy of James Hedberg, licensed under a Creative Commons Attribution-NonCommercial-ShareAlike 3.0 Unported License 16

1.7 Cartoon depiction of photogeneration and e^-/p^+ transport in a (*a*) photodiode, (*b*) photoconductor, (*c*) phototransistor. Note that even though it is drawn larger, the distance between terminals in a two terminal device is much smaller than in the three terminal device 21

1.8 Molecular structures of the organic materials used in UV photodiodes, photoconductors and phototransistors as well as some semiconductors they have been combined with 25

1.9 2,7-dipentyl[1]benzothieno[3,2-*b*][1] benzothiophene (C5-BTBT), the UV sensitive semiconductor studied in this thesis 29

2.1 (*a*) SEM images of CNT-B spin coated on SiO_2 wafer (scale bar 2μm). (*b*) DPP-QT film with a maximum loading of CNT-B (scale bar 1 μm) 45

2.2 Solution UV–Vis spectra. All solutions contain 0.5 wt% DPP-QT polymer in 1,1,2,2-tetrachloroethane with DPP-QT/CNT-A containing 5 wt% CNT-A by solids and DPP-QT/CNT-C containing 5 wt% CNT-C by solids 45

2.3 UV–Vis spectra of 0.5 wt% DPP-QT polymer in 1,1,2,2-tetrachloroethane solution with 5 wt% (*a*) CNT-A and (*b*) CNT-C of the total solutes, before and after centrifuging at 25,000 g for 30 min. The spectra of a dispersion of the same amount of SWCNTs without the polymer were also included 47

2.4 SEM images of CNT films cast on OTS modified silicon wafers. (*a*), (*c*), (*e*) are CNT-A and (*b*), (*d*), (*f*) are CNT-C. Images (*a*) and (*b*) are films cast from a

freshly sonicated solution containing pure CNTs, while (*c*–*f*) are films with an indicated CNT content, in a film of DPP-QT copolymer. Amorphous carbon impurities can be observed as round bright spots in the film. The CNTs were well dispersed with no noticeable aggregates.....48

2.5 AFM images (scan area: 10 μm x 10 μm) of films cast on OTS modified wafers. All films are primarily composed of DPP-QT polymer with varying CNT contents. The images correspond to (*b*) 0 wt%, (*c*) 2 wt%, and (*d*) 5 wt% CNT-A, respectively; (*e*) 2 wt% and (*f*) 5 wt% CNT-C, respectively. Polymer crystal domains are seen to shrink in size with increasing CNT content demonstrating the interruption of the CNTs have on the polymer crystal packing.....50

2.6 XRD of the DPP-QT/CNT-A film shows no interaction of CNTs with polymer crystals. No shifting of the main peak suggesting the CNTs are not being inserted between polymer layers, but are interrupting the packing of the crystal network, causing smaller crystal domains.....51

2.7 Transfer curves for the DPP-QT polymer with various amounts of CNT-A (*a*) and CNT-C (*b*) added by wt% to the film 54

2.8 Mobility and on/off ratio for DPP-QT/CNT-A blend (*a*) and DPP-QT/CNT-C blend (*b*). A maximum mobility was obtained at 2.5 and 2.0 wt% CNT for these two films. The on/off ratio was found to decrease in an exponential fashion corresponding to increasing CNT concentration. The error bars represent the spread of data, with the data points being an average value.....54

S2.1 (*a*) Representation of the structure of graphene. (*b*) An example of how a graphene sheet can be folded into a SWCNT with the m,n translation vectors shown. (*c*), (*d*), (*e*), (*f*), Examples of SWCNTs that can be generated, all of which are semiconducting.....59

S2.2 SEM images of SWCNT films after 2 minutes of probe sonication and left to sit 1 hour before being spin coated. (*a*) Without a polymer the SWCNTs aggregate. (*b*) In the presence of the DPP-QT polymer, the SWCNTs remain dispersed.....61

S2.3 OFET design used to test devices, the semiconductive polymer DPP-QT and a hypothetical SWCNT used to make the semiconductor layer.....62

S2.4 Extra SEM images of semiconductor films.....63

S2.5 Extra AFM images of semiconductor films.....64

S2.6 DPP-QT/ CNT-B at various SWCNT wt%. (*a*), mobility vs SWCNT loading, (*b*) transfer curves.....65

3.1 The diketopyrrolopyrrole-quarterthiophene copolymer (DPP-QT).....81

3.2 (*a*) and (*b*) SEM images of the semiconducting films. (*a*) A pure DPP-QT polymer, showing some crystalline domains of the polymer. (*b*) 2 wt% SWCNTs dispersed in the DPP-QT polymer. The tubes are clearly observed and are randomly oriented. (*c*) and (*d*) AFM images of the semiconducting films. (*c*) DPP-QT polymer, the polycrystalline domains of the material are clearly visible.

(d) 2 wt% SWCNTs dispersed in the DPP-QT polymer. Fewer polycrystalline domains are observed indicating that the SWCNTs disrupt the formation of polycrystalline domains.....82

3.3 Average mobility values without and with SWCNTs for a 40 mm channel length plotted against the work function of the metals.....84

3.4 (*a*), (*b*) Output curves for OTFT having Cu electrodes, without (left) and with (right) SWCNTs and channel lengths of 45 mm and 50 mm respectively. The dashed line represents the slope of the linear region for a V_{GS} = -55 V. The inverse of the slope is equal to the resistance of the device at that V_{GS}. (*c*), (*d*) Channel length vs. resistance for Au and Cu source/drain electrodes at a V_{GS} = -25 V. The resistances were determined from output curves like the ones in (*a*), (*b*). By extrapolating the line of best fit back to the y intercept, the charge injection resistance of the transistor can be determined.....86

S3.1 Cartoon Depiction of the top contact bottom gate FET design, with the work function and HOMO energy levels of the metals used as source/drain contacts and the semiconductor material. The spread in energy level for the unsorted SWCNT's assists in reducing charge injection resistance.....91

S3.2 Transfer curves for OTFTs having Au, Cu and Al electrodes with and without 2 wt% CNT in the DPP-QT film. The transistors have a channel length of 40 μm and a channel width of 1000 μm.....92

S3.3 (*a*) Average mobility (*b*) on/off ratio measurements for the 6 systems studies at various channel lengths 93

S3.4 Average contact resistance vs gate voltage. We observe a divergence towards higher resistances as the V_{GS} approaches the V_{Th} 93

4.1 (*a*) Materials used to form the semiconductor layer of the OTFT and their roles in the film. (*b*) Bottom-gate top-contact transistor design showing how the UV functionality works. (*c*) Optical microscopy images of the two semiconductor films, C5-BTBT appears blue and the polymers appear purple 109

4.2 UV–vis spectra of thin films prepared on glass slides. Absorbance maxima are labeled 112

4.3 Transfer and output curves of the two types of transistors studied. (*a*) and (*c*) were measured under yellow light, (*b*) and (*d*) were measured under an irradiation with 365-nm UV light 113

4.4 Response of OTFTs studied when exposed to UV light (blue-shaded area) at a V_{GS} = 0 V and (*a*) V_{DS} = -0.1 V and (*b*) V_{DS} = -60 V. A 2 s pulse of a V_{GS} = -60 V is used to return the system to its low conductivity state, showing the UV write/erase cycle is repeatable. (*c*) Long-term relaxation measurements of the studied systems when exposed to UV until a saturated I_{DS}. (*d*) Zoom in of (*b*) with curve fitting shown as dotted lines 119

S4.1 Two minute UV irradiation of C5-BTBT:PMMA under various V_{DS} with a constant V_{GS} of 0V followed by removal of UV light to allow relaxation for 45 minutes 129

S4.2 Two minute UV irradiation of C5-BTBT:*p*-DR1 under various V_{DS} with a constant V_{GS} of 0V followed by removal of UV light to allow relaxation for 45 minutes. 129

S4.3 Long Term UV irradiation of C5-BTBT:PMMA at a V_{GS} = 0 V and a V_{DS} = -0.1 V 130

S4.4 Long Term UV irradiation of C5-BTBT:*p*-DR1 at a V_{GS} = 0 V and a V_{DS} = -0.1 V 131

S4.5 Long Term UV irradiation of C5-BTBT:PMMA at a V_{GS} = 0 V and a V_{DS} = -60 V 132

S4.6 Long Term UV irradiation of C5-BTBT:*p*-DR1 at a V_{GS} = 0 V and a V_{DS} = -60 V 133

5.1 (*a*) Materials used to form the semiconductor layer. (*b*) OTFT top contact bottom gate device design. (*c*) Optical microscope images of a PMMA:C5-BTBT film and a PMMA:Azo-1:C5-BTBT film, showing that film morphology is not altered with the addition of the azobenzene small molecule 145

5.2 AFM images of the semiconductor films (scale bar 200 nm). (*a*) Topographical images, (*b*) phase image 147

5.3 Transfer Curves for the 6 systems studied with and without UV light. (*a*) From left to right Azo-4, DR1, Azo-2, PMMA, Azo-3, Azo-1. (*b*) From left to right PMMA, Azo-2, Azo-4, Azo-1, DR1, Azo-3 149

5.4 (*a*) samples irradiated with UV light for 20 minutes to ensure saturation current, the dashed line shows when the UV is removed to show the current decay over time. (*b*) UV write erase cycle of Azo-3:PMMA:C5-BTBT showing the reproducibility and re-writability of the system 151

5.5 (*a*) Cyclic voltammetry measurements of the materials studied. The onset to oxidation ($0/1^{+}$) was used as the experimentally measured HOMO for each system. (*b*) dark boxes, HOMO and LUMO energy levels measured from CV and UV vis, open boxes calculated using DFT theory with a B3LYP/6-311G(d,p) basis set. PMMA from the following reference 155

5.6 The HOMO and LUMO molecular orbitals calculated using DFT theory for (*a*) C5-BTBT, (*b*) Azo-3, (*c*) Azo-2. (*d*), (*e*), (*f*) Experimentally determined HOMO LUMO energy levels of materials involved in charge transfer, explaining how each system reacts to the UV stimulus. The blue arrows represent pathways for electron movement to occur. The red arrow represents a pathway for charge recombination to occur 157

S5.1 Optical Microscope images of films spin coated from 1,1,2,2-tetrachlorethane (TCE) onto an HMDS modified Si/SiO_2 wafer, as well as a

control film spin coated from chlorobenzene. All films show similar morphology when spin coated from the same solvent.....166

S5.2 Transfer curves for all systems studied under dark conditions showing a forward and backward sweep.....167

S5.3 Transfer curves for all systems studied under UV conditions showing a forward and backward sweep.....167

S5.4 Cyclic voltammograms of film materials (vs SCE) showing the onset of reduction or oxidation for.....169

S5.5 UV-vis spectra of film materials with the absorption edge calculations shown.....170

S5.6 (Left side), I_{DS} vs time showing the current rise over a 20 minute UV exposure with the experimental (black) and biexponential curve fitting (red). (Right) I_{DS} decay vs time starting after the 20 minute UV exposure with experimental (black) and biexponential curve fitting (red).....171

S5.7 (Left side), I_{DS} vs time showing the current rise over a 20 minute UV exposure with the experimental (black) and biexponential curve fitting (red). (Right) I_{DS} decay vs time starting after the 20 minute UV exposure with experimental (black) and biexponential curve fitting (red).....172

6.1 DFT calculations of the HOMO (solid boxes), LUMO and LUMO +1 (open boxes) energy levels calculated at the BY3LYP 6-311 G(d,p) level for the

materials used in the semiconductive layer. Grey dashed lines have been added to guide the eye to track the HOMO and LUMO energy levels of C5-BTBT vs the additives 178

6.2 Transfer curves for the studied systems in (*a*) dark conditions and (*b*) under UV illumination..... 180

6.3 (*a*) I_{DS} response at V_{GS} = 0 V during a 20 min irradiation and the 40 min after UV light was removed. (*b*) zoom in of the first 2 min of (*a*) with the 20% of saturation marked with a round blue marker..... 181

6.4 Drain current after being exposed to a 30 second UV exposure, followed by the corresponding gate voltage. All data points were recorded at a V_{GS} = 0 V after the corresponding V_{GS} of the data point was applied for 2 seconds 184

6.5 Optical Microscope image of films spin coated from 1,1,2,2-tetrachlorethane onto an HMDS modified Si/SiO_2 wafer, scale bar is 100μm 188

6.6 Thin film UV vis with the absorbance onset labelled..... 189

7.1 (*a*) Bottom gate top contact TFT device structure, and the materials used to make up the semiconductor layer. (*b*) Transfer curves for the studied systems in the dark and under UV illumination. Output curves for the device in (*c*) the dark and (*d*) under UV illumination 197

7.2 (*a*) Transfer curves of the 2Cl-2NO_2-Anth system under varying UV intensities. (*b*) photoresisitivity (*R*) as a function of P_{inc} with fitting below (black)

and above (blue) P_{inc} saturation and P_{ill} (red) below P_{inc} saturation. Note some data are omitted in (*a*) for viewing clarity. (*c*) I_{DS} response at V_{GS} = 0 V during a 30 second irradiation followed by 5 min with the UV light removed. The inset is the first 20 seconds of irradiation. A red dashed line has been added at 10^{-6} A which was used as the device “on” value. (*d*) Response time of the device to reach 10^{-6} A, vs P_{inc} 199

7.3 I_{DS} response curve with respect to time for a good performing devices, the inlay is a zoom in of the initial irradiation 200

7.4 UV sensing measurements using the 2Cl-2NO_2-Anth system by resetting the system every second measurement with a V_{GS} = -90 V. The plotted data then ignores every second measurement to provide continuous UV sensing. (blue bars have been added to show when the UV light is on) 202

8.1 Potential method to adjust absorbance maximum of BTBT derivatives 212

8.2 Electrode Design allowing for increased surface area with decreased channel length. Additionally the large pads at the ends can allow for the addition of alligator clips as electrode leads, allowing for testing of flexible substrates 213

8.3 Synthesis to generate an all organic substrate with gate and dielectric layer ready for the addition of a solution processed semiconductor 214

List of Abbreviations

AFM	Atomic Force Microscopy
BTBT	benzothiophene
c	Speed of light in a vacuum
C_i	Insulator capacitance
CNT	Carbon Nanotube
CV	Cyclic Voltammetry
CVD	Chemical Vapour Deposition
DFT	Density Functional Theory
DPP-QT	diketopyrrolopyrrole-quarterthiophene
E	Electric field
e^-	electron
E_g	Bandgap energy
EQE	Quantum Efficiency
FET	Field Effect Transistor
g_m	Transconductance
h	Planks constant
HMDS	Hexamethyldisalazane
HOMO	Highest Occupied Molecular Orbital
ITO	Indium Tin Oxide
I_{dark}	Drain source current in the dark
I_{DS}	Drain source current
I_{light}	Drain source current under illumination
I_{ph}	$I_{light} - I_{dark}$
I_{ON}/I_{OFF}	On/off current ratio

λ	Wavelength
L	Channel width
LUMO	Lowest Unoccupied Molecular Orbital
m-CNT	Metallic Carbon Nanotubes
m-SWCNT	Metallic Single Walled Carbon Nanotubes
MISFET	Metal-Insulator-Semiconductor Field Effect Transistor
MOSFET	Metal-Oxide-Semiconductor Field Effect Transistor
N	Density of doping centres
OFET	Organic Field Effect Transistor
OPT	Organic Photo Transistor
OTS-8	octyltrichlorosilane
p^+	hole
P_{ill}	Photocurrent/dark current ratio
P_{inc}	irradiated lights incident power
PMMA	poly(methyl methacrylate)
q	Elementary charge of an electron
R	Photoresponsivity
R_C	Charge injection resistance
R_{DS}	Resistance across the channel
SAM	Self Assembled Monolayer
sc-CNT	Semiconducting Carbon Nanotubes
sc-SWCNT	Semiconducting Single Walled Carbon Nanotubes
SEM	Scanning Electron Microscope
SWCNT	Single Walled Carbon Nanotube
t	Channel thickness
THF	Tetrahydrofuran

μ_{FE}	Field effect mobility
UV-Vis	Ultraviolet Visible
V_{DS}	Drain source voltage
V_{GS}	Gate source voltage
V_{Th}	Threshold voltage
V_{SO}	Switch on voltage
W	Channel length

Important Labeled Molecules

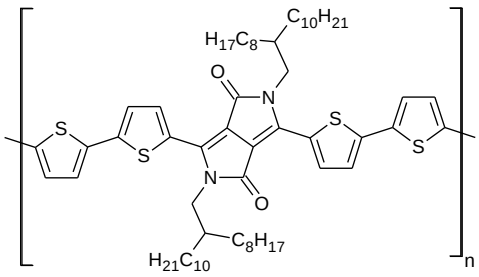

DPP-QT

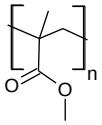

PMMA

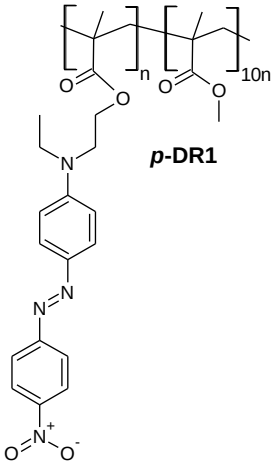

***p*-DR1**

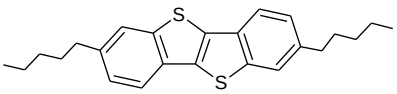

C5-BTBT

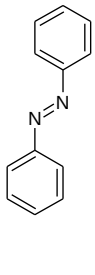

Azo-1

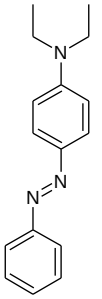

Azo-2

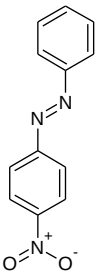

Azo-3

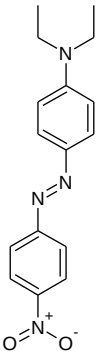

Azo-4

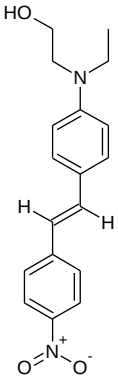

DR1

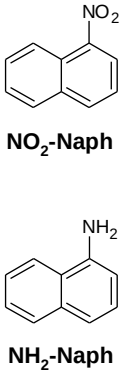

NO_2-Naph

NH_2-Naph

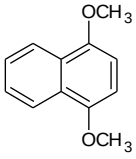

$2OCH_3$-Naph

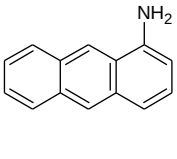

NH_2-Anth

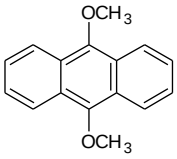

$2OCH_3$-Anth

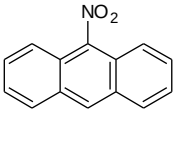

NO_2-Anth

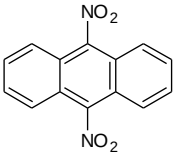

$2NO_2$-Anth

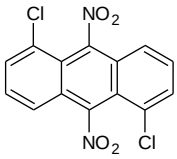

2Cl-$2NO_2$-Anth

Declaration of Academic Achievement

Chad Smithson is the principle author of all five journal articles reproduced in this thesis.

Dr. Shiping Zhu, and Dr. Yiliang Wu were supervisors for all five journal articles.

Dr. Tony Wigglesworth, synthesized the DPP-QT polymer studied in Chapters 2 and 3 as well as the C5-BTBT small molecule studied in Chapter 4.

Sandra Gardner performed SEM analysis for Chapter 2.

Hen-Yong Nie performed AFM analysis for Chapter 2.

Darko Ljubic synthesized the C5-BBT small molecule studied in Chapters 5, 6 and 7.

Each journal article's research was performed during the following timeframe.

Chapter 2: 2012 – 2013

Chapter 3: 2012 – 2013

Chapter 4: 2013 – 2014

Chapter 5: 2014 – 2015

Chapter 6: 2014 – 2015

Chapter 7: 2015

Chapter 1

Introduction / Background Information

1.1 Motivation

This thesis is written as a “sandwich thesis” which is a collection of published works by the author “sandwiched” between an introduction and conclusion. The goal of the research was to produce Organic Field Effect Transistor (OFET) devices utilizing a blended semiconductor layer to enhance the transistor performance. Two major device enhancements were investigated. The first being device mobility improvement through the incorporation of unsorted Single Walled Carbon Nanotubes (SWCNT), and the second was the production of a phototransistor device blind to visible light, but sensitive to UV light. Solution processablity and air stability were important aims of the research. For this reason, only air stable materials that were able to be dissolved in solvents were used. All films were a blend of a polymeric material and at least one other small molecule material or SWCNTs. To help the reader better understand the published works, a brief explanation of the operating principles of an OFET and phototransistor devices is given as well as relevant operation and characterization equations. In addition a small summary of the most prominent UV sensitive organic devices is provided.

1.2 Introduction to organic field effect transistors

The field of semiconductors is massive, with its impact being ubiquitous in our everyday life. By no means can this thesis scratch the surface of semiconductor physics, but instead will direct the reader to equations and topics relevant to this

work. For a greater understanding, the interested reader can consult the abundance of literature on semiconductor physics.[1,2]

Field Effect Transistors (FET) were first proposed back in 1930,[3] with the first metal-oxide-semiconductor FET (MOSFET) being fabricated in 1960.[4] In 1970 organic materials displaying FET properties were reported and in 1976 conducting polymers discovered.[5,6] It was not until 1987 when electrochemically polymerized polythiophene was used in a FET that the concept of the (OFET) was established.[7,8,9] This led to the 2000 Nobel prize in chemistry being awarded for conductive polymers. In the meantime, the more well-known MOSFET also known as a MISFET (Metal-Insulator-Semiconductor FET), became a dominate part of the microelectronics industry due to its superior performance. A general MOSFET device consists of the following parts, a source and drain separated by a semiconductor layer (known as the channel), as well as a gate and dielectric layer where the dielectric layer separates the gate from the semiconductor layer (**Fig 1.1**). The source, drain and gate are highly conductive materials. When a voltage is held constant between the source and drain, the current across the channel can be modulated by applying a gate voltage, which induces a charge accumulation at the semiconductor/dielectric interface, generating a conductive channel. Due to Ohm's law, V=IR, as the resistance of the semiconductor is modulated, the current must change appropriately (**Fig. 1.2**) (note this is accurate only in the linear region, and becomes more complicated in the saturation

region). The result is a simple method to alter current by many orders of magnitude providing one of the most basic building blocks of all electronic devices.

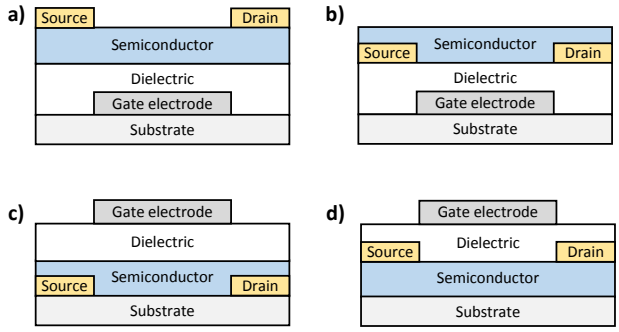

Figure 1.1: The most common OFET device designs. (*a)* top contact bottom gate, (*b)* bottom contact bottom gate, (*c)* bottom contact top gate, (*d)* top contact top gate.

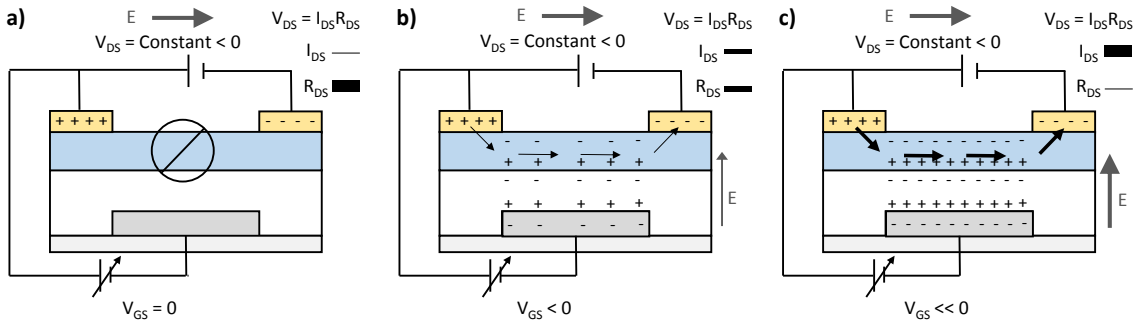

Figure 1.2: The basic operation of a p-type OFET. The I_{DS} current is held constant at a negative value. *(a)* With no V_{GS}, charge cannot pass through the channel, (resistance is high), so the current must remain low. *(b)* As a negative V_{GS} is applied, it induces a separation of p^+ and e^- in the semiconductor, allowing for p^+ conductivity. *(c)* A larger V_{GS} causes more e^-/p^+ separation, further lowering channel resistance, increasing current.

1.3 Device design

Four major designs exist for an OFET. They are top-contact bottom-gate, bottom-contact bottom-gate, top-contact top-gate and bottom-contact top-gate (**Fig. 1.1**). All devices fabricated in this report utilize the top-contact bottom-gate design due to the increased area for charge injection from the source/drain electrodes which results in a lowered charge injection resistance (R_C) increasing device performance.[10] From a manufacturing standpoint, bottom contact devices are easier to fabricate because the organic semiconductor is the last material added, allowing flexibility for how the previous layers are fabricated. However, for research purposes, better performing devices can be made from top contact architecture, allowing one to perform fundamental research on a higher performance system.

1.4 OFET device materials/ fabrication

While countless materials can be used for OFET device fabrication, the literature has adopted a few as the benchmark materials to allow for easy comparison. Undoubtedly the silicon wafer coated with a silicon dioxide layer (Si/SiO_2) is the most widely used gate/dielectric material due to its highly refined manufacturing allowing for extremely repeatable device performance. A wafer can easily be cut to the desired device size, with the SiO_2 layer modified through plasma or ozone treatment to allow for the application of a self-assembled monolayer (SAM). The solution processed equivalent utilizes a number of different materials for the

dielectric, but very commonly uses indium tin oxide (ITO) as the conductive gate, coated on a polymer film such as PMMA. The semiconductor layer can be applied in a number of ways, with the most common being evaporation, solution drop casting, and spin coating. Source and drain electrodes are typically Au, applied by vacuum evaporation or sputtering, but others such as Cu, Al, and Ag are also used. Ag remains the leading candidate for solution processable electrodes as it is easily solubilized and is difficult to oxidize. In this thesis, a top-contact bottom-gate device utilizing a Si/SiO_2 wafer with a SAM and spin coated semiconductor and metal electrodes applied through a shadow mask via evaporation, is used. Device characterization is carried out via three point probe measurements, on a Keithly 4200. **Fig 1.3** provides a cartoon depiction of OFET device fabrication performed in this thesis.

1.5 OFET parameter extraction

1.5.1 Transfer and output curve extractable parameters

The success of the MOSFET was largely due to the enhanced understanding it provided for FET devices. Equations were derived such as that found for the current-voltage measurements across the channel which allows for the characterization of MOSFET devices;

$$I_{DS} = \frac{W}{L}\mu_{FE}C_i\left\{\left(V_{GS} - 2\emptyset_b - \frac{V_{DS}}{2}\right)V_{DS} - \frac{2}{3}\frac{\sqrt{2\epsilon_S q N_a}}{C_i}\left[(V_{DS} + 2\emptyset_b)^{3/2} - (2\emptyset_b)^{3/2}\right]\right\} \textbf{[1]}$$

Where *W* is the channel width and *L* the channel length in (m), μ_{FE} the charge-

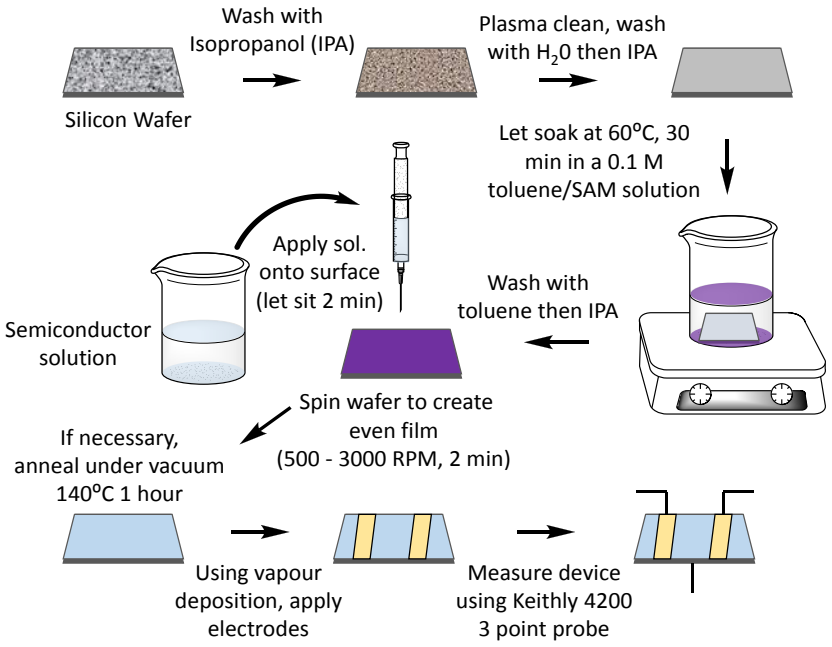

Figure 1.3: Cartoon depiction for the fabrication of OFETs made in this thesis.

carrier field effect mobility in ($cm^2/V \cdot s$), C_i the insulator capacitance per unit area (F/cm^2), ε_S the semiconductor permittivity (F/m), N_a the doping level of the p-type substrate φ_b the potential difference between the Fermi level and the intrinsic Fermi level in (V) and q the elementary charge of an electron (C). Eqn. **[1]** predicts that I_{DS} will increase linearly (linear region) with respect to the V_{DS}, then gradually level off as the V_{DS} approaches the V_{GS} eventually reaching a saturation (saturation region). It has become common practice to use the equations derived for MOSFET devices to characterize OFETs device performance. However, a major difference is that unlike MOSFET devices, OFETs operate in the accumulation regime, not the inversion regime, this simplifies equation **[1]** to; [4,11]

$$I_{DS} = \frac{W}{L}\mu_{FE}C_i\left(V_{GS} - V_{Th} - \frac{V_{DS}}{2}\right)V_{DS} \quad \textbf{[2]}$$

Where;

$$V_{Th} = \frac{qNt}{C_i} \quad \textbf{[3]}$$

N is the density of doping centres (donors or acceptors) and *t* is the channel thickness in (m). The above simplification employs two major assumptions. The first is the gradual channel approximation of drain current relation, which assumes the electric field along the channel is much lower than that across it, which is valid when the distance between the drain and source is much larger than the thickness of the dielectric. The second is that μ_{FE} is constant.[12] **[2]** is a general equation for an OFET, but even simpler equations are extracted for the linear regime ($V_{DS} << V_{GS} - V_{Th}$) and the saturation regime ($V_{DS} > V_{GS} - V_{Th}$);

$$I_{DS,lin} = \frac{WC_i}{L}\mu_{FE}\left(V_{GS} - V_{Th} - \frac{V_{DS}}{2}\right)V_{DS} \qquad (|V_{DS}| << |V_{GS} - V_{Th}|) \quad \textbf{[4]}$$

$$I_{DS,sat} = \frac{WC_i}{2L}\mu_{FE}(V_{GS} - V_{Th})^2 \qquad (|V_{DS}| > |V_{GS} - V_{Th}|) \quad \textbf{[5]}$$

In the linear regime, a plot of $I_{DS,lin}$ vs V_{GS} can allow for the extraction of the V_{Th} and μ_{FE}. In this linear region the device follows Ohm's law with I_{DS} proportional to the drain and gate voltages. Meanwhile in the saturation regime a plot of $(I_{DS,sat})^{1/2}$ vs V_{GS} will provide V_{Th} and μ_{FE}, with the saturation regime being the standard method used for OFET device characterization. In this regime, as the V_{DS} increases and approaches the V_{GS}, the V_{DG} drops to zero causing pinch-off

of the channel. This is when I_{DS} is independent of V_{DS}. Therefore, for a p type device, when V_{DS} is more negative than V_{GS}, I_{DS} tends to saturate due to the pinch off of the accumulation layer. Many materials deviate from this simple model, with much more complicated models existing,[13,14,15,16] but for simplicity, this model is used as the benchmark to compare devices in the literature.

Operation performance is dependent upon two major parameters; (1) Charge transport in the semiconductor layer (mobility μ_{FE}) which is how rapidly charge carriers can move through the material. (2) Contact resistance (R_C), which is the resistance experienced during charge injection and extraction at the source and drain. μ_{FE} can be obtained from the saturation regime, starting with the transconductance $g_{m,sat}$;

$$g_{m,sat} = \frac{\partial I_{DS,sat}}{\partial V_{GS}} = \frac{WC_i}{2L}\mu_{FE}(V_{GS} - V_{Th}) \quad \textbf{[6]}$$

A plot of $g_{m,sat}$ vs V_{GS} will allow one to perform a linear curve fit to extract μ_{Fe} and V_{Th}. In practice this is done by plotting the $\sqrt{I_{DS}}$ vs V_{GS}, in the saturation region using equation **[5]**. Simple manipulation of this equation allows one to extract the required parameters

$$I_{DS,sat} = \frac{WC_i}{2L}\mu_{FE}(V_{GS} - V_{Th})^2 \quad \textbf{[5]}$$

$$\left(\left|I_{DS,sat}\right|\right)^{1/2} = \left(\frac{WC_i}{2L}\mu_{FE}\right)^{1/2}(V_{GS} - V_{Th}) \quad \textbf{[7]}$$

$$\frac{(|I_{DS,sat}|)^{1/2}}{(V_{GS}-V_{Th})} = \frac{\partial(|I_{DS,sat}|)^{1/2}}{\partial V_{GS}} = \left(\frac{WC_i}{2L}\mu_{FE}\right)^{1/2} \quad \textbf{[8]}$$

Where $\frac{\partial(|I_{DS,sat}|)^{1/2}}{\partial V_{GS}}$ is the slope of the linear region. From this we can determine u_{FE}

$$\mu_{FE} = \frac{2L}{WC_i}\left(\frac{\partial(|I_{DS,sat}|)^{1/2}}{\partial V_{GS}}\right)^2 \quad \textbf{[9]}$$

In addition, the V_{Th} is extracted from the x intercept. The V_{Th} for an OFET is the V_{GS} to which localized states are filled causing the Fermi level to move closer to the conduction band, leading to an increase in carrier concentration within it.[17]

$$V_{Th} = \frac{(|I_{DS,sat}|)^{1/2}}{\left(\frac{\partial(|I_{DS,sat}|)^{1/2}}{\partial V_{GS}}\right)} - V_{GS} \quad \textbf{[10]}$$

Traditionally I_{DS}-V_{GS} plots are on a semi-logarithmic scale. From this three more useful characterization parameters can be extracted. The on/off current ratio (I_{ON}/I_{OFF}), the switch on voltage (V_{SO}) and the inverse subthreshold slope. The on/off current ratio is simply the ratio between the device current before the switch on voltage and after current saturation has occurred. This provides a measure of how large the current change for the transistor can be. The V_{SO} is the gate voltage where the current begins to increase in the semi-logarithmic I_{DS}-V_{GS} plot and the inverse subthreshold slope is the slope of the curve between V_{SO}

and V_{Th}. **Fig. 1.4** provides a sample transfer and output curve with all of these parameters labelled.

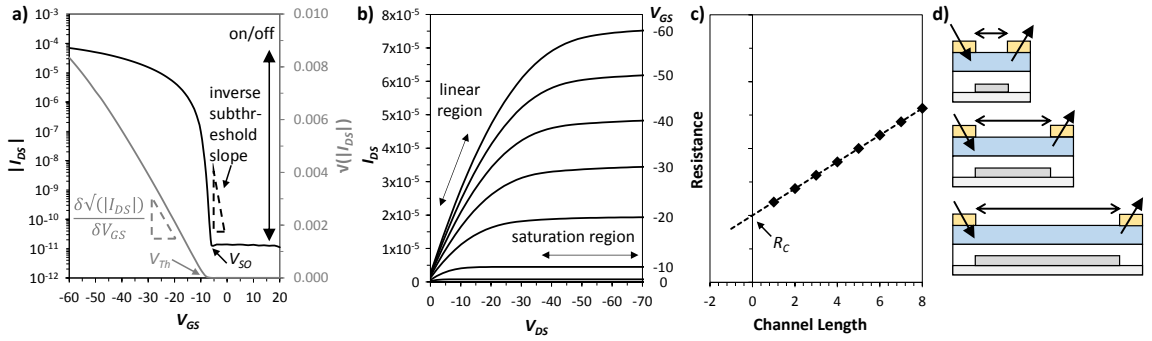

Figure 1.4: (a) Sample I_{DS}-V_{GS} curve with curve features labelled. (*b*) Sample transfer curve. (*c*) Hypothetical curve showing contact resistance (*d*) Cartoon depiction showing contact resistance is independent of channel length.

1.5.2 Contact resistance

Contact resistance (R_C) is another major factor affecting the performance of thin film transistors. To maximize device performance, Ohmic contacts with efficient charge injection are essential. A device always has 2 contact resistance points, one at the source and one at the drain, to which this resistance is independent of channel length. A simple model assumes the resistance across the channel R_{DS} increases linearly with channel length, therefore plotting R_{DS} vs various channel lengths can allow for the extraction of R_C as the intercept.[18] The derivation of this is as follows;

$$\frac{V_{DS}}{I_{DS,lin}}W = R_m W = R_C W + AL \qquad \text{A} = f(R_{ch}) \qquad \textbf{[10]}$$

Where R_mW (Ω·m) is the measured resistivity between source and drain for a given channel width, and A is a parameter related to the channel resistance. Only A is dependent upon L, making the above equation of the form y = mx + b. Therefore, a plot of channel length vs R_mW will yield a linear graph where the slope is A, and the intercept is R_CW (**Fig 1.4**). An ideal device will have an R_C = 0.

1.5.3 Charge carrier density

A semiconductor will have a set number of charge carriers able to take part in conduction. However this can be altered in a number of ways such as adding a dopant material. We can use the equation for V_{Th} **[3]** to determine the increase in carrier density in the active layer between a control and doped conditions by taking the difference between the two.

$$V_{Th}^{doped} - V_{Th}^{control} = \frac{qN_{doped}t}{C_i} - \frac{qN_{control}t}{C_i} \qquad \textbf{[11]}$$

$$\Delta V_{Th} = \frac{qt}{C_i}(N^*) \qquad \textbf{[12]}$$

$$N^* = \frac{\Delta V_{Th} C_i}{qt} \qquad \textbf{[13]}$$

Where ΔV_{Th} is the shift in threshold voltage from the control sample to the doped sample and N^* is the increase in carrier density in the active layer. Traditionally

this is used to estimate the increase in dopant concentration. In this thesis we will use light irradiation as a dopant, so we can be use eqn **[13]** to determine the number of excitons generated for charge transfer when the system is irradiated.[19,20]

1.5 Movement of an electron in an organic thin film

Since their inception, there have been three major fields of OFET's, small molecule OFETs, polymeric OFETS, and blends which typically consist of a small molecule and polymer. Due to the crystalline nature of small molecules, they showed initial success and much of early device design knowledge was obtained from them. To understand the progression of how materials have reached todays designs, one must understand the fundamental mechanisms behind charge transport. Two major mechanisms of electron transport exist; in crystalline materials band transport dominates, while in amorphous materials, charge hopping is dominant. Band transport involves a wave function delocalized over the entire system, making the electron location exist only as probability of the wavefunction. This results in coherent transport, and is very fast. Meanwhile, in the hopping regime, the electron exists as a localized charge carrier on a single molecule or chain segment, to which its movement can be followed between molecules or chain segments making transport incoherent hops. In reality, transport is a mixture of both of these two types, with advanced theories attempting to merge both into one equation, showing a smooth transition from

one regime to the other (**Fig. 1.5**).[21,22] At low temperatures, band transport is dominant, while at higher temperatures, systems transition into the hopping regime with room temperature being a high temperature system. The reason for this is that at higher temperatures, electrons are thermally excited into higher energy molecular orbitals which have a larger 99% probability radius. The result is an increased chance of molecular orbital overlap between molecules, allowing for hopping from one molecule to the next. Band conduction is much faster than hopping, but is difficult to achieve in a solution processed system because it requires a crystalline structure. A result is that for solution processed systems, charge hopping is the dominant form of transport. Therefore, to maximize charge hopping, planar heavily conjugated materials are used which have a large number of π orbitals extending from the system which are able to help delocalize an electron allowing for π-π orbital overlap for hopping to occur.

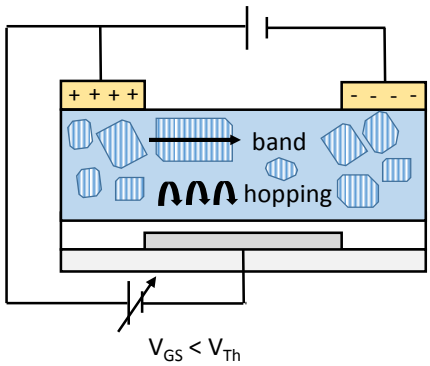

Figure 1.5: Cartoon representation of a hypothetical device which has both band transport in crystalline areas and hopping transport in amorphous areas.

1.7 Historical progression of OFET design

Early work on organic systems was aimed at surpassing the low cost amorphous silicon based devices (a-Si:H) and involved polythiophenes who's conjugated nature created an extended π structure which could allow for π-π orbital overlap. The materials were largely amorphous, making transport dominated by hopping. Quickly research moved to thiophene and acene small molecules where more ordered crystalline structures could be generated increasing molecular overlap and band transport. It became evident that controlling film morphology was essential to increasing mobility.[23] Alkyl side chains were found to enhance solubility while promoting self organization through side chain interdigitization. The result was ordered lamellar stacks of planar materials with increased π-π orbital overlap. Each stack was separated by alkyl side chains, making charge transport occur anisotropically along a chain and between chains via π-π hopping, with little transport occurring between side chain separated stacks. To maximize this film formation, a self-assembled monolayer (SAM) containing alkyl chains was placed at the surface of the dielectric layer. This SAM helps promote molecular self-assembly making the preferred stacking direction be along the plane of the dielectric (edge on).[24] Annealing was another excellent strategy to enhance self-assembly. The next major breakthrough was to assist in generating air stable devices by introducing an electron deficient unit into the conjugated backbone to increase its ionization potential. The result is alternating donor acceptor materials.[25] These materials have been able to form solution processed

films with mobilities >10 $cm^2/V \cdot s$.[26] One other method utilized for device design is the blend of highly semiconducting small molecules with non conducting polymers to assist in film formation.[27,28] In addition reducing charge injection resistance to and from the semiconductor to the source and drain electrodes will help increase device mobility.[29]

The newest wave of design features has been the incorporation of semiconducting nanoparticles into device films due to their well ordered macrostructures. These high aspect ratio materials can show band transport over large distances without requiring the formation of a crystalline film. The family of carbon nanoparticles consisting of Buckyballs, carbon nanotubes and graphene (**Fig 1.6**) have generated the most interest. Chapters 2 and 3 are devoted to this research, focusing on the use of carbon nanotubes.

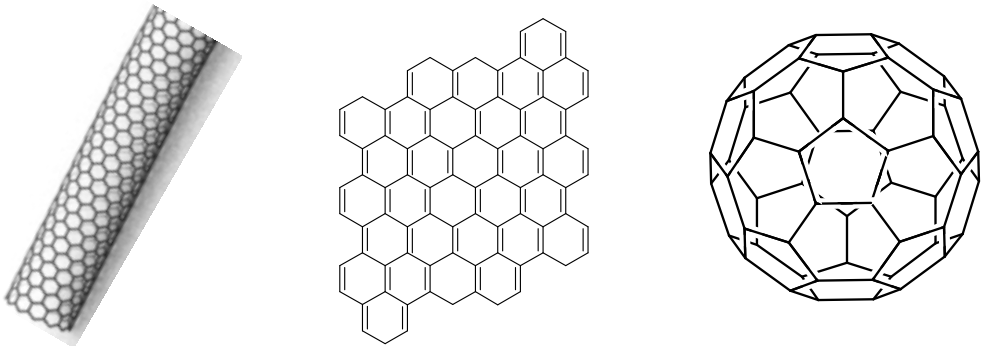

SWCNT **Graphene** **Buckyball**

Figure 1.6: The three major forms of nanocarbon. SWCNT image courtesy of James Hedberg, licensed under a Creative Commons Attribution-NonCommercial-ShareAlike 3.0 Unported License.

Recognizing the pace that device mobility was increasing, we shifted our research focus to the development of OFETs with the advanced functionality of being responsive to UV light, providing another method to operate the device. This is known as photoconductivity, and a brief background on organic phototransistors (OPT) will be given.

1.8 Phototransistor review

1.8.1 General photodetectors

A phototransistor is a subset of a larger group known as photodetectors which are semiconductor devices that can detect optical signals through electronic processes.[1] Two major photodetectors exist, thermal and photon. Thermal detectors detect the change in temperature caused by an incident photon, while the latter allows a photon to excite a charge carrier, causing current. (This thesis focuses on the latter). Photodetectors exploit the photoelectric effect, which requires the formula made famous by Einstein

$$\lambda = \frac{hc}{\Delta E} \qquad \textbf{[14]}$$

λ is the photon wavelength, *h* planks constant, *c* the speed of light in a vacuum, and Δ*E* the change in energy. In this report, Δ*E* is the bandgap energy (E_g) of our photoactive material, providing the minimum wavelength for photon absorption to occur. There are three major processes involved in photodetection. (1) carrier generation by an incident photon. (2) carrier transport and/or multiplication by a current-gain mechanism, (3) extraction of carriers at the terminals to provide the

output current. The number of carriers produced per photon is known as the Quantum Efficiency (EQE), with the ideal EQE being unity. However due to gain effects, this value can be larger than unity. EQE is a fundamental parameter for solar cells and given by the equation

$$EQE = \eta = \frac{(I_{light} - I_{dark})hc}{qP_{inc}A\lambda_{peak}} \quad \textbf{[15]}$$

I_{dark} and I_{light} are the I_{DS} current in the dark and under illumination, q the fundamental unit of charge, P_{inc} the irradiated lights incident power (W/cm^2), A the area of the photoactive material and λ_{peak} the peak wavelength of the incident light.[30] The figures of merit used to identify photodetector based devices were developed for two terminal photodiodes and photoconductors (discussed later), which have very short channel lengths (nm). A result of this is that three terminal phototransistors which have much larger channel lengths (μm), typically have lower figure of merit values than two terminal devices, as electron transport must occur over a much larger distance.

The first figure of merit is the photocurrent/dark current ratio (P_{ill}), which is the difference between the current measured in the dark and under illumination, and has many parallels to a signal to noise ratio.

$$P_{ill} = \frac{(I_{light} - I_{dark})}{I_{dark}} = \frac{I_{ph}}{I_{dark}} = \frac{signal}{noise} \quad \textbf{[16]}$$

For a phototransistor, the P_{ill} is very similar to the on/off ratio, except it must be calculated at the same V_{GS} both in the dark and under illumination. The second figure of merit is photoresponsivity (R), which determines how much light is absorbed compared to how much reaches the device.

$$R = \frac{I_{ph}}{P_{inc}} = \frac{I_{light} - I_{dark}}{P_{inc} \cdot A} \quad \textbf{[17]}$$

Device gain (G) is directly related to the EQE and photoresponsivity by the relation[31]

$$R = \eta \left(\frac{q\lambda}{hc}\right) G \quad \textbf{[18]}$$

In addition to these values, the response time to the photo stimulus as well as the time required to return to the off state are extremely important. No standard exists to characterize these response times, but the most commonly used method is to model the I_{DS} vs t curve using an exponential or biexponential, and quoting the exponential time parameter.

1.8.2 Photochromic devices

Photochromic devices are able to utilize a portion of the electromagnetic spectrum to generate an electrical response. This is done by absorption of a specific or spectrum of wavelengths. Most commonly studied is the visible spectrum, with IR and UV being the next most common. The use of two terminal and three terminal devices have their individual advantages. Two terminal devices are typically fabricated in a vertical stacked sandwich fashion (electrode,

photochromic material, electrode) allowing for thinner layers of material. This comes at the price of having the electrodes partially block the incoming photon, decreasing device efficiency. Meanwhile a three terminal device is typically a planar structure, utilizing the OFET design. This allows a large area for electromagnetic radiation to encounter the device allowing for increased efficiency, but channel lengths are increased.

Three major types of photochromic devices exist. An important distinction between these devices and solar cells is that these devices detect low power light and typically require an external bias. Meanwhile a solar cell uses higher intensity light and converts it to power, requiring no external bias. The three devices are (**Fig 1.7**);

1) A Photodiode
2) A Photoconductor
3) A Phototransistor.

A photodiode works by allowing a photon to strike the semiconductive material generating an exciton. This can be separated into an electron hole pair e^-/p^+, with the p^+ move toward the anode and e^- to the cathode due to the built-in-electric field. The device works in reverse bias mode. The current equals the sum of the dark current and the photocurrent, so minimizing dark current is important for maximizing sensitivity.[32] In a photodiode, the EQE is 1, making the photocurrent proportional to the irradiance. These devices may have a fast

response time, but will always be low current devices due to their lack of gain, making detection over noise difficult. An avalanche photodiode can overcome this shortcoming, but increases device complexity.

In a photoconductor either an e^- or p^+ of an e^-/p^+ pair becomes deeply trapped. Due to the net neutrality of the system, as the untrapped e^- or p^+ is collected at the electrodes, another must be injected into the system to take its place. This will continue until charge recombination occurs. A result of this is that the device can achieve an efficiency over 100% resulting in a gain >> 1.[33]

A phototransistor operates as either a photodiode or photoconductor except it has the added functionality of a gate. The application of V_{GS} induces an orthogonal electric field which can assist in charge separation, as well as positively or negatively affect trapped charge carriers, allowing for a phototransistor to experience signal gain.

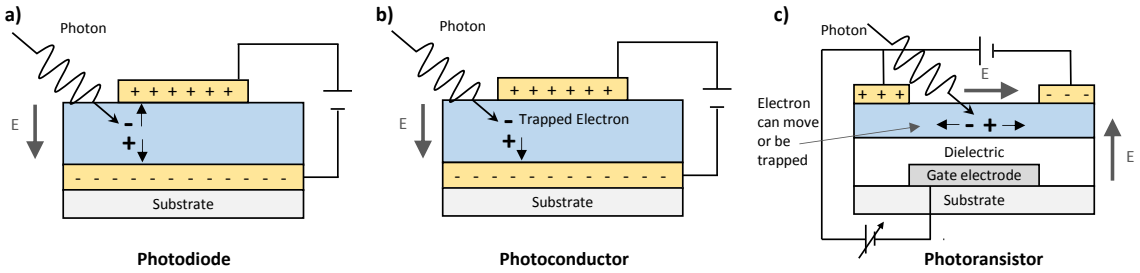

Figure 1.7: Cartoon depiction of photogeneration and e^-/p^+ transport in a (*a)* photodiode, (*b)* photoconductor, (*c)* phototransistor. Note that even though it is drawn larger, the distance between terminals in a two terminal device is much smaller than in the three terminal device.

A general summary of device gain and response times is provided in **Table 1.1**. These values are based on the detection of visible light. The phototransistor falls in the middle of all categories, but is more versatile in its use, due to the advanced functionality provided by the third terminal. For this reason, this thesis focuses on the use of the phototransistor architecture, to which more detail about its operation will be provided.

Table 1.1

Typical values for gain and response time of common photodetectors[1]

Photodetector	Gain	Response Time (s)
Photodiode	1	$10^{-11} – 10^{-8}$
Avalanche Photodiode	10^2-10^4	10^{-10}
Photoconductor	1-10^6	$10^{-8} – 10^{-3}$
Phototransistor	≈10^2	10^{-6}

1.8.3 Phototransistors

The first phototransistor was introduced into optoelectronics in 1951 by William Shockley.[34] Since then numerous organic phototransistors (OPT) have been used. A major advantage of them over diode devices is that the device is an OFET that also has properties of light detection, photo modulation, and electrical field controlled switching functionality.[34] A phototransistor can operate in two different modes. For p-type devices, the first mode is if the $V_{GS} < V_{Th}$ to which the photovoltaic effect dominates. The second mode is when the device is in

depletion $V_{GS} > V_{Th}$, to which I_{DS} increases with optical power due to the photoconductive effect similar to a photodiode. The devices in this thesis were tested in the first mode, using a $V_{GS} = 0$ V.

Like a photoconductor and a photodiode, a phototransistor has an electric field from source to drain. However, it also has the option to generate an electric field from the gate. This third terminal allows one to control the device response to incoming photons. An applied V_{GS} generates an electric field (E) within the semiconductor. This E field can assist in maintaining the separation of e^-/p^+ pairs similar to the Poole-Frenkel effect.[35] Therefore in a phototransistor, the applied V_{GS} can adjust the sensitivity of the device to an incoming photon. Just like a regular FET, the application of a large enough V_{GS} will allow trapped electrons to become free, allowing them to take part in conductivity.

1.8.4 UV Sensitive organic phototransistors

Most literature research involving phototransistors has been limited to the visible range, with few devices tackling the ultra violet (100 – 400 nm). Silicon based systems have seen tremendous success through the visible range, as well as many other inorganic and organic materials, but when we move to the ultra violet range, very few organic materials have been used. **Fig 1.8** and **Table 1.2** provide a list of most of the major organic devices sensitive to UV light as well as what has quickly become the most famous UV sensitive inorganic system, ZnO. ZnO devices have a wide bandgap ($E_g = 3.37$ eV) and work by allowing adsorbed

oxygen molecules on the ZnO surface to capture electrons from the conduction band, enhancing resistivity; $O_2 + e^- \rightarrow O_2^-$. When a UV photon generates an e^-/p^+ pair, the p^+ neutralizes the chemisorbed oxygen, decreasing the semiconductors resistance. $h\nu \rightarrow p^+ + e^-$, $O_2^- \; p^+ \rightarrow O_2$. The result is an increased photocurrent.[36] Meanwhile, the photo-isomerisable diarylethene (DAE), azobenzene, and spiropyran devices work by adjusting their highest occupied molecular orbital (HOMO) or lowest unoccupied molecular orbital (LUMO) to better match that of the electrodes or semiconductive material. This results in more efficient charge transport increasing current. In addition, these systems must all by mixed with a semiconductive polymer to work as a phototransistor. Only a few devices including pentacene, CuPc, 6T and BPTT showed direct UV sensitivity while still providing good semiconductivity, but all show a very broad range of photon sensitivity, stretching into the visible range. Only the inorganics such as TiO_2 and ZnO show sensitivity only in the UV range, leaving a gap in the literature for an organic device sensitive only to UV light.

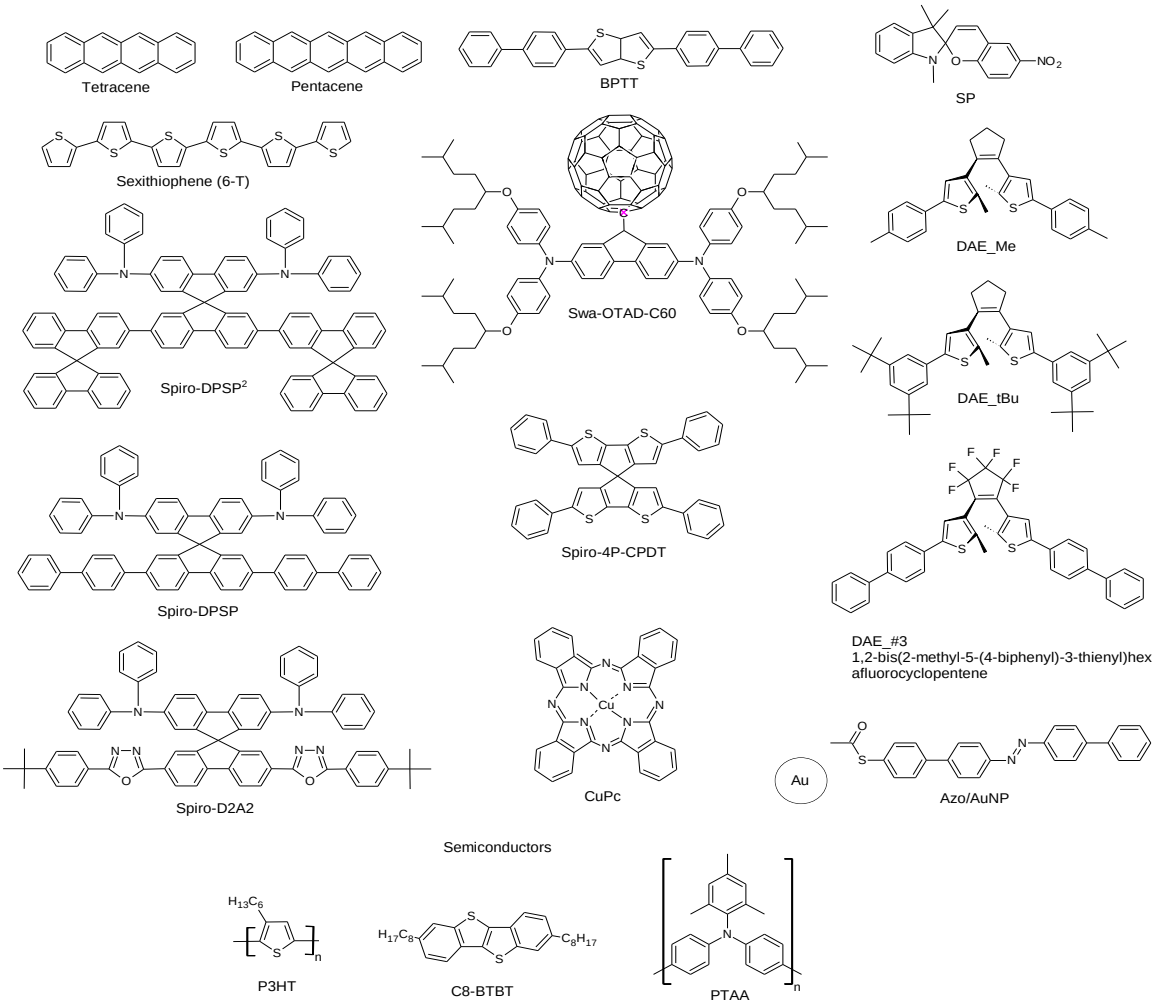

Figure 1.8: Molecular structures of the organic materials used in UV photodiodes, photoconductors and phototransistors as well as some semiconductors they have been combined with.

Table 1.2

List of major organic and inorganic phototransistors sensitive to UV light.

Deposition Method	Semiconductor/ UV Sensitive Material	Structure (Dielectric)	Mobility [cm^2/Vs]	Responsivity (R) (Light source, Intensity)	P_{ill}	t_R *	Ref
Vapor	BPTT	BG/TC(SiO_2)	0.082	82 A/W (380 nm, 1.55 mW/cm^2)	2 x 10^5	N/A	37
Vapor	CuPc	BG/TC(SiO_2)	0.02	0.5-2 A/W (365 nm, 1.55 mW/cm^2)	3 x 10^3	N/A	38
Vapor	Pentacene	BG/TC(SiO_2)	0.49	10-50 A/W (365 nm, 1.55 mW/cm^2)	1.3 x 10^5	N/A	38
Vapor	Pentacene	BG/TC(PMMA)	0.01	0.015 A/W (365 nm, 7 mW/cm^2)	2 x 10^4	0.1 s	39
Vapor	6T	BG/TC(SiO_2)	0.09	1.5-2.4 A/W (365 nm, 1.55 mW/cm^2)	1.3 x 10^3	N/A	40
Vapor	Tetracene	BG/TC(SiO_2)	0.003	N/A A/W (364 nm, 0.64 mW/cm^2)	3 x 10^3	N/A	41

Vapor	Spiro-DPSP	BG/BC(SiO_2, HMDS)	1.3 x 10^{-6}	1 A/W (370 nm, 191 $\mu W/cm^2$)	5 x 10^2	1.5 s	[42]
Vapor	Spiro-$DPSP^2$	BG/BC(SiO_2, HMDS)	2.7 x 10^{-7}	0.44 A/W (370 nm, 64 $\mu W/cm^2$)	2.1 x 10^3	N/A	[43]
Vapor	Spiro-4P-CPDT	BG/BC(SiO_2, HMDS)	1~2 x 10^{-4}	25 A/W (370 nm, 2.4 $\mu W/cm^2$)	290	N/A	[44]
Solution	Swa-OTAD-C60	BG/BC(SiO_2, HMDS)	1.8 x 10^{-6}	0.3 A/W (370 nm, 1.4 $\mu W/cm^2$)	115	N/A	[45]
Blends	P3HT:TiO_2	BG/BC(SiO_2)	N/A	NA (370 ~ 590 nm, 0.2 mW/cm^2)	~10^3	~0.2 s	[46]
Electrospin	ZnO nanowire	2 Terminal	N/A	10^6 A/W (365 nm, 77.5 $\mu W/cm^2$)	10^6		[47]
Thermal evaporation	Zn/O nanotetrapods	2 Terminal	N/A	0.63 A/W (365 nm, 1.5 mW/cm^2)	10^3	4.8 s	[31]
Spray coated from solution	N:ZnO	2 Terminal	N/A	530 A/W (365 nm, 2 $\mu W/cm^2$)	132	~1 s	[48]
Solution	BTBT + DAE_Me	BG/TC(SiO_2)	4.3 x 10^{-3}	(365 nm, 0.6 mW/cm^2)	----	----	[49]

Solution	BTBT + DAE_tBu	BG/TC(SiO_2)	2.1 x 10^{-1}	(365 nm, 0.6 mW/cm^2)	----	----	49
Solution	P3HT + DAE_Me	BG/TC(SiO_2)	1.4 x 10^{-3}	(365 nm, 0.6 mW/cm^2)	----	----	50
Solution	P3HT + DAE_tBu	BG/TC(SiO_2)	1.9 x 10^{-3}	(365 nm, 0.6 mW/cm^2)	----	----	50
Vapor	Spiro(D2A 2)	2 Terminal	----	(380 nm	----	< 400 ns	51
Vapor	DAE_#3	BG/TC(SiO_2)	1.0 x 10^{-5}	7.9*10-9 A/W (300-400 nm 39 mW/cm^2)	75	120 s	52
Solution	PTAA/SP	BG/TC(SiO_2)	1.8x10^{-4}	N/A (340 nm 0.14 mW/cm2)	0.68	1800 s	53
Solution	P3HT/Azo/ AuNP	BG/BC(SiO_2)	1.1x10^{-3}	N/A (365 nm, N/A)	3	>60s	54
Solution	P3HT/DAE _Meth	BG/BC(SiO_2)	2.0x10^{-3}	N/A (365 nm, 62μW/cm^2)	11	5 s	50
Solution	P3HT/Sp	BG/TC(SiO_2)	0.1	N/A (365 nm, 10 uW/cm^2)	10^{-2}	200 s	55

** t_R is the rise time, being how quickly the device responds to UV light*

Referring to device structure, BG = bottom gate, BC = bottom contact, TC = top contact,

Table 1.2 shows the clear lack of organic UV sensitive phototransistors. To this we explore the use of the UV photosensitive 2,7-dipentyl[1]benzothieno[3,2-*b*][1] benzothiophene (C5-BTBT) (**Fig 1.9**), which is capable of acting as both a high mobility semiconductor and a UV active material. We explore how the addition of small molecules into the semiconductor film can affect the electron trapping and detrapping, altering the time required for charge recombination to occur. These systems can have applications in photomemory, logic circuits, UV sensors and photoswitches.

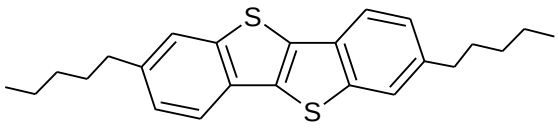

C5-BTBT

Figure 1.9: 2,7-dipentyl[1]benzothieno[3,2-*b*][1] benzothiophene (C5-BTBT), the UV sensitive semiconductor studied in this thesis.

1.9 Outline of thesis chapters

The thesis is divided into 8 chapters, governed by the theme of generating semiconductor blends consisting of a polymeric material and a small molecule or nanomaterials to enhance device performance. Chapters 2, 3, 4, 5, and 7 are a reproduction of published works, to which the reader may find some overlap in the literature review and methods sections.

In Chapter 2 we look at how unsorted single walled carbon nanotubes (SWCNTs) can enhance the mobility of an OFET by blending them with a polymeric semiconductor.

Chapter 3 then explores how the charge injection resistance for various metals can be reduced when unsorted SWCNT's are added to the semiconductor film.

Chapter 4 is an investigation of the UV sensitive properties of C5-BTBT and how it can be used in an OFET. We discover that by blending in a copolymer with an azobenzene pendant group, the UV sensitivity of the system can be greatly enhanced.

Chapter 5 looks deeper into the cause of the increased UV sensitivity when an azobenzene derivative is added. This is accomplished by generating semiconductor blends of C5-BTBT:PMMA:azobenzene derivative and observing the systems transistor properties as well as response and decay times to the UV stimulus. HOMO and LUMO energy levels are determined through cyclic voltammetry (CV) as well as density functional theory (DFT) calculations to provide an explanation for how the azobenzene additives affect charge transfer. Time responsive I_{DS} curves are modelled using a biexponential model.

Chapter 6 maintains the themes of Chapter 5, but explores additives that are not able to isomerize in the solid state (naphthalene and anthracene derivatives). The additives are chosen to be either electron rich or electron deficient, which is found to affect how long, and how strongly the photogenerated e^-/p^+ pair can be

maintained. The V_{GS} required for charge recombination is explored and found to strongly correlate to how electron rich/deficient the additives are.

Chapter 7 explores in more detail the phototransistor properties of the most successful system consisting of C5-BTBT/PMMA/2Cl-2NO_2-Anth. We look into varying the incident light intensity to explore the photosensitivity of the device. A sample of how the system can be used as a sensor device is provided through the use of a V_{GS} program.

Chapter 8 is a conclusions chapter, providing a few examples for future work on the subject.

1.10 References

1. Sze, S. M. & Ng, K. K. *Physics of semiconductor device*. (2007).
2. Neamen, D. *Semiconductor Physics and Devices: Basic Principles*. (2011).
3. Lilienfeld, J. E. Patent. 1–3 (1930).
4. Horowitz, G. Organic Field-Effect Transistors. *Adv. Mater.* **10,** 365–377 (1998).
5. Hideki, S., Louis, E. J., MacDiarmid, A. G., Chiang, C. K. & Heeger, A. J. Synthesis of Electrically-Conducting organic Polymers: Halogen Derivatives of Polyacatylene, (CH)x. *J.C.S., Chem. Commun.* 1–5 (1977).
6. Chiang, C. K. *et al.* Electrical conductivity in doped polyacetylene. *Phys. Rev. Lett.* **39,** 1098–1101 (1977).
7. Tsumura, a., Koezuka, H. & Ando, T. Macromolecular electronic device: Field-effect transistor with a polythiophene thin film. *App. Phys .Lett.* **49,** 1210–1212 (1986).

8. Roncali, J. *et al.* Effects of steric factors on the electrosynthesis and properties of conducting poly(3-alkylthiophenes). *J. Phys. Chem.* **91,** 6706–6714 (1987).

9. Tsumura, A., Koezuka, H. & Ando, T. Polythiophene Field-Effect Transistor: Its Characteristics and Operation Mechanism. *Synth. Met.* **25,** 11–23 (1988).

10. Halik, M. *et al.* High-mobility organic thin-film transistors based on α,α′-didecyloligothiophenes. *J. Appl. Phys.* **93,** 2977–2981 (2003).

11. Sze., S. M. & Ng, K. K. *Physics of Semiconductor Devices Third Edition*. (2006).

12. Li, F., Nathan, A., Wu, Y. & Ong, B. S. *Organic Thin Film Transistor Integration: A Hybrid Approach*. (Wiley-VCH Verlag GmbH & Co. kGaA, 2011).

13. Shea, P. B., Kanicki, J. & Ono, N. Field-effect mobility of polycrystalline tetrabenzoporphyrin thin-film transistors. *J. Appl. Phys.* **98,** 014503 (2005).

14. Marinov, O., Deen, M. J. & Datars, R. Compact modeling of charge carrier mobility in organic thin-film transistors. *J. Appl. Phys.* **106,** (2009).

15. Estrada, M. *et al.* Modeling the behavior of charge carrier mobility with temperature in thin-film polymeric transistors. *Microelectron. Eng.* **87,** 2565–2570 (2010).

16. Jiménez Tejada, J. a. *et al.* Contact effects in compact models of organic thin film transistors: Application to zinc phthalocyanine-based transistors. *Org. Electron. physics, Mater. Appl.* **12,** 832–842 (2011).

17. Horowitz, G., Hajlaoui, R., Bouchriha, H., Bourguiga, R. & Hajlaoui, M. The Concept of 'Threshold Voltage' in Organic Field-Effect Transistors. *Adv. Mater.* **10,** 923–927 (1998).

18. Servati, P., Striakhilev, D. & Nathan, a. Above-threshold parameter extraction and modeling for amorphous silicon thin-film transistors. *IEEE Trans. Electron Devices* **50,** 2227–2235 (2003).

19. Chen, C.-C., Chiu, M.-Y., Sheu, J.-T. & Wei, K.-H. Photoresponses and memory effects in organic thin film transistors incorporating poly(3-hexylthiophene)/CdSe quantum dots. *Appl. Phys. Lett.* **92,** 143105 (2008).

20. Wang, W., Ma, D. & Gao, Q. Optical Programming/Electrical Erasing Memory Device Based on Low-Voltage Organic Thin-Film Transistor. *IEEE T. Electron Dev.* **59,** 1510–1513 (2012).

21. Ortmann, F., Bechstedt, F. & Hannewald, K. Charge transport in organic crystals: Interplay of band transport, hopping and electron-phonon scattering. *New J. Phys.* **12,** (2010).

22. Ortmann, F., Bechstedt, F. & Hannewald, K. Theory of charge transport in organic crystals: Beyond Holstein's small-polaron model. *Phys. Rev. B - Condens. Matter Mater. Phys.* **79,** (2009).

23. Dimitrakopoulos, C. D. & Malenfant, P. R. L. Organic thin film transistors for large area electronics. *Adv. Mater.* **14,** 99–117 (2002).

24. Ong, B. S., Wu, Y., Li, Y., Liu, P. & Pan, H. Thiophene polymer semiconductors for organic thin-film transistors. *Chem. - A Eur. J.* **14,** 4766–4778 (2008).

25. Biniek, L., Schroeder, B. C., Nielsen, C. B. & McCulloch, I. Recent advances in high mobility donor–acceptor semiconducting polymers. *J. Mater. Chem.* **22,** 14803 (2012).

26. Gao, X. & Zhao, Z. High mobility organic semiconductors for field-effect transistors. *Sci. China Chem.* **58,** 947–968 (2015).

27. Hamilton, R. *et al.* High-performance polymer-small molecule blend organic transistors. *Adv. Mater.* **21,** 1166–1171 (2009).

28. Yuan, Y. *et al.* Ultra-high mobility transparent organic thin film transistors grown by an off-centre spin-coating method. *Nat. Commun.* **5,** 3005 (2014).

29. Natali, D. & Caironi, M. Charge injection in solution-processed organic field-effect transistors: Physics, models and characterization methods. *Adv. Mater.* **24,** 1357–1387 (2012).

30. Yu, H., Bao, Z. & Oh, J. H. High-performance phototransistors based on single-crystalline n-channel organic nanowires and photogenerated charge-carrier behaviors. *Adv. Funct. Mater.* **23,** 629–639 (2013).

31. Hassan, N. K., Hashim, M. R. & Allam, N. K. Low power UV photodetection characteristics of cross-linked ZnO nanorods/nanotetrapods grown on silicon chip. *Sensors Actuators, A Phys.* **192,** 124–129 (2013).

32. Baeg, K. J., Binda, M., Natali, D., Caironi, M. & Noh, Y. Y. Organic light detectors: Photodiodes and phototransistors. *Adv. Mater.* **25,** 4267–4295 (2013).

33. Konstantatos, G. & Sargent, E. H. Nanostructured materials for photon detection. *Nat. Nanotechnol.* **5,** 391–400 (2010).

34. Guo, Y., Yu, G. & Liu, Y. Functional organic field-effect transistors. *Advanced Materials* **22,** 4427–4447 (2010).

35. Frenkel, J. On pre-breakdown phenomena in insulators and electronic semi-conductors. *Phys. Rev.* **54,** 647–648 (1938).

36. Humayun, Q., Kashif, M., Hashim, U. & Qurashi, A. Selective growth of ZnO nanorods on microgap electrodes and their applications in UV sensors. *Nanoscale Res. Lett.* **9,** 29 (2014).

37. Noh, Y. Y. *et al.* High-photosensitivity p-channel organic phototransistors based on a biphenyl end-capped fused bithiophene oligomer. *Appl. Phys. Lett.* **86,** 043501 (2005).

38. Noh, Y. Y., Kim, D. Y. & Yase, K. Highly sensitive thin-film organic phototransistors: Effect of wavelength of light source on device performance. *J. Appl. Phys.* **98,** 074505 (2005).

39. Lucas, B. *et al.* Ultraviolet light effect on electrical properties of a flexible organic thin film transistor. *Thin Solid Films* **517,** 6280–6282 (2009).

40. Noh, Y.-Y. *et al.* Effect of light irradiation on the characteristics of organic field-effect transistors. *J. Appl. Phys.* **100,** 094501 (2006).

41. Choi, J. M. *et al.* Comparative study of the photoresponse from tetracene-based and pentacene-based thin-film transistors. *Appl. Phys. Lett.* **88,** 1–3 (2006).

42. Saragi, T. P. I., Pudzich, R., Fuhrmann, T. & Salbeck, J. Organic phototransistor based on intramolecular charge transfer in a bifunctional spiro compound. *Appl. Phys. Lett.* **84,** 2334–2336 (2004).

43. Saragi, T. P. I., Pudzich, R., Fuhrmann-Lieker, T. & Salbeck, J. Light responsive amorphous organic field-effect transistor based on spiro-linked compound. *Opt. Mater. (Amst).* **29,** 879–884 (2007).

44. Saragi, T. P. I., Londenberg, J. & Salbeck, J. Photovoltaic and photoconductivity effect in thin-film phototransistors based on a heterocyclic spiro-type molecule. *J. Appl. Phys.* **102,** 2005–2008 (2007).

45. Saragi, T. P. I., Fetten, M. & Salbeck, J. Solution-processed organic thin-film phototransistors based on donor/acceptor dyad. *Appl. Phys. Lett.* **90,** 2005–2008 (2007).

46. Mok, S. M., Yan, F. & Chan, H. L. W. Organic phototransistor based on poly(3-hexylthiophene)/ TiO2 nanoparticle composite. *Appl. Phys. Lett.* **93,** 2006–2009 (2008).

47. Liu, X. *et al.* All-printable band-edge modulated ZnO nanowire photodetectors with ultra-high detectivity. *Nat. Commun.* **5,** 4007 (2014).

48. Shinde, S. S. & Rajpure, K. Y. Fabrication and performance of N-doped ZnO UV photoconductive detector. *J. Alloy Compd* **522,** 118–122 (2012).

49. Gemayel, M. El *et al.* Optically switchable transistors by simple incorporation of photochromic systems into small-molecule semiconducting matrices. *Nat. Commun.* **6,** 6330 (2015).

50. Orgiu, E. *et al.* Optically switchable transistor via energy-level phototuning in a bicomponent organic semiconductor. *Nat. Chem.* **4,** 675–9 (2012).

51. Lin, H. W. *et al.* Highly efficient visible-blind organic ultraviolet photodetectors. *Adv. Mater.* **17,** 2489–2493 (2005).

52. Hayakawa, R., Higashiguchi, K., Matsuda, K., Chikyow, T. & Wakayama, Y. Optically and electrically driven organic thin film transistors with diarylethene photochromic channel layers. *ACS Appl. Mater. Interfaces* **5,** 3625–30 (2013).

53. Ishiguro, Y., Hayakawa, R., Chikyow, T. & Wakayama, Y. Optical switching of carrier transport in polymeric transistors with photochromic spiropyran molecules. *J. Mater. Chem. C* **1,** 3012 (2013).

54. Raimondo, C. *et al.* Optically switchable organic field-effect transistors based on photoresponsive gold nanoparticles blended with poly(3-hexylthiophene). *PNAS* **109,** 12375–80 (2012).

55. Li, Y., Zhang, H., Qi, C. & Guo, X. Light-driven photochromism-induced reversible switching in P3HT–spiropyran hybrid transistors. *J. Mater. Chem.* **22,** 4261 (2012).

Chapter 2

Using Unsorted Single-Wall Carbon Nanotubes to Enhance Mobility of Diketopyrrolopyrrole-Quarterthiophene Copolymer in Thin-Film Transistors

This chapter involves the work published in the following article, additional information has been added to the supporting information section. The major contribution of this work is that unsorted SWCNT's can be blended with a semiconductive polymer to enhance device mobility up to an optimal loading. Additionally, the method used to prepare the SWCNT's can have a large impact on their performance.

"Using unsorted single-wall carbon nanotubes to enhance mobility of diketopyrrolopyrrole-quarterthiophene copolymer in thin-film transistors"

Reproduced from: Chad S. Smithson, Yiliang Wu, Tony Wigglesworth, and Shiping Zhu; *Organic Electronics*, **2014**, 15, 2639-2646. With permission from Elsevier.

DOI:10.1016/j.orgel.2014.07.021

2.1 Abstract

Organic thin film transistors (OTFTs) were fabricated for the first time using a semiconductor copolymer of diketopyrrolopyrrole-quarterthiophene (DPP-QT) and unsorted single walled carbon nanotubes (SWCNTs). Three different SWCNTs having different tube diameters, length, and shape were used to investigate the effects of carbon nanotubes' properties on dispersion of the SWCNTs in DPP-QT polymer, as well as the mobility and current on/off ratio of

the OTFTs. The DPP-QT polymer was able to selectively disperse two types of SWCNTs. An optimal SWCNT loading was found to be 1.5–2.5 wt% for these SWCNTs, before the on/off ratio fell below 10^5 due to increased metallic tube content of the film. At this optimal loading, the field effect mobility was improved by a factor of two, with the maximum mobility reaching 1.3 $cm^2 V^{-1} s^{-1}$, when the SWCNTs with a short length and small tube diameter were used.

2.2 Preface

This was the original work performed for this dissertation. Important data was obtained from this research, but it was ultimately determined that the project could not compete with the massive number of other research groups and companies performing similar research with much larger research budgets and facilities. With all those resources, they are able to advance the field too quickly for us, as we found that by the time we were publishing our results, the new advancements were already surpassing our results. For this reason, the research was wrapped up, 2 publications were obtained from it and the focus of the research was changed to adding switchable material into OFETS.

2.3 Start of journal article: Introduction

A major goal for printable electronic devices is the development of organic thin-film transistors (OTFTs)[1,2,3]. By replacing the brittle silicon based semiconductor with an organic semiconductor material, new opportunities for low-cost, flexible, and lightweight electronics exist, since an organic semiconductor could be

integrated into large area electronic device via printing techniques in a roll to roll manner.[4] One of the most challenging aspects to this approach is generating a cost effective semiconductor materials with comparable electrical performance to amorphous silicon which has a mobility of 0.5–1 $cm^2 V^{-1} s^{-1}$. Over the past 10 years, a wealth of research has been published using single walled carbon nanotubes (SWCNTs) to generate high mobility films due to their high field effect mobility measured to be 79,000 $cm^2 V^{-1} s^{-1}$ and an intrinsic mobility estimated at 100,000 $cm^2 V^{-1} s^{-1}$.[5] SWCNTs can be incorporated into the semiconductor layer of existing OTFT designs making them an ideal candidate for technology development.[6] Research into individual SWCNT channels grown by chemical vapour deposition (CVD) have been reported,[7,8,9,10] but these methods suffer from their inability to be scaled to production demands. Success has been made depositing filtered films of SWCNTs, but the process still requires multiple steps, making it labour intensive.[11,12] Due to their tendency to aggregate in solution, a film of pure CNTs cannot be solution cast without the aid of a dispersing agent, which can affect film preparation and SWCNT performance.[13,14,15] It has been shown that oxidized or chemically functionalized CNT's are more easily dispersed in solvents than defect free CNT's.[16] However, these methods are not useful for semiconductor electronics, because altering the chemical structure of a CNT diminishes its semiconductor properties.

An alternative approach to generating a pure film of SWCNTs is to use SWCNTs to enhance the performance of organic semiconductors. Due to their high aspect

ratio, a very small amount of SWCNTs can be added to a semiconductor polymer film increasing the films overall mobility.[17] This approach requires the semiconductor to be soluble and able to stabilize a dispersed SWCNT solution. Fortunately most semiconductor polymers consist of a conjugated backbone, allowing for π–π interaction to help prevent the aggregation of CNTs in solution. One of the most studied semiconductors polymers employing this approach is poly(3-alkythiophene).[18,19,20] Although mobility improvements up to 10 times have been reported,[21] due to the low mobility of poly(3-alkythiophene), the absolute mobility values are still very low, for example less than 0.1 $cm^2 V^{-1} s^{-1}$. Recently a new class of semiconductor, diketopyrrolopyrrole-quarterthiophene copolymer with mobility up to 1.0 $cm^2 V^{-1} s^{-1}$, has been reported. It would be interesting to study if the mobility can be further enhanced by using SWCNTs as additive.

A major challenge with SWCNTs is that when synthesized, they are generated as a mixture of approximately 1/3 metallic carbon nanotubes (*m*-CNT) and 2/3 semiconducting carbon nanotubes (*sc*-CNT).[9] The presence of metallic tubes is detrimental for OTFTs because beyond the percolation threshold they can create a conductive pathway essentially short circuiting the device. Additionally they have been found to reduce the on/off ratio of OTFTs.[12] To avoid the detrimental effects caused by *m*-CNTs, SWCNTs are semiconductor enriched. Three major techniques are employed for semiconductor enrichment to separate *m*-CNTs from *sc*-CNTs. Density gradient ultracentrifugation (DGU) has achieved the best purity, but has very small throughput ~1 mg every 48 h.[22,23,24,25,26,27,28] Other

methods such as column chromatography,[29,30] selective oxidation[31] or separation employing SWCNT selective polymers[32,33] offer higher throughput but are still well below commercial requirements. Most literature employing SWCNT films utilizes these semiconductor enriched SWCNTs.[14,34,35,36] The challenge with this approach is that the cost to purify these tubes drives the cost of materials so high that an amorphous silicon film remains a cheaper option.

Instead of using high-cost purified SWCNTs we looked into the cheaper alternative of using unsorted SWCNTs. The focus of this research was to determine if this mixture of metallic and semiconducting tubes could be used as a viable option for mobility enhancement of the new semiconductor copolymer of diketopyrrolopyrrolequarterthiophene, and if so, what physical properties of the unsorted SWCNTs are best for this application.

2.4 Results and discussion

2.4.1 Materials

Three sources of SWCNT were studied in this report, one from Sigma Aldrich which will be abbreviated CNT-A, one from BuckyUSA abbreviated CNT-B and one from Cheap Tubes abbreviated CNT-C. These sources were chosen because these SWCNTs have different tube diameters, length, surface finish, etc. Full descriptions of the SWCNTs can be found in **Table 2.1**. CNT-A has a short average tube length and the smallest tube diameter, CNT-B has a shorter tube length comparable to CNT-A, but larger variation in tube diameter, while CNT-C has the longest tube length of 3–30 μm, and a large tube diameter. In addition

they were all prepared using combustion chemical vapour deposition (CCVD) but were purified by different methods.

Table 2.1

Unsorted SWCNT's and their properties used in this study

Sample ID	Diameter (nm)	Length (μm)	Synthesis Method and Metal Catalyst	Cleaning Method
CNT-A	0.7-0.9	0.5 - 2	CoMoCAT®	HF (aq) wash
CNT-B	0.7-2.5	0.5 - 5	HipCo	Hydroxyl wash
CNT-C	1-2	3 - 30	Co	Plasma purified

The semiconductor diketopyrrolopyrrole-quarterthiophene copolymer (DPP-QT) with a reported mobility of 1 $cm^2V^{-1}s^{-1}$,[1,2] but an average mobility of 0.6 $cm^2V^{-1}s^{-1}$ as measured in our lab was chosen to form the bulk of the semiconductor film, as this polymer has a high baseline mobility. By dissolving the copolymer in 1,1,2,2-tetrachloroethane and adding SWCNTs, the SWCNT aggregates could be dispersed by using an ultrasonic probe for 2 min. The dispersion of SWCNTs in DPP-QT copolymer was then spin coated to generate a semiconductor film and further integrated into OTFTs. The dispersion of SWCNTs in the film, as well as their effect on electrical performance of OTFTs was examined.

2.4.2 Dispersion and thin film characterization

Our previous research into SWCNT dispersions was performed using the Poly[5,50-bis(3-dodecyl-2-thienyl)-2,20-bithiophene] (PQT-12) and HipCo

SWCNTs from BuckyUSA (CNT-B in this study). It has been shown that this SWCNT could be dispersed very well in PQT-12 at high carbon nanotube loading.[37] When the same source SWCNTs were used with the DPP-QT polymer, very few SWCNTs could be stabilized in solution. A modest centrifugation for 15 min at 2050 g appeared to remove almost all the SWCNTs from solution. However, SEM images of films cast from DPP-QT and CNT-B revealed areas of high CNT aggregation and others with no CNT content (**Fig. 2.1**). Because most of the tubes were centrifuged out of the sample, the SWCNT concentration was unknown. All initial SWCNT loading concentrations tested (1–15 wt%), produced roughly the same mobility of 0.97 $cm^2V^{-1}s^{-1}$ and on/off ratio of 4 x 10^7 in OTFTs, suggesting a maximum loading of less than 1 wt%. The improvement caused by the tubes corresponds to a film mobility improvement of 50%, but did not offer the opportunity for further study of SWCNT concentration effects. For this reason we looked to other types of SWCNTs and found excellent stabilization of SWCNTs when the sources were CNT-A and CNT-C. The dispersion was stable for up to a few weeks without forming any agglomeration. Interestingly PQT-12 was unable to stabilize these two SWCNTs in any appreciable amount.

Previous reports have shown that for similar polymers such as the PQT polymer, a blue shift and broadening is observed in the Ultraviolet–Visible spectrum (UV–Vis) due to a π–π interaction caused by the polymer wrapping around the CNTs.[37,38] **Fig. 2.2** provides UV–Vis data with the black line representing a 0.5 wt% solution of DPP-QT copolymer in 1,1,2,2-tetrachloroethane, while the red

and blue curves show the same 0.5 wt% solution with 0.025 wt% CNT-A and CNT-C respectively. These CNT values correspond to 5 wt% solids in solution. There is no peak shifting or line broadening in the UV-Vis, indicating little interaction between the polymer and CNT's in the solution phase.

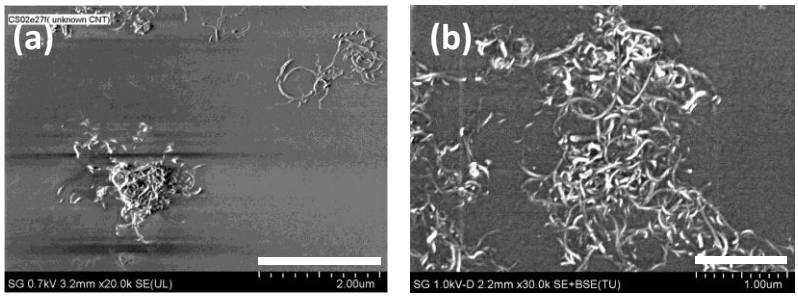

Figure 2.1: (*a*) SEM images of CNT-B spin coated on SiO_2 wafer (scale bar 2μm). (*b*) DPP-QT film with a maximum loading of CNT-B (scale bar 1 μm).

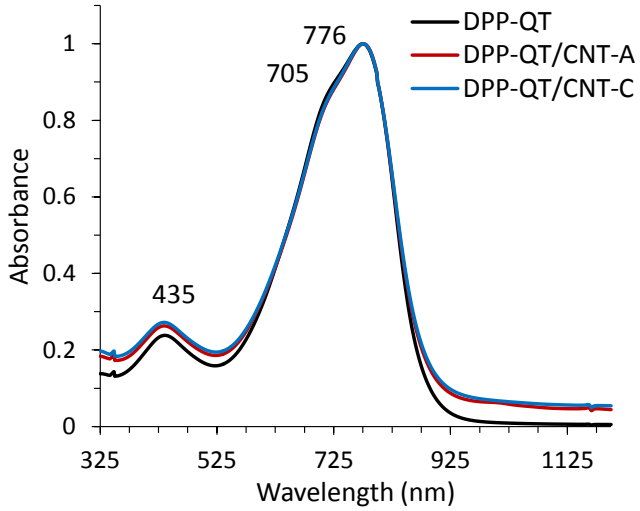

Figure 2.2: Solution UV–Vis spectra. All solutions contain 0.5 wt% DPP-QT polymer in 1,1,2,2-tetrachloroethane with DPP-QT/CNT-A containing 5 wt% CNT-A by solids and DPP-QT/CNT-C containing 5 wt% CNT-C by solids.

Although there is no shifting of the UV–Vis peaks suggesting no significant π–π interaction between DPP-QT and CNTs, the copolymer did stabilize the CNTs in solution for a minimum of 2 weeks. **Fig. 2.3** shows an undiluted UV–Vis sample. When no polymer is present to stabilize the CNTs (blue[1] line), no distinct features are observed and the CNTs can clearly be seen to aggregate within minutes suggesting there is little to no CNTs in solution. However, we observe a CNT signal for the S_{22} band with a maximum at 1006 nm corresponding to a 6,5 chirality,[39] a shoulder at 1172 nm corresponding to the 7,6 or 9,2 chirality,[40] and the S_{11} band with a maximum at 1447 nm corresponding to the 10,8 chirality,[41] when the DPP-QT polymer was present. It is common practice when working with CNTs to centrifuge the aggregates out of solution. To determine if this was necessary, samples were probe sonicated at 35% amplitude for 2 min and centrifuged at 25,000 g for 30 min. No significant change in peak intensity was observed and no visible sign of a precipitate could be observed in the vial, indicating no material was removed during centrifugation. For this reason, all other samples in this report were not centrifuged. The above results indicated that DPP-QT polymer could stabilize these two types of CNTs, but had no selectivity in carbon nanotube chirality.

From the above results it is clear that the CNT-A and CNT-C are being stabilized in solution. To investigate their dispersion, we referred to SEM imaging of a 100 nm spin coated film (**Fig. 2.4**). Due to the high conductivity of the *m*-CNTs and *sc*-CNTs, they require no conductive coating and image much more easily than

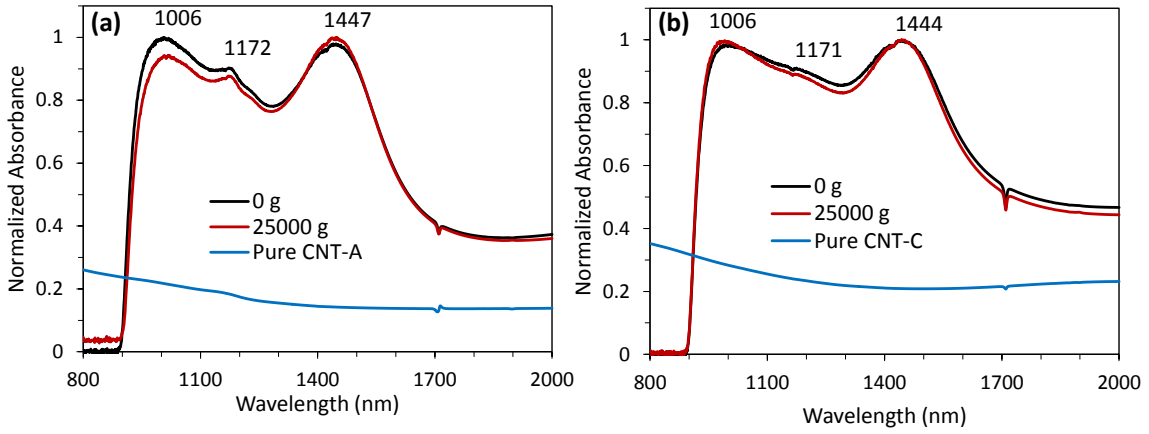

Figure 2.3: UV–Vis spectra of 0.5 wt% DPP-QT polymer in 1,1,2,2-tetrachloroethane solution with 5 wt% (a) CNT-A and (b) CNT-C of the total solutes, before and after centrifuging at 25,000 g for 30 min. The spectra of a dispersion of the same amount of SWCNTs without the polymer were also included.

the copolymer. This provides excellent contrast between the CNT's and copolymer. It should be noted that in all the images the bright spots are amorphous carbon. To produce a film without polymer present, the CNTs had to be spin coated immediately after being probe sonicated. The pure SWCNT films (*a*) and (*b*) display poor coverage where most of the SWCNTs did not adhere to the surface during spin coating. Images (*c*–*f*) show well dispersed CNTs embedded in the polymer matrix. As expected the CNT density increases with increasing CNT loading in the dispersion. Performing a visual count of the CNTs in each image, an average CNT density was determined for each CNT wt%. The results are summarized in **Table 2.2**. In contrast, CNT-B was found to have a low loading capacity and formed aggregates in the film (**Fig. 2.1**). This is likely due to

the hydroxyl washing used to purify CNT-B which can alter the chemical surface of the SWCNTs.

After observing the excellent dispersion of SWCNT in the film, we looked at how these affected film morphology of the polymer. Atomic force microscopy (AFM)

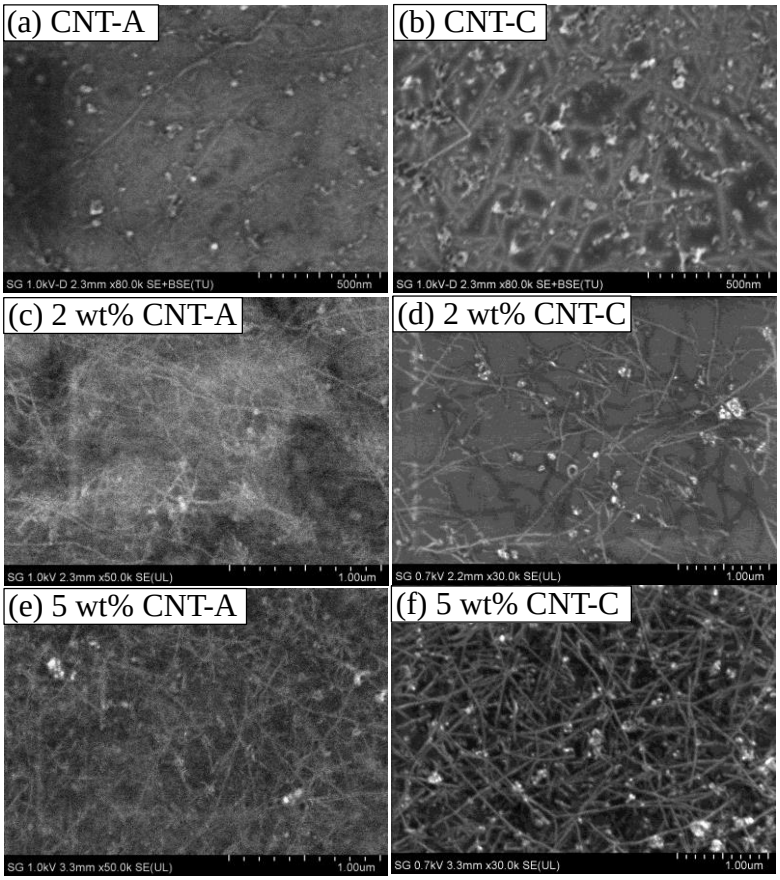

Figure 2.4: SEM images of CNT films cast on OTS modified silicon wafers. (*a*), (*c*), (*e*) are CNT-A and (*b*), (*d*), (*f*) are CNT-C. Images (*a*) and (*b*) are films cast from a freshly sonicated solution containing pure CNTs, while (*c*–*f*) are films with an indicated CNT content, in a film of DPP-QT copolymer. Amorphous carbon impurities can be observed as round bright spots in the film. The CNTs were well dispersed with no noticeable aggregates.

Table 2.2:
Average CNT density determined from a visual count of the SEM images (average of 4 images for each CNT loading concentration)

CNT loading (wt%)	CNT-A (tubes μm^{-2})	CNT-B (tubes μm^{-2})	CNT-C (tubes μm^{-2})
2	11.3	Not dispersed	9.2
5	20.9	Not dispersed	19.6

images of the pure DPP-QT film reveal polycrystalline domains of approximately 0.2-1 μm in size. These organized domains are important for achieving high mobility devices. However, as the SWCNTs were introduced, there is a noticeable decrease in the polycrystalline domain size of the polymer. At 5 wt% CNT content, the polycrystalline domains have been reduced to the nanoscale (**Fig. 2.5**). There are two major ways the CNTs were thought to interact with the polymer. The average radius of a SWCNT is 1 nm, allowing it to insert itself between two layers of a crystalline polymer. If this were to occur, the average d-space between the polymer chains would change, creating a shift in the XRD signal. The other option is that the CNTs would completely interrupt the crystalline packing of the polymer, reducing the size of the polycrystalline domains. This is confirmed by the lack of shifting in the XRD spectra seen in **Fig. 2.6**. The peak at 5.26º corresponds to the interlayer spacing of the polymer (between side chains).[1] The intensity of the peaks cannot be used as a measure of polycrystallinity due to the low angle required during sample collection

generating a large amount of background noise. The observation is consistent with previous reports on systems containing CNTs and other semiconductor polymers.[4,37]

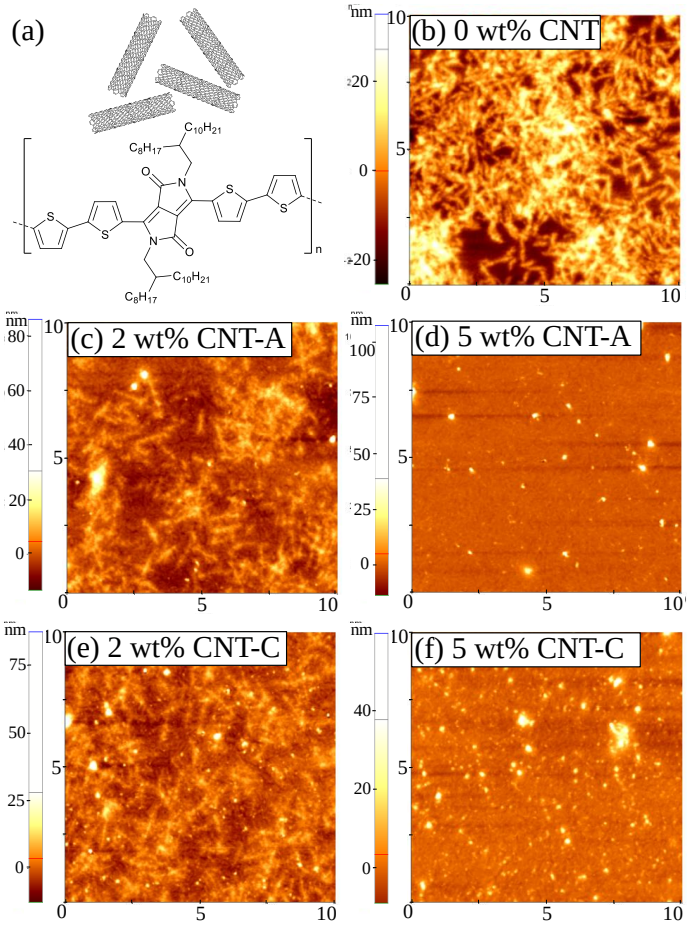

Figure 2.5: AFM images (scan area: 10 µm x 10 µm) of films cast on OTS modified wafers. All films are primarily composed of DPP-QT polymer with varying CNT contents. The images correspond to (*b*) 0 wt%, (*c*) 2 wt%, and (*d*) 5 wt% CNT-A, respectively; (*e*) 2 wt% and (*f*) 5 wt% CNT-C, respectively. Polymer crystal domains are seen to shrink in size with increasing CNT content demonstrating the interruption of the CNTs have on the polymer crystal packing.

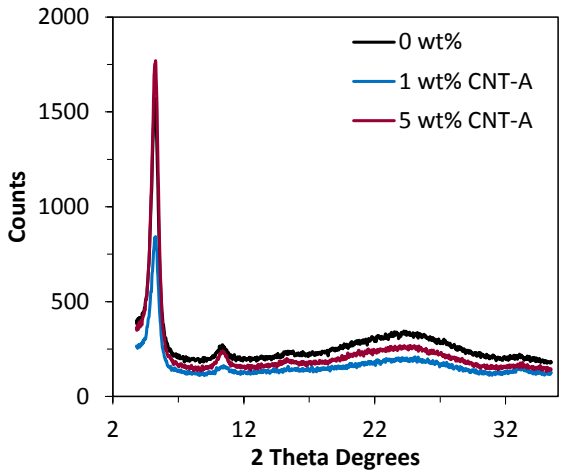

Figure 2.6: XRD of the DPP-QT/CNT-A film shows no interaction of CNTs with polymer crystals. No shifting of the main peak suggesting the CNTs are not being inserted between polymer layers, but are interrupting the packing of the crystal network, causing smaller crystal domains.

2.4.3 Electronic characteristics

OTFT devices were fabricated using varying concentrations of CNT-A and CNT-C. **Fig. 2.7** provides a typical set of data for the I_{SD} vs V_{SG} transfer curves. With increasing CNT concentration, a noticeable decrease in the on/off ratio is observed. This is consistent with other literature findings and is largely due to the high metallic CNT content of the sample.[12,42] Additionally we observe a reduced turn on voltage corresponding to a shifted threshold voltage (V_{Th}) when the SWCNT concentration is increased. This is due to a reduced charge injection resistance caused by the SWCNTs. Results of this were further explored using 3

different metal electrodes (Au, Cu, Al) where the results are summarized in our previous article.[43]

To determine an optimal loading of the unsorted SWCNTs, a series of SWCNT concentrations was measured from 0 to 5 wt%. All data points are a statistical average with a minimum of 8 data points measured for each concentration. Error bars are given for one standard deviation. Referring to **Fig. 2.8**, it is clear that the addition of unsorted SWCNTs has an enhancing effect on the mobility of the DPP-QT/SWCNT film. Despite their interruption of the polycrystalline domains in the film, an increase in mobility is still observed when SWCNT's are added to the film. Both CNT-A and CNT-C show an increase in mobility reaching a maximum at 2.5 and 2.0 wt%, respectively. The decrease preceding these maximum is caused by the onset of percolation of the *m*-SWCNTs. The increasing addition of *m*-SWCNTs has a nearly exponential decrease in the on/off ratio of the film. At 5 wt% SWCNT, the film has nearly reached the percolation limit, providing pathways from source to drain consisting primarily of *m*-SWCNTs generating a short circuited device. Interestingly, reports of films formed from pure SWCNT films hit the percolation limit at a smaller SWCNT density of only 3 CNTs/μm^2 as opposed to the 20 tubes/μm^2 required in this report. From this we can conclude that the separation between SWCNTs caused by the polymeric matrix allows for a larger loading of unsorted SWCNTs before percolation is achieved.[44] For commercial use, these devices require a minimum on/off limit of 10^5, which sets an upper limit to how many unsorted SWCNTs can be added. For these two CNT

sources, the average mobility with a current on/off ratio over 10^5 was 1.1 and 0.72 $cm^2\ V^{-1}\ s^{-1}$, corresponding to an optimal loading concentration of 2.5 wt% and 1.5 wt% for CNT-A and CNT-C, respectively. The maximum mobility for DPP-QT/CNT-A composition was up to 1.3 $cm^2\ V^{-1}\ s^{-1}$. The loading of CNT-A is larger than CNT-C likely because the CNT-A tubes have a shorter tube length and a higher aspect ratio. These results show that although both CNT types can be dispersed in the polymer matrix at variable concentrations, their mobility enhancement is different. CNT-C has a large decrease in on/off ratio even at low concentrations, showing that long tubes allow percolation of *m*-SWCNTs faster than short tubes. The impact of the long *m*-SWCNTs is so detrimental to device performance that CNT-C has almost no positive impact on electrical performance. Therefore we conclude that if one is to use unsorted SWCNTs for mobility enhancement, shorter CNTs are ideal because *m*-SWCNT percolation occurs at higher concentrations. Another consequence of the addition of unsorted SWCNTs is the shift of the threshold voltage. The DPP-QT polymer has an average threshold voltage around -4.0 V. Upon addition of CNTs, the threshold voltages shifted to 6.4 and 6.6 V at 0.5 wt% CNT loading, and subsequently stabilized at around 8.0 and 7.0 V at a higher loading for CNT-A and CNT-C, respectively. Although the threshold voltage shift has a negative impact on the DPP-QT polymer, it could be useful for other semiconductor devices that have a large negative threshold voltages[45,46,47] to shift the value close to 0 V. The increased threshold voltage also caused the subthreshold slope to decrease from

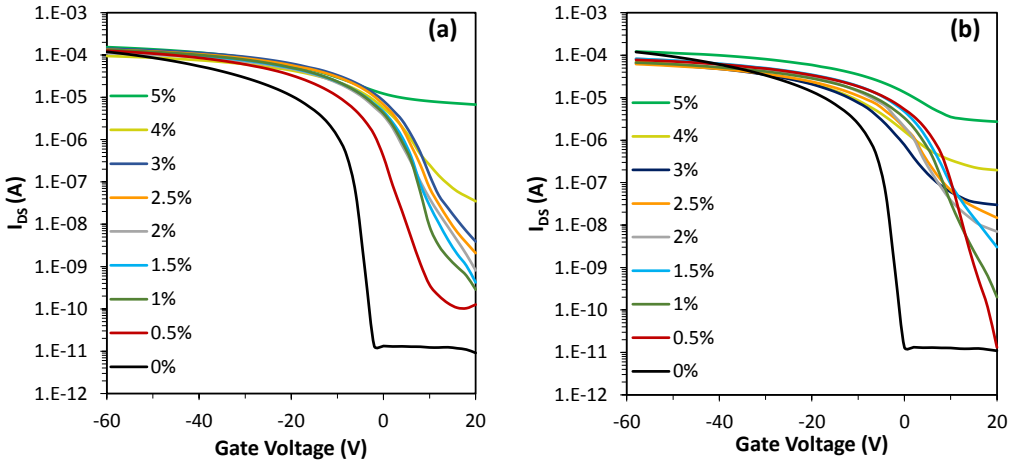

Figure 2.7: Transfer curves for the DPP-QT polymer with various amounts of CNT-A (*a*) and CNT-C (*b*) added by wt% to the film.

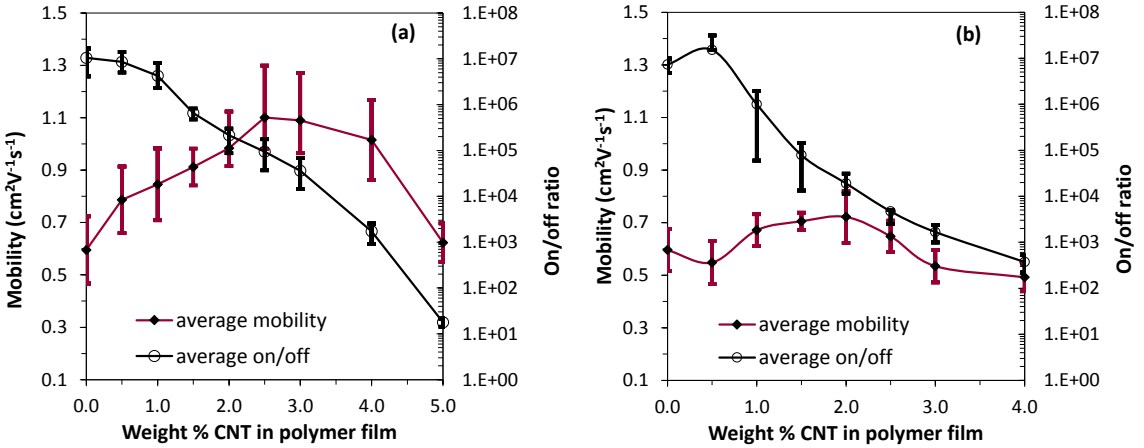

Figure 2.8: Mobility and on/off ratio for DPP-QT/CNT-A blend (*a*) and DPP-QT/CNT-C blend (*b*). A maximum mobility was obtained at 2.5 and 2.0 wt% CNT for these two films. The on/off ratio was found to decrease in an exponential fashion corresponding to increasing CNT concentration. The error bars represent the spread of data, with the data points being an average value.

0.67 dec/V for the pure DPP-QT device to about 0.2 dec/V the DPP-QT/CNT devices having the maximum mobility values.

2.5. Conclusion

We have demonstrated that three types of unsorted SWCNTs can be stabilized by the DPP-QT polymer in a 1,1,2,2-tetrachloroethane solution. The CNT-B source was found to have a low loading capacity, likely due to the hydroxyl washing used to purify the tubes. CNT-A and CNT-C which are not chemically altered during purification were easily dispersed and stabilized by the DPP-QT copolymer. Morphologies of the films showed that the CNT-A and CNT-C were evenly dispersed in the DPP-QT with no large aggregates, while CNT-B formed large aggregated clusters in the film. AFM and XRD measurements indicated that the CNTs interrupt the polycrystalline domains. Smaller polycrystalline domains were observed at higher CNT concentrations. The commercial source of SWCNTs which relates back to SWCNT length, thickness, and cleaning methods, plays an important role in the interaction of the SWCNT with the semiconductor polymer. These dispersions can be spin coated into films on an OTS modified silicon wafer and annealed at 140 ºC to form semiconductor films for OTFTs. The addition of unsorted SWCNTs, consisting of a mixture of approximately 2/3 *sc*-SWCNT and 1/3 *m*-SWCNTs, allowed for mobility enhancement. Maximum loading concentrations for CNT-A and CNT-C were found to be 2.5 wt% and 1.5 wt%, respectively, beyond which the on/off ratio falls below 10^5. The CNTs (CNT-C) with relatively longer length reach percolation at a lower concentration,

causing a quick reduction of the on/off ratio. CNT-A with the relatively shorter length and smaller tube diameter provide the greatest mobility enhancement, approximately doubling the mobility of the pure DPP-QT polymer device.

2.6. Experimental section

2.6.1. Materials and general methods

All solvents were reagent grade purchased from Sigma Aldrich and used as received. CNT-A was purchased from Sigma Aldrich (704,148) (6,5) chirality, carbon >90%, 77% (carbon as SWCNT), 0.7-0.9 nm diameter, 0.5-2 μm length; CNT-B was obtained from Bucky USA BU-203-OH Hydroxy 95 wt%, 0.7-2.5 nm diameter, 0.5–5 μm length; and CNT-C was purchased from Cheap Tubes (SKU-0111) SW/DWCNTs, >99 wt%, 1-2 nm diameter, 3-30 μm length.

DPP-QT was synthesized following the procedure reported by Choi et al.[2] Diketopyrrolopyrrole-quaterthiophene copolymer (DPP-QT) (0.02 g) was dissolved in 1,1,2,2-tetrachlorethane (3.98 g) for 2 h at 80 ºC in the absence of light to form a 0.5 wt% solution. 1.5 mg, of SWCNTs was added to 5.699 g of 0.5 wt% DPP-QT solution. The solution was immersed in an ice bath and probe sonicated on a Branson Digital Sonifier-450 (400 W) at 35% amplitude for 2 min. The resultant solution was a 0.5 wt% solution with a 5 wt% CNT concentration with respect to the polymer weight. All subsequent solutions were created via dilution by adding additional 0.5 wt% DPP-QT solution. For DPP-QT/CNT-B composition, the resultant dark green solution was centrifuged at 2054 g for 15

min and the supernatant collected. The resultant solution was a 0.5 wt% DPP-QT polymer with an unknown CNT concentration.

For SEM, samples were imaged in their native condition (no conductive coating applied) using a Hitachi SU-8000 field emission scanning electron microscope (SEM) operating in deceleration mode with a landing voltage of 700 V. A Park Systems XE-100 AFM operated in dynamic force mode was used to obtain AFM images. A cantilever with a nominal spring constant of 40 N/m, a resonant frequency of 300 kHz and a probe having a radius of 10 nm was used. Each sample had 2-3 spots imaged at each scan size with the most representative image presented in this report. UV-Visible spectra were collected on a Varian Cary UV-Vis-IR Spectrometer. Data in the 325-1150 nm range was collected using a 1 cm cell with a solution diluted to 0.004 wt% DPP-QT. Data in the 800-2000 nm range was collected using a 1 mm cell and an undiluted sample with an undiluted DPP-QT background used for the 0 g and 25,000 g samples. X-ray diffractions (XRD) were obtained using a Co source (D8 Discover) knife edge experiment, 1º incidence, 19.934 cm detector distance, 2 h collection time.

2.6.2. OTFT fabrication and evaluation

All fabrication and characterization of organic thin-film transistor devices (OTFTs) was done under ambient conditions taking precautions to isolate the material and device from light, but no precautions were taken to isolate the material or device from exposure to air or moisture. Bottom-gate TFT devices were built on n-doped silicon wafer as the gate electrode with a 110 nm thermal silicon oxide (SiO_2) as

the dielectric layer. The SiO_2 surface was plasma cleaned for 2 min. The wafer was subsequently rinsed with H_2O than isopropanol and dried with an air stream. The SiO_2 surface was modified with octyltrichlorosilane (OTS-8) by immersing a cleaned silicon wafer substrate in 0.1 M OTS-8 in toluene at 60 ºC for 20 min. The wafer was subsequently rinsed with toluene and isopropanol and dried with an air stream. The semiconductor layer was deposited onto the OTS-8-modified SiO_2 layer by coating one of the above prepared solutions and allowing it to sit on the wafer for 2 min, then spin coating with a 2 s ramp time, at 2000 rpm for 120 s. The sample was vacuum dried at 70 ºC for 30 min and annealed at 140 ºC for 40 min, and allowed to return to room temperature under vacuum. Subsequently, the gold source and drain electrodes were deposited by vacuum evaporation through a shadow mask with a channel length (L) of 90 µm and a width (W) of 1 mm. From I_{DS}-V_{GS} measurements, the mobility was extracted from the saturated regime using the following equation ($V_{DS} > V_{GS}$):

$I_{DS} = \mu C_i(W/2L)(V_{GS} - V_{Th})^2$, where I_{DS} is the drain current, C_i is the capacitance per unit area of the gate dielectric layer, V_{GS} and V_{Th} are the gate voltage and threshold voltage, respectively.

2.7 Supporting information

2.7.1 Additional information about SWCNT

Pure SWCNT's have a measured field effect mobility of 79,000 $cm^2V^{-1}s^{-1}$ and an intrinsic mobility estimated at 100,000 $cm^2V^{-1}s^{-1}$.[5] Multiple methods exist for the generation of SWCNT's including chemical vapour deposition (CVD) laser ablation and a high pressure carbon monoxide process (HiPCo). All methods result in a mixture of semiconducting (*sc*-SWCNT) and metallic nanotubes (*m*-SWCNT) in a ratio of approximately 2/3, 1/3 respectively. The semiconducting vs metallic nature of the tubes is a result of the chirality or wrapping vector of the SWCNT, which is defined by the equation $C_h = na_1 + ma_2$, where a_1 and a_2 are the lattice basis vectors separated by 60° and the indices (*n*,*m*) are positive integers with $n \geq m \geq 0$.[48] If *n* - *m* is a multiple of 3, the tube is metallic, otherwise it is semiconducting (**Fig S2.1**). All multilayer carbon nanotubes (MWCNT) are metallic, so it is important to only use SWCNT in OFETs.

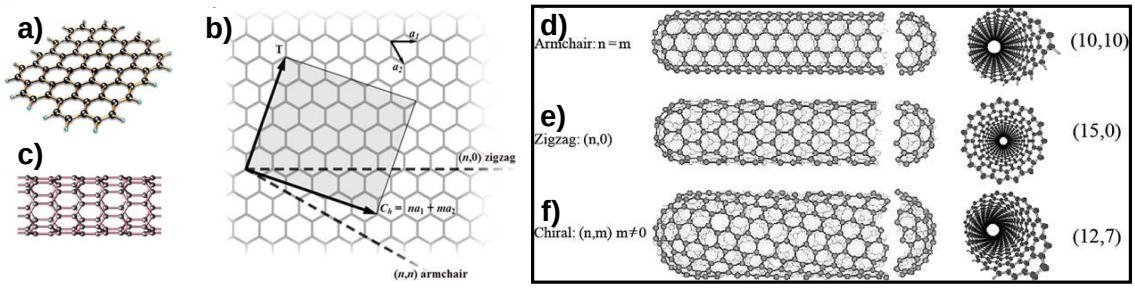

Figure S2.1: (*a*) Representation of the structure of graphene. (b) An example of how a graphene sheet can be folded into a SWCNT with the *m*,*n* translation vectors shown. (*c*), (*d*), (*e*), (*f*), Examples of SWCNTs that can be generated, all of which are semiconducting. Image reproduced with permission from Springer.[48]

The separation of *m*-SWCNT from *sc*-SWCNTs (known as semiconductor enrichment) is a heavily researched area, but to date no industrially feasible method has yet been achieved. Since its publication, some important improvements to the methods mentioned in the paper are an improved column chromatography method utilizing non ionic surfactants able to produce a 90-95% pure *sc*-SWCNT solution,[49] and separation employing a 9-9,dialkylfluorene homopolymer with SWCNT selective properties.[50] Of these methods, I personally believe the use of SWCNT selective polymers has the highest potential to be industrially feasible. The reason for this is that they are able to wrap around a SWCNT, where the polymer backbone/side chains can be altered to match a specific SWCNT tube chirality to selectively remove one chirality of tube from the rest of the batch. Filtering the sample can lead to a solution consisting of polymeric material wrapped around one single SWCNT chirality tube. This can be re-dissolved in a different solvent that will cause the polymer to release the tube, to which the polymer and tubes can then be easily separated.

2.7.2 SWCNT dispersion

One of the most important parameters of the DPP-QT polymer used, is that it is able to stabilize the SWCNTs in solution for an extended period of time. Natively, SWCNT's cluster together forming insoluble aggregates. By using a probe sonicator, a solution of SWCNTs can be separated from each other. **Fig S2.2** provides SEM images of two samples of probe sonicated SWCNTs. Without a

polymer to disperse the tubes, they will begin to re-aggregate immediately, reforming the insoluble aggregates, making solution processing nearly impossible. However, with 0.5 wt% DPP-QT dissolved in solution, the tubes will remained dispersed for at least 2 weeks.

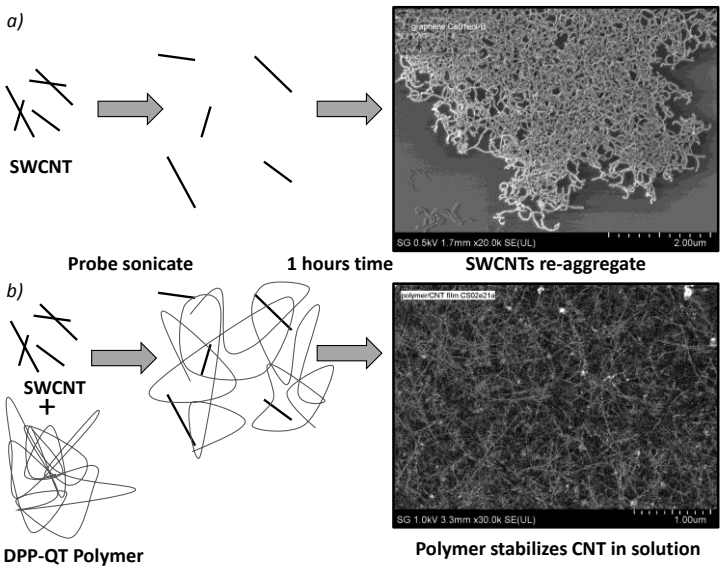

Figure S2.2: SEM images of SWCNT films after 2 minutes of probe sonication and left to sit 1 hour before being spin coated. (*a*) Without a polymer the SWCNTs aggregate. (*b*) In the presence of the DPP-QT polymer, the SWCNTs remain dispersed.

2.7.3 Depiction of transistor device

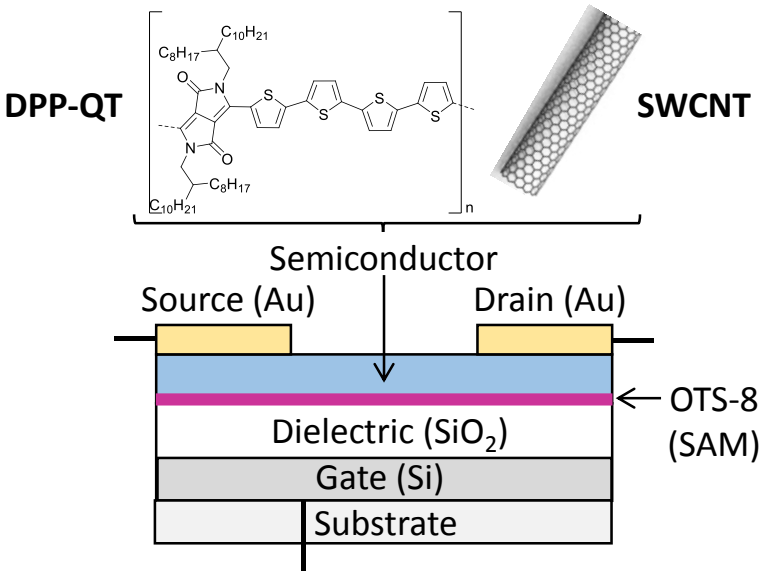

Figure S2.3: OFET design used to test devices, the semiconductive polymer DPP-QT and a hypothetical SWCNT used to make the semiconductor layer. SWCNT image courtesy of James Hedberg, licensed under a Creative Commons Attribution-NonCommercial-ShareAlike 3.0 Unported License.

2.7.4 Additional SEM images

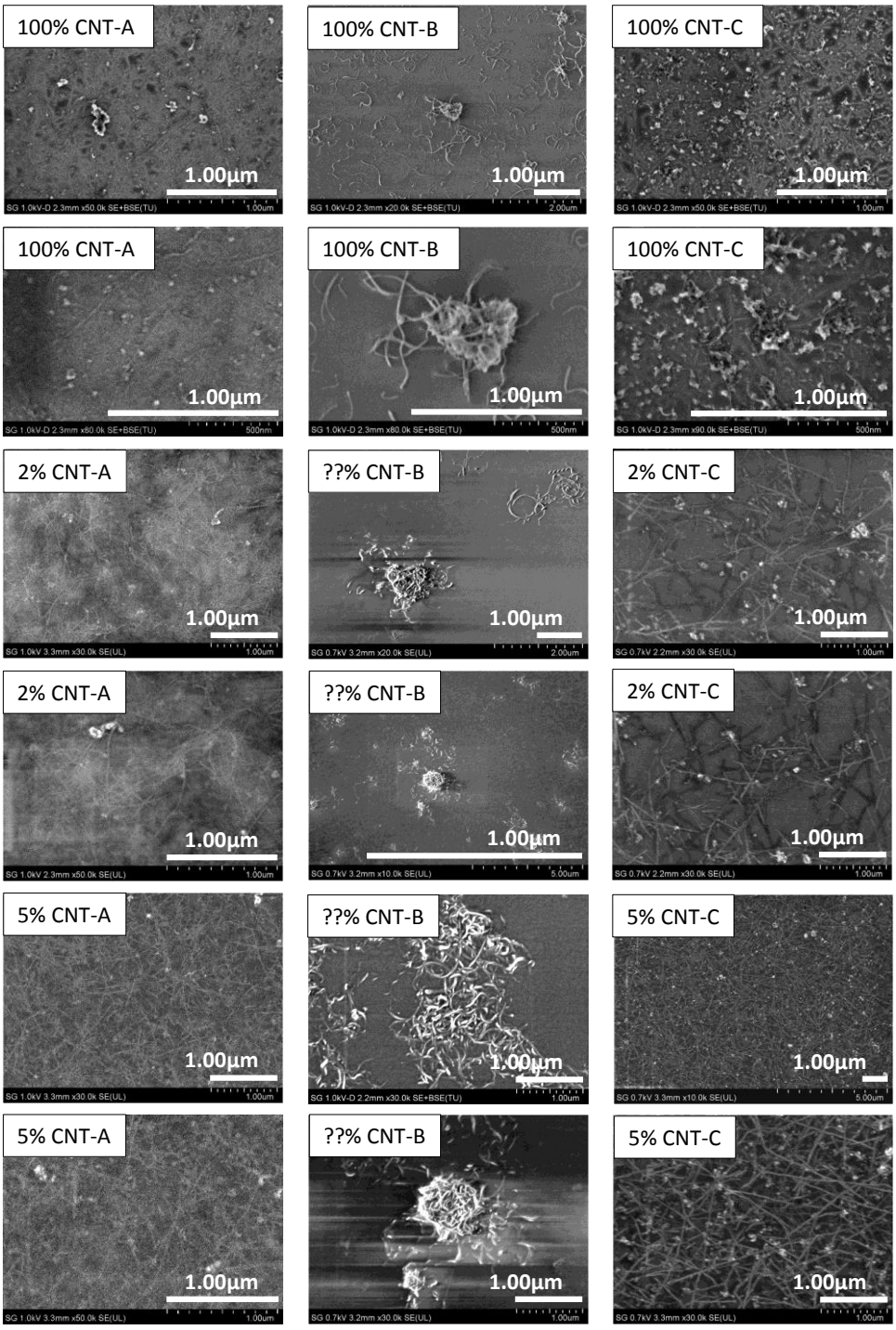

Figure S2.4: Extra SEM images of semiconductor films.

2.7.5 Additional AFM images

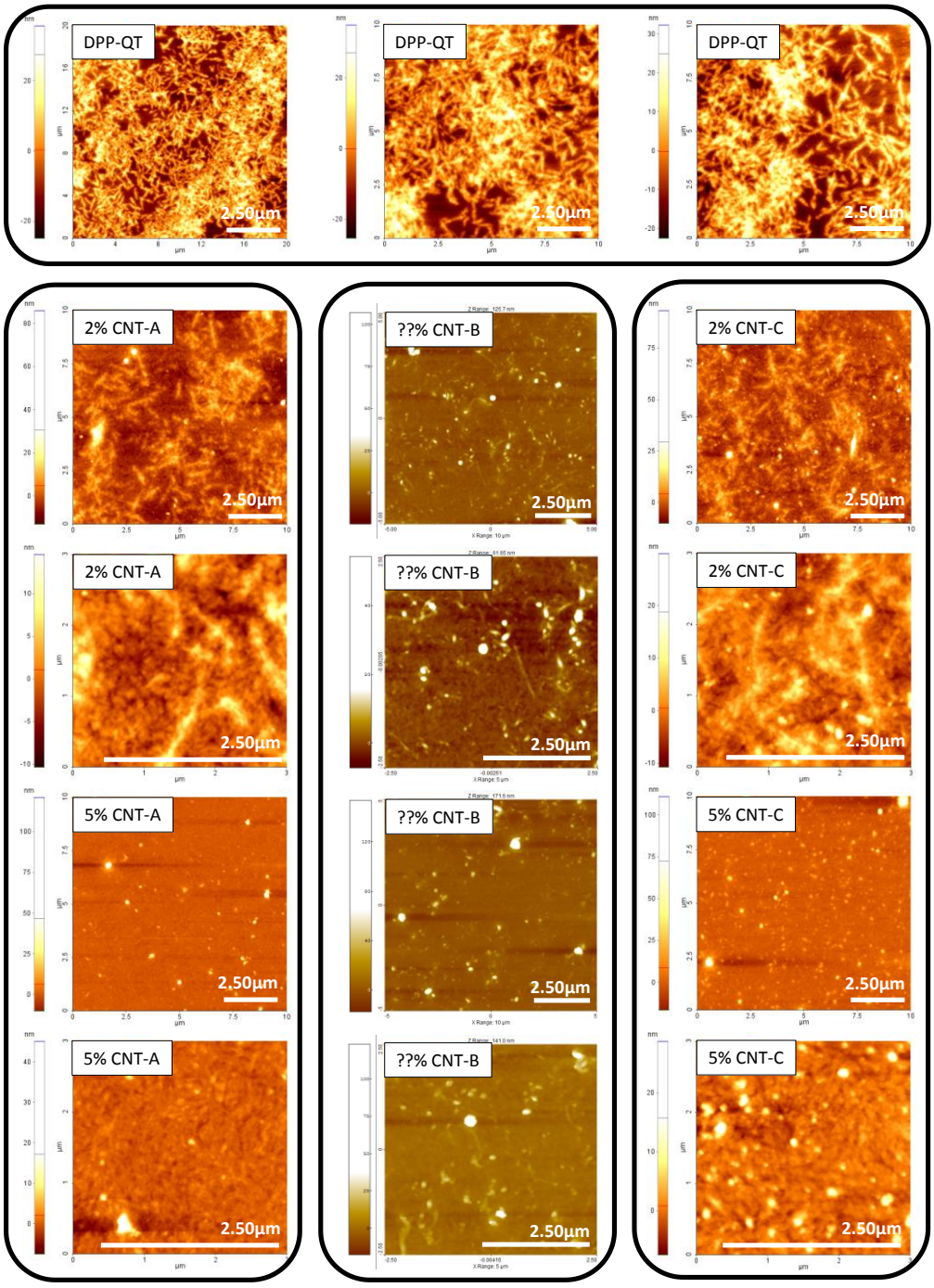

Figure S2.5: Extra AFM images of semiconductor films.

2.7.6 Electrical characterization

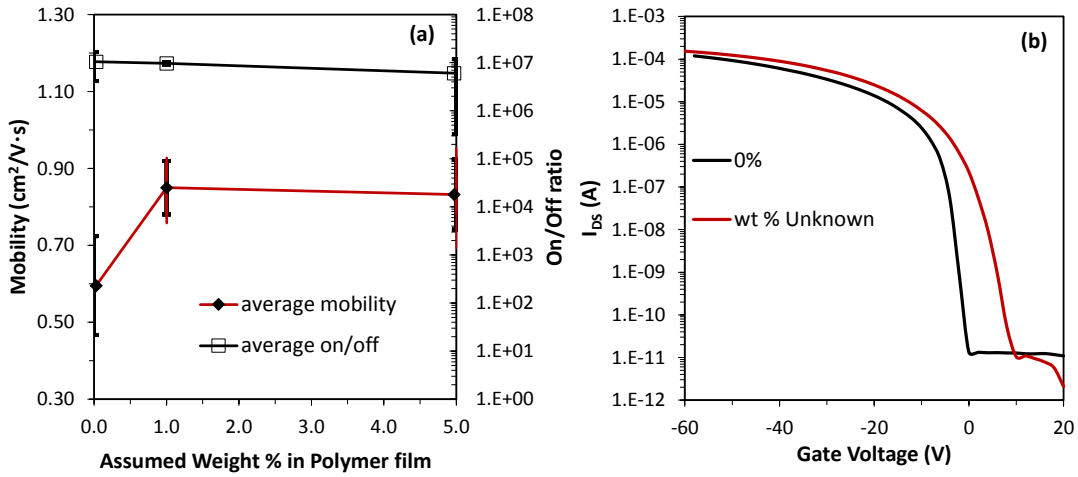

Figure S2.6: DPP-QT/ CNT-B at various SWCNT wt%. (*a*), mobility vs SWCNT loading, (*b*) transfer curves.

Table S2.1

Electrical characterization data for the three systems studies at various SWCNT loadings.

SWCNT wt%		0%	0.5%	1%	1.5%	2%	2.5%	3%	4%	5 %
Mobility $cm^2V^{-1}s^{-1}$	CNT-A	0.60	0.79	0.85	0.89	0.98	1.10	1.09	1.02	0.62
	CNT-B	----	0.75	----	----	----	----	----	----	----
	CNT-C	0.60	0.55	0.67	0.70	0.72	0.65	0.53	0.49	----
On/off ratio	CNT-A	$1.1*10^7$	$8.6*10^6$	$4.3*10^6$	$4.3*10^5$	$2.2*10^5$	$9.4*10^4$	$3.6*10^4$	$1.7*10^3$	18

	CNT-B	----	$1.4*10^{-8}$	----	----	----	----	----	----	----
	CNT-C	$7.3*10^{6}$	$1.5*10^{7}$	$1.0*10^{6}$	$7.9*10^{4}$	$1.9*10^{4}$	$4.7*10^{3}$	$1.7*10^{3}$	$3.7*10^{2}$	----
V_{Th} (V)	CNT-A	-3.5	6.6	6.7	7.3	8.1	8.1	6.2	8.8	17.8
	CNT-B	----	0.0	----	----	----	----	----	----	----
	CNT-C	-3.9	6.4	7.1	7.1	4.8	5.4	6.9	2.1	----

2.8 Appendix

Table A2.1

Mobility and on/off data gathered during device testing for DPP-QT

Mobility	On/off	Mobility	On/off	Mobility	On/off	Mobility	On/off
0.40	4.98E+06	0.37	9.38E+06	0.78	8.26E+06	0.44	1.68E+07
0.37	4.03E+06	0.37	9.38E+06	0.67	8.66E+06	0.51	7.06E+06
0.44	5.48E+06	0.40	2.64E+07	0.67	9.33E+06	0.55	8.74E+06
0.41	5.38E+06	0.44	3.89E+07	0.63	7.81E+06	0.55	8.32E+06
0.75	6.84E+06	0.45	1.06E+07	0.66	7.24E+06	0.61	8.85E+06
0.73	9.77E+06	0.60	9.32E+06	0.56	4.73E+06	0.61	8.55E+06
0.65	8.05E+06	0.59	9.88E+06	0.54	9.71E+06	0.59	2.55E+07
0.72	1.17E+07	0.61	1.04E+07	0.60	1.05E+07	0.52	9.25E+06
0.71	9.61E+06	0.66	7.58E+06	0.61	1.34E+07	0.97	8.87E+06
0.73	1.11E+07	0.65	8.04E+06	0.56	8.30E+06	0.72	1.53E+07
0.78	9.34E+06	0.61	7.56E+06	0.59	9.86E+06		

Table A2.2

Mobility and on/off data gathered during device testing for DPP-QT with various loadings of CNT-A

DPP-QT / CNT-A 99.5 / 0.5 wt%		DPP-QT / CNT-A 99 / 1 wt%		DPP-QT / CNT-A 98.5 / 1.5 wt%		DPP-QT / CNT-A 98 / 2 wt%	
Mobility	**On/off**	**Mobility**	**On/off**	**Mobility**	**On/off**	**Mobility**	**On/off**
0.53	9.33E+06	0.72	9.58E+06	0.98	4.50E+05	0.87	1.28E+05
1.01	3.62E+07	0.68	1.62E+07	0.82	4.73E+05	1.02	9.76E+05
0.84	1.08E+07	1.07	6.27E+06	0.84	5.02E+05	1.00	2.87E+05
0.78	5.99E+06	0.83	1.49E+07	0.92	3.06E+05	0.97	1.51E+05
0.65	8.87E+06	0.86	1.95E+06	0.99	3.85E+05	0.82	4.55E+04
0.87	2.66E+06	0.79	4.53E+06	0.81	5.10E+05	0.98	1.36E+05
0.89	4.79E+06	0.94	1.44E+06	0.95	4.68E+05	1.06	1.53E+05
0.74	3.03E+06	1.01	9.64E+05	0.82	4.86E+05	0.98	4.10E+05
0.88	1.21E+06	0.75	6.71E+06			1.25	6.25E+04
0.90	1.66E+07	1.02	1.18E+06			0.96	2.02E+05
0.70	4.66E+06	0.75	9.42E+05			0.86	1.60E+04
0.72	4.31E+06	0.62	2.32E+06			1.06	1.60E+04
0.73	3.19E+06	1.00	4.96E+05				
		0.88	4.01E+05				
		0.92	2.48E+05				
		0.70	2.23E+05				

Table A2.2 Continued

DPP-QT / CNT-A 97.5 / 2.5 wt%		DPP-QT / CNT-A 97 / 3 wt%		DPP-QT / CNT-A 96 / 4 wt%		DPP-QT / CNT-A 95 / 5 wt%	
Mobility	**On/off**	**Mobility**	**On/off**	**Mobility**	**On/off**	**Mobility**	**On/off**
1.38	1.12E+05	1.19	1.36E+04	0.85	8.89E+02	0.59	2.02E+01
0.98	1.98E+05	0.89	4.09E+03	0.86	1.16E+03	0.50	1.53E+01
1.21	1.36E+05	1.03	7.20E+03	1.01	6.22E+02	0.63	2.31E+01
1.16	6.55E+04	0.89	4.05E+03	1.15	1.02E+03	0.54	1.68E+01
0.86	1.59E+03	1.37	6.67E+03	0.94	1.36E+03	0.65	1.90E+01
1.01	1.87E+03	0.97	3.77E+03	1.02	9.62E+02	0.72	2.10E+01
1.11	2.20E+03	0.86	2.34E+03	1.14	1.21E+03	0.68	1.18E+01
1.37	1.28E+03	1.12	2.05E+03	1.07	1.50E+03	0.68	1.64E+01
1.26	2.60E+05	1.23	1.49E+05	0.80	2.91E+03		
0.97	9.28E+04	1.09	4.52E+04	0.93	2.67E+03		
0.94	1.00E+05	1.21	6.04E+04	0.80	2.81E+03		
0.96	1.62E+05	1.10	6.40E+04	0.99	2.20E+03		
		0.97	8.95E+04	1.22	1.30E+03		
		1.00	3.95E+04	1.02	1.83E+03		
		1.42	5.27E+04	1.12	1.87E+03		
		1.10	3.55E+04	1.34	3.30E+03		

Table A2.3

Mobility and on/off data gathered during device testing for DPP-QT with various loadings of CNT-B, no wt% given as it could not be determined

Mobility	On/off	Mobility	On/off	Mobility	On/off	Mobility	On/off
0.88	1.18E+06	0.98	2.62E+08	0.76	1.18E+07	0.95	3.20E+07
0.85	2.70E+05	0.95	3.20E+07	0.76	1.38E+07	0.94	6.99E+06
0.95	5.19E+05	0.94	6.99E+06	0.74	1.32E+07	1.15	2.89E+07
0.93	1.21E+06	1.15	2.89E+07	1.13	4.92E+06	0.72	9.45E+06
0.78	1.00E+07	0.72	9.45E+06	1.13	3.24E+06	0.66	9.99E+06
0.84	1.19E+07	0.66	9.99E+06	1.39	1.77E+06	0.76	1.04E+07
0.73	1.33E+07	0.76	1.04E+07	1.28	5.18E+05	0.86	1.53E+07
0.69	1.00E+07	0.86	1.53E+07	1.55	5.79E+06	1.00	7.52E+06
1.55	5.79E+06	1.00	7.52E+06	1.08	5.39E+06	0.95	3.76E+08
1.08	5.39E+06	0.95	3.76E+08	1.50	2.61E+06	0.82	1.05E+08
1.50	2.61E+06	0.82	1.05E+08	1.18	3.49E+05	0.89	7.69E+06
1.18	3.49E+05	0.89	7.69E+06	0.98	2.62E+08		

Table A2.4

Mobility and on/off data gathered during device testing for DPP-QT with various loadings of CNT-C

DPP-QT / CNT-C 99.5 / 0.5 wt%		DPP-QT / CNT-C 99 / 1 wt%		DPP-QT / CNT-C 98.5 / 1.5 wt%		DPP-QT / CNT-C 98 / 2 wt%	
Mobility	**On/off**	**Mobility**	**On/off**	**Mobility**	**On/off**	**Mobility**	**On/off**
0.52	5.65E+06	0.72	2.97E+06	0.76	5.53E+04	0.72	1.04E+04
0.44	7.33E+06	0.76	1.48E+06	0.71	5.66E+04	0.64	3.79E+04
0.69	4.15E+07	0.63	1.29E+06	0.69	2.75E+04	0.62	1.48E+04
0.64	3.17E+06	0.72	8.52E+05	0.70	6.05E+04	0.75	1.61E+04
0.49	1.00E+07	0.60	8.06E+05	0.69	2.23E+05	0.88	2.24E+04
0.53	4.09E+07	0.69	1.19E+05	0.72	1.21E+05	0.76	1.12E+04
0.52	4.81E+06	0.63	2.37E+05	0.72	2.53E+04	0.59	2.62E+04
0.55	8.11E+06	0.62	2.44E+05	0.65	5.97E+04	0.81	1.35E+04

DPP-QT / CNT-C 97.5 / 2.5 wt%		DPP-QT / CNT-C 97 / 3 wt%		DPP-QT / CNT-C 96 / 4 wt%	
Mobility	**On/off**	**Mobility**	**On/off**	**Mobility**	**On/off**
0.67	4.98E+03	0.42	1.05E+03	0.49	4.45E+02
0.55	2.22E+03	0.61	1.16E+03	0.52	3.73E+02
0.60	1.11E+04	0.59	2.34E+03	0.49	1.51E+02
0.63	4.92E+03	0.55	1.81E+03	0.59	2.09E+02
0.61	5.40E+03	0.56	2.33E+03	0.44	4.70E+02
0.74	3.09E+03	0.47	2.61E+03	0.43	5.91E+02
0.68	2.67E+03	0.53	1.04E+03	0.49	3.74E+02
0.70	3.24E+03	0.53	1.05E+03		

2.9 References

1. Li, Y. *et al.* Annealing-free high-mobility diketopyrrolopyrrole-quaterthiophene copolymer for solution-processed organic thin film transistors. *J. Am. Chem. Soc.* **133,** 2198–204 (2011).

2. Ha, J. S., Kim, K. H. & Choi, D. H. 2,5-Bis(2-octyldodecyl)pyrrolo[3,4-c]pyrrole-1,4-(2H,5H)-dione-Based DonorAcceptor Alternating Copolymer Bearing 5,50-Di (thiophen-2-yl)-2,20-biselenophene Exhibiting 1.5 cm2 3 V -1 3 s-1 Hole Mobility in Thin-Film Transistors. *J. Am. Chem. Soc.* **133,** 10364–10367 (2011).

3. Li, J. *et al.* A stable solution-processed polymer semiconductor with record high-mobility for printed transistors. *Scientific Reports* **2,** 1–9 (2012).

4. Hsieh, G.-W. *et al.* High performance nanocomposite thin film transistors with bilayer carbon nanotube-polythiophene active channel by ink-jet printing. *J. Appl. Phys.* **106,** 123706 (2009).

5. Dürkop, T., Getty, S. a., Cobas, E. & Fuhrer, M. S. Extraordinary Mobility in Semiconducting Carbon Nanotubes. *Nano Lett.* **4,** 35–39 (2004).

6. Cao, Q. & Rogers, J. a. Ultrathin Films of Single-Walled Carbon Nanotubes for Electronics and Sensors: A Review of Fundamental and Applied Aspects. *Adv. Mater.* **21,** 29–53 (2009).

7. Fuhrer, M. S., Kim, B. M., Dürkop, T. & Brintlinger, T. High-Mobility Nanotube Transistor Memory. *Nano Lett.* **2,** 755–759 (2002).

8. Tans, S. J., Verschueren, A. R. M. & Dekker, C. Room-temperature transistor based on a single carbon nanotube. *Nature* **393,** 49–52 (1998).

9. Rutherglen, C., Jain, D. & Burke, P. Nanotube electronics for radiofrequency applications. *Nat. Nanotechnol.* **4,** 811–9 (2009).

10. Kocabas, C. *et al.* Experimental and theoretical studies of transport through large scale, partially aligned arrays of single-walled carbon nanotubes in thin film type transistors. *Nano Lett.* **7,** 1195–202 (2007).

11. Timmermans, M. Y. *et al.* Effect of carbon nanotube network morphology on thin film transistor performance. *Nano Res.* **5,** 307–319 (2012).

12. Sun, D. *et al.* Flexible high-performance carbon nanotube integrated circuits. *Nat. Nanotechnol.* **6,** 156–61 (2011).

13. Wu, Z. *et al.* Transparent, conductive carbon nanotube films. *Science (80-.).* **305,** 1273–6 (2004).

14. Rouhi, N., Jain, D., Zand, K. & Burke, P. J. Fundamental limits on the mobility of nanotube-based semiconducting inks. *Adv. Mater.* **23,** 94–9 (2011).

15. Lay, M. D., Novak, J. P. & Snow, E. S. Simple Route to Large-Scale Ordered Arrays of Liquid-Deposited Carbon Nanotubes. *Nano Lett.* **4,** 603–606 (2004).

16. Kim, D. S., Nepal, D. & Geckeler, K. E. Individualization of single-walled carbon nanotubes: is the solvent important? *Small* **1,** 1117–24 (2005).

17. Zou, J. *et al.* Dispersion of Pristine Carbon Nanotubes Using Conjugated Block Copolymers. *Adv. Mater.* **20,** 2055–2060 (2008).

18. Ikeda, A., Nobusawa, K., Hamano, T. & Kikuchi, J. Single-walled carbon nanotubes template the one-dimensional ordering of a polythiophene derivative. *Org. Lett.* **8,** 5489–92 (2006).

19. Giulianini, M. *et al.* Regioregular poly(3-hexyl-thiophene) helical self-organization on carbon nanotubes. *Appl. Phys. Lett.* **95,** 013304 (2009).

20. Lee, H. W. *et al.* Selective dispersion of high purity semiconducting single-walled carbon nanotubes with regioregular poly(3-alkylthiophene)s. *Nat. Commun.* **2,** 1–8 (2011).

21. Song, Y. J., Lee, J. U. & Jo, W. H. Multi-walled carbon nanotubes covalently attached with poly (3-hexylthiophene) for enhancement of field-effect mobility of poly (3-hexylthiophene)/ multi-walled carbon nanotube composites. *Carbon N. Y.* **48,** 389–395 (2010).

22. Feng, Y., Miyata, Y., Matsuishi, K. & Kataura, H. High-Efficiency Separation of Single-Wall Carbon Nanotubes by Self-Generated Density Gradient Ultracentrifugation. *J. Phys. Chem. C* **115,** 1752–1756 (2011).

23. Sangwan, V. K. *et al.* Fundamental Performance Limits of Transistors Achieved Using Hybrid Molecular Dielectrics. *ACS Nano* 7480–7488 (2012).

24. Arnold, M. S., Green, A. a, Hulvat, J. F., Stupp, S. I. & Hersam, M. C. Sorting carbon nanotubes by electronic structure using density differentiation. *Nat. Nanotechnol.* **1,** 60–5 (2006).

25. Fagan, J. A., Becker, M. L., Chun, J. & Hobbie, E. K. Length Fractionation of Carbon Nanotubes Using Centrifugation. *Adv. Mater.* **20,** 1609–1613 (2008).

26. Ghosh, S., Bachilo, S. M. & Weisman, R. B. Advanced sorting of single-walled carbon nanotubes by nonlinear density-gradient ultracentrifugation. *Nat. Nanotechnol.* **5,** 443–50 (2010).

27. Arnold, M. S., Stupp, S. I. & Hersam, M. C. Enrichment of single-walled carbon nanotubes by diameter in density gradients. *Nano Lett.* **5,** 713–8 (2005).

28. Green, A. A. & Hersam, M. C. Nearly single-chirality single-walled carbon nanotubes produced via orthogonal iterative density gradient ultracentrifugation. *Adv. Mater.* **23,** 2185–90 (2011).

29. Tanaka, T., Urabe, Y., Nishide, D. & Kataura, H. Continuous Separation of Metallic and Semiconducting Carbon Nanotubes Using Agarose Gel. *Appl. Phys. Express* **2,** 125002 (2009).

30. Tanaka, T., Jin, H., Miyata, Y., Fujii, S. & Suga, H. Simple and Scalable Gel-Based Semiconducting Carbon Nanotubes 2009. *Nano Lett.* **9,** 1497–1500 (2009).

31. Miyata, Y., Maniwa, Y. & Kataura, H. Selective oxidation of semiconducting single-wall carbon nanotubes by hydrogen peroxide. *J. Phys. Chem. B* **110,** 25–9 (2006).

32. Mistry, K. S., Larsen, B. A. & Blackburn, J. L. High-yield dispersions of large-diameter semiconducting single-walled carbon nanotubes with tunable narrow chirality distributions. *ACS Nano* **7,** 2231–2239 (2013).

33. Nish, A., Hwang, J.-Y., Doig, J. & Nicholas, R. J. Highly selective dispersion of single-walled carbon nanotubes using aromatic polymers. *Nat. Nanotechnol.* **2,** 640–6 (2007).

34. Stranks, S. D., Habisreutinger, S. N., Dirks, B. & Nicholas, R. J. Novel Carbon Nanotube-Conjugated Polymer Nanohybrids Produced By Multiple

Polymer Processing. *Adv. Mater.* 1–7 (2013). doi:10.1002/adma.201205250

35. Wang, C. *et al.* Wafer-scale fabrication of separated carbon nanotube thin-film transistors for display applications. *Nano Lett.* **9,** 4285–91 (2009).

36. Engel, M. *et al.* Thin film nanotube transistors based on self-assembled, aligned, semiconducting carbon nanotube arrays. *ACS Nano* **2,** 2445–52 (2008).

37. Derry, C., Wu, Y., Zhu, S. & Deen, J. Composite Semiconductor Material of Carbon Nanotubes and Poly[5,5′-bis(3-dodecyl-2-thienyl)-2,2′-bithiophene] for High-Performance Organic Thin-Film Transistors. *J. Electron. Mater.* **42,** 3481–3488 (2013).

38. Star, A. *et al.* Preparation and Properties of Polymer-Wrapped Single-Walled Carbon Nanotubes. *Angew. Chem Int. Ed* **40,** 1721–1725 (2001).

39. Kang, Y. K. *et al.* Helical wrapping of single-walled carbon nanotubes by water soluble poly(p-phenyleneethynylene). *Nano Lett.* **9,** 1414–8 (2009).

40. Liu, J. & Hersam, M. C. Recent Developments in Carbon Nanotube Sorting and Selective Growth. *MRS Bulletin* **35,** 315–321 (2010).

41. Bachilo, S. M. *et al.* Structure-assigned optical spectra of single-walled carbon nanotubes. *Science (80-.).* **298,** 2361–6 (2002).

42. Sangwan, V. K. *et al.* Optimizing transistor performance of percolating carbon nanotube networks. *App. Phys .Lett.* **97,** 043111 (2010).

43. Smithson, C. S., Zhu, S., Wigglesworth, T. & Wu, Y. Unsorted single walled carbon nanotubes enabled the fabrication of high performance organic thin film transistors with low cost metal electrodes. *Chem. Commun.* **49,** 8791–3 (2013).

44. Snow, E. S., Novak, J. P., Campbell, P. M. & Park, D. Random networks of carbon nanotubes as an electronic material. *Appl. Phys. Lett.* **82,** 2145–47 (2003).

45. Lei, T., Dou, J.-H. & Pei, J. Influence of alkyl chain branching positions on the hole mobilities of polymer thin-film transistors. *Adv. Mater.* **24,** 6457–61 (2012).

46. Kim, G. *et al.* A Thienoisoindigo-Naphthalene Polymer with Ultrahigh Mobility of 14.4 cm(2)/V·s That Substantially Exceeds Benchmark Values for Amorphous Silicon Semiconductors. *J. Am. Chem. Soc.* **136,** 9477–83 (2014).

47. Sonar, P. *et al.* High mobility organic thin film transistor and efficient photovoltaic devices using versatile donor–acceptor polymer semiconductor by molecular design. *Energy Environ. Sci.* **4,** 2288 (2011).

48. Chen, C. & Zhang, Y. in *Nanowelded Carbon Nanotubes: From Field-Effect Transistors to Solar Microcells* (eds. Avouris, P. et al.) 2–12 (Springer, 2008). doi:10.1007/978-3-642-01499-4

49. Gangoli, V. S. *et al.* Using Nonionic Surfactants for Production of Semiconductor-type Carbon Nanotubes by Gel-based Affinity Chromatography. *Nanomater. Nanotechnol.* 1 (2014). doi:10.5772/58828

50. Ding, J. *et al.* Enrichment of large-diameter semiconducting SWCNTs by polyfluorene extraction for high network density thin film transistors. *Nanoscale* **6,** 2328–39 (2014).

Chapter 3

Unsorted Single Walled Carbon Nanotubes Enabled the Fabrication of High Performance Organic Thin Film Transistors With Low Cost Metal Electrodes

This chapter involves the work published in the following article, additional information has been added to the supporting information as well as tables of data as an appendix. The major contribution of this work is that we have shown that unsorted single walled carbon nanotubes can assist in reducing the charge injection resistance of metal electrodes who's work function does not closely match the highest occupied molecular orbital of the semiconductor.

"Unsorted single walled carbon nanotubes enabled the fabrication of high performance organic thin film transistors with low cost metal electrodes"

Reproduced from: Chad S. Smithson, Yiliang Wu, Tony Wigglesworth, and Shiping Zhu; *Chem. Commun.*, **2013**, 49, 8791-8793. With permission from The Royal Society of Chemistry.

DOI: 10.1039/C3CC43920H

3.1 Abstract

Transistors with a diketopyrrolopyrrole-quarterthiophene (DPP-QT) polymer and low-cost Al or Cu electrodes were studied. Albeit a large charge injection resistance exists between DPP-QT and Al or Cu, the resistance was dramatically reduced when unsorted single walled carbon nanotubes (SWCNTs) were blended into the DPP-QT film. This led to a high mobility of 0.64 and 1.1 $cm^2 V^{-1} s^{-1}$, respectively, for Al and Cu devices, which is similar or even better than the device using gold electrodes (0.78 $cm^2 V^{-1} s^{-1}$).

3.2 Start of paper

Organic thin-film transistors (OTFTs) have attracted extensive research interest in the past decade, as they are promising candidates for low-cost, flexible circuitry in applications such as e-paper, plastic displays, radio frequency identification tags, and large area photonics.[1] A significant amount of effort has been devoted in recent years to improve the performance of OTFTs, mainly through new semiconductor design[2,3] and optimization of semiconductor film morphology and semiconductor/dielectric interfaces.[4,5,6] Many different small molecules and polymers are used in the semiconductive layer, with the preferred structure being highly conjugated to facilitate strong π-π stacking. This stacking allows for excellent charge transfer through the π-electron overlap to produce a high charge carrier mobility. However, the choice of electrode materials is limited to matching the HOMO level of the semiconductor to the work function of the source and drain electrodes to reduce charge injection resistance. For p-type semiconductors, expensive Au having a work function of 5.1 eV is the most commonly used electrode. Low-cost metals such as Cu and Al are rarely used due to a large charge injection barrier and significantly lower performance.

An attractive alternative to polymer semiconductors for field-effect transistors (FET) is single walled carbon nanotubes (SWCNTs), due to their near perfect conjugated network with no dangling bonds. In 1998 the first SWCNT FET was created using a single SWCNT as the semiconducting channel.[7,8] Since then a

host of research studies on CNT devices consisting of pure SWCNT channels have been performed.[9] These devices exhibit a Schottky barrier to conduction.[10,11] For p-type devices this barrier can be reduced by matching the Fermi level of the source/drain metal to the valence band of the SWCNT. It has been found that a larger diameter SWCNT channel and a Pd electrode have nearly no Schottky barrier,[12] providing nearly ballistic transport.[13] Additionally, one dimensional electrostatic effects around CNTs promote charge carrier tunnelling across the contact Schottky barriers allowing for more efficient charge injection.[14] This makes SWCNTs an extremely attractive alternative to Si based devices, unfortunately there is no cost effective method to generate a pure CNT channel. An alternative method to utilize their excellent charge injection properties has been to incorporate SWCNTs into the electrodes of small molecule transistors such as pentacene[15] and copper hexadecafluorophthalocyanine (FCuPc).[16] These devices have been shown to exhibit one order of magnitude decrease in charge injection resistance.[15] However this technique again requires difficult fabrication to incorporate SWCNTs into the electrodes. A third more feasible option is to disperse CNTs within a polymeric matrix forming the semiconducting layer. This approach has been popularized by dispersing high cost purified and sorted SWCNTs.[17,18,19,20] A problem with this is that SWCNTs are generally produced in a 2:1 semiconducting:metallic ratio and the cost to separate the metallic from semiconducting CNTs is very high. Research groups typically avoid using

unsorted SWCNTs because if too many metallic SWCNTs are incorporated into the film a percolation network is generated creating a short circuit. However, at concentrations below the percolation threshold, SWCNTs can be incorporated to help reduce charge injection resistance into the polymer matrix as well as enhance charge transport of the film.

In this communication we used the diketopyrrolopyrrolequarterthiophene copolymer[2,3] (DPP-QT) (**Fig. 3.1**) with a HOMO of -5.2 eV and three different electrode metals Au, Cu and Al with work functions of -5.1 eV, -4.8 eV, and -4.3 eV, respectively. Films with and without SWCNTs (HOMO –(5.05-4.8 eV))[1] were generated and their mobility and charge injection characteristics were investigated. We show that by using SWCNTs to reduce the charge injection barrier for low work function metals such as Cu and Al, the mobility of the film can be dramatically increased to be similar or better than Au. Our method provides a very simple and cost effective way to enhance the performance of OTFTs through the use of a small amount of unsorted SWCNTs.

A 0.5 wt% DPP-QT in 1,1,2,2-tetrachloroethane solution was first prepared. A dispersion of 2 wt% SWCNT with respect to the total weight of DPP-QT and SWCNT was prepared by probe sonicating the SWCNTs in the above 0.5 wt% DPP-QT solution, resulting in a very stable DPP-QT/SWCNT dispersion. The concentration of SWCNTs in the dispersion is approximately 0.01 wt%. Both the DPP-QT solution and the DPP-QT/SWCNT dispersion were spin coated onto an octyltrichlorosilane (OTS-8) modified silicon wafer with a 200 nm SiO_2 layer,

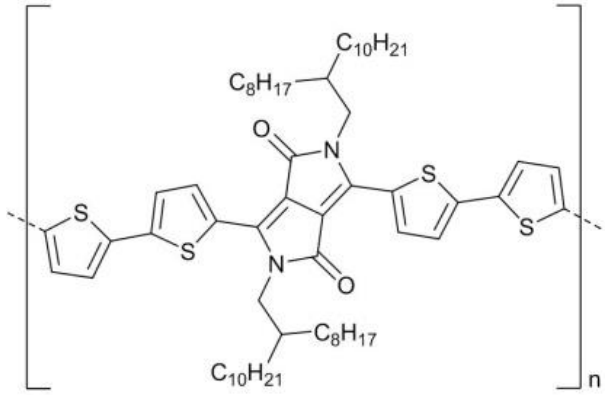

Figure 3.1: The diketopyrrolopyrrole-quarterthiophene copolymer (DPP-QT).

yielding an ~30 nm semiconductor layer. Electrodes were deposited using a shadow mask, except for channel lengths below 40 μm, which were formed using a 20 μm wire. After fabrication, devices were stored under vacuum in the dark, and measured in air within 2 hours of being removed from vacuum.

AFM and SEM images confirm that the SWCNTs are well dispersed in the film. **Fig. 3.2*(a)*** and ***(b)*** show SEM images of the DPP-QT film with and without SWCNTs. The SWCNTs are clearly observed and are randomly dispersed in the film. The AFM images (**Fig. 3.2*(c)*** and ***(d)***) reveal that the polymer forms polycrystalline domains. With the addition of 2 wt% SWCNTs, the polymer still forms polycrystalline domains, with the number of domains seen to reduce showing that the SWCNTs interrupt the packing of the polymer.

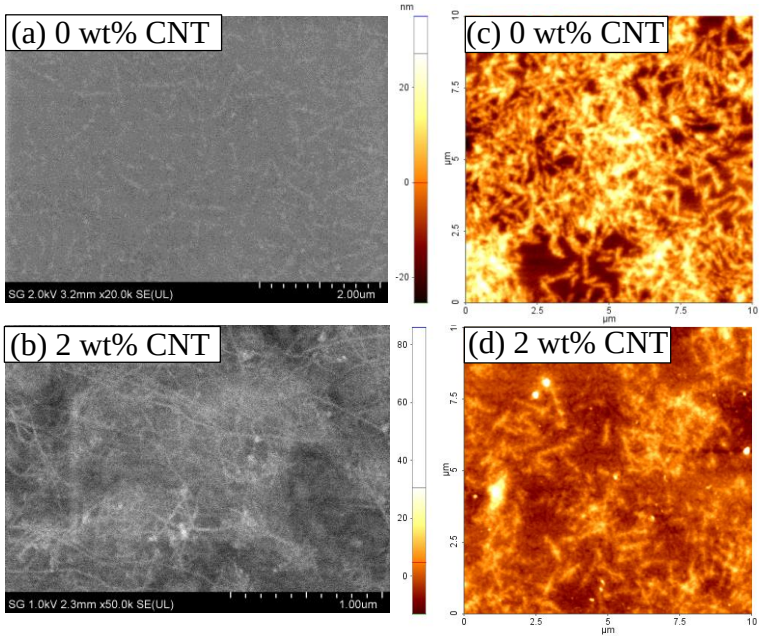

Figure 3.2: *(a)* and *(b)* SEM images of the semiconducting films. *(a)* A pure DPP-QT polymer, showing some crystalline domains of the polymer. *(b)* 2 wt% SWCNTs dispersed in the DPP-QT polymer. The tubes are clearly observed and are randomly oriented. *(c)* and *(d)* AFM images of the semiconducting films. *(c)* DPP-QT polymer, the polycrystalline domains of the material are clearly visible. *(d)* 2 wt% SWCNTs dispersed in the DPP-QT polymer. Fewer polycrystalline domains are observed indicating that the SWCNTs disrupt the formation of polycrystalline domains.

To calculate mobility the following formula was used:

$$I_{DS} = \mu C_i (W/2L)(V_{GS} - V_{Th})^2$$

where I_{DS} is the drain current, V_{GS} is the gate voltage, V_{Th} is the threshold voltage, μ is the mobility of the film, W and L are, respectively, the width and length of the transistor, and C_i is the capacitance per unit area of the dielectric layer. The HOMO of the DPP-QT polymer is -5.2 eV,[2] and is therefore expected

to have the highest mobility with Au electrodes because Au's work function most closely matches the HOMO of the polymer reducing the charge injection resistance. We observed μ_{Au} = 0.64 $cm^2 V^{-1} s^{-1}$ followed by a very small decrease when Cu is used (μ_{Cu} = 0.58 $cm^2 V^{-1} s^{-1}$) and a large drop for Al (μ_{Al} = 0.040 $cm^2 V^{-1} s^{-1}$). When the SWCNTs were added to the film, the mobility of the three types of devices was enhanced. Three batches of devices were prepared, each consisting of 8 transistors of each type. The devices exhibited reproducible mobilities, and a high current on/off ratio of over 10^5, as shown in the transfer curves (**Fig. S3.1**). The average mobility values and their deviation are shown in **Fig. 3.3**. The mobility of devices with Au electrodes increased slightly ($\mu_{Au,CNT}$ = 0.78 $cm^2 V^{-1} s^{-1}$), which is expected because SWCNTs caused little change in the charge injection resistance. Mobility of devices with Al electrodes was increased to nearly the same value as Au (μ_{AlCNT} = 0.64 $cm^2 V^{-1} s^{-1}$) revealing that the SWCNTs have a large effect on its charge injection. Although Al is prone to oxidation in air, we believe that the formation of Al_2O_3 on the surface of electrodes prevents further oxidation, thus a stable semiconductor/ electrode interface exists for the top-contact devices. For Cu, there is a large increase in the mobility value ($\mu_{Cu,CNT}$ = 1.1 $cm^2 V^{-1} s^{-1}$). This is because the work function of Cu and the HOMO of the SWCNTs match up very well. When stored in a low humidity chamber (<30%) in the dark, the devices showed good stability with no or little change in electrical performance over 1 month. Attempts to make transistors using the unsorted SWCNTs were not successful, as the SWCNTs

could not be dispersed in the solvent without DPP-QT. However, we believe that the high mobility was contributed by the polymer rather than the SWCNTs, as the devices showed a high current on/off ratio. Unsorted SWCNT devices would yield a very low current on/off ratio due to the presence of a large amount of conductive nanotubes.

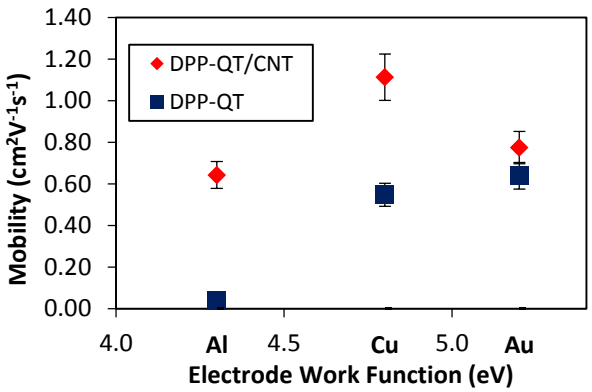

Figure 3.3: Average mobility values without and with SWCNTs for a 40 mm channel length plotted against the work function of the metals.

To better understand these mobility changes, we looked at the output curves of the devices to determine the charge injection resistance. Measuring the slope of the linear region of the output curve provides the inverse resistance of the material for a specific gate voltage. **Fig. 3.4** provides an example of an output curve using Cu electrodes and films with and without SWCNTs. The linear region is marked with a dashed line. When these resistances are plotted against the channel length a linear increase in resistance is observed corresponding to the resistance of the film (**Fig. 3.4**). A linear regression to the y intercept provides the charge injection resistance from the metal electrodes into and out of the film. It

should be noted that the resistance measurements of Cu and Al devices without SWCNTs showed a large variation. This is due to the very low current in the linear regime for these low performance devices. Although the resistance values may not be accurate, the trend is clear that both the charge injection resistance and its variation were reduced significantly upon addition of SWCNTs. The data are summarized in **Table 1**. For Au there is a small increase in charge injection resistance from 0.21 to 0.87 MΩ likely because the SWCNT HOMO level does not match that of Au as well as the DPP-QT polymer. For Cu the charge injection resistance is decreased by an order of magnitude from ~21 to 2.4 MΩ. The largest improvement is observed for Al with a change of 3 to 4 orders of magnitude from 10^4–10^5 MΩ to ~45 MΩ. These results reveal that a small percent of SWCNTs in the film can have a dramatic impact on the charge injection value, thus, the mobility improvements of the devices.

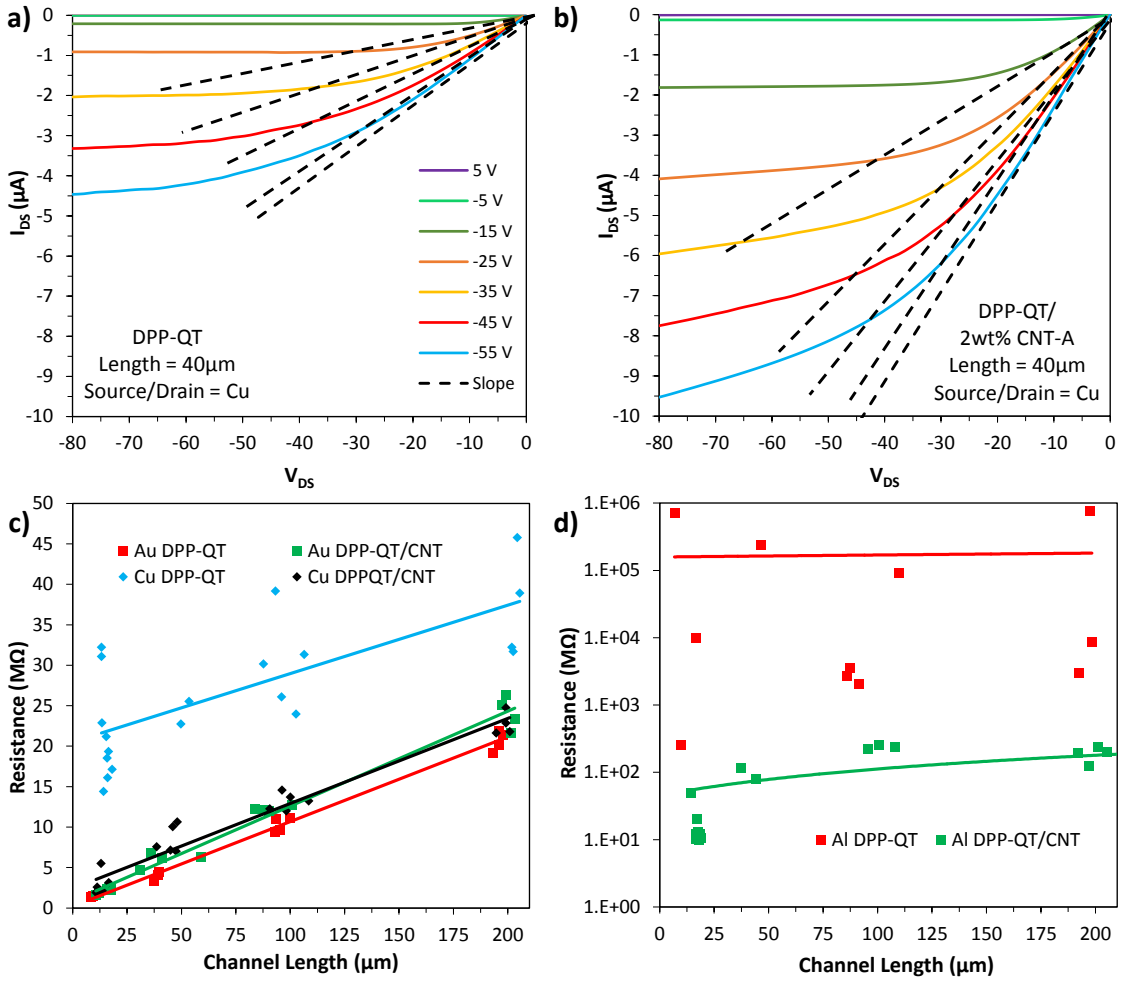

Figure 3.4: *(a)*, *(b)* Output curves for OTFT having Cu electrodes, without (left) and with (right) SWCNTs and channel lengths of 45 mm and 50 mm respectively. The dashed line represents the slope of the linear region for a V_{GS} = -55 V. The inverse of the slope is equal to the resistance of the device at that V_{GS}. *(c)*, *(d)* Channel length vs. resistance for Au and Cu source/drain electrodes at a V_{GS} = -25 V. The resistances were determined from output curves like the ones in *(a)*, *(b)*. By extrapolating the line of best fit back to the y intercept, the charge injection resistance of the transistor can be determined.

Table 3.1 Contact resistance for a gate voltage of -25 V		
Drain/Source Metal (Work Function)	**Contact Resistance (MΩ)**	
	DPP-QT	**DPP-QT/2wt% CNT-A**
Gold (5.1 eV)	0.21	0.87
Copper (4.8 eV)	~21	2.4
Aluminium (4.3 eV)	10^4 -10^5	~45

This research presents an opportunity to utilize low cost electrodes such as Cu or Al by simply incorporating a small amount of unsorted SWCNT into the film. Through AFM and SEM, we have shown that the SWCNTs can be evenly distributed throughout the film and still allow the polymer to form polycrystalline domains. Preparation of the solution only requires a 2 minute probe sonication, allowing the semiconductive layer to be formed from one solution, an important factor if we wish to form low cost transistors. We have shown that the HOMO level of the semiconductive layer and the work function of the metal do not need to be aligned to achieve a low charge injection value if SWCNTs are present. This has led to mobility improvements for Cu and Al devices from 0.58 and 0.040 to 1.1 and 0.64 $cm^2\ V^{-1}\ s^{-1}$, respectively. In the future the use of unsorted SWCNTs could open a new field of transistor production from low cost metals.

3.3 Supplementary information

3.3.1 Experimental

***Preparation of Diketopyrrolopyrrole-Quaterthiophene Copolymer (DPP-QT) solution*:**

DPP-QT was synthesized following the procedure reported by Choi et al [J. S. Ha, K. H. Kim, and D. H. Choi, JACS, 2011, 133, 10364–10367]. The DPP-QT polymer (0.02 g) was dissolved in 1,1,2,2-tetrachlorethane (3.98 g) for 2 hours at 80 ºC in the absence of light to form a 0.5 wt% solution.

***Preparation of DPP-QT / SWCNT dispersion*:**

A dispersion of 5 wt% SWCNT respective to the total weight of the DPP-QT and SWCNT was first prepared by adding 1.5 mg of Sigma Aldrich (704148) (6,5) chirality, carbon >90 %, 77% (carbon as SWCNT), 0.7 – 0.9 nm diameter, 0.5 – 2 μm length, to 5.6985 g of 0.5 wt% DPP-QT solution. The mixture was immersed in an ice bath and probe sonicated on a Branson Digital Sonifier-450 (400 W) at 35% amplitude for 2 min. Originally, the resultant dark green dispersion was centrifuged at 25,000 g force for 30 min and the supernate was collected. After the centrifuge, no precipitate was observed at the bottom of the container. The SWCNTs were well dispersed and remained in the polymer solution. Therefore, the centrifuge step was deemed unnecessary and no longer performed. This DPP-QT/SWCNT dispersion was further diluted using the 0.5 wt% DPP-QT solution, yielding a dispersion of 2 wt% SWCNT respective to the total weight of the DPP-QT and SWCNT, for OTFT device fabrication. The concentration of SWCNTs in the dispersion is around 0.01 wt%.

3.3.2 OTFT Fabrication and Evaluation:

All fabrication and characterization of organic thin-film transistor devices (OTFTs) was done under ambient conditions taking precautions to isolate the material and device from light, but no precautions were taken to isolate the material or device from exposure to air or moisture. After fabrication, devices were stored under vacuum in the dark, and measured in air within 2 hours of being removed from vacuum. Bottom-gate TFT devices were built on n-doped silicon wafer as the gate electrode with a 200-nm thermal silicon oxide (SiO_2) as the dielectric layer. The SiO_2 surface was plasma cleaned for 2 minutes. The wafer was subsequently rinsed with H_2O then isopropanol and dried with an air stream. The SiO_2 surface was modified with octyltrichlorosilane (OTS-8) by immersing the cleaned silicon wafer substrate in 0.1 M OTS-8 in toluene at 60 ºC for 20 min. The wafer was subsequently rinsed with toluene and isopropanol and dried with an air stream. The DPP-QT solution or DPP-QT/SWCNT dispersion was dispensed onto the OTS-8-modified SiO_2 layer allowed to sit for 2 min, then spun with a 2 s ramp time, at 2000 rpm for 120 s, yielding ~ 30 nm semiconductor layer. The semiconductor films were vacuum dried at 70 ºC for 30 min and annealed at 140 ºC for 40 min, and allowed to cool to room temperature under vacuum. The same semiconductor thin films were used for OTFT devices as well as SEM and AFM characterization. To complete OTFT devices, the Au, Cu and Al source and drain electrodes were deposited by vacuum evaporation through a

shadow mask on top of the semiconductor layer with channel lengths of 40, 90, 190 and 370 μm and a width of 1 mm. To generate channel lengths below 40 μm, a 20 μm microwire was taped (at the sample edge) onto a wafer. The appropriate metal was deposited and the wire was removed, revealing a 20 μm channel. Using an electrode tip, the edges were scratched to generate a channel width of approximately 1mm. The actual channel lengths and widths were measured using an optical microscope.

From I_{DS}-V_{GS} measurements, the mobility was extracted from the saturated regime using the following equation ($V_{DS} > V_{GS}$): $I_{DS} = C_i\mu_{FE}(W/2L)(V_{GS} - V_{Th})^2$. Where I_{DS} is the drain current, C_i is the capacitance per unit area of the gate dielectric layer, V_{GS} and V_{Th} are respectively the gate voltage and threshold voltage. V_{Th} of the device was determined from the relationship between the square root of I_{DS} at the saturated regime and V_{GS} of the device by extrapolating the measured data to $I_{DS} = 0$.

3.3.3 Instrumentation

SEM Imaging Samples were imaged in their native condition (no conductive coating applied) using a Hitachi SU-8000 field emission scanning electron microscope (SEM) operating in deceleration mode with a landing voltage of 700V.

3.3.4 Atomic Force Microscopy

Samples were collected on a Park Systems XE-100 AFM operated in dynamic force mode. Each image had 2-3 samples imaged with the most representative sample displayed in this report.

3.3.5 Additional Electrical Characterization

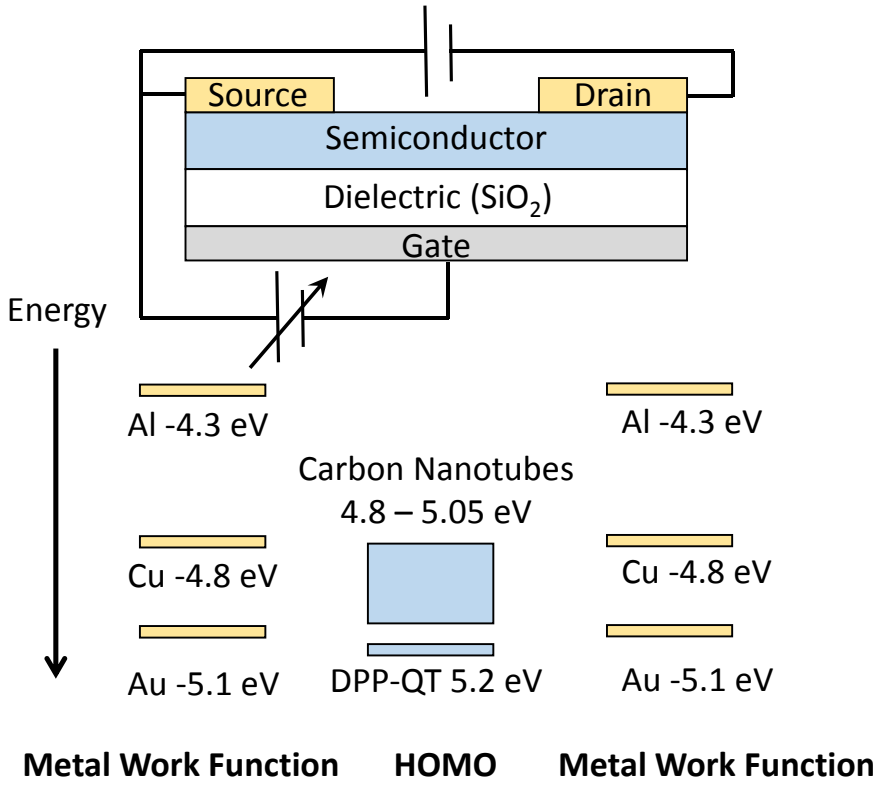

Figure S3.1: Cartoon Depiction of the top contact bottom gate FET design, with the work function and HOMO energy levels of the metals used as source/drain contacts and the semiconductor material. The spread in energy level for the unsorted SWCNT's assists in reducing charge injection resistance.

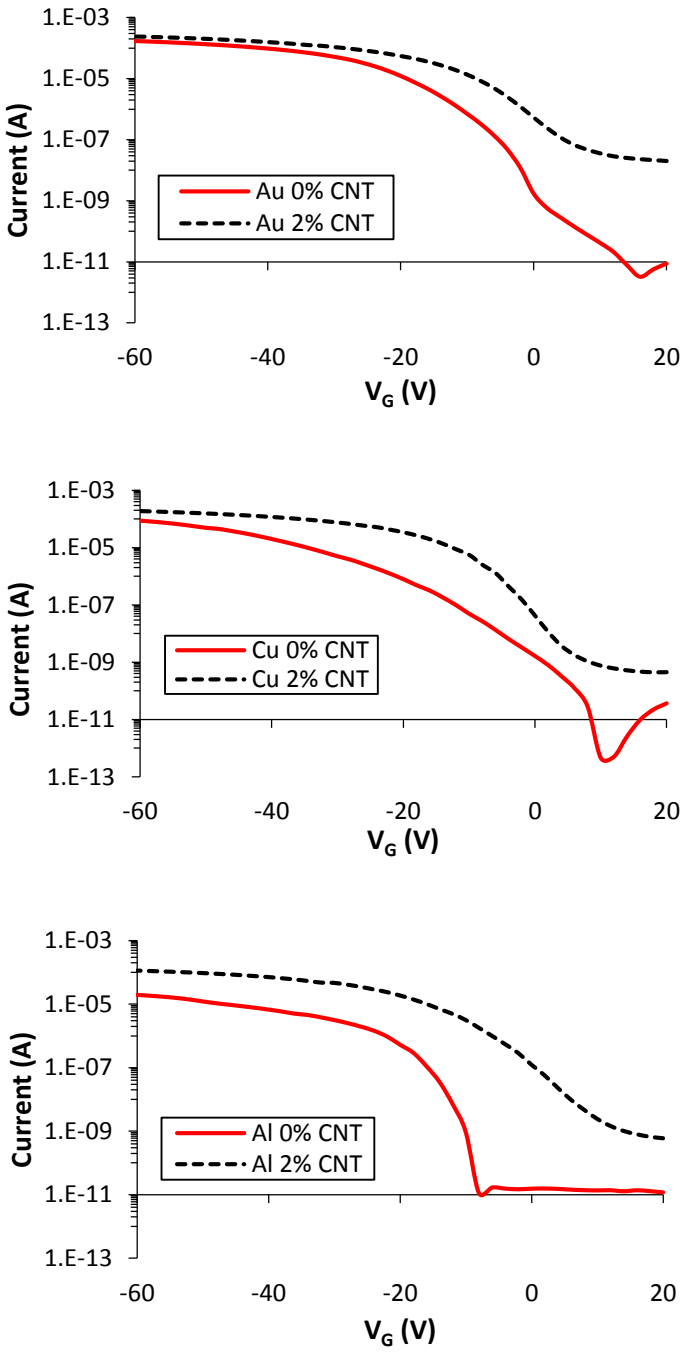

Figure S3.2: Transfer curves for OTFTs having Au, Cu and Al electrodes with and without 2 wt% CNT in the DPP-QT film. The transistors have a channel length of 40 µm and a channel width of 1000 µm.

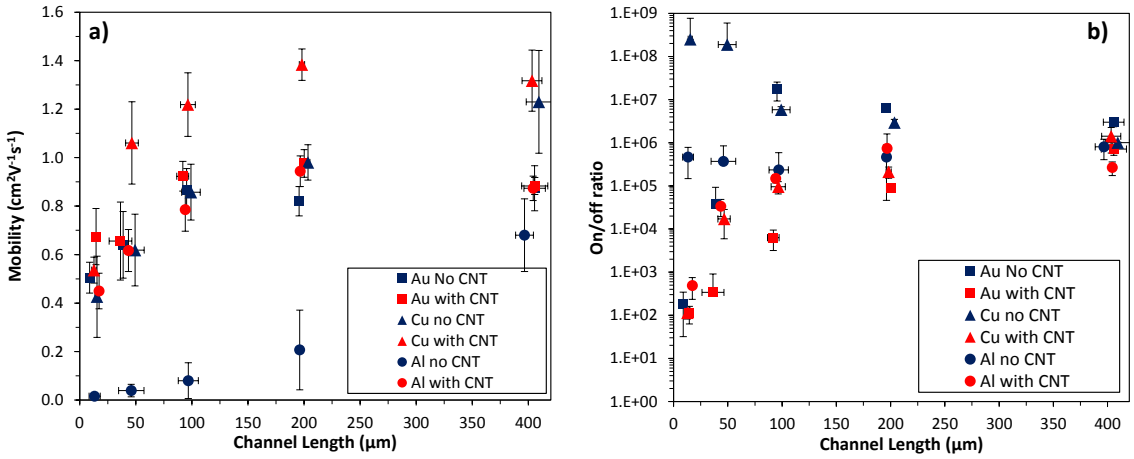

Figure S3.3: (*a*) Average mobility (*b*) on/off ratio measurements for the 6 systems studies at various channel lengths.

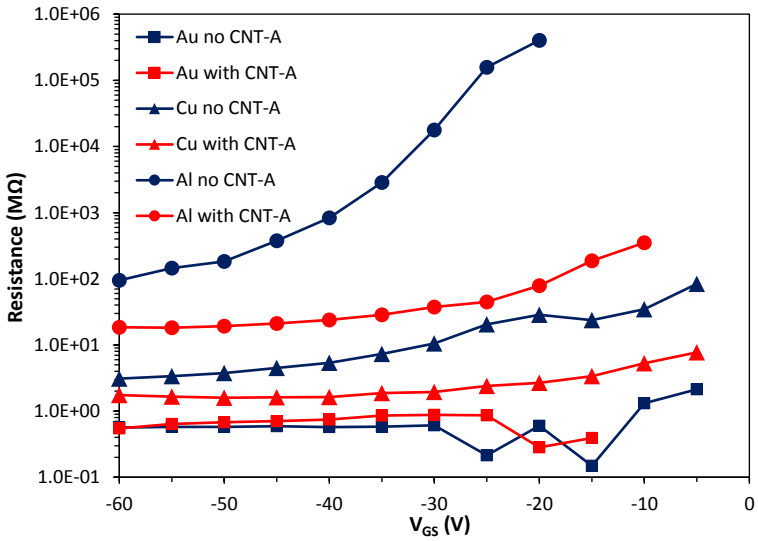

Figure S3.4: Average contact resistance vs gate voltage. We observe a divergence towards higher resistances as the V_{GS} approaches the V_{Th}.

3.4 Appendix B

Table A3.1

Electrical Characterization of devices using Au electrodes at various channel lengths

(bold values are the average for each channel length)

Gold no CNT			Gold with CNT		
Channel Length (μm)	**Mobility ($cm^2V^{-1}s^{-1}$)**	**On/off**	**Channel Length (μm)**	**Mobility ($cm^2V^{-1}s^{-1}$)**	**On/off**
8.6	0.46	2.98E+02	10.6	0.51	5.30E+01
9.2	0.55	7.75E+01	12.1	0.64	7.39E+01
			15.8	0.80	1.76E+02
			16.9	0.65	1.32E+02
			17.4	0.77	1.24E+02
14.6 +/- 3	**0.67 +/- 0.12**	**(1.12 +/- 0.5)*10^1**	**8.9 +/- 0.4**	**0.51 +/- 0.06**	**(1.9 +/- 1.6) *10^2**
37.4	0.67	1.01E+05	17.5	0.83	2.07E+02
39.2	0.49	2.58E+03	28.2	0.52	1.13E+02
39.6	0.76	1.24E+04	30.8	0.48	5.99E+01
			33.6	0.47	1.17E+02
			33.6	0.71	1.26E+02
			33.9	0.60	6.89E+01

			34.9	0.56	6.49E+01
			35.9	0.68	3.23E+02
			41.3	0.74	2.72E+02
			41.6	0.78	4.15E+02
			46.3	0.51	2.11E+03
			58.7	0.99	1.88E+02
38.7 +/- 1.2	**0.64 +/- 0.14**	**(3.9 +/- 5.4)*10^4**	**36.3 +/- 10**	**0.66 +/- 0.16**	**(3.4 +/- 5.7) *10^2**
92.9	0.89	1.65E+07	84.0	0.90	8.39E+03
93.6	0.74	6.74E+06	85.6	0.87	8.03E+03
95.1	0.94	2.05E+07	85.7	0.99	2.08E+03
100.0	0.90	2.58E+07	88.3	0.87	2.98E+03
			89.6	0.95	7.36E+03
			89.9	1.02	3.74E+03
			90.1	0.91	9.77E+03
			90.2	0.86	5.41E+03
			90.6	0.88	7.34E+03
			90.7	0.97	2.76E+03
			92.8	0.81	7.26E+03
			95.9	1.00	3.70E+03
			96.8	0.89	1.12E+04

			98.2	0.89	1.23E+04
			100.8	0.99	3.18E+03
			101.7	0.97	5.41E+03
95.4 +/-3.2	**0.87 +/- 0.09**	**(1.7 +/- 0.8)*10^{7}**	**91.9 +/- 5.3**	**0.92 +/- 0.06**	**(6.3 +/- 3.2) *10^{3}**
193.0	0.88	6.35E+06	191.8	0.89	7.01E+04
195.8	0.75	6.71E+06	197.4	0.94	1.06E+05
195.9	0.86	6.51E+06	199.0	0.92	8.12E+04
197.8	0.79	6.28E+06	201.6	1.06	8.90E+04
			202.2	0.98	9.86E+04
			202.6	1.02	9.31E+04
			203.2	1.02	8.41E+04
			203.2	0.98	1.02E+05
1.95.6 +/- 1.9	**0.82 +/- 0.06**	**(6.5 +/- 1.9)*10^{5}**	**200.1 +/- 4**	**0.98 +/- 0.06**	**(9.1 +/- 1.2) *10^{4}**
399.4	0.98	3.73E+06	397.9	0.92	6.41E+05
400.8	0.81	2.62E+06	400.2	0.85	5.60E+05
416.6	0.83	2.63E+06	419.2	0.88	9.42E+05
405.6 +/- 9.6	**0.87 +/- 0.09**	**(3.0 +/- 0.6)*10^{6}**	**405.8 +/- 12**	**0.88 +/- 0.04**	**(7.1 +/- 2.0) *10^{5}**

Table A3.2

Electrical Characterization of devices using Al electrodes at various channel lengths

(bold values are the average for each channel length)

Aluminum no CNT			Aluminum with CNT		
Channel Length (μm)	**Mobility ($cm^2V^{-1}s^{-1}$)**	**On/off**	**Channel Length (μm)**	**Mobility ($cm^2V^{-1}s^{-1}$)**	**On/off**
6.8	0.010	6.78E+05	14.5	0.33	4.41E+02
9.6	0.010	8.22E+05	16.7	0.50	2.53E+02
14.7	0.020	5.31E+05	16.8	0.45	4.36E+02
16.7	0.020	2.59E+05	16.9	0.34	1.13E+03
18.8	0.020	3.55E+04	17.1	0.46	3.93E+02
			17.4	0.45	5.85E+02
			18.3	0.49	3.78E+02
			18.5	0.47	4.24E+02
			18.9	0.56	3.63E+02
13.3 +/- 5.0	**0.016 +/- 0.005**	**(4.7 +/- 3.2)*10^5**	**17.2 +/- 1.3**	**0.45 +/- 0.07**	**(4.9 +/- 2.5) *10^2**
33.2	0.060	1.17E+06	36.8	0.44	2.86E+04
38.1	0.030	4.22E+05	37.4	0.61	1.67E+04
46.5	0.030	7.66E+04	39.1	0.68	2.13E+04
49.4	0.005	8.49E+02	42.4	0.56	6.25E+04

62.6	0.070	1.89E+05	44.3	0.73	3.19E+04
			44.6	0.64	3.29E+04
			45.5	0.61	2.49E+04
			45.6	0.58	3.50E+04
			55.8	0.70	5.12E+04
46.0 +/- 11	**0.039 +/- 0.026**	**(3.7 +/- 4.7)*10^5**	**43.5 +/- 5.7**	**0.62 +/- 0.09**	**(3.4 +/- 1.5) *10^4**
86.2	0.160	3.75E+05	86.0	0.69	1.19E+05
87.2	0.080	1.12E+05	87.0	0.74	1.53E+05
91.3	0.200	9.86E+05	90.9	0.64	1.20E+05
98.6	0.060	6.71E+04	91.0	0.76	1.10E+05
100.5	0.010	1.59E+03	91.8	0.65	1.29E+05
104.5	0.010	4.98E+03	91.9	0.83	1.53E+05
109.8	0.040	9.50E+04	94.1	0.88	1.51E+05
			94.5	0.87	1.36E+05
			95.8	0.86	1.45E+05
			98.1	0.81	2.25E+05
			100.8	0.81	1.64E+05
			108.0	0.89	1.80E+05
96.9 +/- 9.0	**0.080 +/- 0.074**	**(2.4 +/- 3.5)*10^5**	**94.2 +/- 6.0**	**0.79 +/- 0.09**	**(1.5 +/- 0.3) *10^5**
192.7	0.330	8.32E+05	191.9	0.95	3.66E+05

197.6	0.020	5.16E+03	192.4	0.97	5.51E+05
198.4	0.270	5.68E+05	193.3	0.84	2.81E+05
			195.6	0.89	4.88E+05
			196.9	0.94	2.67E+06
			201.4	1.03	3.59E+05
			205.2	0.99	4.79E+05
196.2 +/- 3	**0.207 +/- 0.16**	**(4.7 +/- 4.2)*10^5**	**196.7 +/- 5.0**	**0.94 +/- 0.06**	**(7.4 +/- 8.5) *10^5**
396.6	0.680	8.06E+05	398.4	0.82	3.72E+05
			401.7	0.92	2.37E+05
			412.9	0.88	1.92E+05
396.6 +/- 8	**0.68 +/- 0.15**	**(8.1 +/- 4.0)*10^5**	**404.3 +/- 7.6**	**0.87 +/- 0.05**	**(2.7 +/- 0.9) *10^5**

Table A3.3

Electrical Characterization of devices using Cu electrodes at various channel lengths

(bold values are the average for each channel length)

Copper no CNT			Copper with CNT		
Channel Length (μm)	**Mobility ($cm^2V^{-1}s^{-1}$)**	**On/off**	**Channel Length (μm)**	**Mobility ($cm^2V^{-1}s^{-1}$)**	**On/off**
13.2	0.24	1.69E+09	10.7	0.55	8.78E+01
13.2	0.11	4.69E+07	11.3	0.47	6.81E+01
13.4	0.58	7.38E+06	11.4	0.55	1.58E+02
14.1	0.43	7.36E+06	12.3	0.55	1.22E+02
15.5	0.57	9.69E+06	13.0	0.48	1.49E+02
15.9	0.55	1.25E+08	13.7	0.63	9.93E+01
16.0	0.63	3.07E+08	16.6	0.52	1.17E+02
16.5	0.34	2.39E+08			
18.1	0.47	5.82E+07			
18.2	0.34	1.83E+07			
15.4 +/- 1.9	**0.43 +/- 0.17**	**(2.5 +/- 5.1)*10^8**	**12.7 +/- 2.0**	**0.54 +/- 0.05**	**(1.14 +/- 0.3) *10^2**
37.0	0.4	2.78E+08	38.6	1.04	5.44E+03
44.8	0.4	1.18E+09	38.6	1.13	7.37E+03
47.2	0.74	9.63E+06	40.5	1.07	9.38E+03

47.6	0.63	7.99E+06	43.8	0.76	8.27E+03
49.0	0.62	1.31E+07	44.2	1.13	1.38E+04
49.7	0.81	1.31E+07	45.0	1.15	1.35E+04
53.5	0.69	9.52E+06	46.0	1.27	3.63E+04
65.8	0.66	6.83E+06	47.5	1.18	1.61E+04
			48.1	0.85	1.70E+04
			48.3	1.28	4.44E+04
			50.2	1.22	2.59E+04
			50.5	1.07	1.38E+04
			50.5	0.88	1.13E+04
			60.2	0.82	1.72E+04
49.3 +/- 8.2	**0.62 +/- 0.15**	**(1.9 +/- 4.1)*10^{8}**	**45.6 +/- 5.7**	**1.1 +/- 0.17**	**(1.7 +/- 1.1) *10^{4}**
87.7	0.78	5.90E+06	85.7	1.31	9.00E+04
93.2	0.76	7.63E+06	90.0	1.15	5.25E+04
96.0	1.01	6.37E+06	90.2	1.31	9.76E+04
96.3	0.84	6.06E+06	90.6	1.25	9.49E+04
97.4	0.91	6.24E+06	91.9	1.16	5.27E+04
102.6	0.72	4.69E+06	95.2	1.27	9.14E+04
106.4	1.03	5.35E+06	96.2	1.34	1.24E+05
114.0	0.81	4.32E+06	96.4	1.23	9.24E+04

			98.2	1.33	9.95E+04
			100.0	1.23	1.15E+05
			101.6	0.91	4.36E+04
			106.7	0.98	1.09E+05
			108.5	1.34	1.21E+05
99.2 +/- 8.2	**0.86 +/- 0.12**	**(5.8 +/- 1.4)*10^{6}**	**96.5 +/- 6.5**	**1.22 +/- 0.13**	**(9.5 +/- 3.0) *10^{4}**
201.8	0.94	2.59E+06	194.7	1.40	2.66E+05
202.5	0.9	2.45E+06	196.1	1.36	2.52E+05
204.3	1.06	3.09E+06	196.2	1.34	1.37E+05
205.5	1.02	3.66E+06	198.3	1.42	2.60E+05
			199.2	1.43	2.02E+05
			199.2	1.44	2.66E+05
			200.9	1.43	2.02E+05
			201.0	1.25	1.10E+05
203.5 +/- 1.7	**0.98 +/- 0.07**	**(3.0 +/- 0.5)*10^{6}**	**198.2 +/- 2.3**	**1.38 +/- 0.06**	**(2.1 +/- 0.6) *10^{5}**
401.4	1.08	1.02E+06	397.7	1.40	1.99E+06
417.4	1.38	9.98E+05	397.8	1.20	2.20E+05
			401.4	1.45	1.99E+06
			416.3	1.22	1.46E+06
409.4 +/- 11	**1.23 +/- 0.21**	**(1.0 +/- 0.02)*10^{6}**	**403.3 +/- 8.8**	**1.32 +/- 0.13**	**(1.4 +/- 0.8) *10^{6}**

Table A3.4

Extrapolated contact resistance for various V_{GS} values

	Contact Resistance (MΩ)					
V_{GS}	Au no CNT	Au with CNT	Cu no CNT	Cu with CNT	Al no CNT	Al with CNT
-5	2.14	-0.88	83.76	7.73	N/A	N/A
-10	1.32	-0.12	34.68	5.29	N/A	3.51E+02
-15	0.15	0.39	23.67	3.37	N/A	1.87E+02
-20	0.60	0.28	28.61	2.68	4.01E+05	7.86E+01
-25	0.21	0.87	20.53	2.40	1.58E+05	4.49E+01
-30	0.61	0.87	10.49	1.95	1.77E+04	3.74E+01
-35	0.58	0.86	7.33	1.87	2.86E+03	2.84E+01
-40	0.57	0.74	5.35	1.62	8.37E+02	2.39E+01
-45	0.59	0.71	4.49	1.61	3.76E+02	2.11E+01
-50	0.58	0.68	3.77	1.59	1.83E+02	1.93E+01
-55	0.58	0.64	3.38	1.66	1.45E+02	1.82E+01
-60	0.56	0.55	3.11	1.74	9.51E+01	1.85E+01

3.5 References

1. Hsieh, G. *et al.* High performance nanocomposite thin film transistors with bilayer carbon nanotube- polythiophene active channel by ink-jet printing High performance nanocomposite thin film transistors with bilayer carbon nanotube-polythiophene active channel by ink-jet p. *J. Appl. Phys.* 123706 (2009). doi:10.1063/1.3273377

2. Li, Y. *et al.* Annealing-free high-mobility diketopyrrolopyrrole-quaterthiophene copolymer for solution-processed organic thin film transistors. *J. Am. Chem. Soc.* **133,** 2198–204 (2011).

3. Ha, J. S., Kim, K. H. & Choi, D. H. 2,5-Bis(2-octyldodecyl)pyrrolo[3,4-c]pyrrole-1,4-(2H,5H)-dione-Based DonorAcceptor Alternating Copolymer Bearing 5,50-Di (thiophen-2-yl)-2,20-biselenophene Exhibiting 1.5 cm2 3 V -1 3 s-1 Hole Mobility in Thin-Film Transistors. *J. Am. Chem. Soc.* **133,** 10364–10367 (2011).

4. Shao, W., Dong, H., Jiang, L. & Hu, W. Morphology control for high performance organic thin film transistors. *Chem. Sci.* **2,** 590 (2011).

5. Wu, Y. *et al.* Controlled orientation of liquid-crystalline polythiophene semiconductors for high-performance organic thin-film transistors. *Appl. Phys. Lett.* **86,** 1–3 (2005).

6. Wu, Y., Liu, P. & Ong, B. S. Organic thin-film transistors with poly(methyl silsesquioxane) modified dielectric interfaces. *Appl. Phys. Lett.* **89,** 2004–2007 (2006).

7. Tans, S. J., Verschueren, A. R. M. & Dekker, C. Room-temperature transistor based on a single carbon nanotube. *Nature* **393,** 49–51 (1998).

8. Martel, R., Schmidt, T., Shea, H. R., Hertel, T. & Avouris, P. Single- and multi-wall carbon nanotube field-effect transistors. *Appl. Phys. Lett.* **73,** 2447 (1998).

9. Lee, C. W. *et al.* Solution-processable carbon nanotubes for semiconducting thin-film transistor devices. *Adv. Mater.* **22,** 1278–82 (2010).

10. Sydoruk, V. A. *et al.* Noise spectroscopy of transport properties in carbon nanotube field-effect transistors. *Carbon N. Y.* **53,** 252–259 (2013).

11. Heinze, S. *et al.* Carbon Nanotubes as Schottky Barrier Transistors. *Phys. Rev. Lett.* **89,** 106801 (2002).

12. Javey, A., Guo, J., Wang, Q., Lundstrom, M. & Dai, H. Ballistic carbon nanotube field-effect transistors. *Nature* **424,** 654–657 (2003).

13. Zhang, Z. *et al.* Doping-Free Fabrication of Carbon Nanotube Based Ballistic CMOS Devices and Circuits. *Nano Lett.* **7,** 3603–3607 (2007).

14. Cicoira, F., Aguirre, C. M. & Martel, R. Making contacts to n-type organic transistors using carbon nanotube arrays. *ACS Nano* **5,** 283–90 (2011).

15. Aguirre, C. M., Ternon, C., Paillet, M., Desjardins, P. & Martel, R. Carbon nanotubes as injection electrodes for organic thin film transistors. *Nano Lett.* **9,** 1457–61 (2009).

16. Lefenfeld, M., Blanchet, G. & Rogers, J. a. High-Performance Contacts in Plastic Transistors and Logic Gates That Use Printed Electrodes of DNNSA-PANI Doped with Single-Walled Carbon Nanotubes. *Adv. Mater.* **15,** 1188–1191 (2003).

17. Huang, Y. Y. & Terentjev, E. M. Dispersion of Carbon Nanotubes: Mixing, Sonication, Stabilization, and Composite Properties. *Polymers (Basel).* **4,** 275–295 (2012).

18. Lee, H. W. *et al.* Selective dispersion of high purity semiconducting single-walled carbon nanotubes with regioregular poly(3-alkylthiophene)s. *Nat. Commun.* **2,** 1–8 (2011).

19. Tsukamoto, J., Mata, J. & Matsuno, T. Organic Field Effect Transistors Using Composites of Semiconductive Polymers and Single-Walled Carbon Nanotubes. *Jpn. J. Appl. Phys., Part 2* **46,** L396–L398 (2007).

20. Geng, J. *et al.* Effect of SWNT Defects on the Electron Transfer Properties in P3HT/SWNT Hybrid Materials. *Adv. Funct. Mater.* **18,** 2659–2665 (2008).

Chapter 4

A More Than Six Orders of Magnitude UV-Responsive Organic Field-Effect Transistor Utilizing a Benzothiophene Semiconductor and Disperse Red 1 for Enhanced Charge Separation

This chapter is a reproduction of the following published article in Advanced Materials. The major contribution of this work is that we show we can use the C5-BTBT semiconductor in a UV active phototransistor who's UV response can be increased if a copolymer of DR1 and PMMA (*p*-DR1) is blended into the film.

"A More Than Six Orders of Magnitude UV-Responsive Organic Field-Effect Transistor Utilizing a Benzothiophene Semiconductor and Disperse Red 1 for Enhanced Charge Separation"

Reproduced from: Chad S. Smithson, Yiliang Wu, Tony Wigglesworth, and Shiping Zhu; *Adv. Mater*; **2015**, 27, 228-233. With permission from John Wiley and Sons.

DOI: 10.1002/adma.201404193

4.1 Abstract

A more than six orders of magnitude UV-responsive organic field-effect transistor is developed using a benzothiophene (BTBT) semiconductor and strong donor-acceptor Disperse Red 1 as the traps to enhance charge separation. The device can be returned to its low drain current state by applying a short gate bias, and is completely reversible with excellent stability under ambient conditions.

4.2 Start of paper: Introduction

Organic electronics is a technology that has made great leaps forward over the past decades. The flexible characteristic of organic electronic devices, in coupling with potential low-cost manufacturing processes, makes them very appealing for applications such as memories, large-area sensors, displays, etc. Organic thin-film transistors (OTFTs), one of the most attractive devices, have been the subject of intense research recently, because they cannot only be used as the transistor component for constructing integrated circuits and backplanes, but also offer excellent possibilities to function as sensors and memory devices.[1,2,3,4,5,6,7] Due to the nearly endless possibilities available for organic materials, sensors can be generated to fit nearly any demand. Here, we report a discovery of OTFTs with a very large UV response. We used a UV-sensitive semiconductor 2,7-dipentyl[1]benzothieno[3,2- *b*][1] benzothiophene (C5-BTBT) in combination with a polymer containing strong donor and acceptor moieties (**Fig 4.1 (*a*)**) to fabricate the OTFT and found that a very small amount (≈5%) of disperse red 1 (DR1), an azobenzene derivative incorporated into the semiconductor layer, dramatically increased the UV response of the devices. Our device showed a UV response as long as the drain source voltage $|V_{DS}| > 0$ V. Even at the gate voltage $V_{GS} = 0$ V, a UV response of up to six orders of magnitude could be achieved and maintained after the UV light was removed. A large negative gate voltage pulse returned the system to its original low current state. Interestingly, the device exhibited such remarkable response to UV light only, which makes it an excellent candidate for long sought-after organic UV-A sensor. [8,9,10,11,12] Being

inert to visible light is a major advantage over standard UV sensors that typically use complicated waveguides to separate visible light from UV before sensing can occur.[13]

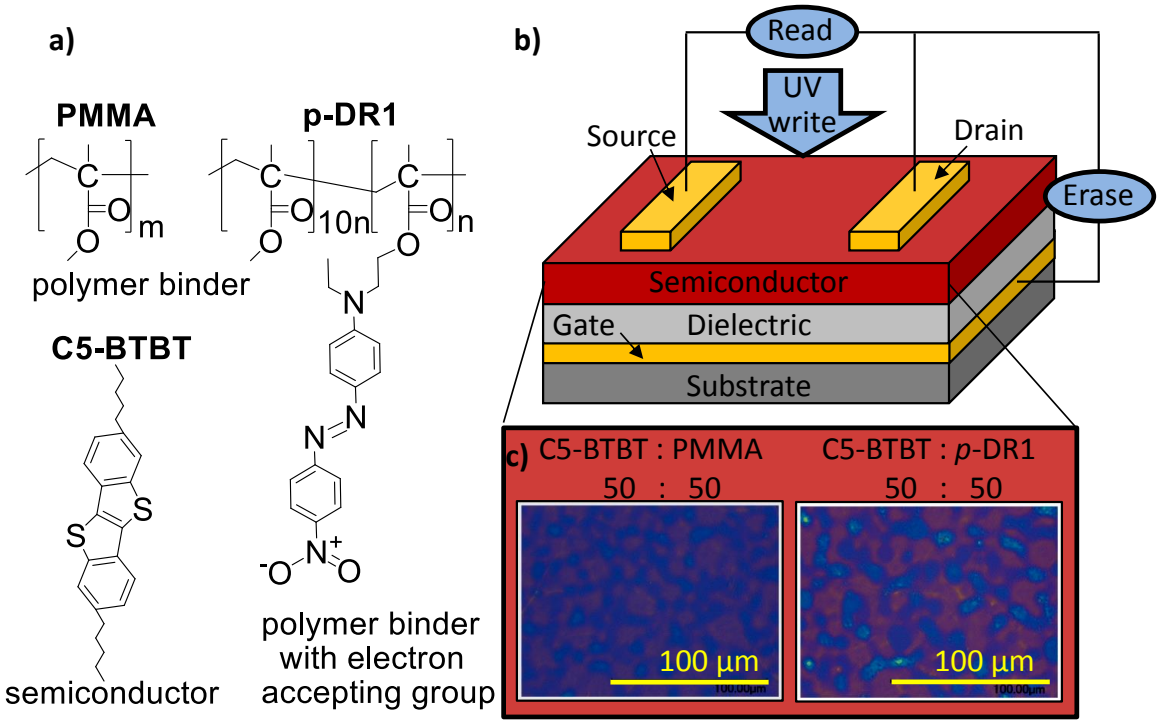

Figure 4.1: (*a*) Materials used to form the semiconductor layer of the OTFT and their roles in the film. (*b*) Bottom-gate top-contact transistor design showing how the UV functionality works. (*c*) Optical microscopy images of the two semiconductor films, C5-BTBT appears blue and the polymers appear purple.

The alkyl substituted organic semiconductor C_n-BTBT (*n* represents the number of carbon atoms in the alkyl chain) is air stable, soluble in a range of solvents,

and optically transparent to visible light.[14,15] Films generated from a solution containing only C_n -BTBT showed poor coverage with large grain boundaries, thus producing low performance devices. However, when spin coated from a solution containing C_n-BTBT and an insulating polymer binder, a technique first demonstrated in 2005,[16,17] uniform and consistent films with high mobilities could be obtained. Large BTBT crystal domains could be obtained from a BTBT:PMMA solution by controlling the solvent evaporation,[18] while off-centre spin coating techniques have produced OTFTs with mobilities up to 43 $cm^2V^{-1}s^{-1}$ using BTBT in polystyrene binder.[19] We chose C5-BTBT as the semiconductor in our study, since it has a short insulting alkyl chain, yet good solubility. Instead of polystyrene, poly(methyl methacrylate) (PMMA) was used as the polymer binder, because the carbonyl groups may function as electron traps to help separate photoinduced electron and hole pairs. To further increase electron trapping capability, a copolymer (*p*-DR1) of methyl methacrylate and (E)-2-(ethyl(4-((4-nitrophenyl)diazenyl) phenyl)amino)ethyl methacrylate was synthesized. We believe that the strong donor–acceptor DR1 moiety functions as a deeper trap in the semiconductor layer, thus enhancing the charge separation efficiency. Using a copolymer provides additional benefits in terms of film uniformity and morphology over the small molecule DR1. Spin coating of two different small molecular components usually results in vertical phase separation,[20] and the film morphology has been found to play an important role in transistor performance of a polymer and small molecule blend.[21] Bottom-gate top-contact OTFTs were

fabricated using the blended semiconductor composition on an n^{++}-silicon substrate with 200-nm SiO_2 as the gate dielectric layer, and Au source and drain electrodes (**Fig. 4.1 (*b*)**). The optimal blend was found to be at a 1:1 weight ratio of (C5-BTBT:PMMA) or (C5-BTBT: *p*-DR1), producing the highest on/off ratio and mobility. Optical microscopy images (**Fig. 4.1 (*c*)**) revealed that the film morphology of (C5-BTBT:PMMA) and (C5-BTBT: *p*-DR1) were very similar, with both C5-BTBT and the polymer binders forming interpenetrated continuous phases.

Fig. 4.2 provides thin film UV-vis absorbance spectra of PMMA, *p*-DR1, C5-BTBT, and their mixtures. PMMA is optically transparent to UV and visible light showing no absorbance in the measured range. *p* -DR1 has a characteristic absorbance caused by the azobenzene pendent group at 472 nm. Azobenzene compounds also have absorbance in the UV, which can cause solid state isomerization. However for donor–acceptor-type azobenzenes, this isomerization from *trans* to *cis* can thermally revert back to the *trans* form within seconds even in a polymer film[22,23] and has been found to have little impact on transistor performance.[24] The semiconductor C5-BTBT shows a strong absorbance in the UV-A range with a maximum at 354 nm.

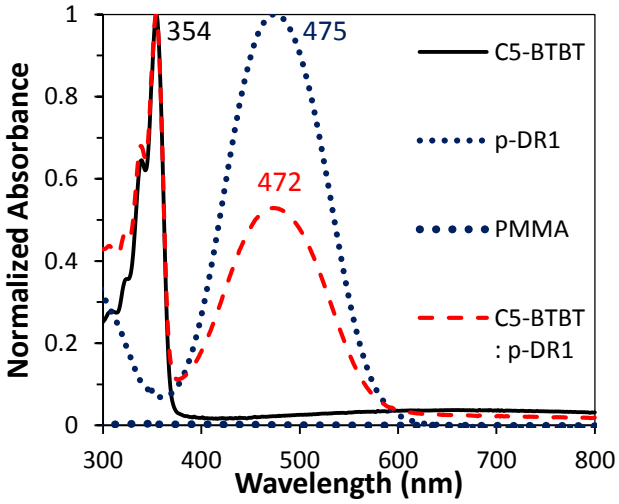

Figure 4.2: UV–vis spectra of thin films prepared on glass slides. Absorbance maxima are labeled.

The transfer and output curves for these two systems are shown in **Fig. 4.3**. Three different drain source voltages were used; V_{DS} = -60, -0.1, and 0 V, which correspond to the saturation region, the linear region, and the gate leakage (at no drain bias) of the OTFTs, respectively. When no UV was present, the (C5-BTBT:PMMA) blend behaved as a typical *p* -type transistor with a threshold voltage (V_{Th}) of -25.9 V. When *p*-DR1 was used as the polymer binder, the presence of the strong electron donating amine group resulted in a significant shift of the V_{Th} to -49.7 V by trapping holes around it. In both cases, little to no hysteresis was observed.

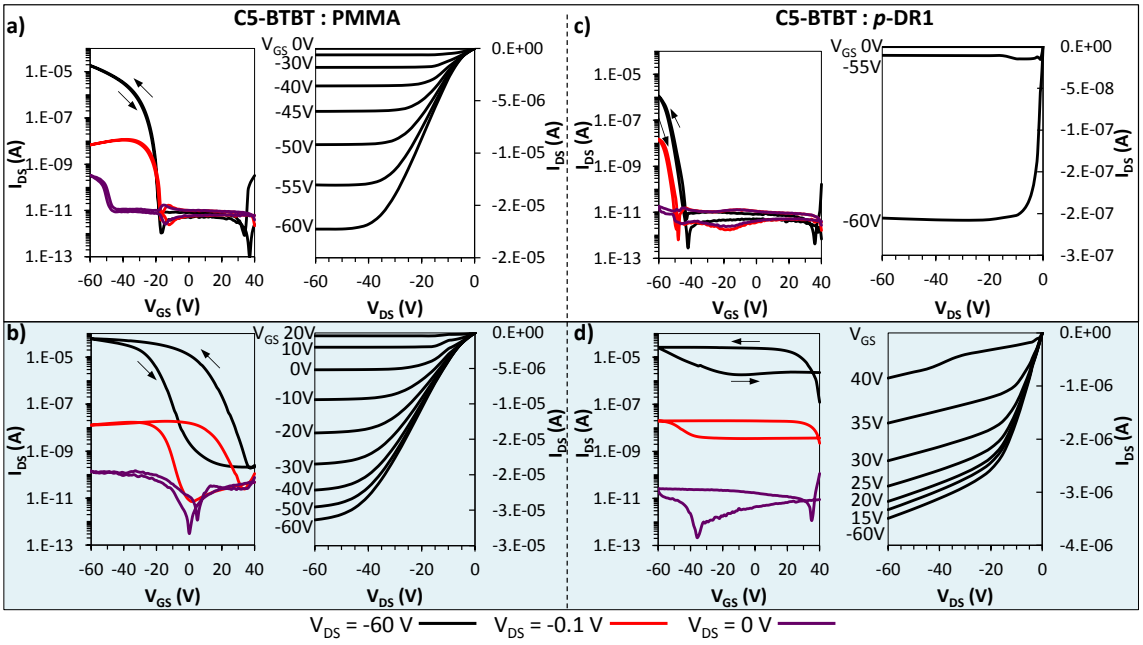

Figure 4.3: Transfer and output curves of the two types of transistors studied. (*a*) and (*c*) were measured under yellow light, (*b*) and (*d*) were measured under an irradiation with 365-nm UV light.

When exposed to UV-A, both films showed a dramatic change in I_{DS} -V_{GS} characteristics, as long as a drain bias was used ($V_{DS} \neq 0$ V). The (C5-BTBT:PMMA) film showed a 45 V shift of the V_{Th} to 19.8 V and a large hysteresis effect. The threshold voltage shift is ascribed to the electron hole pair formation when exposed to UV-A, increasing the hole density in the film. The hysteresis is a result of bias stress causing electron hole pair recombination at a large negative gate bias.[25] When *p*-DR1 was used in the film, the threshold voltage shifted over 90 V from -49.7 to 41.7 V. This extreme shift is assisted by the charge accepting nature of the nitro group of DR1, capable of accepting and trapping the

photostimulated electrons. This device demonstrated a much larger hysteresis phenomenon. In addition, the drain current exhibited a plateau on the return sweep and did not reach the original low current state. Detail electrical properties of the devices, including mobility, on/off ratio, and threshold voltages, were extracted from the transfer curves and summarized in the Supporting Information. Similarly, output curves of the (C5-BTBT:PMMA) system demonstrated typical *p*-type OTFT behavior. When exposed to UV light, the devices approached saturation at a lower V_{GS} than that when no UV light was used. The extreme V_{Th} shifts of the (C5-BTBT: *p*-DR1) system resulted in a device that did not turn on until a large negative gate voltage was used when no UV was present. When exposed to UV light, the device was already turned on at a high positive gate voltage. This offers a very large gate voltage window for sensing to occur. The significant difference in *I-V* characteristics of these two systems was considered as follows. The donor–acceptor-type DR1 moiety functions as stronger and deeper trap than PMMA. Upon irradiation with the same UV-light, namely, at the same charge generation rate, stronger traps causes more efficient charge separation, and deeper traps resulted in slower charge recombination, thus a larger threshold shift and a higher current during the return sweep.

The increase in charge carrier density (ΔN^*) upon UV irradiation can be estimated by the following equation $\Delta N^* = C_i \Delta V_{Th}/e$, where C_i = 15 nF cm^{-2} is the capacitance per unit area of the dielectric layer, ΔV_{Th} is the shift of the threshold

voltage, and *e* is the elementary charge.[26,27] When exposed to UV light, the increase in carrier concentration for (C5-BTBT:PMMA) is 4.28×10^{12} cm^{-2} and (C5-BTBT: *p*-DR1) is 8.56×10^{12} cm^{-2}. The latter has an increase in charge carrier density approximately two times that of the former. It should be noted that both systems showed no response when exposed to visible light such as a laser having a wavelength of 488 or 633 nm, although the DR1 moiety has a strong absorbance in the visible range. The fact that the systems showed a response to UV only, indicates that the increase in charge carrier density is due to the excitation of the C5-BTBT semiconductor. Further investigation of this mechanism is underway.

The very strong UV response has been investigated in detail. To minimize power consumption, we measured devices at the gate voltage $V_{GS} = 0$ V, and looked at high and low drain source voltages of $V_{DS} = -60$ V and $V_{DS} = -0.1$ V, respectively. When exposed to UV light, a dramatic I_{DS} increase was observed (**Fig. 4.4**). The increased I_{DS} remained even after the UV light was removed, keeping the device in a metastable state of higher conductivity. This metastable conductance state is most likely caused by the photoexcitation of an electron from C5-BTBT which is then trapped by either DR1 or PMMA, leaving behind a positive charge carrier.[24,28,29,30] If a large negative gate bias is applied (e.g., -60 V), the device returns to its original low current value of $\approx 1 \times 10^{-12}$ A. The large negative V_{GS} bias can accelerate the recombination of positive charge carriers with the trapped

electrons, thus reducing the charge carrier density.[26,31,32,33] This phenomenon could be taken advantage of to generate a UV sensor or light-triggered memory device. OTFT design could be a benefit for large-area image sensors based on a transistor array, as each transistor can be addressed separately in an active matrix manner. The three-terminal structure of OTFT also enables an additional reset option of the device by applying a gate bias. **Fig. 4.4 (*b*)** shows a series of writing/erasing cycles corresponding to a device "erased" using a V_{GS} = -60 V for 2 s followed by "writing or sensing" with UV light to generate a large increase in I_{DS} . As seen in **Fig. 4.4**, the device maintained this large I_{DS} after the UV source was removed but was easily erased by the application of another V_{GS} = -60 V. The writing/erasing phenomenon is repeatable for hundreds of cycles without fatigue for both (C5-BTBT:PMMA) and (C5-BTBT: *p*-DR1) systems under ambient conditions, but with a dramatically larger and faster response for the (C5-BTBT: *p*-DR1) system. Specifically, a UV response over six orders of magnitude was achieved for (C5-BTBT: *p*-DR1) device at the V_{DS} = -60 V, and more than three orders of magnitude at the V_{DS} = -0.1 V. Such low operation voltages (V_{GS} = 0 V and V_{DS} = -0.1 V) could be an advantage for fabricating devices with very low power consumption.

To further investigate the UV response of these devices, we measured their UV response over an extended period of time (e.g., 12 h). **Fig. 4.4 (*c*)** provides long-term measurements for the studied systems. The devices were exposed to UV

light until a saturated I_{DS} value was achieved. The I_{DS} saturation value for the (C5-BTBT: *p*-DR1) system was achieved in less than 30 s, which is much faster than that for the (C5-BTBT:PMMA) system that required over 90 min, suggesting the DR1 enhances electron trapping likely by providing deeper energy traps than PMMA. When the UV light was removed, the I_{DS} decayed, most likely due to detrapping or electron hole pair recombination. The detrapping could be governed by the spatial distance between carriers to be combined. As positive charge carriers are combined with trapped electrons, the conductivity of the device decreases at a characteristic rate corresponding to the spatial separation of these charges, a phenomenon that has been seen before for other organic electronics.[26,31,32,33]

We analyzed the writing and the decay processes using two biexponential equations, assuming a fast and a slow rate.[9,34,35] The following biexponential Equation (1) was used for the UV writing

$$I_{DS} = A\left(1 - e^{(-k_A t)}\right) + B\left(1 - e^{(-k_B t)}\right) \quad (1)$$

where *A* and *B* are constants measured in (*A*) with the saturation value of the drain source $I_{DS(max)}$ = (*A* + *B*), k_A and k_B are the fast and slow rates, and *t* is time in (s). Equation (2) was used for the decay or relaxation curve

$$I_{DS} = Ce^{(-k_C t)} + De^{(-k_D t)} + E \quad (2)$$

where *C*, *D,* and *E* are constants measured in (*A*) with *E* representing the I_{DS} at an infinite time after the UV light was removed, ($C + D + E$) = $I_{DS(max)}$, k_C and k_D are the fast and slow decay rates. An example of the fitting can be found in **Fig. 4.4 (*d*)** for the (C5-BTBT: *p* -DR1) at a V_{DS} = -60 V. Fitting of the long term measurements up to 12 h for all four sample conditions can be found in the Supporting Information with the parameters summarized in **Table 1**.

Table 4.1

Fitting parameters used to model the UV writing and relaxation curves

	Writing			
	C5-BTBT:PMMA		**C5-BTBT/*p*-DR1**	
V_{DS}	**-0.1 V**	**-60 V**	**-0.1 V**	**-60 V**
A	$2.30*10^{-9}$	$9.03*10^{-7}$	$1.34*10^{-8}$	$2.19*10^{-5}$
k_A	$3.15*10^{-2}$	$1.27*10^{-2}$	$8.04*10^{-2}$	$8.02*10^{-2}$
B	$6.77*10^{-9}$	$4.59*10^{-6}$	$3.39*10^{-9}$	$5.02*10^{-6}$
k_B	$4.30*10^{-4}$	$2.30*10^{-4}$	$9.11*10^{-3}$	$8.95*10^{-3}$
	Relaxation			
	C5-BTBT:PMMA		**C5-BTBT/*p*-DR1**	
V_{DS}	**-0.1 V**	**-60 V**	**-0.1 V**	**-60 V**
C	$3.71*10^{-9}$	$4.00*10^{-6}$	$1.01*10^{-8}$	$2.26*10^{-5}$
k_C	$1.07*10^{-2}$	$3.06*10^{-3}$	$3.97*10^{-3}$	$9.07*10^{-3}$
D	$8.81*10^{-10}$	$1.87*10^{-7}$	$4.29*10^{-9}$	$2.80*10^{-6}$
k_D	$2.70*10^{-3}$	$3.80*10^{-4}$	$3.56*10^{-4}$	$6.07*10^{-4}$
E	$9.34*10^{-12}$	$1.18*10^{-8}$	$4.36*10^{-10}$	$8.49*10^{-7}$

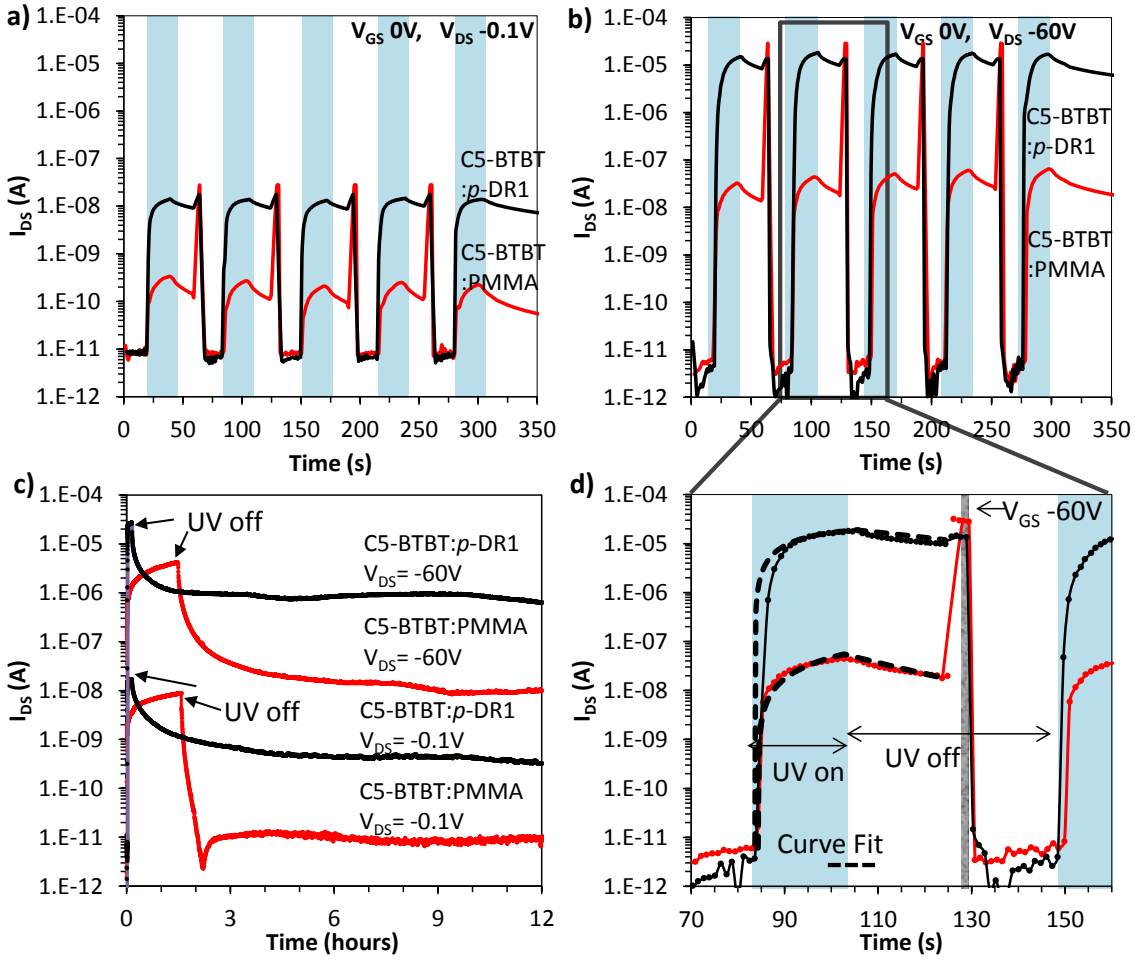

Figure 4.4: Response of OTFTs studied when exposed to UV light (blue-shaded area) at a V_{GS} = 0 V and (*a*) V_{DS} = -0.1 V and (*b*) V_{DS} = -60 V. A 2 s pulse of a V_{GS} = -60 V is used to return the system to its low conductivity state, showing the UV write/erase cycle is repeatable. (*c*) Long-term relaxation measurements of the studied systems when exposed to UV until a saturated IDS. (*d*) Zoom in of (*b*) with curve fitting shown as dotted lines.

For the writing process, the fast writing rate (k_A) of (C5-BTBT: *p*-DR1) system is approximately six times faster than that of (C5-BTBT:PMMA) system. Accordingly the response time (the reciprocal of the k_A) is six times shorter being 13 s for (C5-BTBT: *p* -DR1) compared with 80 s for (C5-BTBT:PMMA). These response times are in the same order as organic P3HT/DEA systems[36] and inorganic ZnS/ZnO blends,[37] but are slower than specially synthesized ZnO nanorods, which showed millisecond response.[9] The slower writing rate (k_B) of (C5-BTBT: *p*-DR1) is one order of magnitude larger than that of (C5-BTBT:PMMA), which helps explain why the former device reaches saturation so much faster. Both the fast and slow relaxation rates are similar for the (C5-BTBT:PMMA) and (C5-BTBT: *p*-DR1) systems, except for the (C5:BTBT:PMMA) system at a V_{DS} = -0.1 V. However, the amplitude of the slow relaxation term (*D*) (which dominates on the minutes to hours timescale) is much larger for the (C5-BTBT:PMMA) system, as being calculated at 19% and 29% of the saturated I_{DS} , in contrast to 4.5% and 10.5% for the (C5-BTBT: *p*-DR1) device, when measured at V_{DS} = -0.1 and -60 V, respectively. Due to the spatial separation of the electron and hole, detrapping eventually reaches a metastable state where it no longer occurs, represented by the term *E* of Equation (2). At this point, the probability that any trapped electron is close enough to a hole to recombine is nearly zero, which results in a metastable state that requires another stimulus to return the system to its completely detrapped state such as a large negative gate bias. Although the relaxation time is longer than that of previously reported systems,[9,36,37] our three-

terminal transistor design enables the use of gate pulse to switch the device off immediately. The high current retention over long time could allow the device to function not only as a sensor but also as a light induced memory device. At this moment, we are not able to assign the physical meanings to these rates, but we believe the deeper traps of the (C5-BTBT: *p*-DR1) system likely favor charge separation and inhibit charge combination, thus, allowing the system to achieve saturation faster than the (C5-BTBT:PMMA) system upon UV irradiation. Nevertheless, the large *E* value (8.49×10^{-7} A) of the (C5-BTBT: *p*-DR1) system indicated an excellent stability of the UV response.

In summary, we present a UV-sensitive material system (C5-BTBT: *p*-DR1) and its device utilizing the OTFT structure. The device demonstrates a strong change in current when exposed to UV-A, likely due to the photoexcitation of an electron in the C5-BTBT molecule, which is then trapped by both PMMA and DR1 leaving behind a positively charged hole. The addition of DR1 as a pendant group on the PMMA matrix provides more easily accessible and deeper traps, allowing the UV response to occur faster. For the (C5-BTBT: *p*-DR1) system, electron hole pair generation results in a threshold voltage shift from -49.7 to 41.7 V. Within 13 s at a V_{GS} = 0 V, the I_{DS} shows a UV response over six orders of magnitude for a V_{DS} = -60 V and three orders of magnitude for a V_{DS} = -0.1 V and maintains this high current after the UV light was removed demonstrating a slow relaxation. The device can be returned to its low drain current ground state by applying a short 1-

2 s gate bias of -60 V. The system is stable under visible light at ambient conditions and completely reversible. Mathematical models of the writing and the decay processes using a biexponential equations were proposed, revealing fast and slow processes. The relaxation process for the (C5-BTBT: *p*-DR1) systems show a smaller amplitude than the (C5-BTBT:PMMA) system suggesting that DR1 is providing an increased energy barrier to detrapping. This UV response offers the possibility of generating a UV-A sensor that is transparent to visible light, requires no complicated waveguides, and can operate at low voltages. It also has the potential to function as an optically programmed/electronically erased memory device.

4.3 Experimental section

Materials : Hexamethyldisalazane (HMDS), chlorobenzene, and poly(methyl methacrylate) (MW = 140 000) were purchased from Aldrich and used as received. *p*-DR1 synthesis can be found in the Supporting Information. C5-BTBT was synthesized at Xerox Research Center of Canada using a proprietary method and purified using preparative GPC and recrystallized twice from hexanes.

Device Fabrication and Characterization: All fabrication and characterization of OTFT devices was done under ambient conditions. Bottom-gate TFT devices were built on an *n* -doped silicon wafer as the gate electrode with a 200 ±10 nm

thermal silicon oxide (SiO_2) as the gate dielectric layer. The SiO_2 surface was plasma cleaned for 2 min. The wafer was subsequently rinsed with H_2O then isopropanol and dried with an air stream. The SiO_2 surface was modified with HMDS by immersing the cleaned silicon wafer substrate in 0.1 M HMDS in toluene at 60 ºC for 20 min. The wafer was subsequently rinsed with toluene and isopropanol and dried with an air stream. The semiconductor layer was deposited onto the HMDS-modified SiO_2 layer by coating a chlorobenzene solution containing C5-BTBT (1 wt%) and PMMA (1 wt%) or C5-BTBT (1 wt%) and *p*-DR1 (1 wt%) and allowing it to sit on the wafer for 2 min. This was then spin coated at 2000 rpm for 120 s using a 2-s ramp time. After drying the semiconductor layer under vacuum for 30 min, gold source and drain electrodes were deposited by vacuum evaporation through a shadow mask with a channel length (L) of 80 ± 5 µm and a width (W) of 950 ±10 µm.

Electrical characteristics of the devices were measured in a humidity (30% RH) and temperature (21 ºC) controlled room under yellow light on a Keithly 4200 Semiconductor Characterization System. Before measurements the back of the silicon wafers were sanded to remove any oxide layer, allowing it to be the gate of the device.

All UV irradiation was performed using a UVP Blak-Ray B-100AP High-Intensity UV Inspection Lamp (100 watt 365 nm bulb). The lamp was held over the sample at a distance of ≈10 cm producing a light intensity of 4.0 ± 0.5 mW cm^{-2}.

4.4 Acknowledgements

This work was supported in part by a Xerox Research Foundation and a Collaborative Research & Development grant from NSERC.

4.5 Supporting information

4.5.1 Synthesis of *p*-DR1

THF was purchased from Sigma Aldrich, stirred over Lithium hydride for 1 hour, filtered and distilled from sodium/benzophenone under nitrogen. Monomer methyl methacrylate (MMA, Aldrich, 99%) was distilled under vacuum. After passing through a column of inhibitor remover, it was stored at -20°C before use. Methacryloyl chloride, disperse red 1, azobisisobutyronitrile, anhydrous triethylamine, reagent grade isopropanol, toluene, chlorobenzene, methanol, hexanes and ethyl acetate were purchased from Sigma Aldrich and used as received

(E)-2-(ethyl(4-((4-nitrophenyl)diazenyl)phenyl)amino)ethyl methacrylate (DR1 monomer): Under N_2, in a 100 mL round bottom flask dried in an oven overnight, 4.156 g (13.2 mmol) of disperse red 1 were dissolved in 30 mL of THF and 13 mL of triethylamine and surrounded by an ice bath. Over a one hour period a clear colourless solution consisting of 4 mL (35.8 mmol) of methacryloyl chloride dispersed in 20 mL of THF was added dropwise to the dark red disperse red 1 solution. A white gas was released in the vessel until the addition was

completed and a dark red precipitate was formed. After 1.5 hours, the solution was warmed to room temperature and allowed to stir overnight. The solvent was removed under vacuum, leaving an oily red solid, which was dissolved in chloroform and purified by column chromatography using a 25/75 v/v ethyl acetate/hexanes mixture. The final product was dried under vacuum 3 hours yielding 4.25 g (11.1 mmol) of red powder 84.1% yield. ^{1}H NMR (200MHz, $CDCl_3$, δ): 8.32 (d, 2H), 7.91 (t, 4H), 6.82 (d, 2H), 6.11 (s, 1H), 5.60 (s, 1H), 4.38 (t, 2H), 3.73 (t, 2H), 3.55 (q, 2H). 1.94 (s, 3H), 1.27 (t, 3H); UV–vis (thin film on glass slide): λ_{max} (ε) = 489 nm; Anal. calcd for ($C_{20}H_{22}N_4O_2$): C 62.82, H 5.80, N 14.65; found: C 61.21, H 6.03, N 14.00.

(E)-2-(ethyl(4-((4-nitrophenyl)diazenyl)phenyl)amino)ethyl methacrylate-co-methyl methacrylate copolymer (p-DR1): Under N_2, in a 25 mL round bottom flask dried in an oven overnight, 0.500 g (1.31 mmol) DR1-monomer and 1.394 mL (13.1 mmol) methyl methacrylate was added. 0.0215 g (0.131 mmol) of azobisisobutyronitrile dissolved in 5 mL of THF was added to the solution, creating a dark red slurry. This was immediately immersed in an oil bath at 60 ºC and reacted for 17 hours producing a thick red solution. After cooling to room temperature, the thick red liquid was washed 3 times with 20 mL of H_2O which caused it to form a sticky red mass. The material was dissolved in 25 mL of THF producing a clear red solution. To this 50 mL of methanol was added precipitating out a red solid. This was filtered and washed 3 times with 10 mL of

methanol. The resultant red solid was dried under vacuum for 3 hours 1.2375 g. (M_n = 48,700 PDI = 1.88); ^{1}H NMR ($CDCl_3$, 200MHz),

Co-polymer composition determined from the integration of the ^{1}H NMR, $(C_{20}H_{22}N_4O_2)x(C_5H_8O_2)y$ peak (d, 8.32) x = 1, peak (t, 1.94) y = 11.86 ; UV–vis (thin film on glass slide): λ_{max} (ε) = 475 nm; Anal. calcd for $(C_{20}H_{22}N_4O_2)x(C_5H_8O_2)y$: (C 62.82, H 5.80, N 14.65)x (C 59.98, H 8.05)y. Found: C 58.94, H 7.60, N 2.12 $\therefore$ x = 1, y = 5.86

4.5.2 Solution preparation

Table S4.1.

Materials used to prepare solutions for spin coating

Solution[a)]	C5-BTBT (g)	PMMA (g)	*p*-DR1 (g)	Chlorobenzene (g)
***sol*-1**	----	0.0400	----	3.96
***sol*-2**	0.0400	----	----	3.96
***sol*-3**	----	----	0.0400	3.96
***sol*-4**	0.0400	0.0400	----	3.92
***sol*-5**	0.0400	----	0.0400	3.92

a) All solutions were passed through a 45 µm filter before use

UV-Vis Sample Preparation*:* Glass microscope slides were cleaned with isopropanol and air dried. ***sol*-(1,2,3,5)** were drop cast onto the glass slides where they sat for 2 minutes before being spin coated at 500 RPM for 90 sec using a 5 sec ramp time. These samples were used to acquire UV-Vis measurements on a Cary 5000 UV-Vis-NIR Spectrometer using a blank glass slide as the background.

4.5.3 Additional electronic characterization

Table S4.2

Electronic properties of the OTFTs under ambient conditions and exposed to UV light (V_{DS} = -60 V)

	UV-off		UV-on	
	BTBT/PMMA	**BTBT/*p*-DR1**	**BTBT/PMMA**	**BTBT/*p*-DR1**
Mobility ($cm^2V^{-1}s^{-1}$)	0.190	0.129	0.377	0.778
On/Off ratio	$2.23*10^6$	$1.27*10^5$	$3.20*10^5$	$2.17*10^2$
V_{Th} (V)	-25.9	-49.7	19.8	41.7

Table S4.3

Electronic properties of the OTFTs under ambient conditions and exposed to UV light (V_{DS} = -0.1 V)

	UV-off		UV-on	
	BTBT/PMMA	**BTBT/*p*-DR1**	**BTBT/PMMA**	**BTBT/*p*-DR1**
Mobility ($cm^2V^{-1}s^{-1}$)	0.001	0.002	0.0003	0.001
On/Off ratio	$1.17*10^3$	$1.34*10^3$	$7.68*10^2$	9.08
V_{Th} (V)	-16.35	-49.3	27.1	45.7

4.5.4 Long term irradiation measurements at various V_{GS}

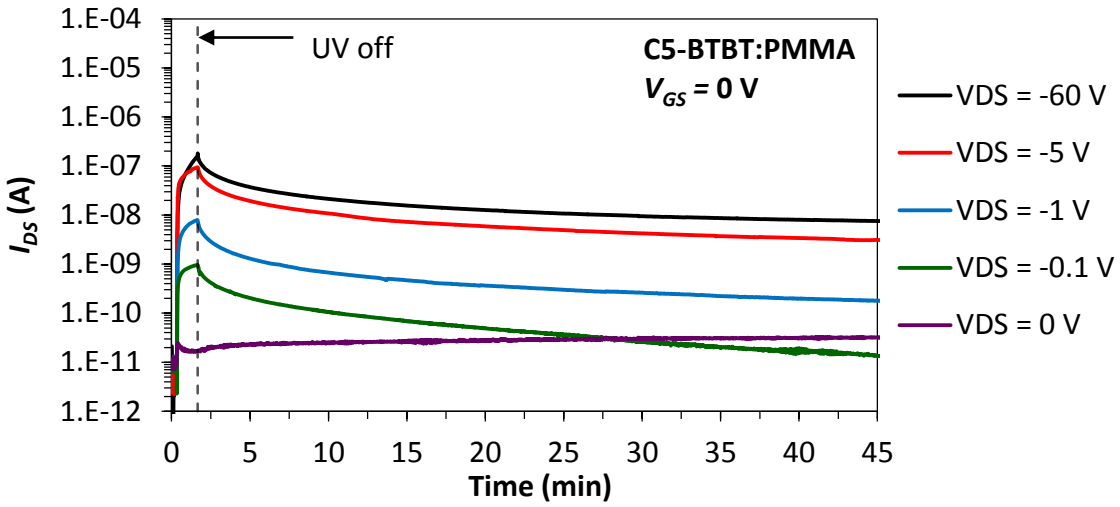

Figure S4.1: Two minute UV irradiation of C5-BTBT:PMMA under various V_{DS} with a constant V_{GS} of 0V followed by removal of UV light to allow relaxation for 45 minutes.

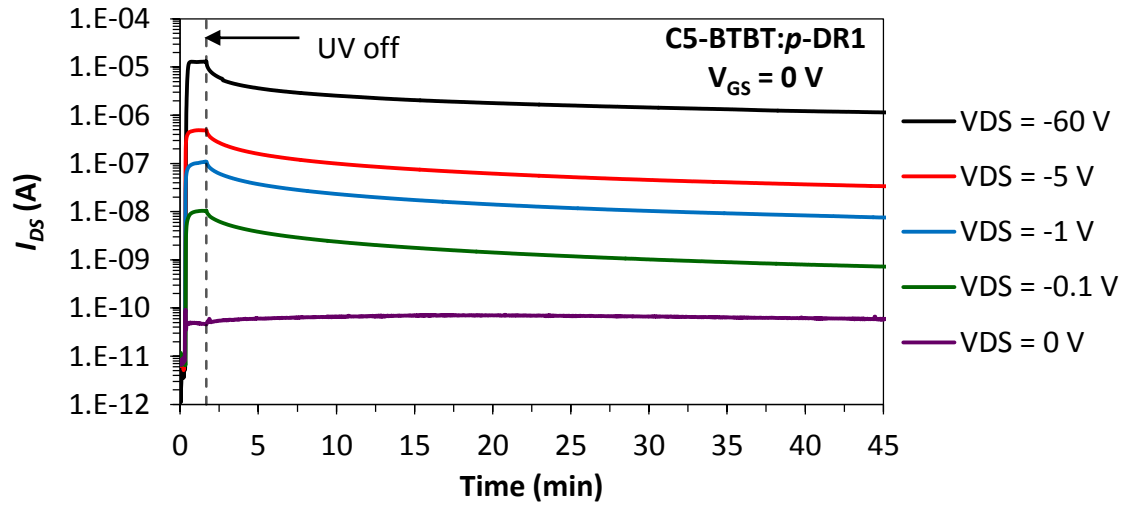

Figure S4.2: Two minute UV irradiation of C5-BTBT:p-DR1 under various V_{DS} with a constant V_{GS} of 0V followed by removal of UV light to allow relaxation for 45 minutes.

4.5.5 Biexponential fitting curves

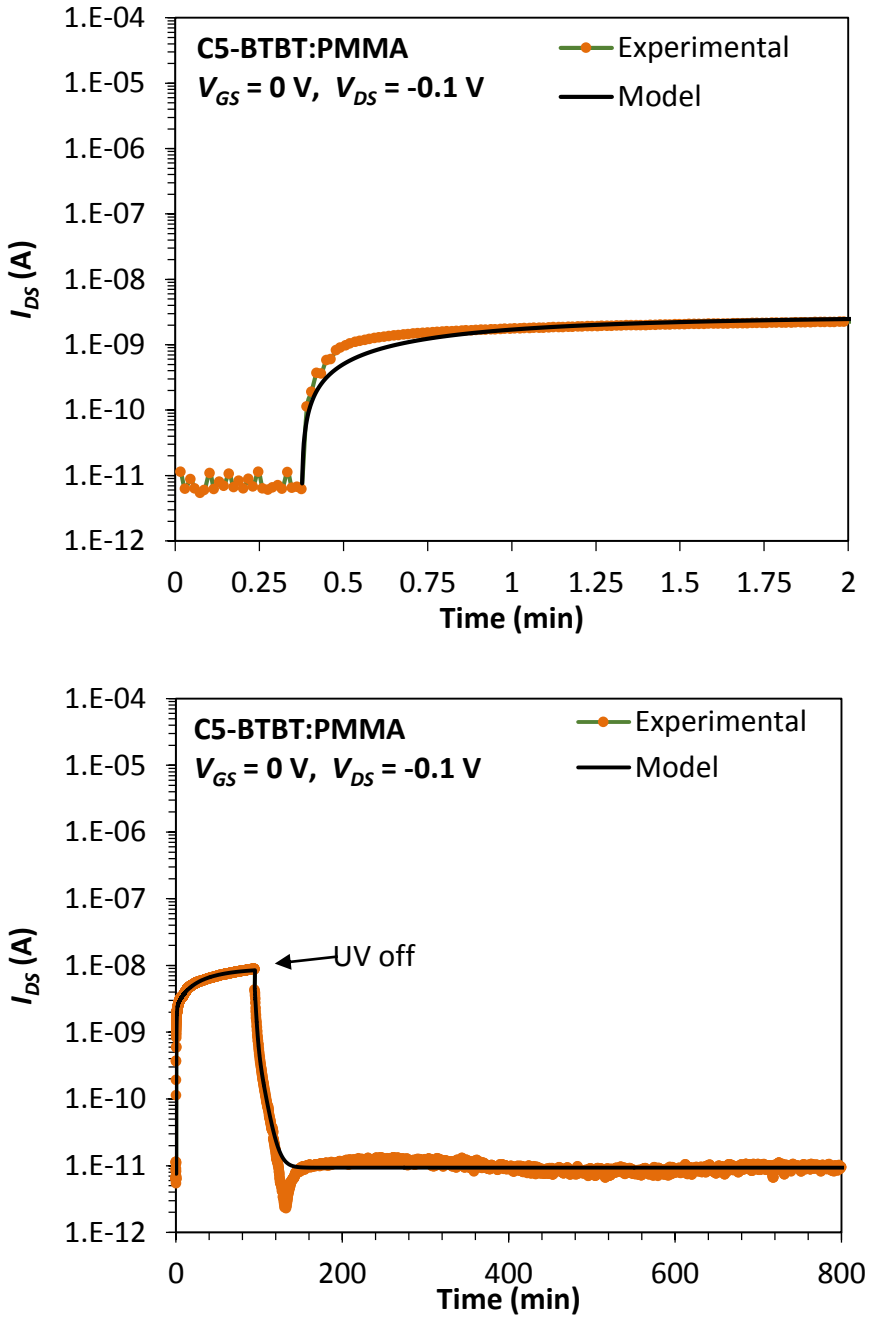

Figure S4.3: Long Term UV irradiation of C5-BTBT:PMMA at a V_{GS} = 0 V and a V_{DS} = -0.1 V.

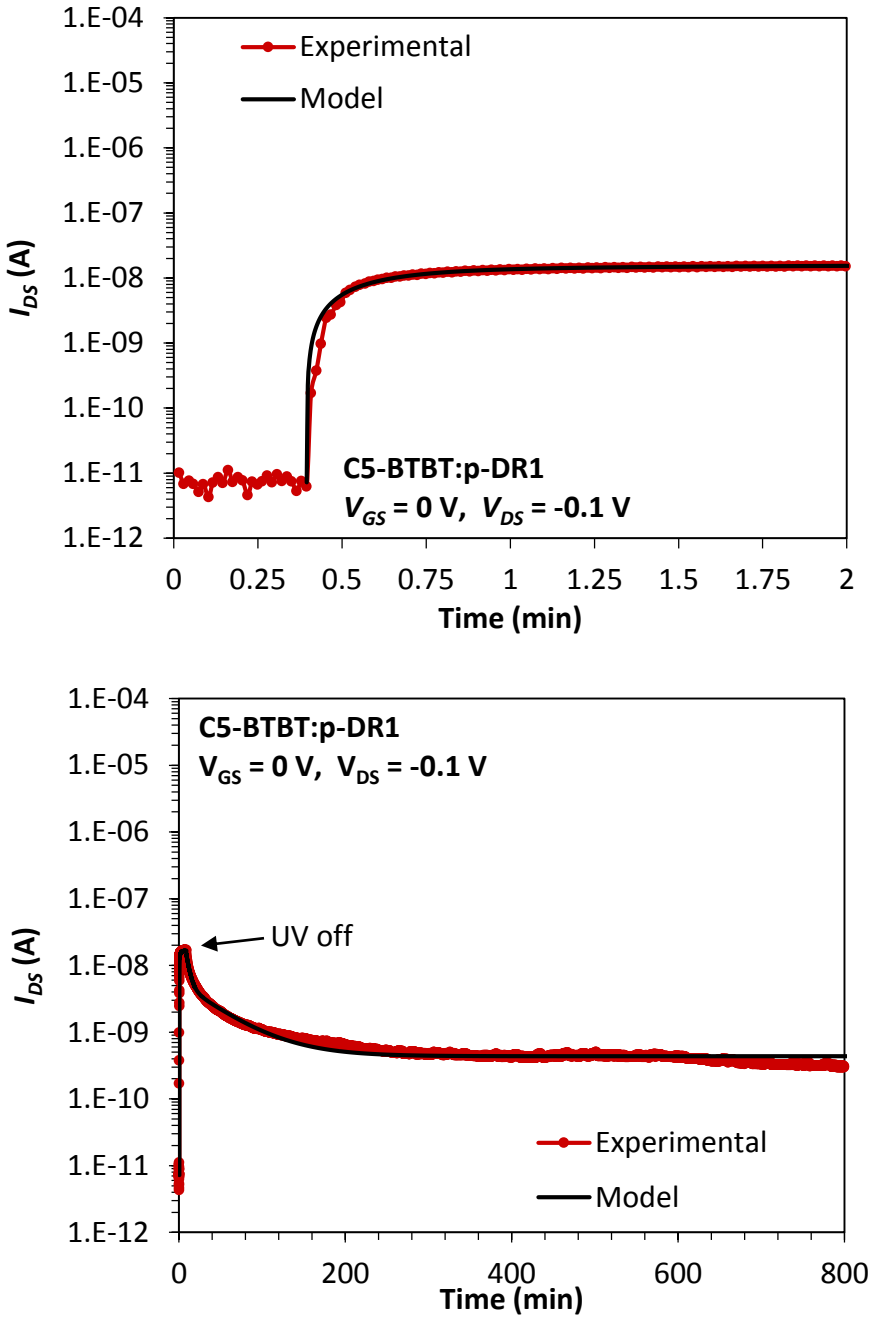

Figure S4.4: Long Term UV irradiation of C5-BTBT:*p*-DR1 at a V_{GS} = 0 V and a V_{DS} = -0.1 V.

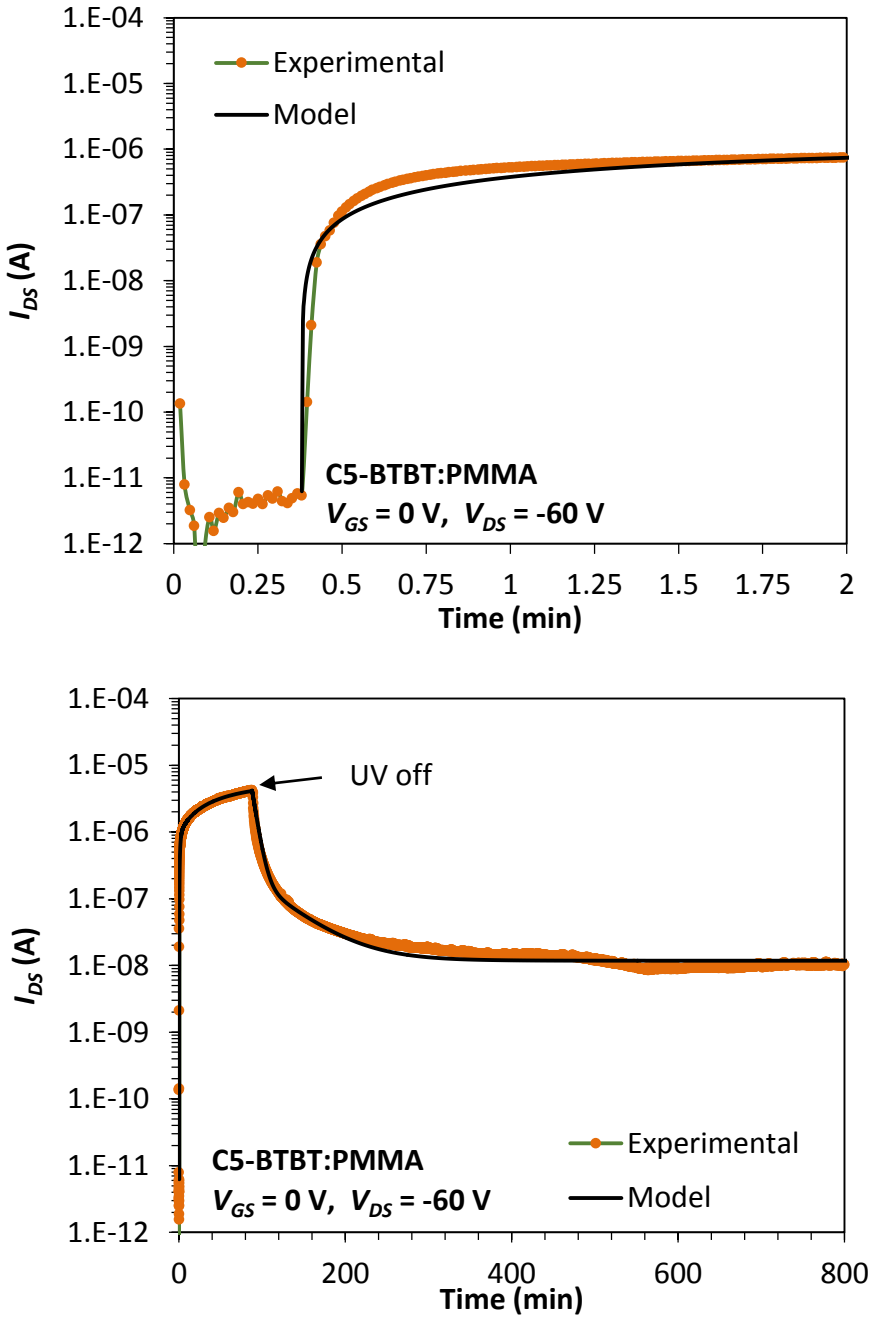

Figure S4.5: Long Term UV irradiation of C5-BTBT:PMMA at a V_{GS} = 0 V and a V_{DS} = -60 V.

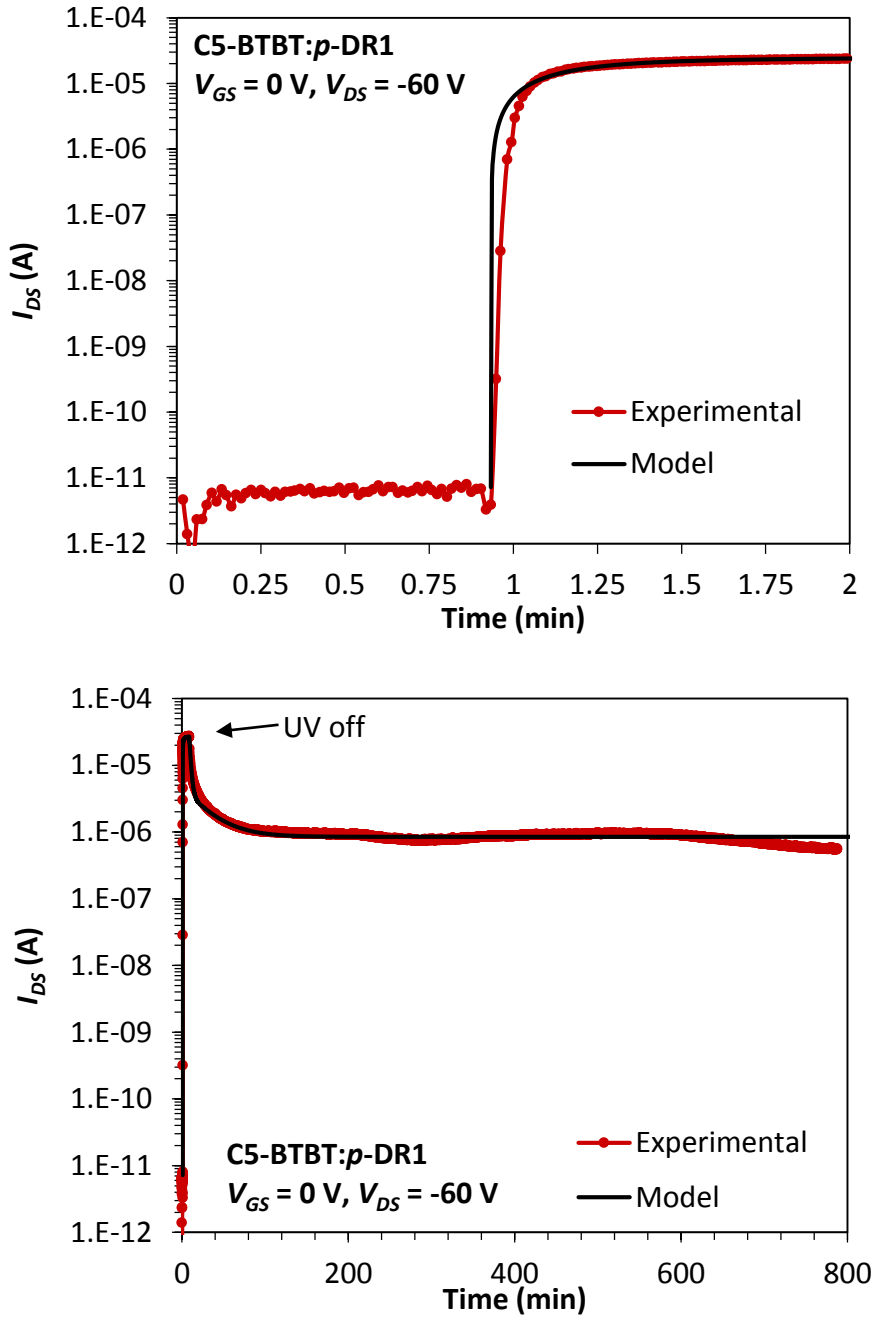

Figure S4.6: Long Term UV irradiation of C5-BTBT:*p*-DR1 at a V_{GS} = 0 V and a V_{DS} = -60 V.

4.6 References

1. Dong, H., Zhu, H., Meng, Q., Gong, X. & Hu, W. Organic photoresponse materials and devices. *Chem Soc. Rev.* **41,** 1754–808 (2012).

2. Wakayama, Y., Hayakawa, R. & Seo, H.-S. Recent progress in photoactive organic field-effect transistors. *Sci. Technol. Adv. Mat.* **15,** 024202 (2014).

3. Chiu, M.-Y., Chen, C.-C., Sheu, J.-T. & Wei, K.-H. An optical programming/electrical erasing memory device: Organic thin film transistors incorporating core/shell CdSe@ZnSe quantum dots and poly(3-hexylthiophene). *Org. Electron.* **10,** 769–774 (2009).

4. Mohamad, K. A., Goto, K., Uesugi, K. & Fukuda, H. Poly(3-hexylthiophene)/Fullerene Organic Thin-Film Transistors: Investigation of Photoresponse and Memory Effects. *Jpn. J. Appl. Phys.* **49,** 06GG09 (2010).

5. Uesugi, K. & Fukuda, H. Optical Responses and Optically Program Electrically Erase Memory in Organic Transistors. in *Photonics (ICP), 2011 IEEE 2nd International Conference on* 1–4 (2011).

6. Li, L. *et al.* High performance field-effect ammonia sensors based on a structured ultrathin organic semiconductor film. *Adv. Mater.* **25,** 3419–25 (2013).

7. Zhang, L. *et al.* Large-area, flexible imaging arrays constructed by light-charge organic memories. *Sci. Rep.* **3,** 1080 (2013).

8. Wang, Z. *et al.* A flexible UV nanosensor based on reduced graphene oxide decorated ZnO nanostructures. *Nanoscale* **4,** 2678–84 (2012).

9. Gedamu, D. *et al.* Rapid fabrication technique for interpenetrated ZnO nanotetrapod networks for fast UV sensors. *Adv. Mater.* **26,** 1541–50 (2014).

10. Cicek, E. *et al.* Crack-free AlGaN for solar-blind focal plane arrays through reduced area epitaxy. *Appl. Phys. Lett.* **102,** 051102 (2013).

11. Ray, D. & Narasimhan, K. L. High response organic visible-blind ultraviolet detector. *Appl. Phys. Lett.* **91,** 093516 (2007).

12. Sheng, X. *et al.* Silicon-Based Visible-Blind Ultraviolet Detection and Imaging Using Down-Shifting Luminophores. *Adv. Opt. Mater.* **2,** 314–319 (2014).

13. Liu, K., Sakurai, M. & Aono, M. ZnO-based ultraviolet photodetectors. *Sensors* **10,** 8604–34 (2010).

14. Ebata, H. *et al.* Highly Soluble [1] Benzothieno [3 , 2-b] benzothiophene (BTBT) Derivatives for High-Performance, Solution-Processed Organic Field-Effect Transistors. *J. Am. Chem. Soc.* **129,** 15732–15733 (2007).

15. Minemawari, H. *et al.* Inkjet printing of single-crystal films. *Nature* **475,** 364–7 (2011).

16. Nelson, B. K., Vogel, D. E., Napierala, M. E. & Lee, T.-C. All-inkjet printed thin film transistor. (2007).

17. Vogel, D. E. & Nelson, B. K. Bottom gate thin film transistors. **2,** (2009).

18. Kumatani, A. *et al.* Solution-processed, Self-organized Organic Single Crystal Arrays with Controlled Crystal Orientation. *Sci. Rep.* **2,** 393 (2012).

19. Yuan, Y. *et al.* Ultra-high mobility transparent organic thin film transistors grown by an off-centre spin-coating method. *Nat. Commun.* **5,** 3005 (2014).

20. Smith, J. *et al.* Solution-processed organic transistors based on semiconducting blends. *J. Mater. Chem.* **20,** 2562–2574 (2010).

21. Smith, J. *et al.* The Influence of Film Morphology in High-Mobility Small-Molecule:Polymer Blend Organic Transistors. *Adv. Funct. Mater.* **20,** 2330–2337 (2010).

22. Wu, Y. *et al.* Photoinduced Alignment of Polymer Liquid Crystals Containing Azobenzene Moieties in the Side Chain . 3 . Effect of Structure of Photochromic Moieties on Alignment Behavior. *Macromolecules* **9297,** 4457–4463 (1998).

23. Bohm, N. *et al.* Spectroscopic Investigation of the Thermal Cis - Trans Isomerization of Disperse Red 1 in Hybrid Polymers. *Macromolecules* **29,** 2599–2604 (1996).

24. Tseng, C.-W., Huang, D.-C. & Tao, Y.-T. Electric bistability induced by incorporating self-assembled monolayers/aggregated clusters of

azobenzene derivatives in pentacene-based thin-film transistors. *ACS Appl. Mater. Interfaces* **4,** 5483–91 (2012).

25. Salleo, A. & Street, R. A. Light-induced bias stress reversal in polyfluorene thin-film transistors. *J. Appl. Phys.* **94,** 471 (2003).

26. Chen, C.-C., Chiu, M.-Y., Sheu, J.-T. & Wei, K.-H. Photoresponses and memory effects in organic thin film transistors incorporating poly(3-hexylthiophene)/CdSe quantum dots. *Appl. Phys. Lett.* **92,** 143105 (2008).

27. Wang, W., Ma, D. & Gao, Q. Optical Programming/Electrical Erasing Memory Device Based on Low-Voltage Organic Thin-Film Transistor. *IEEE T. Electron Dev.* **59,** 1510–1513 (2012).

28. Dutta, S. & Narayan, K. S. Gate-Voltage Control of Optically- Induced Charges and Memory Effects in Polymer Field-Effect Transistors. *Adv. Mater.* **16,** 2151–2155 (2004).

29. Narayan, K. S. & Kumar, N. Light responsive polymer field-effect transistor. *Appl. Phys. Lett.* **79,** 1891 (2001).

30. Queisser, H. J. & Theodorou, D. E. Decay kinetics of persistent photoconductivity in semiconductors. *Phys. Rev. B* **33,** 4027–4033 (1986).

31. Barra, M., Bloisi, F., Cassinese, A., Di Girolamo, F. V. & Vicari, L. Photoinduced long-term memory effects in n-type organic perylene transistors. *J. Appl. Phys.* **106,** 126105–3 (2009).

32. Liu, X. *et al.* Multifunctional organic phototransistor-based nonvolatile memory achieved by UV/ozone treatment of the Ta_2O_5 gate dielectric. *ACS Appl. Mater. Interfaces* **6,** 8337–44 (2014).

33. Borghetti, J. *et al.* Optoelectronic Switch and Memory Devices Based on Polymer-Functionalized Carbon Nanotube Transistors. *Adv. Mater.* **18,** 2535–2540 (2006).

34. Breiner, T. *et al.* Blends of Poly (methacrylate) Block Copolymers with Photoaddressable Segments. *Macromolecules* **40,** 2100–2108 (2007).

35. Wu, Y., Natansohn, A. & Rochon, P. Photoinduced Birefringence and Surface Relief Gratings in Novel Polyurethanes with Azobenzene Groups in the Main Chain. *Macromolecules* **34,** 7822–7828 (2001).

36. Orgiu, E. *et al.* Optically switchable transistor via energy-level phototuning in a bicomponent organic semiconductor. *Nat. Chem.* **4,** 675–9 (2012).

37. Hu, L. *et al.* An optimized ultraviolet-A light photodetector with wide-range photoresponse based on ZnS/ZnO biaxial nanobelt. *Adv. Mater.* **24,** 2305–9 (2012).

Chapter 5

Effect of Azobenzene Derivatives on UV-Responsive Organic Thin-Film Phototransistors Using a 2,7-dipentylbenzo[b]benzo[4,5] thieno[2,3-d]thiophene Semiconductor

Effect of Azobenzene Derivatives on UV-Responsive Organic Thin-Film Phototransistors Using a 2,7-dipentylbenzo[b]benzo[4,5] thieno[2,3-d]thiophene Semiconductor

This chapter is a reproduction of the following published article accepted for publication July 02, 2015, in The Journal of Material Chemistry C. The major contribution of this work is that we show that the HOMO/LUMO energy levels as well as the electron accepting or donating nature of small molecule additives can be used to predict how they will affect the UV phototransistor properties of our C5-BTBT:PMMA blended phototransistor.

Reproduced from: Chad S. Smithson, Darko Ljubic, Yiliang Wu, and Shiping Zhu; *J. Mater. Chem. C*, **2015**. With permission from The Royal Society of Chemistry.

DOI: 10.1039/C5TC01251A

5.1 Abstract

We have studied a UV responsive phototransistor and how the addition of various azobenzene derivatives alters the rise and relaxation times when exposed to and removed from UV light respectively. A three-component semiconductor system was studied consisting of a UV responsive material C5-BTBT, a polymer binder PMMA, and 1 of 5 different azobenzene materials for UV response enhancement.

The highest occupied molecular orbital (HOMO) and lowest unoccupied molecular orbital (LUMO) were determined experimentally and found from DFT theory. Azobenzene units with a pendent nitro group have lower HOMO and LUMO levels than the semiconductor C5-BTBT. This combined with their electron withdrawing nature allow them to stabilize excited electrons, extending the lifetime of excitons, keeping the system at a high current longer. Using a bi-exponential model, we see the relaxation rate constant τ increase from 278 to 578 s when nitro-azobenzene was used. Meanwhile, when azobenzene contains the electron donating unit NH_2, the HOMO of the material was found to be higher than that of C5-BTBT. This allowed another pathway for excited electrons to decay to their ground state, causing hole pair recombination, reducing I_{DS}. The relaxation curves when UV light is removed demonstrate a clear increase in decay rate over the control system, showing the charge donating amino-azobenzene assist in charge recombination.

5.2 Start of paper: Introduction

Organic Thin-Film Transistor (OTFT) technology offers many new opportunities for future electronic development.[1] One opportunity is the advanced functionality that can be applied to an OTFT by altering the semiconductor material, something that cannot be done for silicon based devices. Among the advanced OTFTs a need exists for easy to fabricate UV sensitive devices for a number of applications including ultraviolet

sensing and memory. UV sensors can be generated from either a UV-diode, or UV-OTFT. In both devices, charge carrier density is altered by an incident UV light. In UV-OTFTs the drain current (I_{DS}) is increased by altering the gate voltage (V_{GS}) whereas, a UV-diode does not require a gate voltage for I_{DS} enhancment.[2,3] A major necessity for these devices to separate them from silicon based devices is the need for them to be blind to the visible spectrum. Current UV sensors require the use of inorganic materials such as Si, Cd, Ga Ge[4] and ZnO[5,6,7,8] and often require waveguides to split the light allowing only UV light to enter the sensor.[9] The use of these waveguides complicates device structure (increasing costs), and reduces efficiency due to loss and a need to block the sensor from the original incoming UV light.

Photoswitching is one promising option where the response of the material to a photo stimuli dictates the device's switching speed. Gold nanoparticles have been used for this approach.[10] Another common way to utilize photoswitching is to generate a bistable device based on the OTFT design and incorporate photochromic materials such as spiropyran[11], or diarylethane[12,13,14] into the semiconductor. Typically these materials are mixed with a semiconducting polymer such as poly(3-hexylthiophene-2,5-diyl) (P3HT).[15] The devices function by altering the highest occupied molecular orbital (HOMO) of the photochromic material when photo stimulated so it more closely matches that of the semiconductor or work

function of the electrodes.[16] Another approach for UV-OTFTs is to utilize a small molecule semiconductor that has a specific UV absorption such as BPTT, which absorbs at 380 nm with a photocurrent to dark current ratio of $2x10^5$.[17] For all the mentioned organic devices, if they can match inorganic device quality and sensitivity, the advantages associated with organic electronics can be gained including solution processability, potential device flexibility, and reduced manufacturing costs.

In this paper we investigate a photosensitive OTFT where a photon excites an electron to a higher energy state generating an exciton, which through the applied drain source voltage (V_{DS}) allows for the generation of an electron-hole pair, increasing the devices conductivity.[18] It has been observed that the bulk of charge transport occurs at the semiconductor/dielectric interface, where we expect the generated holes to remain while the electrons accumulate at the drain.[19] Knowing this we have expanded upon our original report which demonstrated that the UV sensitive material 2,7-dipentylbenzo[b]benzo[4,5] thieno[2,3-d]thiophene (C5-BTBT), which has an absorption edge that begins at 367 nm and peaks at 354 nm, making it completely transparent to the visible spectrum exhibits this type of photoconductivity. C5-BTBT is an excellent semiconductor and has shown high mobility values when used in OTFTs. In addition, it is solution processable and air stable, making it an ideal candidate for electronic devices. When mixed with a polymer binder such

as poly(methylmethacryate) (PMMA), consistent and well dispersed films are formed. From these films we were able to generate bottom-gate top-contact OTFTs using a silicon wafer as the gate with a 200 nm SiO_2 layer as the dielectric and Au as the source and drain. The 1:1 blend of C5-BTBT:PMMA forms a semiconductor film with a modest mobility that we measured to be approximately 0.1 $cm^2V^{-1}sec^{-1}$. This mobility can be increased by two orders of magnitude through advanced printing techniques or the use of other polymer binders to alter the morphology.[2,20] The most interesting feature of this device is that, when exposed to UV light, with no gate bias present and a drain source voltage of -60 V, a slow 6 order of magnitude increase in current is observed (the “on state”), which can be returned to its low current “off state” state by pulsing the system with a gate voltage of -60 V.[21] This photo-induced conductance is the source of study in this paper to which we develop guidelines for how to decrease the device response time to UV stimulus and extend its “on state” lifetime for memory devices or decrease the “on state” lifetime for sensors.

Our previous work used a disperse red 1 (DR1)-methyl methacrylate copolymer as both a binding matrix and for device enhancement, allowing the device to reach maximum current faster and extending decay lifetime compared to when pure PMMA was used as the binding matrix. In order to screen numerous materials, we replaced the DR1-PMMA copolymer with

PMMA and a series of azobenzene small molecules to determine which has the strongest effect on the device performance and why. This approach causes an overall decrease in device performance because we go from a two-component system to a three-component system where the phase separation in the films is more complicated. However, this is acceptable, because it eliminates the cumbersome step of synthesizing numerous copolymers, allowing for a much faster and wider screening of materials. The materials include azobenzene containing no substituents (**Azo-1**), azobenzene containing an electron donating amino group (**Azo-2**), azobenzene containing an electron accepting nitro group (**Azo-3**), an azobenzene material with both groups (**Azo-4**) and the **DR1** small molecule so the results could be compared to the previous work (see **Fig. 5.1**). In addition, density function theory (DFT) calculations were used in conjunction with cyclic voltammetry and UV-vis measurements to estimate the highest occupied molecular orbital (HOMO) and lowest unoccupied molecular orbital (LUMO) energy levels of the materials both theoretically and experimentally. These measurements show that the placement of both the HOMO and LUMO directly influences the turn on time and decay rate of the systems. In addition we found that the choice of an electron withdrawing or electron donating substituent, influence the device performance.

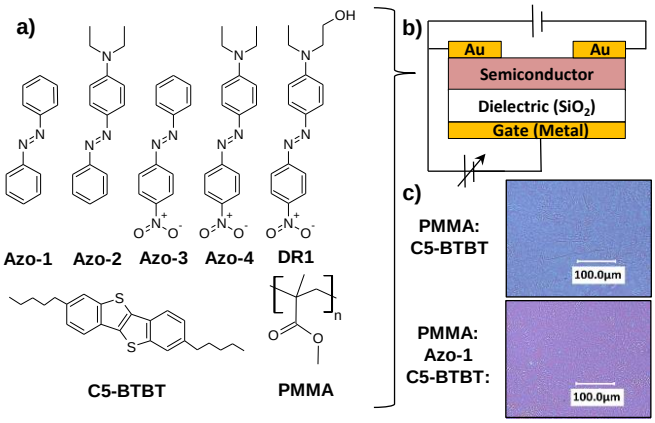

Figure 5.1: (*a)* Materials used to form the semiconductor layer. (*b)* OTFT top contact bottom gate device design. (*c)* Optical microscope images of a PMMA:C5-BTBT film and a PMMA:Azo-1:C5-BTBT film, showing that film morphology is not altered with the addition of the azobenzene small molecule.

5.3 Experimental / Results

All films were spin coated from a 1,1,2,2-tetrachloroethane (TCE) solution. TCE was chosen because it was able to completely dissolve all the materials used in this study to generate uniform films. The film morphology was not altered with the addition of azobenzene small molecules. When spin coated from the same solvent at the same conditions, films with different azobenzene additives also exhibited the similar morphology as shown in the optical images (Supporting Information **Fig. S5.1**). However, comparing the results of a C5-BTBT:PMMA film spin coated from chlorobenzene solution reported previously to films prepared from TCE, we observe different morphologies. Optical images of films made from

TCE showed a large number of striations typical of polycrystalline domains (**Fig. S5.1**). The dispersion of these domains is very even but generates a significantly larger number of grain boundaries than films obtained from chlorobenzene solution. As a result, the device prepared from TCE showed a lower mobility and lower saturation current. The lower performance is acceptable because all films in this report are made from TCE; therefore they have the same morphology allowing comparisons among each other. AFM measurements were performed to confirm the morphology were similar (**Fig. 5.2**). Topographical images show that all films have a relatively low surface roughness and are composed of small (~10 nm) spherical features evenly dispersed in the PMMA matrix. The phase images provide more information, making it easy to distinguish between the small molecules and the polymer binder. **C5-BTBT** forms discrete spherical crystal domains within the film, with a large amount of overlap to form a percolating network. It appears that the **C5-BTBT** domains are slightly bigger with less discrete edges when the polar azobenzene materials are present (**Azo-2**, **Azo-3**, **Azo-4** and **DR1**), suggesting the polarity of the additive has an effect on **C5-BTBT** crystallization in the film. Unfortunately we cannot distinguish between the phase of the azobenzene additive and that of the semiconductor **C5-BTBT.**

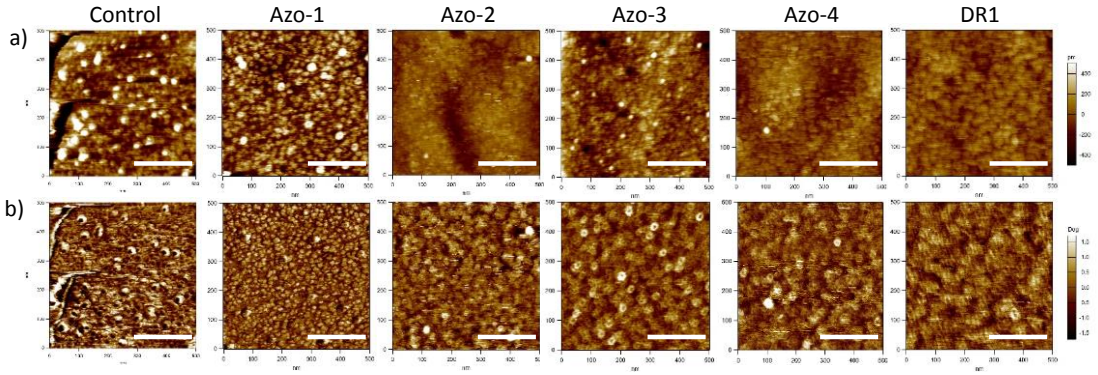

Figure 5.2: AFM images of the semiconductor films (scale bar 200 nm). (*a*) Topographical images, (*b*) phase image.

Transfer curves in the dark demonstrate typical p-type behaviour for all samples (**Fig. 5.3**). By considering the system containing no azobenzene small molecules (PMMA:C5-BTBT) as our control system, observations can be made as follows. Addition of azobenzene containing an amino group (**Azo-2**, **Azo-4**, **DR1**) shifted the threshold voltage (V_{Th}) towards the negative direction (**Table 1**) compared to the control. This is indicative of charge traps being introduced into the system.[22] Meanwhile, azobenzene samples that do not contain amine groups (**Azo-1**, **Azo-3**), showed a V_{Th} shift in the positive direction compared to the control to about -4 V, which suggests the filling of charge traps.[2] When the UV light was on, the V_{Th} of the control sample was shifted by only 14 V, while all the azobenzene containing samples showed much larger shifts, indicating the addition of the azobenzene small molecule allows for an increase in the number of charge carriers when exposed to UV light. It has been reported in the past

that electrons generated by illumination fill the traps, causing the shift in threshold voltage.[23,22] The largest ΔV_{Th} occurs when a pendent amino group is present. The ΔV_{Th} can be used to estimate the increase in charge carrier density from dark to UV conditions, using the equation

$$\Delta N^* = C_i \Delta V_{Th} / e \quad \textbf{[1]}$$

where C_i = 15 nF cm^{-2} is the capacitance per unit area of the dielectric layer, ΔV_{Th} is the shift of the threshold voltage, and e is the elementary charge.[24,25,26] The photocurrent/dark-current ratio (P_{ill}) was calculated at a V_{GS} = 0 V using equation **[2]**.

$$P_{ill} = \frac{(I_{light} - I_{dark})}{I_{dark}} \quad \textbf{[2]}$$

where I_{light} and I_{dark} is the measured current under UV irradiation and in the dark respectively. These data are summarized in **Table 5.1**. A large photocurrent ratio eliminates the need for additional circuitry to increase the device gain and can be used as a figure of merit for device performance. These devices exhibit a photocurrent/dark-current ratio between 3-6 orders of magnitude which is large enough to unambiguously distinguish between the “off state” and “on state”. Return sweeps for the transfer curves were measured, but make the graphs too cluttered. They can be found in the supporting information. It should be noted that in the dark, little to no hysteresis was observed. However, under UV irradiation, the gate bias stress causes separated charges to recombine creating a large hysteresis effect.[27]

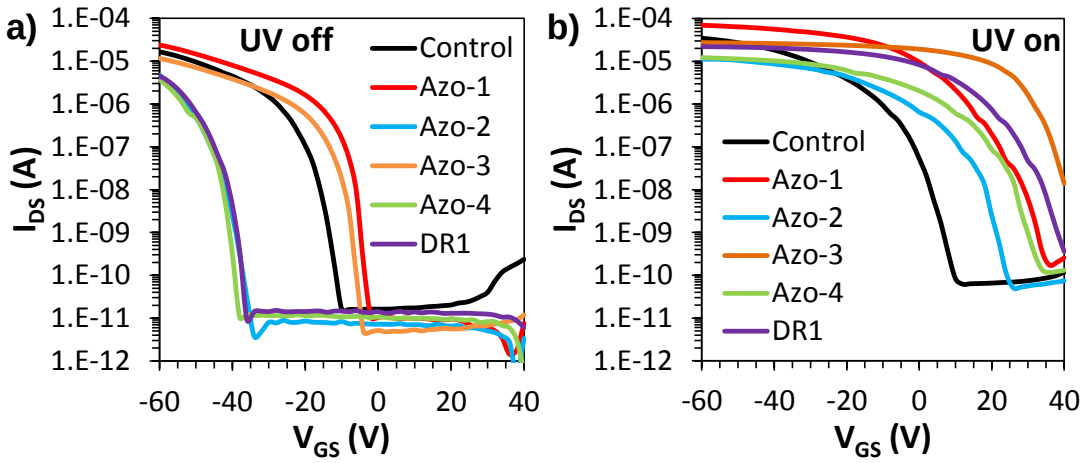

Figure 5.3: Transfer Curves for the 6 systems studied with and without UV light. (*a*) From left to right Azo-4, DR1, Azo-2, PMMA, Azo-3, Azo-1. (*b*) From left to right PMMA, Azo-2, Azo-4, Azo-1, DR1, Azo-3.

Table 5.1

Electronic Characterization Data for the systems studied in dark and under UV light

Sample	P_{ill}	Mobility dark ($cm^2V^{-1}sec^{-1}$)	V_{Th} Dark (V)	V_{Th} UV on (V)	ΔV_{Th} (V)	ΔN^*
Control	$3.3*10^3$	0.10	-17	-3	14	$1.87*10^{12}$
Azo-1	$9.2*10^5$	0.08	-4	18	23	$3.56*10^{12}$
Azo-2	$9.0*10^4$	0.10	-43	12	55	$5.62*10^{12}$
Azo-3	$3.7*10^6$	0.04	-8	38	46	$3.93*10^{12}$
Azo-4	$1.9*10^5$	0.08	-42	23	65	$6.74*10^{12}$
DR1	$5.8*10^5$	0.10	-42	29	70	$7.12*10^{12}$

Similar to our previous report[21], all devices showed completely reversible behaviour. The devices were turned to their "on state" by applying a UV stimulus, while a large gate bias stress (V_{GS} = -60 V) returned them to their "off state". We were interested in how to speed up the rise times and alter the decay times for use as either a memory device (long decay time) or a sensor (short decay time). **Fig. 5.4** provides the current response of devices over time when exposed to UV light for 20 minutes. All devices reached a saturation current within this period of time, the UV light was then removed and the decay of the I_{DS} was measured. The response and decay curves were fitted using biexponential models, one for the current rise when exposed to UV light **[3]** and one for the decay when the UV light was removed **[4]**.

$$I_{DS} = A\left(1 - e^{(-t/\tau_A)}\right) + B\left(1 - e^{(-t/\tau_B)}\right) + E \qquad \textbf{[3]}$$

$$I_{DS} = Ce^{(-t/\tau_C)} + De^{(-t/\tau_D)} + F \qquad \textbf{[4]}$$

where A, B, C, D, E and F are constants measured in (A), t is time in (s), τ_A and τ_B, are rise times given in (s), τ_C and τ_D, are decay times given in (s). The biexponential models consist of a fast and slow exponential τ term. **Table 5.2** summarizes the fitted values for each curve where the fast term was used as a measure of stimulus response speed and decay speed. For response times, devices containing nitro groups responded faster than the others. Those containing an amino group respond slower than pure azobenzene, likely due to the increased number of low energy traps

generated from the amino groups. Over a 20 minute UV exposure, all the devices eventually reach a saturation value with azobenzene taking the longest of all the samples. There was a significant difference in the decay times of the devices. Devices containing electron accepting groups remained in the high current state, displaying slow decay times. Meanwhile the azobenzene containing electron donating groups (amino groups) displayed a significantly faster decay rate. Interestingly the DR1 sample does not follow the trend of the other amine containing groups, which could be caused by the additional electron withdrawal due to the OH pendent group on the amine unit.

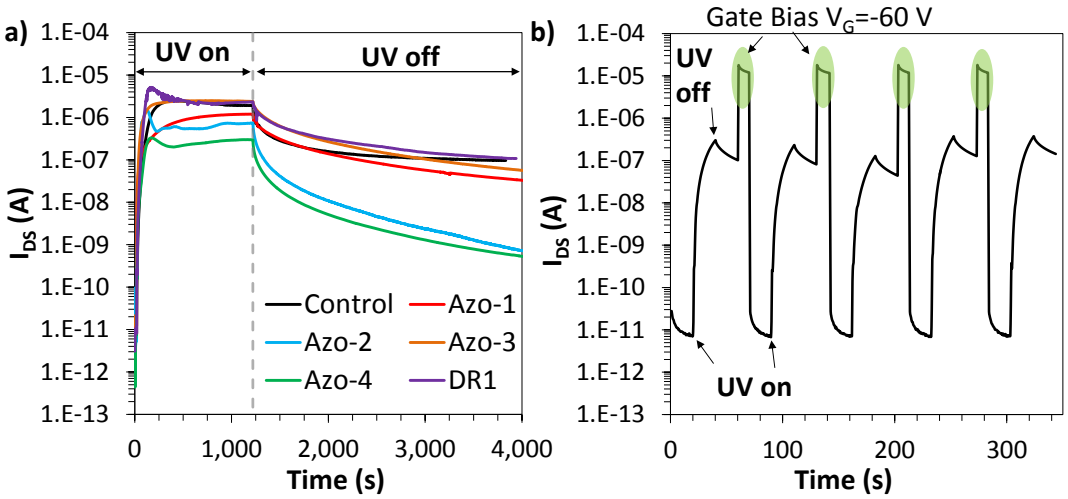

Figure 5.4: (*a*) samples irradiated with UV light for 20 minutes to ensure saturation current, the dashed line shows when the UV is removed to show the current decay over time. (*b*) UV write erase cycle of Azo-3:PMMA:C5-BTBT showing the reproducibility and re-writability of the system.

Table 5.2

Values used to model the rise and decay curves of the samples

Writing (UV light exposure)					
	A (A)	τ_A *(s)*	*B (A)*	τ_B *(s)*	*E*
Control	$1.45*10^{-6}$	499	$9.00*10^{-7}$	$1.2*10^{3}$	$7.67*10^{-12}$
Azo-1	$1.20*10^{-6}$	371	$1.60*10^{-19}$	$6.7*10^{3}$	$1.21*10^{-11}$
Azo-2	$6.59*10^{-7}$	249	$8.05*10^{-8}$	$1.1*10^{6}$	$6.16*10^{-12}$
Azo-3	$2.40*10^{-6}$	125	$1.32*10^{-8}$	$1.4*10^{5}$	$7.67*10^{-12}$
Azo-4	$2.01*10^{-7}$	225	$2.20*10^{-6}$	$2.3*10^{5}$	$7.67*10^{-12}$
DR1	$2.01*10^{-6}$	306	$8.19*10^{-7}$	$2.8*10^{3}$	$7.67*10^{-12}$
Decay (UV light removed)					
	C (A)	τ_C ***(s)***	***D (A)***	τ_D ***(s)***	***E***
PMMA	$1.02*10^{-6}$	18	$5.35*10^{-7}$	278	$1.10*10^{-7}$
Azo-1	$5.38*10^{-7}$	55	$4.58*10^{-7}$	516	$3.94*10^{-8}$
Azo-2	$6.93*10^{-7}$	50	$4.06*10^{-8}$	649	$9.00*10^{-11}$
Azo-3	$1.15*10^{-6}$	80	$8.48*10^{-7}$	578	$5.68*10^{-8}$
Azo-4	$2.70*10^{-7}$	47	$2.97*10^{-8}$	493	$4.37*10^{-10}$
DR1	$1.01*10^{-6}$	67	$7.85*10^{-7}$	580	$1.11*10^{-7}$

5.4 HOMO LUMO energy level determination.

Given the very similar morphology of these systems, to understand the significant difference in photoresponse, we looked at the HOMO and LUMO energy levels of all materials involved in the charge transfer. DFT calculations using Gaussian 03 were performed using the B3LYP/6-311G(d,p) basis set to determine the energy levels of the HOMO and LUMO of each material. Hybrid functionals such as this one carry an

average error of 0.2 eV. To provide an experimental comparison for the DFT calculations, cyclic voltammetry measurements were performed (**Fig. 5.5**). Cyclic voltammetry measurements have been shown to be an excellent method to approximate the HOMO of a material. Varying viewpoints on how to analyze and standardize CV measurements exist in the literature,[28,29] making the comparison of HOMO and LUMO data difficult to achieve. Therefore, clearly stating the values used when converting CV measurements to the vacuum level is necessary for comparison with other works. We have chosen to follow the method set forth in 2011 by Cardona and Bazan,[30] which uses the onset of oxidation ($E_{onset,\ ox}$) obtained from cyclic voltammetry to determine the HOMO which is shown to have an accuracy of approximately 0.1 eV when compared to ultraviolet photoelectron spectroscopy (UPS) measurments.[28] To convert to the Fermi level the following equation is used;

$$E_{HOMO} = -(E_{[onset,\ ox\ vs\ Fc+/Fc]} + 5.1)(eV) \quad \textbf{[5]}$$

where the $E_{1/2}$ of the ferrocenium couple (Fc^{+}/Fc) in CH_3CN is given a value of 0.4 eV vs the saturated calomel electrode (SCE)[31] with SCE being 0.24 eV vs the normal hydrogen electrode (NHE) and NHE being -4.46 eV vs the vacuum level. Although it is possible to use $E_{onset,\ red}$ in the above equation to determine the LUMO value, a more accurate LUMO is obtained when the bandgap energy E_g is assumed to be equal to the $E_{onset\ opt}$

obtained from the optical edge of UV-vis measurements. This value is easily converted from nm to eV using the conversion;

$$E_{onset\ opt} = hc/\lambda = 1240(eV \cdot nm)/\lambda \quad \textbf{[6]}$$

where *h* is planks constant, *c* is the speed of light in a vacuum and λ the wavelength where the onset of absorbance occurs in the UV-Vis spectrum. The LUMO is determined using the following equation;

$$E_{LUMO} = E_{HOMO} + E_{onset\ opt} \quad \textbf{[7]}$$

A general trend is observed, where the experimental HOMO-LUMO levels are found at a lower energy than the calculated values **Fig. 5.5**. This is expected as calculated values will always overestimate energy levels, and they do not take into account the solvent effect that occurs during CV measurements. However, the position of the HOMO and LUMO relative to one another is consistent across the experimental and calculated data, demonstrating that one or the other method can be used to obtain comparable HOMO/LUMO energy levels. To simplify, the rest of this report will focus on the experimental HOMO and LUMO levels. The HOMO of **Azo-1** and **Azo-3** are lower than that of the C5-BTBT. Meanwhile, all samples containing an amino group **Azo-2**, **Azo-4** and **DR1**, have a HOMO above that of C5-BTBT. The LUMO energy levels for all the materials are fairly close in energy with all of them being lower than that of C5-BTBT.

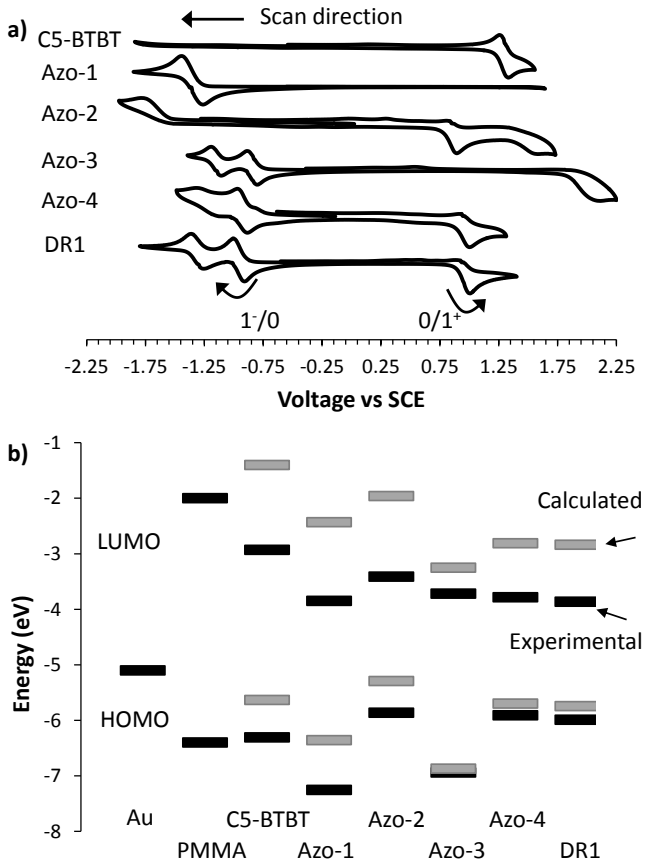

Figure 5.5: (*a*) Cyclic voltammetry measurements of the materials studied. The onset to oxidation ($0/1^+$) was used as the experimentally measured HOMO for each system. (*b*) dark boxes, HOMO and LUMO energy levels measured from CV and UV vis, open boxes calculated using DFT theory with a B3LYP/6-311G(d,p) basis set. PMMA from the following reference.[32]

5.5 Charge transfer and trapping based upon HOMO LUMO energy levels

The transistors studied here can be grouped into three different categories based on the relative positions of the azobenzene HOMO/LUMO energy levels compared to that of C5-BTBT. In the control system C5-

BTBT:PMMA (**Fig. 5.6 (*d*)**), we observe that the HOMO of both materials are very close and because band theory assumes bands are not discreet energy levels, but instead a spread of the density of states, we can assume these two materials have overlapping HOMO levels. When irradiated with 365 nm UV light, an electron from the C5-BTBT valance band (HOMO) can be excited into the LUMO of the material leaving a hole in the valance band for conductance to occur. This hole is moved through the material due to the external V_{SD}, causing conductance to occur resulting in an increased current. While this is occurring, the electron can travel in the conductance band (LUMO) of C5-BTBT, but does not have the energy to enter the LUMO of PMMA as its LUMO lies higher in energy than the C5-BTBT LUMO, limiting the distance the electron can travel as it will eventually be stopped by PMMA. This excited electron will eventually return to its ground state causing a charge recombination.

When an azobenzene derivative is added to the system two new scenarios are generated (**Fig. 5.6 (*e*), (*f*)**). The second category occurs for both **Azo-1** and **Azo-3**, where the HOMO of the azo is energetically unfavorable for the Azo unit to move an electron into a hole on C5-BTBT or PMMA and it therefore will not take part in hole conductance. The LUMO of these Azo systems is lower in energy than that of C5-BTBT. Therefore an excited electron on C5-BTBT can fall from the C5-BTBT conductance band into the LUMO of the Azo material. **Azo-3** has a strong electron withdrawing nitro

group (which we see from the calculated molecular orbital, has a LUMO with a large electron concentration on the nitro group **Fig. 5.6 (*b*)**). able to trap an excited electron for a longer time period than C5-BTBT. Because the HOMO of nitroazobenzene should not take part in hole transport, there is no lower energy Azo state for the electron to decay to. Therefore, as long as the Azo group retains the excited electron, hole conductance can occur. With time the excited electron will decay back to recombine with a hole on either C5-BTBT or PMMA. This dependence of the recombination

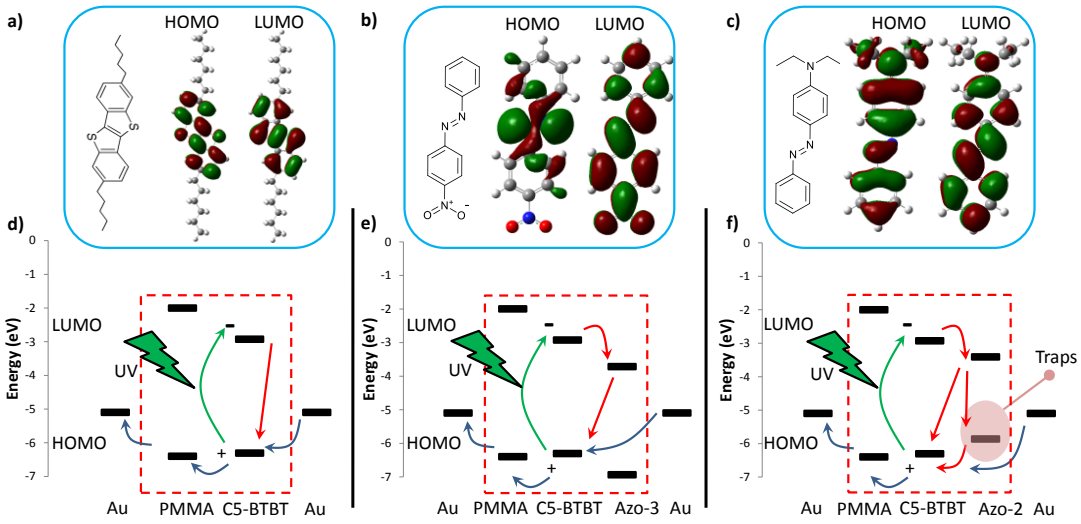

Figure 5.6: The HOMO and LUMO molecular orbitals calculated using DFT theory for (*a*) C5-BTBT, (*b*) Azo-3, (*c*) Azo-2. (*d*), (*e*), (*f*) Experimentally determined HOMO LUMO energy levels of materials involved in charge transfer, explaining how each system reacts to the UV stimulus. The blue arrows represent pathways for electron movement to occur. The red arrow represents a pathway for charge recombination to occur.

of the excitons on the strength of the electron accepting material, provides a method to extend the hole lifetime after the UV source is removed.

Table 5.3

Cyclic Voltammetry and UV-Vis Data used to experimentally determine the HOMO and LUMO levels as well as the calculated HOMO and LUMO values

Material	$E_{Onset\ Red}$ (eV)[a)]	HOMO (eV) Exper[b)]	HOMO (eV) Calc[c)]	$E_{opt\ onset}$ (nm)[d)]	E_g (eV) Exper[e)]	E_g (eV) Calc[c)]	LUMO (eV) Exper[f)]	LUMO (eV) Calc[c)]
C5-BTBT	1.21	-6.31	-5.63	367.1	3.38	4.23	-2.93	-1.40
Azo-1	-1.25[g)]	-7.25[g)]	-6.36	364.2	3.40	3.92	-3.85[g)]	-2.43
Azo-2	0.76	-5.86	-5.29	505.5	2.45	3.33	-3.41	-1.96
Azo-3	1.84	-6.94	-6.87	384.8	3.22	3.62	-3.72	-3.25
Azo-4	0.81	-5.91	-5.70	583.5	2.13	2.89	-3.78	-2.81
DR1	0.89	-5.99	-5.74	583.7	2.12	2.91	-3.86	-2.84

[a)] Values determined from cyclic voltammetry vs SCE, scan rate 200 mV, solvent CH_3CN, electrolyte NBu_4PF_6, Pt electrodes

[b)] Values determined from cyclic voltammetry Vs Fermi level using equation [5]

[c)] Obtained using DFT with a B3LYP 6-311G(d,p) basis set;

[d)] Obtained from UV-vis

[e)] Using equation [6]

[f)] Obtained from equation [7]

[g)] only the oxidation peak was obtained from CV, so its onset was used as the LUMO and the UV-vis was used to determine the HOMO

The final category occurs for the amino containing azobenzene systems (**Azo-2**, **Azo-4** and **DR1**) who's HOMOs are higher in energy than C5-BTBT and PMMA while their LUMOs are lower in energy than C5-BTBT. When UV light excites an electron on C5-BTBT, a ground state electron from the Azo HOMO can decay into the lower energy C5-BTBT HOMO filling the generated hole and placing the hole on the higher energy amine-azobenzene HOMO. This is a trap which will prevent conductance because electrons will need to be raised in energy to fill this hole. Therefore enough excitons must first be generated to fill all the holes before conductance can occur. As a result it takes longer for a device to turn on. Like the previous scenario, the excited electrons can decay into the lower energy LUMO of the Azo group. It is possible the Azo system will already have donated an electron from its HOMO to fill the hole generated by C5-BTBT, therefore this excited electron can decay down to its electron deficient HOMO. Alternatively the electron can combine with a hole by decaying directly from the LUMO level to fill a hole in the C5-BTBT/PMMA conductance band. The calculated molecular orbital for the LUMO of these materials shows no molecular orbital density on the amino groups **Fig. 5.6 (*c*)**, supporting the idea that the material is more likely to donate an electron which can cause charge recombination. The result of this is an expected slower write time and increased decay rate.

Two other scenarios exits, but did not fall into the azobenzene systems studied here. Those systems are when the HOMO is lower than C5-BTBT and the LUMO is higher than C5-BTBT. This system is expected to have no appreciable effect on the systems performance, and will just take up physical space in the system generating gaps in the band structure. The other when both the HOMO and LUMO are higher than those of C5-BTBT respectively. In this scenario, we expect a slower write time due to the traps caused by the material. The decay rate should also be faster because the traps provide a smaller bandgap where excited electrons can decay to and recombine. Therefore this scenario would be similar to case three discussed above.

If we wish to generate a memory device we want to choose a material that has a HOMO lower than C5-BTBT and a LUMO lower than the C5-BTBT LUMO. Additionally the material should contain a large amount of electron accepting groups so it can stabilize an excited electron for an extended period of time. Meanwhile if we want a sensor, we wish to choose a material that has a HOMO that matches C5-BTBT and a LUMO lower than C5-BTBT. The material should contain electron donating groups to help expedite the hole pair recombination process.

5.6 Conclusions

We explored the UV response of an OTFT consisting of C5-BTBT as a UV stimulant, PMMA as a polymer binder, and a series of azobenzene units containing different substituents. HOMO and LUMO energy levels were calculated and measured experimentally. Systems containing azobenzene with the electron donating amine groups, had HOMO values higher than that of C5-BTBT, which introduced charge traps into the system causing a slower response to the UV stimulus because the traps needed filling. In addition they had faster decay rates because the electron donating nature of the amine group combined with the charge traps provided an additional pathway for charge recombination to occur. Meanwhile, systems containing electron donating nitro groups were found have a much slower decay rate once the UV light was removed compared to systems without nitro groups because of the electron withdrawing nature of the nitro group, being able to stabilize an excited electron. These results provide a method to determine what materials can be mixed with C5-BTBT to enhance its UV response and either extend the decay time (memory device) (electron donating groups), or decrease the decay time (sensor device) (electron accepting groups). This roadmap can be used for future work to generate more effective UV devices.

5.7 Acknowledgements

This work was made possible with the facilities of the Shared Hierarchical Academic Research Computing Network SHARCNET: www.sharcnet.ca and Compute/Calcul Canada.

5.8 Supporting information

5.8.1 Experimental

A. Materials

4-(diethylamino)azobenzene (98%) (**Azo-2**) was purchased from Alfa Aesar and used as received. The following materials were purchased from Sigma Aldrich ferrocene ($Fe(Cp)_2$), Bis(pentamethylcyclopentadienyl)iron(II) ($Fe(Cp^*)_2$), azobenzene (99%) (**Azo-1**), 4-nitroazobenzene (90%) (**Azo-3**), diethyl-(4-(4-nitro-phenylazo)-phenyl)-amine, disperse red 1 (95%) (**DR1**), 2-[Ethyl[4-[2-(4-nitrophenyl)ethenyl]phenyl]amino]ethanol (98%) (**Azo-4**), PMMA (M_N =140,000), HPLC grade CH_3CN, reagent grade isopropanol, toluene and 1,1,2,2-tetrachloroethane(TCE). $(Fe(Cp)_2)$ and $(Fe(Cp^*)_2)$ were purified by sublimation. **Azo-3** was dissolved in ethyl acetate and filtered to remove impurities, the solvent was then removed using a rotary evaporator. It was then dried 60°C under vacuum overnight. All other samples were used as received. C5-BTBT was prepared using the methods outlined in reference [33,20].

B. UV-Vis sample preparation/measurements

Glass microscope slides were cleaned with isopropanol and air dried. Solutions from **Table S5.1** were drop cast onto the glass slides where they sat for 2 minutes before being spin coated at 500 RPM for 90 sec using a 5 sec ramp time. These samples were used to acquire UV-Vis measurements on a Cary 5000 UV-Vis-NIR Spectrometer using a glass slide with a 40.0 mg PMMA, 3.96 g TCE solution spin coated on it as the background.

Table S5.1

Materials used to prepare solutions for spin coating[a)]

Sample[b)]	Mass (mg)	mmoles	PMMA mass (mg)	C5-BTBT (mg)[c)]	TCE (g)
Azo-1	2.4	0.0133	37.6	40.0	3.92
Azo-2	3.4	0.0133	36.6	40.0	3.92
Azo-3	3.0	0.0133	37.0	40.0	3.92
Azo-4	4.0	0.0133	36.0	40.0	3.92
DR1	4.2	0.0133	36.0	40.0	3.92

[a]C5-BTBT and PMMA UV-vis spectra can be found in reference[21]

[b]All solutions were passed through a 0.45 µm filter before use

[c]The solutions used for UV-vis were the same composition except no C5-BTBT was added and its weight was replaced by an equivalent weight of TCE.

C. Cyclic voltammetry measurements

Pt was used as the working, reference and counter electrodes. Solutions were 2×10^{-3} M test compound and 0.1 M $N(Bu_4)PF_6$ as the supporting electrolyte in CH_3CN. Solutions containing the electrolyte, test compound and

solvent were stirred with a bubbling stream of argon for 5 minutes before measurements were taken. During measurements, the chamber was sealed with a flow of argon over the solution. Scan rates of 100 mV/s and 200 mV/s were used. Data was collected on a PAR (Princeton Applied Research) model 283 potentiostat (using PAR PowerCV software). Ferrocene (1.9 mg, 0.002 M) was added as a reference to zero the spectra. For samples where the ferrocene halfwave could not be distinguished from the analyte, $Fe(Cp^*)_2$ (3.3. mg, 0.002 M) was used in its place. All samples were standardized vs SCE , where $E_{1/2}$ of the ferrocenium couple (Fc^+/Fc) in CH_3CN is given a value of 0.4 eV vs (SCE).[31] These spectra were then converted to the vacuum scale by applying the following formula $E_{HOMO} = -(E_{[onset,\ ox\ vs\ Fc+/Fc]} + 5.1)(eV)$.[30]

Table S5.2

Materials used to prepare solutions for cyclic voltammetry

Sample	Mass (mg)	Molarity (mol/L)	$N(Bu)_4PF_6$ mass (g)	$N(Bu)_4PF_6$ molarity (mol/L)	CH_3CN (mL)
Azo-1	1.8	0.002	0.1937	0.1	5
Azo-2	2.5	0.002	0.1937	0.1	5
Azo-3	2.3	0.002	0.1937	0.1	5
Azo-4	3.0	0.002	0.1937	0.1	5
DR1	3.0	0.002	0.1937	0.1	5

D. Electrical measurements

Sample preparation and characterization was performed in a similar manor to that outlined in our previous paper,[21] with the following differences; Solution compositions are different and outlined above in **Table S5.2**. Spin coating conditions were changed from 2000 rpm to 3000 rpm. Measurements were no longer performed under humidity controlled conditions and instead measured under ambient conditions.

5.8.2 Experimental Data

E. Optical microscopy measurements

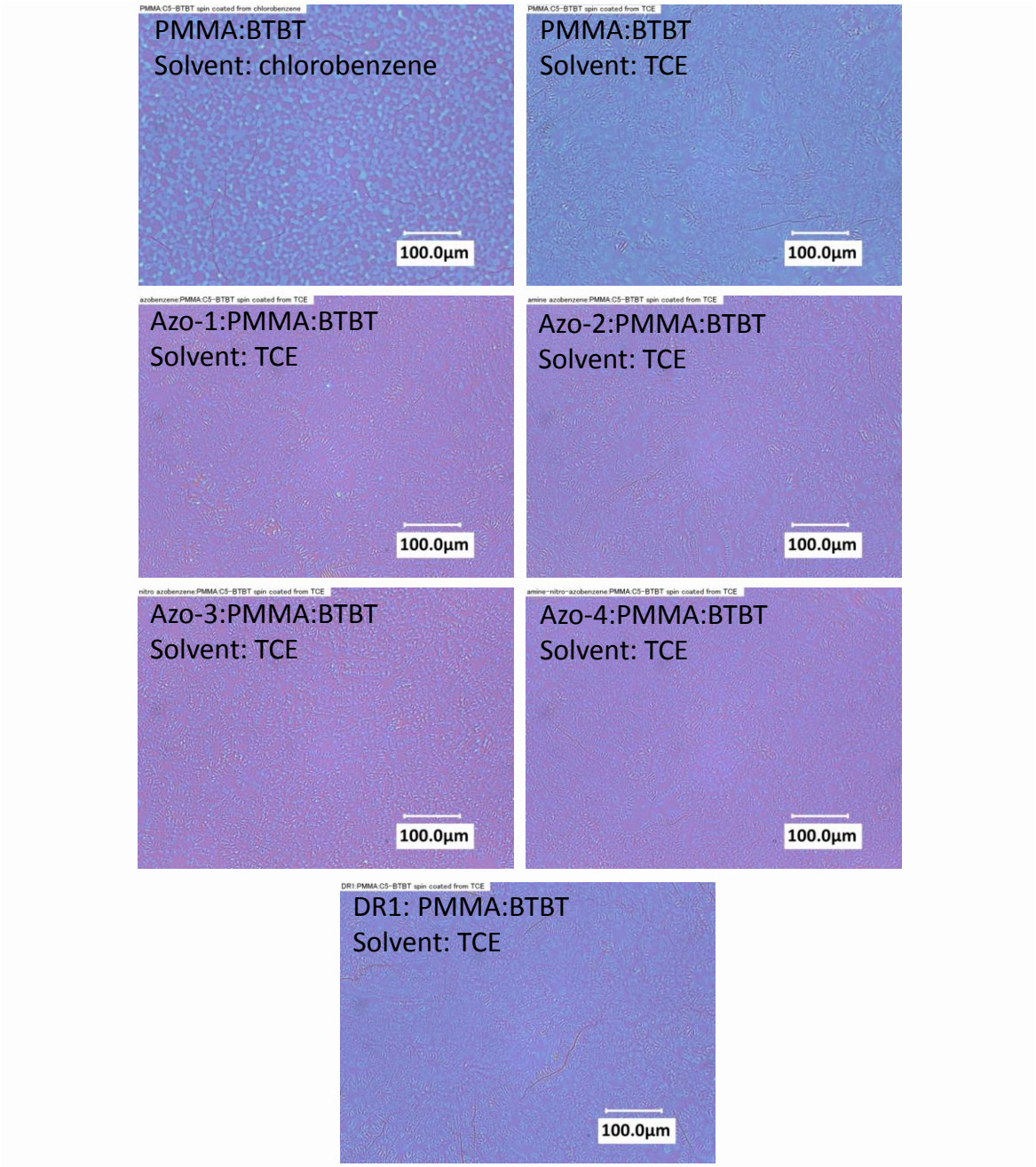

Figure S5.1: Optical Microscope images of films spin coated from 1,1,2,2-tetrachlorethane (TCE) onto an HMDS modified Si/SiO_2 wafer, as well as a control film spin coated from chlorobenzene. All films show similar morphology when spin coated from the same solvent.

F. Transfer curves

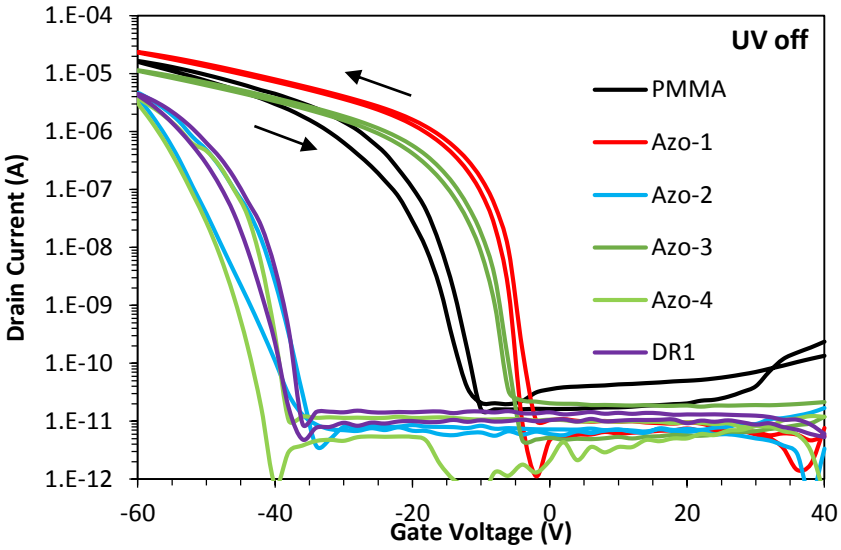

Figure S5.2: Transfer curves for all systems studied under dark conditions showing a forward and backward sweep.

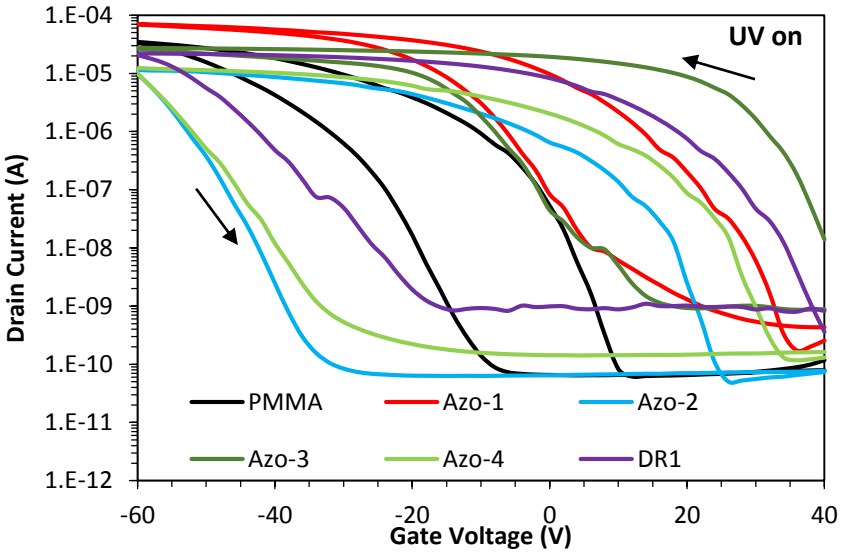

Figure S5.3: Transfer curves for all systems studied under UV conditions showing a forward and backward sweep.

G. Cyclic voltammetry results

Table S5.3

Cyclic Voltammetry Data, all values in (eV)[a)]

Material	$E_{Onset}^{0/1+}$	$E_{1/2}^{0/1+}$	$E_{1/2}^{1+/2+}$	$E_{1/2}^{1-/0}$	$E_{1/2}^{2-/1-}$
C5-BTBT	1.21	1.31	----	----	----
Azo-1	----	----	----	-1.33	----
Azo-2	0.76	0.92[b)]	1.61[b)]	-1.76	----
Azo-3	1.84	2.13[b)]	----	-0.83	-1.13
Azo-4	0.81	0.93[b)]	----	-0.91	-1.32[b)]
DR1	0.89	1.03[b)]	----	-0.94	-1.29

[a)] Values determined from cyclic voltammetry vs SCE, with the onset of oxidation or reduction reported

[b)] Irreversible oxidation or reduction

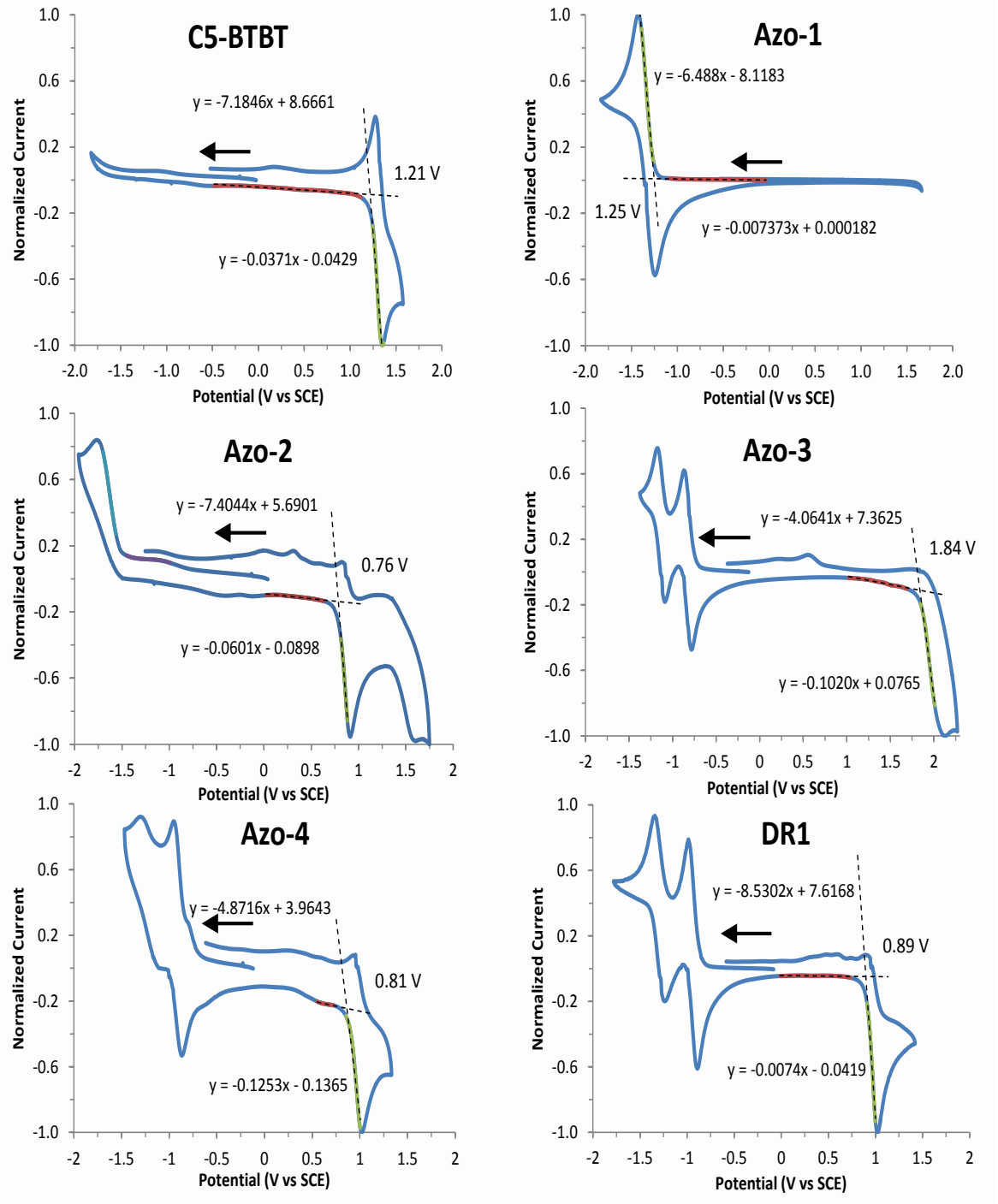

Figure S5.4: Cyclic voltammograms of film materials (vs SCE) showing the onset of reduction or oxidation for.

H. UV-Vis measurements

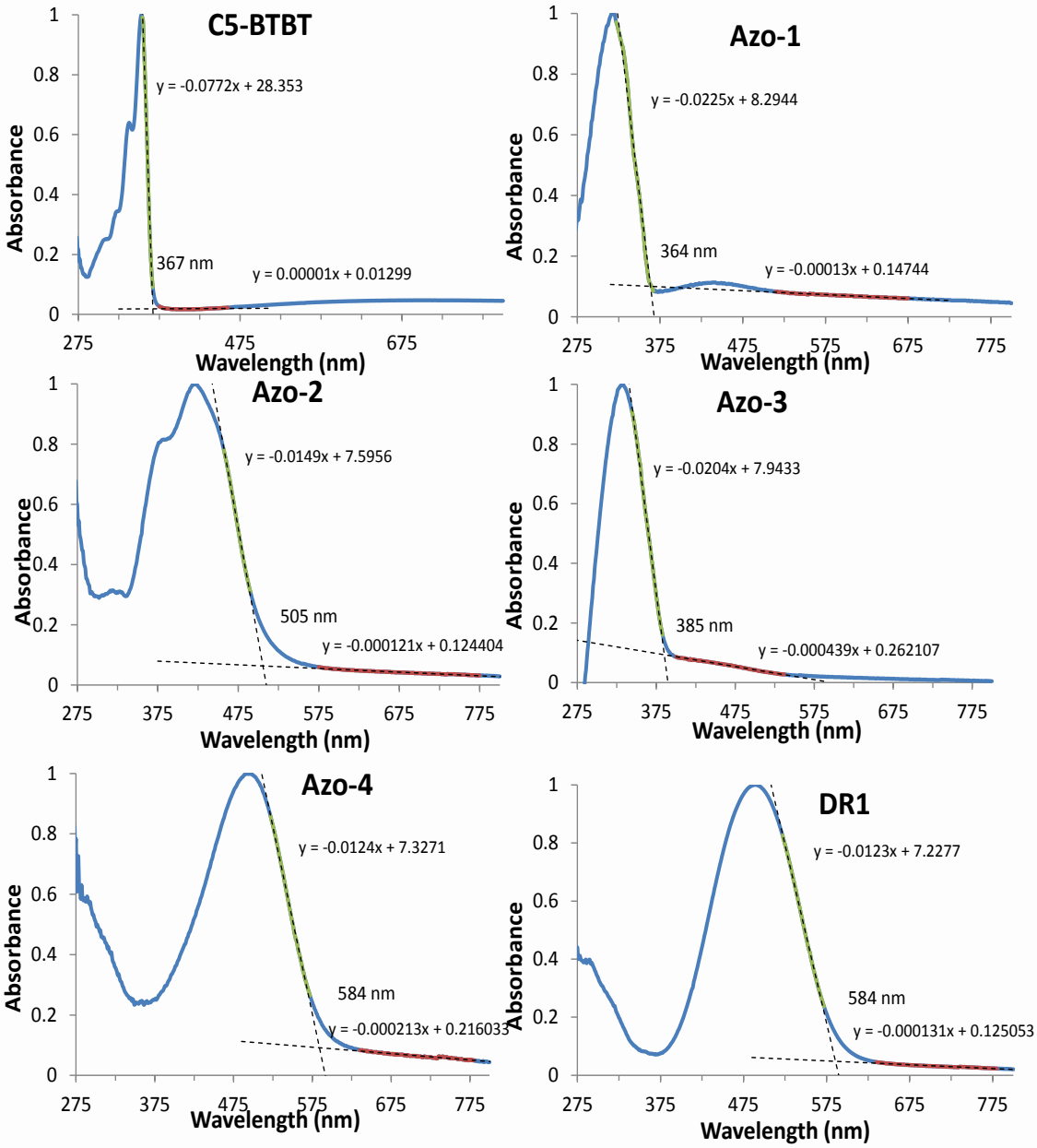

Figure S5.5: UV-vis spectra of film materials with the absorption edge calculations shown.

I. Rise and decay measurements with experimental modeling

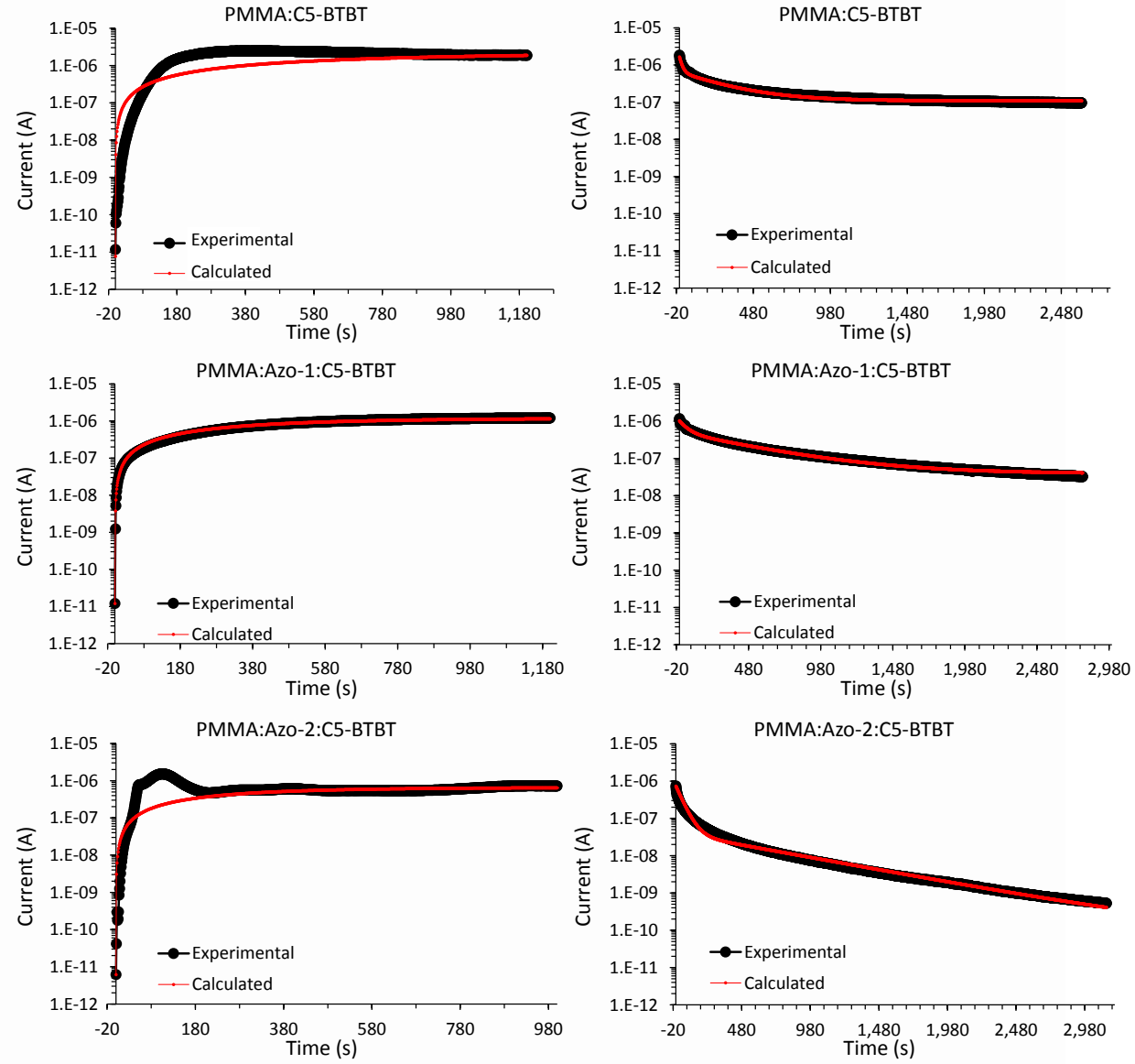

Figure S5.6: (Left side), I_{DS} vs time showing the current rise over a 20 minute UV exposure with the experimental (black) and biexponential curve fitting (red). (Right) I_{DS} decay vs time starting after the 20 minute UV exposure with experimental (black) and biexponential curve fitting (red).

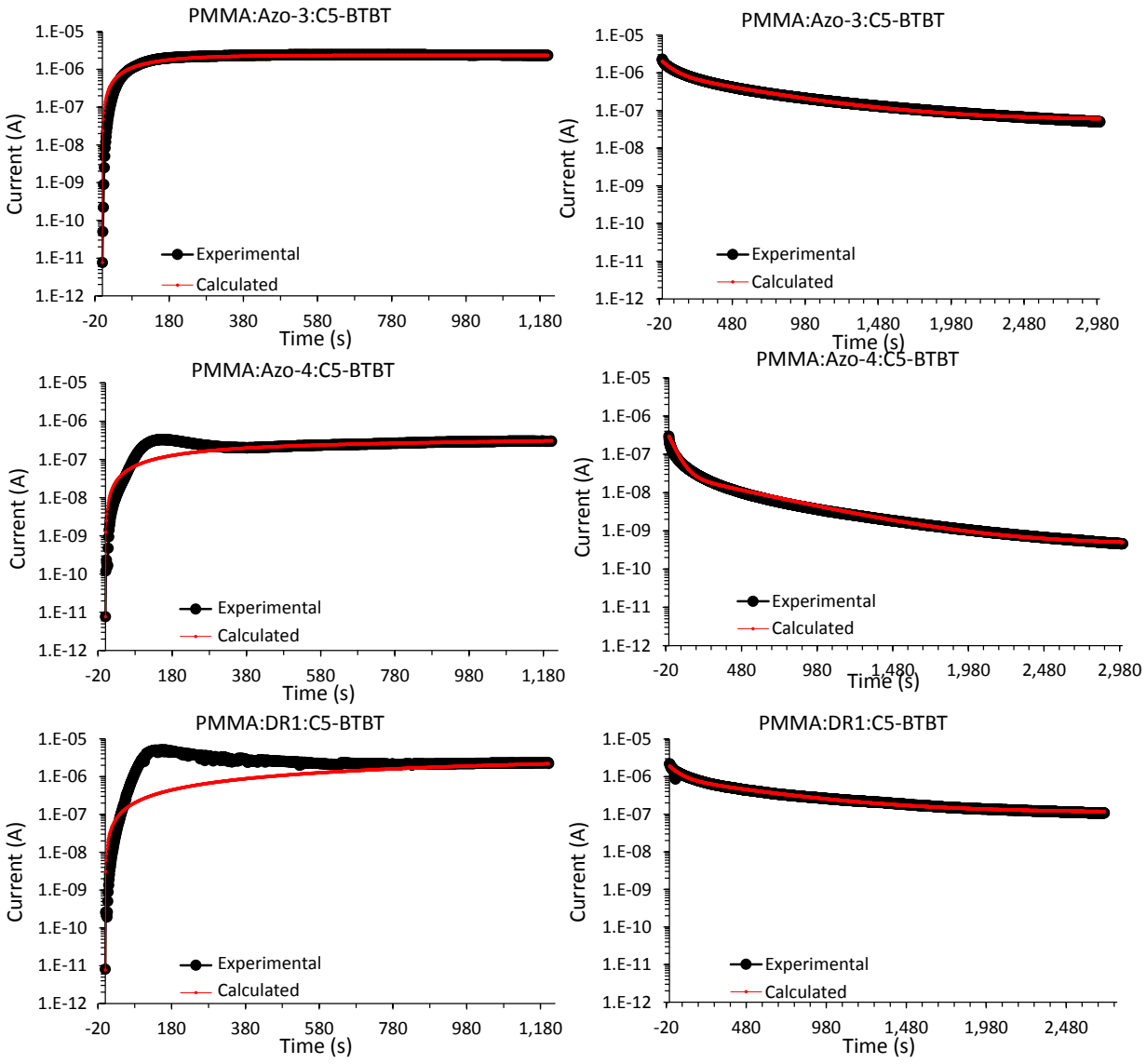

Figure S5.7: (Left side), I_{DS} vs time showing the current rise over a 20 minute UV exposure with the experimental (black) and biexponential curve fitting (red). (Right) I_{DS} decay vs time starting after the 20 minute UV exposure with experimental (black) and biexponential curve fitting (red).

5.9 References

1. Sirringhaus, H. 25th anniversary article: Organic field-effect transistors: The path beyond amorphous silicon. *Adv. Mater.* **26,** 1319–1335 (2014).

2. Yu, H., Bao, Z. & Oh, J. H. High-performance phototransistors based on single-crystalline n-channel organic nanowires and photogenerated charge-carrier behaviors. *Adv. Funct. Mater.* **23,** 629–639 (2013).

3. Hwang, H. *et al.* Organic phototransistors with nanoscale phase-separated polymer/polymer bulk heterojunction layers. *Nanoscale* **3,** 2275–2279 (2011).

4. Razeghi, M. & Rogalski, A. Semiconductor ultraviolet photodetectors. *J. Appl. Phys.* **79,** 7433–73 (1996).

5. Jandow, N. N., Hassan, H. A., Yam, F. K., Ibrahim, K. & Gateva, S. in *Photodetectors* 3–32 (2009).

6. Chai, G., Lupan, O., Chow, L. & Heinrich, H. Crossed zinc oxide nanorods for ultraviolet radiation detection. *Sensor. Actuat. A-Phys.* **150,** 184–187 (2009).

7. Zhang, F., Ding, Y., Zhang, Y., Zhang, X. & Wang, Z. L. Piezo-phototronic Effect Enhanced Visible and Ultraviolet Photodetection Using a ZnO-CdS Core-Shell Micro/nanowire. *ACS Nano* **6,** 9229–9236 (2012).

8. Das, S. N. *et al.* ZnO single nanowire-based UV detectors. *Appl. Phys. Lett.* **97,** 02213 (2010).

9. Chaaya, A. A., Bechelany, M., Balme, S. & Miele, P. ZnO 1D nanostructures designed by combining atomic layer deposition and electrospinning for UV sensor applications. *J. Mater. Chem. A* **2,** 20650–20658 (2014).

10. Raimondo, C. *et al.* Optically switchable organic field-effect transistors based on photoresponsive gold nanoparticles blended with poly(3-hexylthiophene). *PNAS* **109,** 12375–80 (2012).

11. Shen, Q. *et al.* Reversible photomodulation of organic transistor performance by conformation-induced capacitive coupling. *Acta Phys - Chim Sin* **26,** 1941–1946 (2010).

12. Orgiu, E. *et al.* Optically switchable transistor via energy-level phototuning in a bicomponent organic semiconductor. *Nat. Chem.* **4,** 675–9 (2012).

13. Frisch, J. *et al.* Photoinduced reversible changes in the electronic structure of photochromic diarylethene films. *Appl. Phys. A* **113,** 1–4 (2013).

14. Gemayel, M. El *et al.* Optically switchable transistors by simple incorporation of photochromic systems into small-molecule semiconducting matrices. *Nat. Commun.* **6,** 6330 (2015).

15. Sayago, J., Rosei, F. & Santato, C. Organic photonics: Blending organic building blocks. *Nat. Photonics* **6,** 639–640 (2012).

16. Hayakawa, R., Higashiguchi, K., Matsuda, K., Chikyow, T. & Wakayama, Y. Optically and electrically driven organic thin film transistors with diarylethene photochromic channel layers. *ACS Appl. Mater. Interfaces* **5,** 3625–30 (2013).

17. Noh, Y. Y. *et al.* High-photosensitivity p-channel organic phototransistors based on a biphenyl end-capped fused bithiophene oligomer. *Appl. Phys. Lett.* **86,** 043501 (2005).

18. Liu, X. *et al.* Flexible, low-voltage and high-performance polymer thin-film transistors and their application in photo/thermal detectors. *Adv. Mater.* **26,** 3631–6 (2014).

19. Kronemeijer, A. J. *et al.* Two-dimensional carrier distribution in top-gate polymer field-effect transistors: Correlation between width of density of localized states and urbach energy. *Adv. Mater.* **26,** 728–733 (2014).

20. Ebata, H. *et al.* Highly soluble [1]benzothieno[3,2-b]benzothiophene (BTBT) derivatives for high-performance, solution-processed organic field-effect transistors. *J. Am. Chem. Soc.* **129,** 15732–15733 (2007).

21. Smithson, C. S., Wu, Y., Wigglesworth, T. & Zhu, S. A More Than Six Orders of Magnitude UV-Responsive Organic Field-Effect Transistor Utilizing a Benzothiophene Semiconductor and Disperse Red 1 for Enhanced Charge Separation. *Adv. Mater.* **27,** 228–233 (2015).

22. Wang, X. *et al.* Device physics of highly sensitive thin film polyfluorene copolymer organic phototransistors. *J. Appl. Phys.* **107,** 024509 (2010).

23. Pal, T., Arif, M. & Khondaker, S. I. High performance organic phototransistor based on regioregular poly(3-hexylthiophene). *Nanotechnology* **21,** 325201 (2010).

24. Chen, C.-C., Chiu, M.-Y., Sheu, J.-T. & Wei, K.-H. Photoresponses and memory effects in organic thin film transistors incorporating poly(3-hexylthiophene)/CdSe quantum dots. *Appl. Phys. Lett.* **92,** 143105 (2008).

25. Wang, W., Ma, D. & Gao, Q. Optical Programming/Electrical Erasing Memory Device Based on Low-Voltage Organic Thin-Film Transistor. *IEEE T. Electron Dev.* **59,** 1510–1513 (2012).

26. Horowitz, G. Organic Field-Effect Transistors. *Adv. Mater.* **10,** 365–377 (1998).

27. Egginger, M., Bauer, S., Schwödiauer, R., Neugebauer, H. & Sariciftci, N. S. Current versus gate voltage hysteresis in organic field effect transistors. *Monatsh. Chem.* **140,** 735–750 (2009).

28. Leijtens, T. *et al.* Hole Transport Materials with Low Glass Transition Temperatures and High Solubility for Application in Solid-State Dye-Sensitized Solar Cells. *ACS Nano* **6,** 1455–1462 (2012).

29. Djurovich, P. I., Mayo, E. I., Forrest, S. R. & Thompson, M. E. Measurement of the lowest unoccupied molecular orbital energies of molecular organic semiconductors. *Org Electron* **10,** 515–520 (2009).

30. Cardona, C. M., Li, W., Kaifer, A. E., Stockdale, D. & Bazan, G. C. Electrochemical considerations for determining absolute frontier orbital energy levels of conjugated polymers for solar cell applications. *Adv. Mater.* **23,** 2367–71 (2011).

31. Connelly, N. G. & Geiger, W. E. Chemical Redox Agents for Organometallic Chemistry. *Chem Rev.* **96,** 877–910 (1996).

32. Zhang, Y., Wang, X., Liu, Y., Song, S. & Liu, D. Highly transparent bulk PMMA/ZnO nanocomposites with bright visible luminescence and efficient UV-shielding capability. *J. Mater. Chem.* **22,** 11971 (2012).

33. Saito, M. *et al.* One-step synthesis of [1]benzothieno[3,2-b][1]benzothiophene from o-chlorobenzaldehyde. *Tetrahedron Lett.* **52,** 285–288 (2011).

Chapter 6

UV Response Time Manipulation Using Non Isomerizable Naphthalene and Anthracene Based Additives

6.1 DFT calculations

The success of the work utilizing azobenzene additives led us to investigate other materials that could have even more pronounced phototransistor affects when combined with C5-BTBT, specifically faster turn on times and longer memory retention times. To achieve this we focused our studies on materials that would not isomerize, were planar, soluble, and could be altered to have electron rich or deficient pendent groups. Naphthalene and anthracene derivatives were used as they fit all the above criteria.

Chapter 5's work showed that DFT calculations of molecular orbital (MO) energy levels can help predict how the additive will affect the system. **Fig. 6.1** provides a summary of the HOMO, LUMO and LUMO +1 energy levels of the studied materials. Position of the additives HOMO and LUMO compared to the UV sensitive C5-BTBT semiconductor are crucial to device performance. For sensing speeds, the elimination of charge traps is desired. A HOMO lower in energy than C5-BTBT, can help fill charge traps, increasing sensing speeds, while a HOMO higher than C5-BTBT will add traps, slowing sensing speeds. Once a UV photon is absorbed by C5-BTBT, it will excite an electron on C5-BTBT to an unoccupied MO. From there it can decay back down to its HOMO, causing hole pair charge recombination, or through π-π-orbital overlap, can hop onto an empty equal or lower lying LUMO of the additive. The LUMO of this

additive can either extend or decrease the lifetime of electron hole recombination depending on how strongly it can stabilize the electron. Therefore, the additives LUMO and electron affinity affect how long the device remains in its high conductivity state.

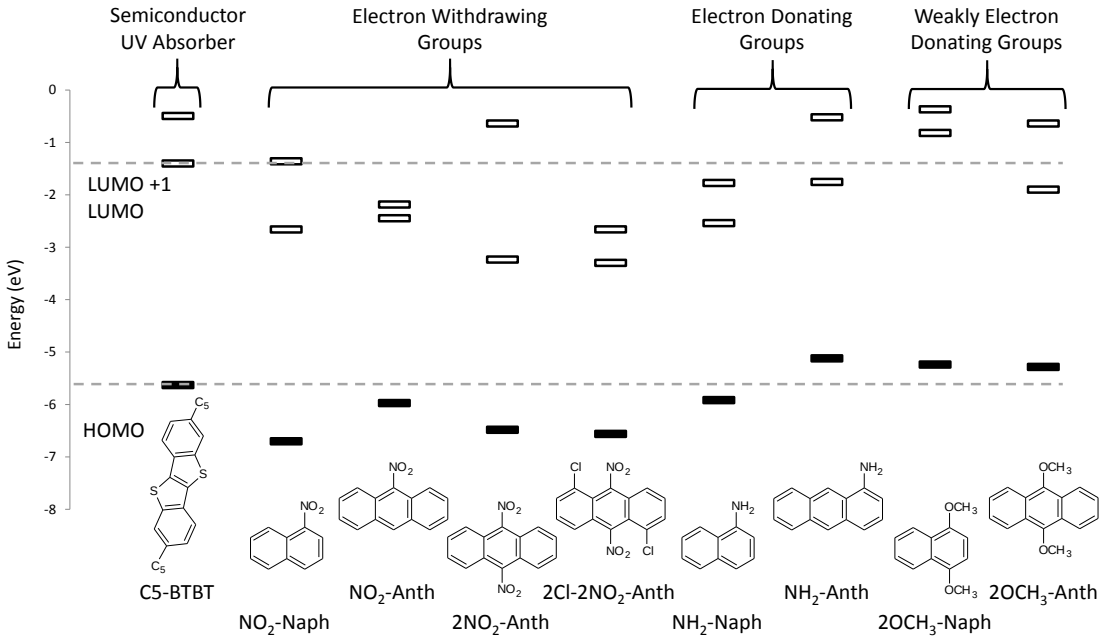

Figure 6.1: DFT calculations of the HOMO (solid boxes), LUMO and LUMO +1 (open boxes) energy levels calculated at the BY3LYP 6-311 G(d,p) level for the materials used in the semiconductive layer. Grey dashed lines have been added to guide the eye to track the HOMO and LUMO energy levels of C5-BTBT vs the additives.

6.2 Results / discussion

6.2.1 Transfer curves

OFET devices were spin coated from a solution of additive, PMMA and C5-BTBT. Optical microscopy images of the films show they are of similar morphology and UV-Vis shows all samples absorb somewhere between 465-345 nm. **Fig. 6.2** provides transfer curves for all the systems studied in dark conditions and under UV irradiation. By comparing systems to the PMMA:C5-BTBT control, we see the effects of each additive, with a major effect being the introduction or removal of charge traps. In a p-type semiconductor, a trap is a material with a filled MO able to donate electrons to holes in the valance band, preventing conduction, while not taking part in hole conduction itself. As expected additives with a HOMO level higher in energy than C5-BTBT (**NH_2-Anth**, **2OCH_3-Naph**, **2OCH_3-Anth**), introduced additional traps into the system, shifting the V_{Th} to more negative values. Despite **NH_2-Naph's**, HOMO being just below that of C5-BTBT we observe a small negative V_{Th} shift of -6 V which could be a result of the imprecision of DFT calculations. All additives with a HOMO lower in energy than C5-BTBT, showed a V_{Th} shift in the positive direction indicating the filling of charge traps.> When under UV illumination, all the systems show a large V_{Th} shift, with the ΔV_{Th} being 3-5 times larger than the control, indicating there is an increased number of sustained charge carriers.

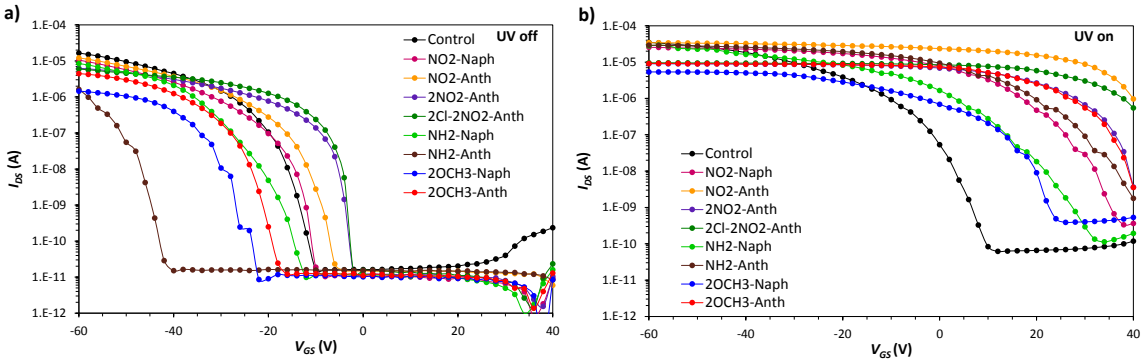

Figure 6.2: Transfer curves for the studied systems in (*a*) dark conditions and (*b*) under UV illumination.

All devices showed increased P_{ill} and R at a V_{GS} = 0 V with results summarized in **Table 6.1**. The highest values are obtained for additives containing electron accepting groups, which are expected to trap photogenerated electrons the longest, preventing recombination, resulting in a higher photocurrent. **NO_2-Anth** showed the greatest increase in P_{ill} of $1.6*10^6$ which is 3 orders of magnitude greater than the control and the highest R value of 7.8 A/W. However as we will see in chpt. 8, these devices are being measured at a saturation R value.

6.2.2 UV response times

Device speeds are very important and were measured for illumination (sensing). Unfortunately each of our tested systems reached a different saturation value, which made evaluating response times difficult. For this reason, we chose to characterize the sensing speed by taking the time required to reach 20% of the maximum photocurrent because this value is high enough to unambiguously

determine between the off and on state (**Fig. 6.3**). The devices showed a fast initial increase in photocurrent, followed by a slow increase which has been observed many times in the literature[2,3] and is similar to our previous work. All devices had faster sensing speeds than the 110 s control time, with the two fastest **NO_2-Anth** and **2NO_2-2Cl-Anth** being 8.8 and 1.6 s respectively (**Table 6.1**). The fastest sensing times for these systems can be attributed to both their trap filling characteristics as well as the easily accessible LUMO and LUMO+1 located well below that of C5-BTBT.

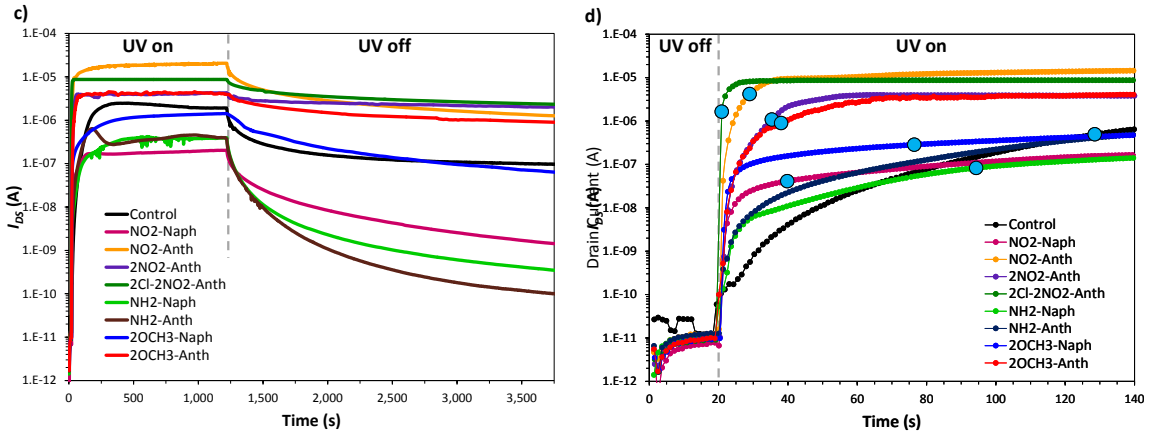

Figure 6.3: (*a*) I_{DS} response at V_{GS} = 0 V during a 20 min irradiation and the 40 min after UV light was removed. (*b*) zoom in of the first 2 min of (*a*) with the 20% of saturation marked with a round blue marker.

Table 6.1

Electrical characterization parameters of the systems studied at a P_{inc} = 3.8 mWcm^{-2} and V_{DS} = -60 V

	V_{Th} (V)					Time to reach 20% saturation value (s)		
Sample	**UV off**	**UV on**	**ΔV_{Th} (V)**	***P_{ill}***	**R (A/W)**	**UV on (rise)**	**UV off (decay)**	**Reset V_{GS} (V)**
Control	-17	-3	14	$3.3*10^3$	0.02	110.2	108	-55
NO_2-Naph	-17	28	45	$7.3*10^5$	2.6	19.7	151	-35
NO_2-Anth	-13	46	59	$1.6*10^6$	7.8	8.8	392	-60
$2NO_2$-Anth	-2	40	42	$5.7*10^5$	2.3	15.0	>2400	-75
$2Cl_2$-$2NO_2$-Anth	-1	49	50	$5.5*10^5$	2.8	1.6	>2400	-90
NH_2-Naph	-24	16	40	$1.4*10^5$	0.54	75.4	55	-25
NH_2-Anth	-44	30	74	$6.1*10^5$	3.0	59.3	239	-40
2**OCH_3-Naph**	-27	20	47	$6.8*10^5$	0.23	56.1	373	-35
$2OCH_3$-Anth	-23	39	62	$6.6*10^5$	2.4	19.1	> 2400	-70

Relaxation lifetimes are dependent on how fast charge recombination of an electron hole pair occurs. **Table 1** summarizes how long each system takes to decay to 20% of its saturation value. Only **NH_2-Naph** has a faster decay rate (55s) than the control system 108 s, which can be attributed to its 2 MO's lower in energy than C5-BTBT combined with the poor electron stabilization of

naphthalene and the electron donating amino group. Meanwhile the stronger electron stabilizing anthracene systems showed longer decay rates, with both **NO_2-Anth** and **2Cl-2NO_2-Anth** which have 2 MO's below that of C5-BTBT having decay rates greater than 2400s. The strong electron accepting nature of the pendent groups helps extend the lifetime of the photocurrent by preventing electron hole recombination. The decay rates are too slow for use in sensors, but show promise for memory based devices.

6.2.3 V_{GS} reset

As can be seen by **Fig 6.3 (*a*)**, all devices show a persistent photocurrent, which is caused by the maintained separation of electron hole pairs generated from the UV source. A large enough negative gate bias is able to force trapped electrons to be released allowing for the recombination of electron hole pairs, returning the system to its initial low condition off state. This ability to reset the system through a gate bias offers advanced functionality for devices. By illuminating each device for 20 sec, followed by the application of a gate voltage, we were able to determine how strong of a negative bias is required to return each system to its off state (**Fig. 6.4)**. As expected the additive with electron donating groups required a gate voltage lower than the control of -55 V, with the **NH_2-Naph** group resetting at -25 V. Meanwhile, additives with electron accepting groups required much stronger biases, with the **2Cl-2NO_2-Anth** system having the strongest at -90 V. The **NO_2-Naph** system is an anomaly that we believe is caused by a

decreased electron stabilization of the less conjugated naphthalene system vs anthracene.

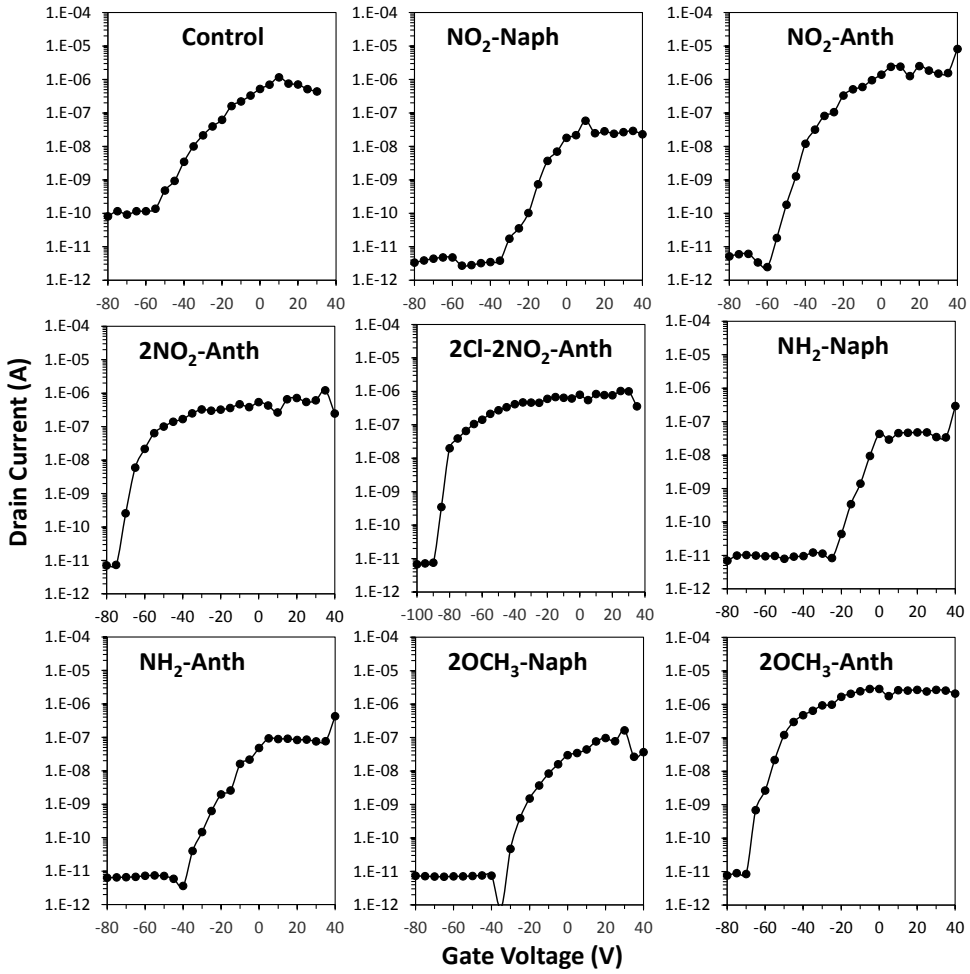

Figure 6.4: Drain current after being exposed to a 30 second UV exposure, followed by the corresponding gate voltage. All data points were recorded at a V_{GS} = 0 V after the corresponding V_{GS} of the data point was applied for 2 seconds.

6.3 Conclusion

The above additives contained either electron donating or accepting groups, expected to increase UV decay rates or extend them respectively. We see this trend most strongly displayed in the systems that through DFT calculations have both a LUMO and LUMO+1 lower in energy than C5-BTBT. With the increased number of MO's available, the chances a UV excited electron could decay onto the additive were increased. From that point, the electron donating or accepting properties of the additive impacted how long the photocurrent could be maintained after the UV stimulus was removed. The V_{GS} required to return the system to its ground state corresponded well to the lifetime of the persistent photocurrent, with the **NO_2-Anth** and **2Cl-2NO_2-Anth** systems showing the longest lifetimes, and **NH_2-Naph** the shortest.

6.4 Experimental / additional characterization

6.4.1 Materials

The following materials were purchased from Sigma Aldrich, 1-naphthylamine (≥ 99%) (**NH_2-Naph**), 4—aminoanthracene (90%) (**NH_2-Anth**), 1,4-dimethoxynaphthalene (97%) (**OCH_3-Naph**), 9,10-dimethoxy-anthracene (**2OCH_3-Anth**), 9-nitroanthracene (93%) (**NO_2-Anth**), 9,10-dinitro-anthracene (98%) (**2NO_2-Anth**), 1,5-dichloro-9,10-dinitro-anthracene (**2Cl-2NO_2-Anth**), PMMA (M_N =140,000), reagent grade isopropanol, toluene and 1,1,2,2-tetrachloroethane (TCE). (**NO_2-Anth**) was re-crystallized from ethyl acetate.

(**NH_2-Anth**) were dissolved in ethyl acetate and filtered to remove impurities, the solvent was then removed using a rotary evaporator. These samples were then dried 60°C under vacuum overnight. All other samples were used as received. C5-BTBT was prepared using the methods described in chapters 4 and 5. Sample preparation and testing equipment is the same as chapter 5.

6.4.2 UV-Vis sample preparation / measurements

The same procedures of chapter 5 were used but concentrations from **Table 6.2**.

Table 6.2

Materials used to prepare solutions for spin coating[a)]

Sample[b)]	Mass (mg)	mmoles	PMMA (mg)	C5-BTBT (mg)[c)]	TCE (g)
Control	4.0	0.0133	36.0	40.0	3.92
NO_2-Naph	2.3	0.0133	37.7	40.0	3.92
NO_2-Anth	3.0	0.0133	37.0	40.0	3.92
2NO_2-Anth	2.0	0.0133	38.0	40.0	3.92
2Cl_2-2NO_2-Anth	4.5	0.0133	35.5	40.0	3.92
NH_2-Naph	1.9	0.0133	38.1	40.0	3.92
NH_2-Anth	2.6	0.0133	37.4	40.0	3.92
2**OCH_3-Naph**	2.5	0.0133	37.5	40.0	3.92
2OCH_3-Anth	3.2	0.0133	36.8	40.0	3.92

b) *All solutions were passed through a 45 µm filter before use*

c) *The solutions used for UV-vis were the same composition except no C5-BTBT was added and its weight was replaced by an equivalent weight of TCE.*

6.4.3 Electrical measurements

See **Table 6.3** for additional electrical characterization

Table 6.3

Additional electrical characterization

	Mobility ($cm^2/V \cdot s$)		On/off ratio		V_{Th} (V)		
	UV off	**UV on**	**UV off**	**UV on**	**UV off**	**UV on**	**ΔN***
Control	0.10	0.16	$1.0*10^6$	$5.6*10^5$	-17	-3	$1.87*10^{12}$
NO_2-Naph	0.08	0.13	$3.1*10^7$	$1.2*10^5$	-17	28	$4.19*10^{12}$
NO_2-Anth	0.06	0.42	$7.9*10^5$	$3.6*10^1$	-13	46	$5.50*10^{12}$
2NO_2-Anth	0.03	0.08	$5.0*10^7$	$4.1*10^4$	-2	-40	$3.99*10^{12}$
2Cl_2-2NO_2-Anth	0.05	0.11	$2.3*10^7$	$5.5*10^2$	-1	49	$4.69*10^{12}$
NH_2-Naph	0.09	0.08	$6.8*10^5$	$2.6*10^5$	-24	16	$3.72*10^{12}$
NH_2-Anth	0.03	0.13	$9.9*10^4$	$1.6*10^4$	-44	30	$7.68*10^{12}$
2**OCH_3-Naph**	0.03	0.02	$3.0*10^7$	$7.7*10^5$	-27	20	$4.35*10^{12}$
2OCH_3-Anth	0.05	0.08	$9.6*10^7$	$4.0*10^4$	-23	39	$5.83*10^{12}$

6.4.4 Optical microscopy measurements

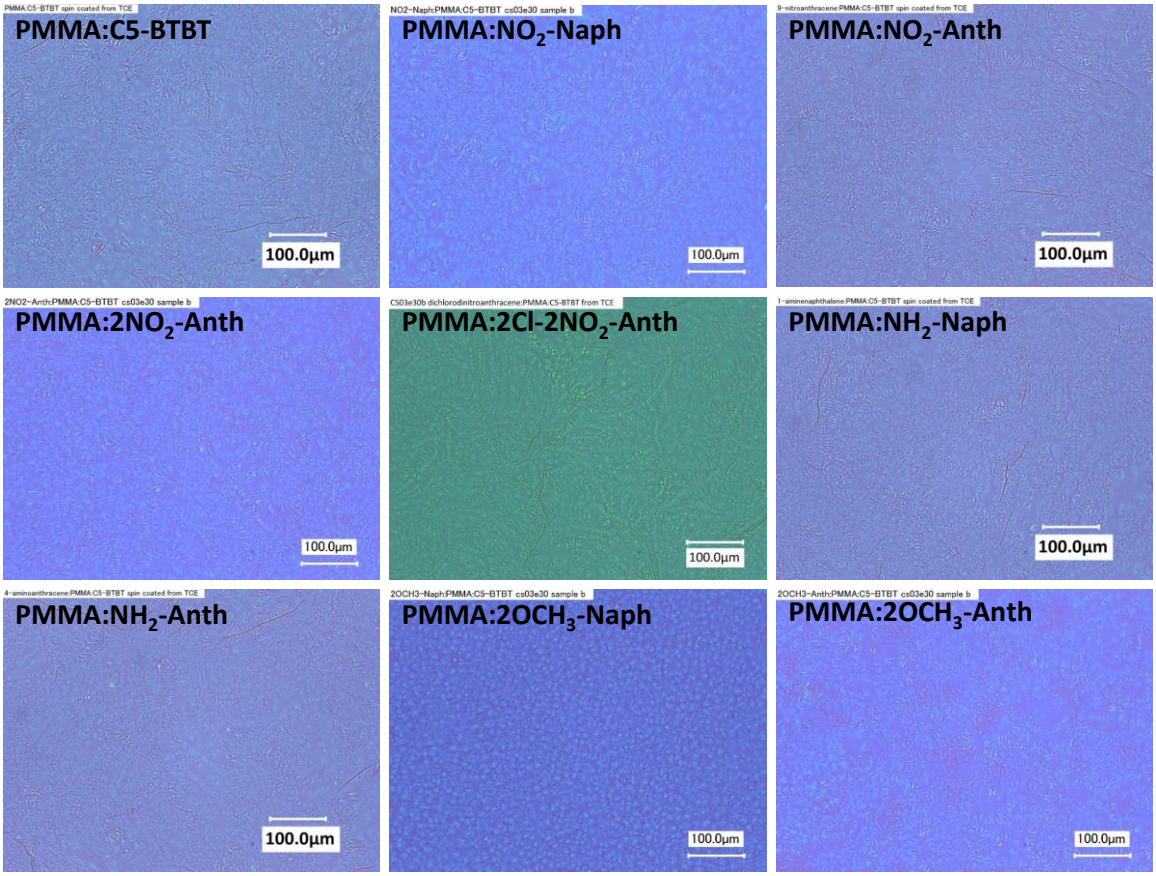

Figure 6.5: Optical Microscope image of films spin coated from 1,1,2,2-tetrachlorethane onto an HMDS modified Si/SiO2 wafer, scale bar is 100µm.

6.4.5 UV-Vis measurements

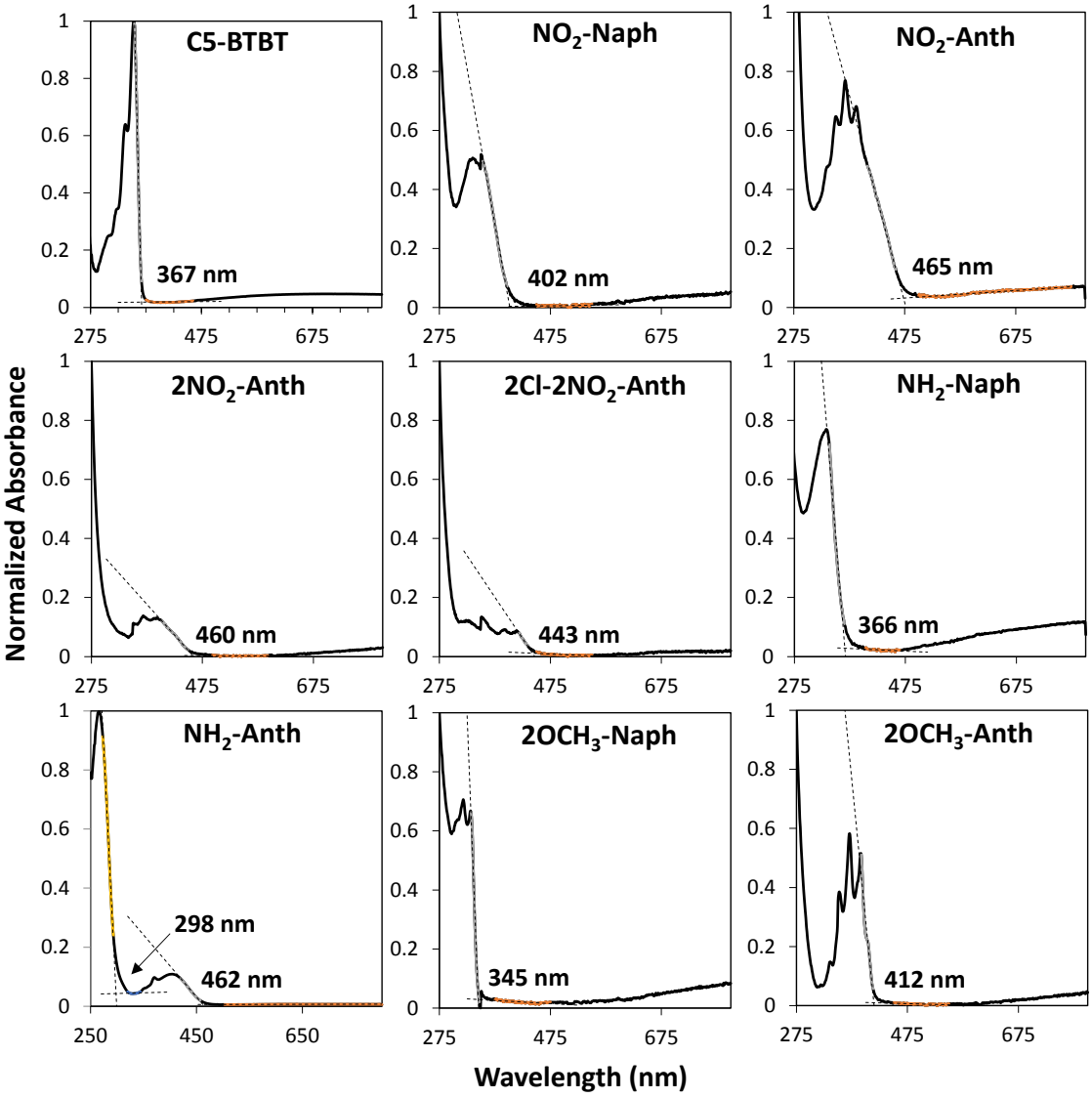

Figure 6.6: Thin film UV vis with the absorbance onset labelled.

6.5 References

1. Wang, X. *et al.* Device physics of highly sensitive thin film polyfluorene copolymer organic phototransistors. *J. Appl. Phys.* **107,** 024509 (2010).

2. Cho, M. Y. *et al.* Highly sensitive, photocontrolled, organic thin-film transistors using soluble star-shaped conjugated molecules. *Adv. Funct. Mater.* **18,** 2905–2912 (2008).

3. Gedamu, D. *et al.* Rapid fabrication technique for interpenetrated ZnO nanotetrapod networks for fast UV sensors. *Adv. Mater.* **26,** 1541–50 (2014).

Chapter 7

Rapid UV-A Photo Detection, Using a BTBT Organic Field Effect Transistor Enhanced by a 1,5-dichlor-9,10-dintiro-anthracene Additive

This chapter is a reproduction of the following article submitted for publication on July 21, 2015 to Applied Physics Letters. The major contribution of this chapter is that having understood the effects of the HOMO/LUMO and electron accepting nature of small molecule additives from chapters 5 and 6, we chose the strongest performing system and explored its UV phototransistor properties in more depth.

"**Rapid UV-A Photo Detection, Using a BTBT Organic Field Effect Transistor Enhanced by a 1,5-dichlor-9,10-dintiro-anthracene Additive"**

Chad S. Smithson, Darko Ljubic, Yiliang Wu, and Shiping Zhu;

7.1 Abstract

Using the organic thin-film transistor architecture, a UV-A sensitive phototransistor was produced using an organic semiconductor 2,7-dipentyl[1]benzothieno[3,2- *b*][1] benzothiophene (C5-BTBT) and a strong electron accepting, non-photoisomerization additive 1,5-dichloro-9,10-dintiro-anthracene (2Cl-2NO_2-Anth). At 0 gate bias the photoresponsivity of the device begins to saturate at a P_{inc} = 1 mW/cm^2, where a photo to dark current ratio of $P_{ill} > 10^5$ is observed with a photoresponsivity of 9 A/W. The photoresponsivity was increased with the decrease of P_{inc}, reaching 40 A/W at a P_{inc} = 0.0427 mW/cm^2. A persistent photocurrent with a $P_{ill} > 10^5$ was observed for greater than 2 hours, demonstrating

the potential use for rewritable photo memory. We also showed that by applying a V_{GS} program consisting of a reset pulse of -90 V every 2nd data point, the device can perform as a UV sensor or switch, acting on the timescale of 600 ms.

7.2 Start of paper

The production of advanced electronic materials will always prove to have value for future devices.[1] Amongst these materials, photosensitive devices are able to produce incredible technologies ranging from solar cells to artificial eye detection.[2] The phototransistors, a device where the incident light modulates the charge carrier density within the channel[3] producing a photocurrent, offers a variety of advanced designs including optical sensors, optical memory, and optical switches, all of which present exciting opportunities for future technology integration.[4,5] Research attention using phototransistors has been focused on utilizing visible light, while other parts of the electromagnetic spectrum are largely ignored. Sensors able to detect Ultra Violet (UV) light, ranging from 100 – 400 nm have many applications including, air quality monitoring, environment monitoring, bio-medical instrumentation, space communications and research, high temperature flame detection, and plasma research[6,7,8] as well as optical memory,[9,10] and optical switching devices[11]. All of these technologies can be implemented using the three terminal Thin-Film Transistor (TFT) architecture, which can reduce noise and amplify electrical signals giving it a distinct advantage over diode devices.[1]

Although silicon based technology remains the dominate force in the field, more robust and adaptable UV based devices are emerging. Current research for UV sensing typically uses wide band-gap metal oxide semiconductors such as ZnO films and nanowires,[12,13,14,15,16,17,18,19] as well as other inorganic materials such as GaN, ZnSe, and AlGaN.[20] There are select examples of organic phototransistors with the most prominent being azobenzene[21,22] spiropyran,[23] furylfulgid and diarylethene[24,25,26,27,28], which are all able to isomerize in the solid state.[29] Other interesting devices such as Au-nanoparticles coated with azobenzene derivatives have been used as photoswitchs.[30] The mechanism for the generation of photocurrent differ among devices. Spiropyran, diarythethylene and azobenzene adjust their HOMO/LUMO energy levels through isomerization to better match the semiconductor HOMO or electrode work function. Meanwhile, ZnO nanowires react with O_2, trapping electrons allowing hole conductivity.

Two common figures of merit are used to characterize phototransistors and sensors. The first is the photocurrent/dark current ratio, which is the difference between the current measured in the dark and that under illumination, $P_{ill} = \frac{(I_{light} - I_{dark})}{I_{dark}}$, where I_{light} and I_{dark} are the drain source (I_{DS}) currents under UV illumination and in the dark respectively. The second is photoresponsivity, which determines how much light is absorbed compared to how much reaches the

device, $R = \frac{I_{light} - I_{dark}}{P_{inc} \cdot A}$, where P_{inc} is the irradiated lights incident power (W/cm^2) and A is the area of the channel (cm^2).[2] Amorphous silicon devices have an R value of 300 A/W, making a benchmark for organic materials to beat. In addition to these values, (1) air stability, (2) high sensitivity, (3) UV response speeds, (4) time required to return to the off state, and (5) ease of fabrication are important characteristics to be considered.

Using the 3 terminal device structure, we have created a UV-A sensitive phototransistor that performs well on all the above mentioned criteria. The device uses the photoactive 2,7-dipentyl[1]benzothieno[3,2- *b*][1] benzothiophene (**C5-BTBT**) semiconductor mixed with polymethyl methacrylate (PMMA) to form the semiconductor of a field effect transistor (**Fig. 7.1**). With the addition of a small amount of a strong electron accepting 1,5-dichloro-9,10-dintiro-anthracene (**2Cl-2NO$_2$-Anth**) compound, the photoresponse of the device was dramatically increased. The photoconductivity of this report has a similar mechanism to ZnO nanowires. The p-type UV sensitive semiconductor absorbed photon generates an exciton, which dissociates into free charges, an electron (e^-) and hole (p^+). Through the induced source drain electric field, p^+ are swept from the system while the e^- remains trapped in the film, generating a persistent photocurrent.[31,4,22,32]

The semiconductor by solids consisted of 5 mol% **2Cl-2NO$_2$-Anth** with respect to **C5-BTBT**. PMMA was then added to make up the difference in weight so there was an equal wt% C5-BTBT vs PMMA and **2Cl-2NO$_2$-Anth** combined. The solids were dissolved in 1,1,2,2-tetrachloroethane to form a 1.0 wt% solution. Bottom-gate, top-contact thin-film transistors were fabricated by spin coating the solution at 3000 RPM onto a Si wafer containing a 200 ± 10 nm SiO_2 dielectric layer modified with a monolayer of hexamethyldisilazane (HMDS). Gold electrodes were evaporated through a shadow mask, generating devices with a length and width of 85 ± 5 and 950 ± 10 μm, respectively. Electrical characterization was performed under ambient conditions using a Keithly SCS 4200, at a V_{DS} = -60 V. A Black-Ray B-100AP High-Intensity UV Inspection Lamp with a 365 nm bulb was used for UV irradiation at various intensity which was measured with a Vernier UV-A sensor.

Measurements were initially taken at a high P_{inc} = 3.8 mW/cm^2, to obtain data under UV saturation conditions. Transfer and output curves for the device can be found in **Fig. 7.1**. From the transfer curve, we observe a V_{Th} of -24 V. This V_{th} is shifted to much higher values >100 V, under UV illumination, a direct result of the photogenerated current. Little hysteresis exists under dark conditions, but a strong hysteresis is seen under UV illumination. This is a result of the strong negative bias, causing charge recombination. Measuring the device at a V_{GS} = 0 V, we observe a large P_{ill} = 5.5*10^5, with an R = 2.8 A/W. The low R value is a

result of measuring the device under saturation conditions, and as seen further in this report increases at lower UV intensities. Comparing this to the literature, on average, devices have an R value in the range 10^{-1} – 10^{1} A/W.[33] ZnO nanowires have pushed this value to 10^{6} A/W, but at the trade-off of $P_{ill} < 10^{1}$.[19] The output curves under dark conditions shows typical p-type FET behavior.

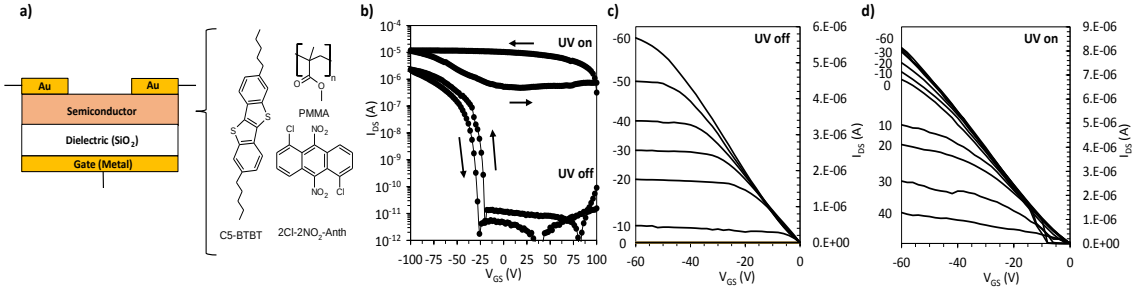

Figure 7.1: (*a*) Bottom gate top contact TFT device structure, and the materials used to make up the semiconductor layer. (*b*) Transfer curves for the studied systems in the dark and under UV illumination. Output curves for the device in (*c*) the dark and (*d*) under UV illumination.

The sensitivity of the device was tested by varying the UV light intensities in the range 0.043 to 3.8 mW/cm^2 (**Fig. 7.2**). A progressive shift of V_{th} can be observed, where the device reaches saturation at 1.07 mW/cm^2. This saturation becomes more evident when looking at a plot of P_{ill} vs P_{inc} (**Fig. 7.2 (*b*)**, red curve). Below this saturation value, a curve can be fit with the equation $P_{ill} = 8*10^5(P_{inc})^{0.52}$ which can be simplified to $P_{ill} = 8*10^5(P_{inc})^{1/2.}$ Above 1 mW/cm^2 P_{ill} plateaus for all higher intensities, showing this to be the saturation of photocurrent. Plotting R vs P_{inc} below 1 mW/cm^2, shows the relationship R =

$9.3(P_{inc})^{-1/2}$ suggesting the R is inversely proportional to the square root of P_{inc}. At saturation R = 9.02 A/W. As the light intensity exceeds saturation, we see a deviation from linearity, colored in blue, fitted by the equation $R = 9.6(P_{inc})^{-0.96}$, which is approximately $R = 9.6/P_{inc}$ implying an inverse relationship between intensity and photoresponsivity. This change from an inverse square root relationship to an inverse relationship can be attributed to the fact that after saturation generated charge carriers will combine almost immediately as they cannot be sustained as a persistent photocurrent.

Literature UV sensing speeds cover many orders of magnitude from nanoseconds to minutes,[7,34,33,19]. Often the increase in response speeds comes at the price of decreased R, P_{ill} or difficult device fabrication. This device shows a fast initial increase in photocurrent, followed by a slow increase which has been observed many times in the literature.[35,36] UV response times under various P_{inc}, were measured and evaluated by how long it took the device to reach an $I_{DS} = 10^{-6}$ A given by the red dashed line in **Fig. 7.2 (c)**. A plot of these response time vs P_{inc} is provided, showing that after the device reaches saturation, response times plateau at ~ 1.6 s. Below saturation, the response time can be fitted to the following equation, $t_{response} = 18/\exp(2P_{inc})$. The decay speed appears to be independent of P_{inc}. Therefore below the saturation intensity of P_{inc} = 1 mW/cm^2, there is a tradeoff between response time P_{ill} and R.

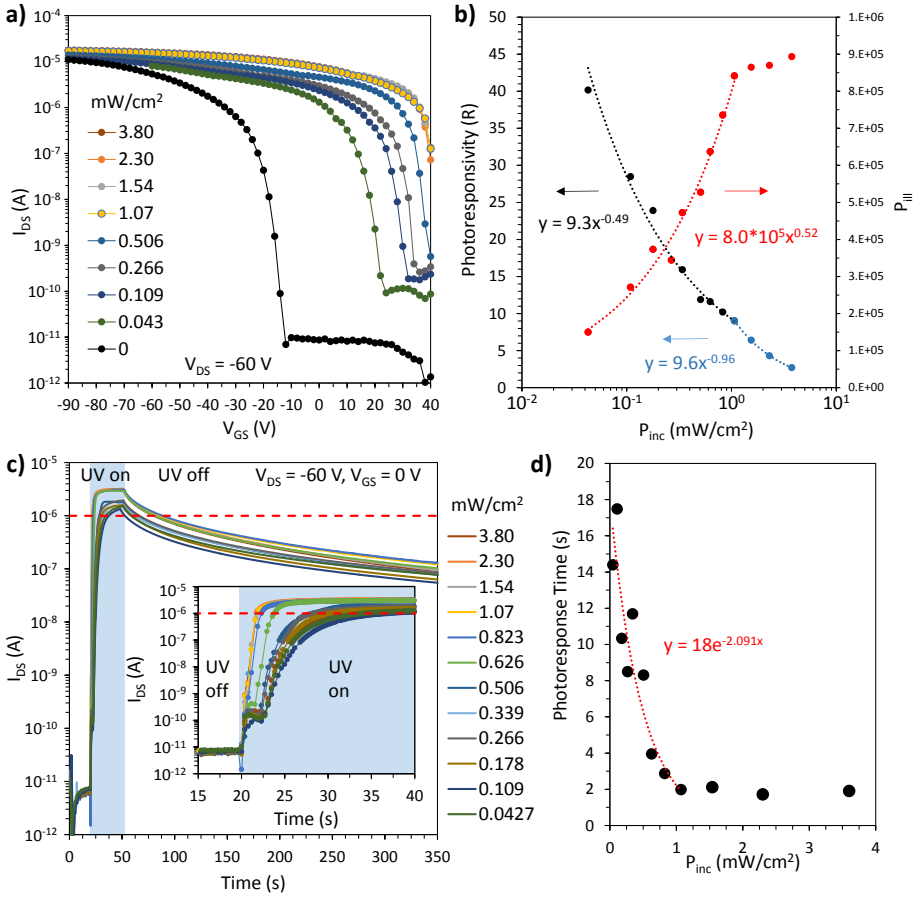

Figure 7.2: (*a*) Transfer curves of the 2Cl-2NO$_2$-Anth system under varying UV intensities. (*b*) photoresisitivity (*R*) as a function of P_{inc} with fitting below (black) and above (blue) P_{inc} saturation and P_{ill} (red) below P_{inc} saturation. Note some data are omitted in (*a*) for viewing clarity. (*c*) I_{DS} response at V_{GS} = 0 V during a 30 second irradiation followed by 5 min with the UV light removed. The inset is the first 20 seconds of irradiation. A red dashed line has been added at 10^{-6} A which was used as the device "on" value. (*d*) Response time of the device to reach 10^{-6} A, vs P_{inc}.

Because **2Cl-NO$_2$-Anth** aids in maintaining e^-/p^+ separation, dispersion **of 2Cl-2NO$_2$-Anth** plays an important role in device fabrication. We did not optimize dispersion in this report as our intention in the future is to do this by generating a copolymer. However, we did observe some examples where the device showed very exceptional behavior. **Fig. 7.3** is an example where the devices' persistent photocurrent allowed for a P_{ill} retention well about 10^5 for 2 hours after the UV source was removed. This demonstrates that with proper fabrication, a photo memory device can be generated.

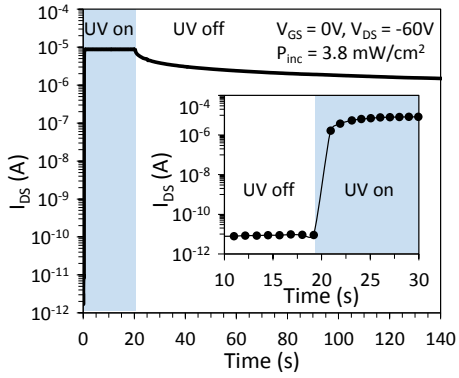

Figure 7.3: I_{DS} response curve with respect to time for a good performing devices, the inlay is a zoom in of the initial irradiation.

The persistent photocurrent of the devices allows for its use in organic memory, unfortunately, the long decay lifetime of all the tested devices makes them ineffective as sensors. However, they can be changed into sensors by applying a repeating reset to the devices. A measurement was taken every 300 msec (the limit of the measuring instrument) at a V_{GS} = 0 V and V_{DS}= -60 V. Every second

data point was a pulse at V_{GS} = -90 V which was found to be a strong enough negative gate bias to immediately return the system to the low current off state. All other data points were measured with a V_{GS} = 0 V. This makes every second measurement a fresh data set with the negative gate bias returning the system to its starting state. When analyzing the data, every second measurement can be ignored, providing a UV response plot on the timescale of 600 ms. From the response curves, we see that the device responds fast enough to provide an accurate data set. Two red dashed lines are added to the **Fig 7.4** to provide a definitive on (10^{-6} A) and off ($5*10^{-10}$ A) for the device. The fast UV response time combined with the ability to reset on command, provides the opportunity for this system to be used as a sensor or photoswitch.

We have generated a UV-A active phototransistor with a solution processable, air stable, semiconductive layer that requires no annealing. Unlike most literature organic UV phototransistors, this device does not employ isomerization to produce a UV photocurrent. The photocurrent saturates at P_{inc} = 1 mW/cm^2. Below this point, we observe $P_{ill} = 8*10^5 P_{inc}^2$, with a maximum of $9*10^5$ and $R = 9.3(P_{inc})^{-1/2}$ having a value of 9.02 A/W at saturation. Photoresponse speeds approximately follow the equation, $t_{response} = 18/\exp(2P_{inc})$, with a response time of ~ 1.6 s at photocurrent saturation. Devices were shown to be able to maintain a photocurrent with a $P_{ill} > 10^5$ for over 2 hours, providing opportunities for photomemory. We also demonstrated the slow decay time of the device can be

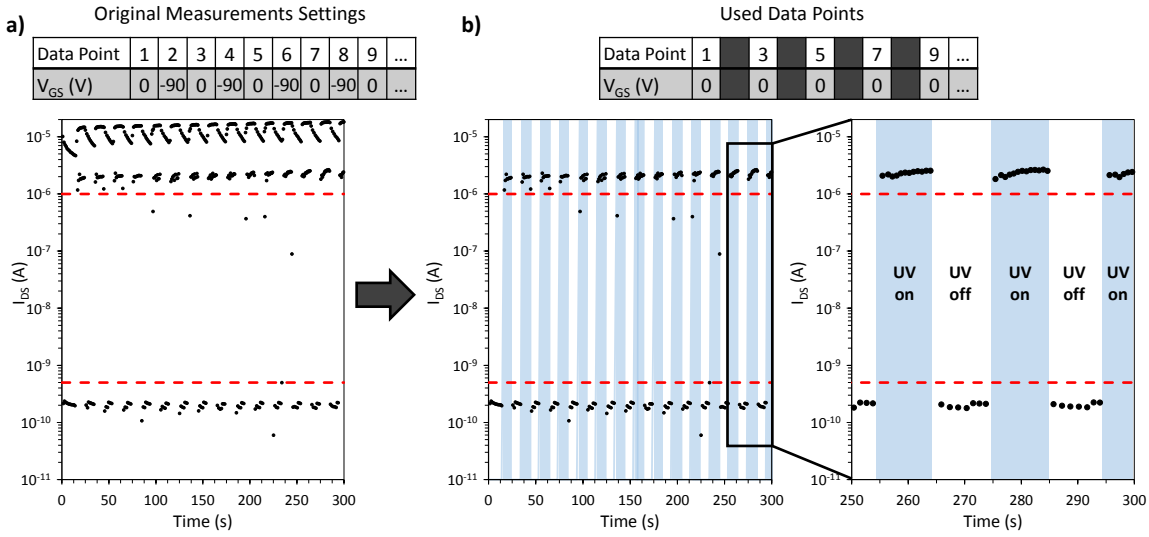

Figure 7.4: UV sensing measurements using the 2Cl-2NO$_2$-Anth system by resetting the system every second measurement with a V_{GS} = -90 V. The plotted data then ignores every second measurement to provide continuous UV sensing. (blue bars have been added to show when the UV light is on)

worked around by using a V_{GS} program to change the device into a photosensor. The ease of fabrication, and stability of this system, combined with literature comparable UV response times, P_{ill} and R values, makes it an exciting candidate for future UV based devices.

7.3 References

1. Wakayama, Y., Hayakawa, R. & Seo, H.-S. Recent progress in photoactive organic field-effect transistors. *Sci. Technol. Adv. Mat.* **15,** 024202 (2014).

2. Liu, X. *et al.* Flexible, low-voltage and high-performance polymer thin-film transistors and their application in photo/thermal detectors. *Adv. Mater.* **26,** 3631–3636 (2014).

3. Yu, H., Bao, Z. & Oh, J. H. High-performance phototransistors based on single-crystalline n-channel organic nanowires and photogenerated charge-carrier behaviors. *Adv. Funct. Mater.* **23,** 629–639 (2013).

4. Baeg, K. J., Binda, M., Natali, D., Caironi, M. & Noh, Y. Y. Organic light detectors: Photodiodes and phototransistors. *Adv. Mater.* **25,** 4267–4295 (2013).

5. Sirringhaus, H. 25th anniversary article: Organic field-effect transistors: The path beyond amorphous silicon. *Adv. Mater.* **26,** 1319–1335 (2014).

6. Shinde, S. S. & Rajpure, K. Y. Fabrication and performance of N-doped ZnO UV photoconductive detector. *J. Alloy Compd* **522,** 118–122 (2012).

7. Hassan, N. K., Hashim, M. R. & Allam, N. K. Low power UV photodetection characteristics of cross-linked ZnO nanorods/nanotetrapods grown on silicon chip. *Sensors Actuators, A Phys.* **192,** 124–129 (2013).

8. Panda, S. K. & Jacob, C. Preparation of transparent ZnO thin films and their application in UV sensor devices. *Solid. State. Electron.* **73,** 44–50 (2012).

9. Gu, M., Li, X. & Cao, Y. Optical storage arrays: a perspective for future big data storage. *Light Sci. Appl.* **3,** e177 (2014).

10. Ogawa, K. Two-Photon Absorbing Molecules as Potential Materials for 3D Optical Memory. *Appl. Sci.* **4,** 1–18 (2014).

11. Castet, F. *et al.* Design and characterization of molecular nonlinear optical switches. *Acc. Chem. Res.* **46,** 2656–2665 (2013).

12. Liu, X. *et al.* All-printable band-edge modulated ZnO nanowire photodetectors with ultra-high detectivity. *Nat. Commun.* **5,** 4007 (2014).

13. Bai, S. *et al.* High-performance integrated ZnO nanowire UV sensors on rigid and flexible substrates. *Adv. Funct. Mater.* **21,** 4464–4469 (2011).

14. Campos, L. C., Guimarães, M. H. D., Goncalves, a. M. B., De Oliveira, S. & Lacerda, R. G. ZnO UV photodetector with controllable quality factor and photosensitivity. *AIP Adv.* **3,** 0–6 (2013).

15. Das, S. N. *et al.* ZnO single nanowire-based UV detectors. *Appl. Phys. Lett.* **97,** 02213 (2010).

16. Chaaya, A. A., Bechelany, M., Balme, S. & Miele, P. ZnO 1D nanostructures designed by combining atomic layer deposition and electrospinning for UV sensor applications. *J. Mater. Chem. A* **2,** 20650–20658 (2014).

17. Humayun, Q., Kashif, M., Hashim, U. & Qurashi, A. Selective growth of ZnO nanorods on microgap electrodes and their applications in UV sensors. *Nanoscale Res. Lett.* **9,** 29 (2014).

18. Bian, X. *et al.* UV sensing using film bulk acoustic resonators based on Au/n-ZnO/piezoelectric-ZnO/Al structure. *Sci. Rep.* **5,** 9123 (2015).

19. Dhara, S. & Giri, P. Enhanced UV photosensitivity from rapid thermal annealed vertically aligned ZnO nanowires. *Nanoscale Res. Lett.* **6,** 504 (2011).

20. Chai, G., Lupan, O., Chow, L. & Heinrich, H. Crossed zinc oxide nanorods for ultraviolet radiation detection. *Sensors Actuators, A Phys.* **150,** 184–187 (2009).

21. Loucif-Saibi, R., Nakatani, K., Delaire, J. a, Dumont, M. & Sekkat, Z. Photoisomerization and Second Harmonic Generation in Disperse Red One-Doped and -Functionalized Poly(methy1 methacrylate) Films. *Chem. Mater.* **5,** 229–236 (1993).

22. Tseng, C.-W., Huang, D.-C. & Tao, Y.-T. Electric bistability induced by incorporating self-assembled monolayers/aggregated clusters of azobenzene derivatives in pentacene-based thin-film transistors. *ACS Appl. Mater. Interfaces* **4,** 5483–91 (2012).

23. Berkovic, G., Krongauz, V. & Weiss, V. Spiropyrans and Spirooxazines for Memories and Switches. *Chem. Rev.* **100,** 1741–1754 (2000).

24. Irie, M. Photochromism of diarylethene molecules and crystals. *Proc. Jpn. Acad. Ser. B. Phys. Biol. Sci.* **86,** 472–483 (2010).

25. Frisch, J. *et al.* Photoinduced reversible changes in the electronic structure of photochromic diarylethene films. *Appl. Phys. A* **113,** 1–4 (2013).

26. Hayakawa, R., Higashiguchi, K., Matsuda, K., Chikyow, T. & Wakayama, Y. Optically and electrically driven organic thin film transistors with diarylethene photochromic channel layers. *ACS Appl. Mater. Interfaces* **5,** 3625–30 (2013).

27. Orgiu, E. *et al.* Optically switchable transistor via energy-level phototuning in a bicomponent organic semiconductor. *Nat. Chem.* **4,** 675–9 (2012).

28. Gemayel, M. El *et al.* Optically switchable transistors by simple incorporation of photochromic systems into small-molecule semiconducting matrices. *Nat. Commun.* **6,** 6330 (2015).

29. Zhang, J., Zou, Q. & Tian, H. Photochromic materials: More than meets the eye. *Adv. Mater.* **25,** 378–399 (2013).

30. Raimondo, C. *et al.* Optically switchable organic field-effect transistors based on photoresponsive gold nanoparticles blended with poly(3-hexylthiophene). *PNAS* **109,** 12375–80 (2012).

31. Feng, C., Marinov, O., Deen, M. J., Selvaganapathy, P. R. & Wu, Y. Sensitivity of the threshold voltage of organic thin-film transistors to light and water. *J. Appl. Phys.* **117,** 185501 (2015).

32. Ji, Z. *et al.* Phototransistors and Photoswitches From an Ultraclosely <formula formulatype='inline'><tex Notation='TeX'> π</tex></formula>-Stacked Organic Semiconductor. *IEEE Electron Device Lett.* **33,** 1619–1621 (2012).

33. Liu, K., Sakurai, M. & Aono, M. ZnO-based ultraviolet photodetectors. *Sensors* **10,** 8604–34 (2010).

34. Gedamu, D. *et al.* Rapid fabrication technique for interpenetrated ZnO nanotetrapod networks for fast UV sensors. *Adv. Mater.* **26,** 1541–50 (2014).

35. Cho, M. Y. *et al.* Highly sensitive, photocontrolled, organic thin-film transistors using soluble star-shaped conjugated molecules. *Adv. Funct. Mater.* **18,** 2905–2912 (2008).

36. Gedamu, D. *et al.* Rapid fabrication technique for interpenetrated ZnO nanotetrapod networks for fast UV sensors. *Adv. Mater.* **26,** 1541–50 (2014).

Chapter 8

Conclusions and Future Work

8.1 Conclusions

The theme of this thesis was to utilize the OFET device design and alter the semiconductor layer by generating blends of materials. Through these blends, the features of two unique materials could be jointly utilized to enhance device performance. Two major device enhancements were studied, mobility enhancement utilizing unsorted SWCNT's, and photo-stimulation using the UV sensitive C5-BTBT. Some key conclusions regarding this research were reached and are as follows.

8.1.1 SWCNT research conclusions

Semiconductor enriched single walled carbon nanotubes are highly expensive and can only be fabricated on a milligram scale. In addition, solution processing of a pure SWCNT solution results in a film of CNT clusters reducing their mobility through CNT/CNT junctions. To bypass these two major problems, we explored if the DPP-QT semiconductive polymer mixed with unsorted SWCNTs which are a combination of 1/3 metallic, 2/3 semiconductive could enhance the mobility of the OFET device, while still producing well dispersed consistent films. Three commercial brands of SWCNT's were studied to which we found they could be dispersed within the DPP-QT polymer but catalysts and cleaning conditions used during CNT fabrication had a strong impact on their dispersion and overall mobility. The high aspect ratio of the semiconductive tubes and their near

ballistic mobility, did show an increase in overall device mobility approximately doubling it. However as the CNT concentration was increased, the negative effects of the *m*-SWCNT's became more apparent, reducing the device on off ratio until it was no longer feasible as a commercial device. The conclusion was that the addition of 2.0 wt% SWCNT from sigma Aldrich (CNT-A) which were produced by CCVD CoMoCAT® technique and cleaned by a HF (aq) wash produced the highest mobility while maintaining an on/off ratio > 10^5.

We then explored if unsorted SWCNT's could reduce the charge injection barrier from the source and drain into the semiconductor when different source/drain metals were used (Au, Cu, Al). Due to the mixture of CNT chirality's, there was a broad spread in the HOMO level of the SWCNT. This provided a pathway to help match the work function of the electrodes with that of the DPP-QT polymer. Au already had a good energy match with DPP-QT and no major effect was observed by the SWCNTs. Cu had moderate energy mismatch, resulting in a reduction by 1 order of magnitude, and Al which had the greatest energy mismatch had a reduction by 10^3 orders of magnitude. The conclusion to this was that due to the unsorted nature of the SWCNT's, their broad HOMO energy spectrum could be utilized to reduce the charge injection ratio of low cost metals, allowing for the use of these metals with semiconductive polymers that they would otherwise pair poorly with.

This research was very relevant to the industry, but it has become apparent that if SWCNT's are to become a major factor in printed electronics, they will need to be

sorted SWCNTs. We were not equipped to perform SWCNT sorting research and the pace of the research was so fast, that by the time we would be properly equipped, the industry research would have already eclipsed us. For this reason we moved on to other research involving blend technology.

8.1.2 Phototransistor research conclusions

During the research period of this thesis (3.5 years), the average mobility of organic materials surpassed the amorphous silicon (a-Si:H) threshold of 1 $cm^2V^{-1}s^{-2}$, with devices reaching as high as 47 $cm^2V^{-1}s^{-2}$. With this barrier breached, advanced functional OFET devices could be investigated. To this end, we performed an in depth study of the semiconductor C5-BTBT, which had been shown to have mobility values > 10 $cm^2V^{-1}s^{-2}$ and a sharp absorption at 354 nm (UV-A range), but no absorption in the visible range, making it visible blind. This made it an ideal candidate for phototransistor research. The general principle of a phototransistor is that an absorbed photon creates an exciton which can be separated into an e^-/p^+ pair through the electric field from the source drain. Our original device which was a 1:1 C5-BTBT/PMMA blend (PMMA generated even films and is UV-A and visible light blind), did demonstrate photoconductivity but at a slow rate with a poor maximum P_{ill} value. It was our belief that charge recombination was the major reason for this poor performance. Therefore if recombination could be controlled, we could enhance device performance. This was achieved by the addition of 5% of another small molecule. The HOMO and LUMO energy levels of these small molecules was investigated. Our results

showed that if the materials HOMO was higher in energy than that of C5-BTBT, it would act as a charge trap, further slowing the UV response of the device. Also if the LUMO was lower in energy, it could accept an e^-, allowing for better charge separation, resulting in faster illumination times and a higher P_{ill}. If the small molecule was electron deficient by containing groups such as NO_2 or Cl, it would act as an electron trap of an excited electron, allowing for the maintained separation of the e^-/p^- pair. This could be utilized as an electronic memory device. Meanwhile if the additive contained an electron rich group such as NH_2, it would allow for faster charge recombination, decreasing the time it took for the system to return to its low current off state when UV illumination was removed.

The best performing device was that containing the highly electron deficient additive **2Cl-2NO$_2$-Anth**. This was further investigated and found to have a high R value and P_{ill} even down to light intensities as low as 10^{-2} mW/cm^2. We demonstrated that the gate of the OFET could be utilized to force charge recombination, returning the system to its off state with a quick negative pulse, allowing for its use as both a memory device and sensor with sensitivity on the millisecond timescale. The potential of this system was demonstrated with this device, and our polymeric *p*-DR1:C5-BTBT system demonstrated that if the additive was part of the polymer binding matrix, its increased dispersion allows for even better device performance. To this end we conclude the research performed in this thesis, and now guide the reader to some future goals for this work.

8.2 Future Work

8.2.1 Building a more efficient system

We showed that by incorporating the additive onto the binding polymer matrix increases its dispersion within the film, allowing for increased interaction with the C5-BTBT semiconductor. Therefore we can improve the systems performance by reducing the number of materials used. To begin, the choice of polymer can be changed from PMMA to an electron deficient or electron rich polymer, provided it has the appropriate HOMO LUMO levels to interact correctly with C5-BTBT and remains blind to visible and UV light. This can generate a two-component semiconductor film allowing for increased interaction between C5-BTBT and the polymer. The start of this research has already been performed within our group displaying very promising results.[1]

The ideal system would consist of only one material. This could be generated by creating an A-B polymer of C5-BTBT and another material. The second material either being electron deficient or electron rich. The anthracene backbone used in this thesis offers an excellent starting point for this type of synthesis.

8.2.2 Altering the electronic nature of C5-BTBT

The phototransistor research of this thesis used only the C5-BTBT semiconductor which has a sharp absorbance at 354 nm making it sensitive to a very small band of electromagnetic radiation. This is useful for many purposes, but can the C5-BTBT structure be modified to shift its absorbance maximum. Countless

literature examples show that it should be possible be adding pendent groups to shift this absorbance maximum both higher and lower (**Fig 8.1**). In doing this, we can generate a series of transistors all utilizing the same fabrication techniques, but each using a different BTBT based semiconductor which has been tuned to a specific wavelength.

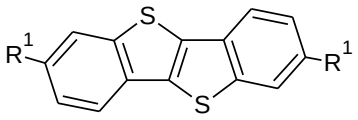

Adjust R^1 to alter absorbance peak of the BTBT derivative

Figure 8.1: Potential method to adjust absorbance maximum of BTBT derivatives.

8.2.3 Electrode design

Throughout this research, we have utilized the traditional OFET electrode design of a parallel source and drain for device testing. Phototransistors can operate with a much higher sensitivity by maximizing the surface area while minimizing the channel length. This is because excited electrons will have a shorter distance to travel to reach the source and drain, reducing the chances of charge recombination by defects or impurities. The simplest method to do this is to create an interdigitated device pattern such as that shown below in **Fig. 8.2**.

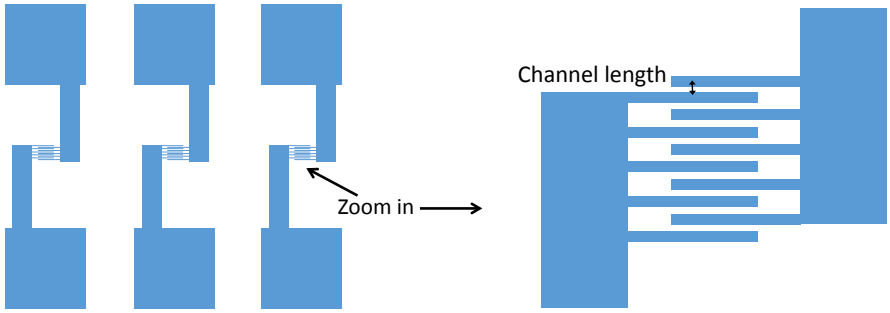

Figure 8.2: Electrode Design allowing for increased surface area with decreased channel length. Additionally the large pads at the ends can allow for the addition of alligator clips as electrode leads, allowing for testing of flexible substrates.

8.2.4 Generating an all organic device

The goal of all organic electronics is to remove the brittle silicon components and replace them with flexible organic materials. We can test if this system will perform on a flexible device design. A good suggested starting point for this synthesis is to use a PET/ITO substrate/gate and spin coat on a PVP:HDA dielectric layer (**Fig 8.3**).[2,3] The semiconductor can be spin coated on this followed by the addition of source and drain electrodes. This device architecture already has an example in the literature using C8-BTBT to generate incredibly high mobility devices,[4] so we know fabrication is possible.

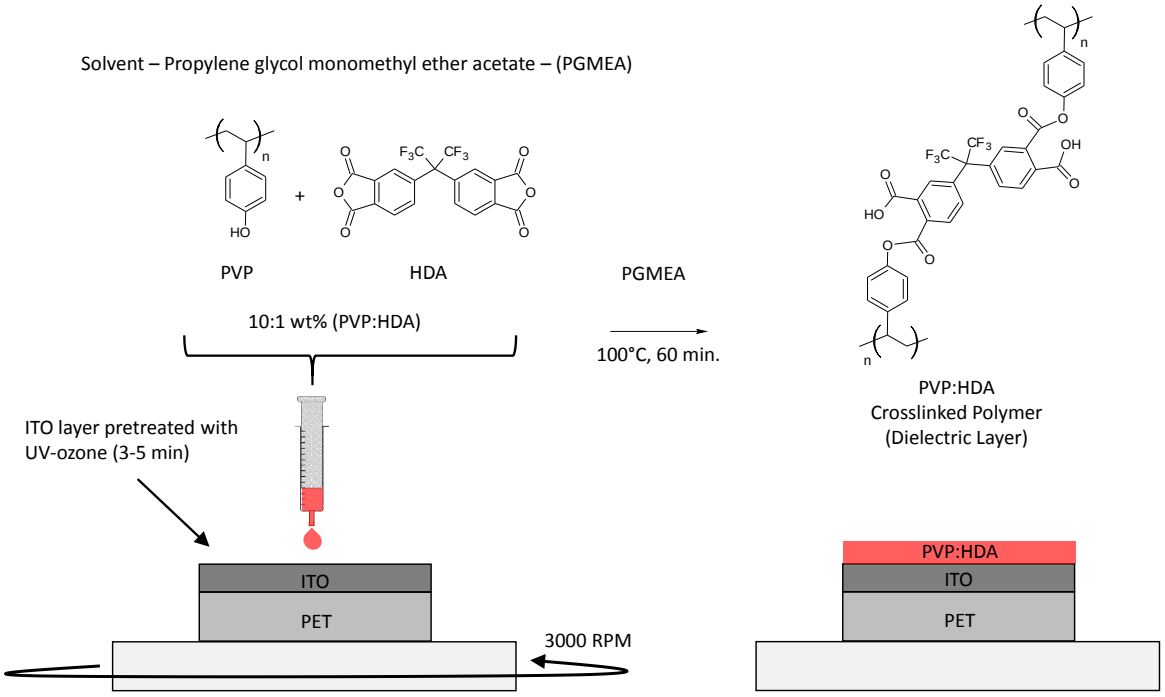

Figure 8.3: Synthesis to generate an all organic substrate with gate and dielectric layer ready for the addition of a solution processed semiconductor.

8.3 Contributions of this thesis work

The work of this thesis can be summarized in three major contributions to the scientific community:

1) The wide HOMO energy spread of unsorted SWCNT's allows them to be used to reduce the charge injection resistance between an energy mismatched electrode and semiconductive channel.

2) We developed a narrow wavelength UV phototransistor that is solution processable and air stable, utilizing a UV sensitive semiconductor.
3) We developed a methodology for choosing appropriate materials to be used in conjunction with the UV sensitive semiconductor to modulate device performance.

8.4 Final thoughts

The continued advancement of organic electronics and printed electronics undoubtedly shows that they will become commercially relevant in the near future. For this reason a thorough understanding of how to manipulate material choices to add advanced functionality will become an essential field. It is my hope that through my use of blended systems, I have been able to provide additional insight into how one can better choose the appropriate material to achieve their device goals.

8.5 References

1. Ljubic, D., Smithson, C. S., Wu, Y. & Zhu, S. Highly UV-Sensitive and -Responsive Benzothiophene/Dielectric Polymer Blend-Based Organic Thin-Film Phototransistor. *Adv. Electron. Mater.* n/a–n/a (2015). doi:10.1002/aelm.201500119

2. Roberts, M. E. *et al.* Cross-Linked Polymer Gate Dielectric Films for Low-Voltage Organic Transistors. *Chem. Mater.* **21,** 2292–2299 (2009).

3. Roberts, M. E., Mannsfeld, S. C. B., Stoltenberg, R. M. & Bao, Z. Flexible, plastic transistor-based chemical sensors. *Org. Electron.* **10,** 377–383 (2009).

4. Yuan, Y. *et al.* Ultra-high mobility transparent organic thin film transistors grown by an off-centre spin-coating method. *Nat. Commun.* **5,** 3005 (2014).